eman ta zabal zazu

Universidad
del País Vasco

Euskal Herriko
Unibertsitatea

DOCTORAL THESIS

DEVELOPMENT OF HEUSLER – ALLOY – BASED MAGNETOCALORIC INKS FOR 2D – 3D PRINTING

BOSCO RODRIGUEZ CRESPO

2024

Supervisors:

Dr. Daniel Salazar

Prof. Volodymyr Chernenko

Este trabajo de investigación para optar al Grado de Doctor por la Universidad del País Vasco (UPV/EHU) se ha realizado en colaboración entre el Basque Center for Materials, Applications and Nanostructures (BCMaterials), el Departamento de Electricidad y Electrónica de la Facultad de Ciencia y Tecnología y el instituto Funktionale Materialien (FM) de TU Darmstadt.

Por otro lado, la tesis ha sido posible gracias a la financiación obtenida desde diferentes fuentes a nivel nacional y estatal, como la beca para la formación de personal investigador con instituciones y empresas (PIFI20/10) otorgada por la UPV/EHU.

Asimismo, esta tesis también ha sido posible gracias a la ayuda financiera del Ministerio de Ciencia, Innovación y Universidades (Proyecto RTI2018-094683-B-C53-54) y el Departamento de Educación del Gobierno Vasco (Proyecto IT1245-19). También agradecer a la financiación del Departamento de Industria y Educación del Gobierno Vasco mediante los programas ELKARTEK y PIBA (PIBA-2018-06).

Agradecimientos

Cuando empecé este viaje hace poco más de cuatro años, nunca imaginé la profundidad del compromiso y las adversidades que encontraría en el camino. La realización de esta tesis doctoral ha sido una travesía llena de desafíos y descubrimientos, y hoy, al llegar al final de este capítulo, me siento profundamente agradecido por todas las personas que han sido parte de esta experiencia. Lo más difícil de escribir estas líneas va a ser no olvidar de mencionar a todas las personas, pues en esta etapa son muchas con las que he tenido la fortuna de compartir experiencias y conocimientos.

En primer lugar, quiero expresar mi agradecimiento a mis directores de tesis Dr. Daniel Salazar y Prof. Volodymyr Chernenko, pues sin ellos ni su apoyo nada de esto hubiera sido posible. Su guía experta, apoyo inquebrantable y confianza en mí han sido fundamentales para este logro. Han sido no solo mentores, sino también modelos a seguir que me han inspirado a alcanzar mis metas académicas. Agradecer también a mi tutor Jon Gutiérrez por su ayuda.

Quiero agradecer también a la Fundación BCMaterials por la gran oportunidad que me dieron para poder realizar allí la tesis y a la Universidad del País Vasco (UPV/EHU) por otorgarme la beca para la formación de personal investigador con instituciones y empresas (PIFI20/10).

A mi familia, a quienes debo tanto, quiero agradecerles por su apoyo constante. A mis padres, por inculcarme valores y proporcionarme la base sólida desde la que he podido construir mi carrera profesional y personal.

En el laboratorio hemos acabando formando un equipo excepcional de compañeros y, sobre todo amigos, entre Andrés G, James R, Mariana R, Santiago C y los numerosos visitantes y colaboradores que nos han acompañado a lo largo de estos años. Cada uno ha aportado su granito de arena a que cada día ir a trabajar sea más ameno. Las discusiones intelectuales y no tan intelectuales en los cafés diarios (la razón real por la que todos venimos al trabajo) y las colaboraciones que hemos forjado han sido esenciales para hacer que la tesis sea mucho más disfrutable.

La tesis ha traído consigo una sucesión de muchos altibajos los cuales han sido sobrellevados mucho mejor gracias a la compañía y motivación de mis compañeros. En especial, mi grupo de metaleros metalúrgicos, J Napal, A Reizábal, D Payno, P González, A García, F Zheng, N Barroso, P Lazpita, JM Porro, N Perinka, S Lanceros, el equipo de administración de BCMaterials y todos los compañeros con los que he coincidido y colaborado.

I also want to thank to all the people of Funktionale Materialien (FM) from TU Darmstadt, that allowed me to make a three month stay in their center, where I had the opportunity to work with people that are a world reference for the subject of my thesis and that let me work in their facilities. In special, thank you Prof. Dr. O Gutfleisch, Dr. K Skokov, Dr. F Scheibel, Dr. A Aubert, Dr. S Ener, K Schäfer, B Beckmann, Rafael G, Dr. L Pfeuffer, Dr. L Schäfer, M Laux and all the people that made my stay unforgettable.

También quiero agradecer al personal de servicios generales de la universidad, por su gran apoyo y ayuda a la hora de poder hacer uso de sus equipos. A Iñaki Orue, por las eternas peleas con el VSM y el SQUID y a Aitor Larrañaga por su gran ayuda a la hora de hacer medidas de difracción de rayos X.

Y, por último, pero no menos importante, a Dídac Mesa Romeu, por ser el hermano mayor que nunca tuve, y por permitirme usar algunas de sus increíbles astrofotografías nocturnas para la contraportada de la tesis y algunos capítulos.

Gracias por haber sido parte integral de este capítulo de mi vida.

Con aprecio sincero,

Bosco.

Resumen

En la búsqueda de tecnologías de refrigeración sostenibles y eficientes en energía, el estudio de los efectos calóricos ha surgido como una vía prometedora. Esta tesis doctoral se embarca en una exploración extensa del efecto magnetocalórico, con el objetivo principal de permitir la impresión 3D rentable de estructuras magnetocalóricas utilizando materiales respetuosos con el medio ambiente. La investigación abarca la síntesis de aleaciones Heusler magnéticas con memoria de forma, la preparación de cintas metálicas, tratamientos térmicos, producción de polvo y la transformación de estos materiales en tintas imprimibles, culminando en la fabricación aditiva de estructuras 3D complejas con propiedades magnetocalóricas conservadas en cada paso.

La tesis comienza con una introducción exhaustiva de los efectos calóricos, con un enfoque en el efecto magnetocalórico. El efecto magnetocalórico, caracterizado por cambios de temperatura en respuesta a variaciones en el campo magnético, representa una vía alternativa para soluciones de enfriamiento sostenible y gestión térmica eficiente en energía. Entre los materiales existentes que muestran el efecto magnetocalórico, la tesis se centra en una familia de materiales llamada aleaciones magnéticas de memoria de forma Heusler, específicamente en aquellas basadas en combinaciones de Níquel y Manganeso con otros elementos.

El primer paso de la tesis es proporcionar una visión general completa de los materiales magnetocalóricos del tipo Heusler, con un enfoque en sus propiedades estructurales y magnéticas. Esta sección incluye una exploración detallada del efecto magnetocalórico, las transiciones de fase y los principios subyacentes de estos materiales. El estudio profundiza en la incorporación de ciertos elementos en los sistemas de aleaciones, elucidando su impacto

profundo en las propiedades de las aleaciones Heusler y la mejora del efecto magnetocalórico. El trabajo se centra en lograr composiciones de aleación óptimas que equilibren la eficiencia y las consideraciones ambientales.

La investigación pasa de la exploración teórica basada en la investigación de la literatura a la implementación práctica a medida que se fabrican múltiples aleaciones magnetocalóricas de Heusler mediante diferentes técnicas. Empleando la técnica de *melt-spinning*, las aleaciones se transforman en cintas metálicas, allanando el camino para la optimización posterior a través de tratamientos térmicos estratégicamente diseñados. Se realiza un estudio sistemático de los tratamientos térmicos para afinar las propiedades magnéticas y magnetocalóricas de las cintas, con el fin de lograr las propiedades óptimas.

Un avance innovador en la tesis gira en torno a la transformación de las cintas en tintas imprimibles para su posterior implementación en impresión 2D y 3D. A través de molienda mecánica, las cintas se convierten en polvo, al cual se le realizan tratamientos térmicos para contrarrestar los efectos de la degradación del material inducida por la molienda. Este polvo más adelante se mezcla con diversos polímeros biodegradables, entre ellos celulosa, que es un polímero respetuoso con el medio ambiente y con mucha biodisponibilidad, para crear tintas imprimibles para aplicaciones de fabricación aditiva, inaugurando la capacidad de elaborar estructuras 3D, preservando las propiedades magnetocalóricas de las cintas.

Para desarrollar tanto la técnica de impresión 2D, mediante serigrafía, como la de 3D, mediante el proceso llamado impresión por extrusión, primeramente, se emplearon polvos metálicos comerciales (Hierro, Aluminio, Silicio) sin ninguna funcionalidad, dado que estos polvos son económicos y fáciles de obtener. De esta forma se abrió la puerta a, primeramente, desarrollar la ruta de creación y optimización de tintas imprimibles y, después, a encontrar las limitaciones de las técnicas de impresión, y encontrar las estructuras que eran imprimibles y encontrar las limitaciones que cada técnica de impresión tenía.

Una vez encontrados los parámetros que optimizaban los procesos de impresión se implementó a los polvos magnetocalóricos para así obtener films 2D y estructuras 3D magnetocalóricas de diversas formas y tamaños.

La primera validación de las tintas magnetocalóricas se realizó mediante impresión 2D por serigrafía. Las primeas pruebas de impresión se realizan imprimiendo figuras geométricas muy simples de una sola capa y posteriormente se aplican múltiples capas para aumentar así la cantidad de material funcional que contiene el film impreso. Debido a la naturaleza de la celulosa, se obtuvieron films flexibles con un alto contenido en material magnetocalórico, que podrían servir para aplicaciones en dispositivos de electrónica. Además, estos films impresos preservan las propiedades magnetocalóricas del material funcional precursor, quedando así validad la técnica de impresión 2D para materiales magnetocalóricos (ver Figura 1).

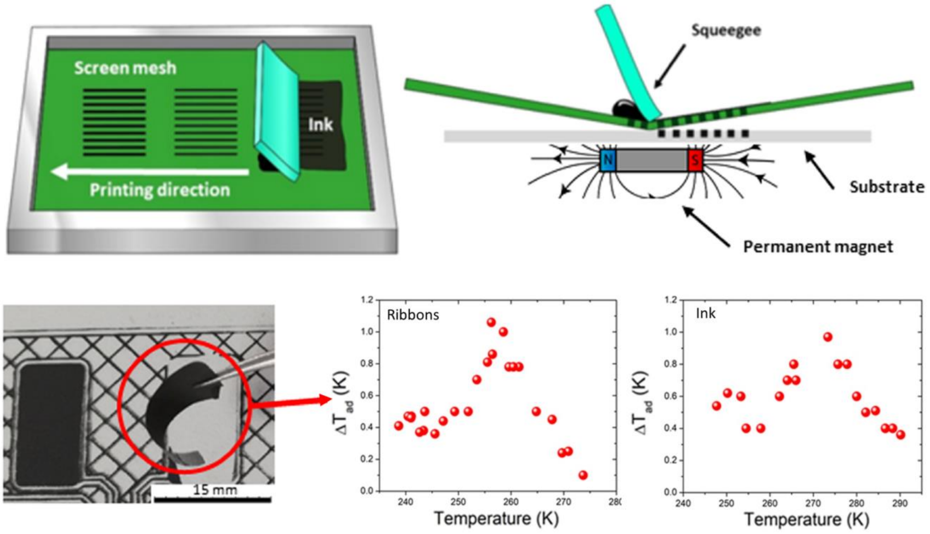

Figure 1: Esquema del proceso de impresión 2D por serigrafía. Las propiedades magnetocalóricas del film flexible impreso son análogas a las de las cintas, que constituyen el material precursor.

Una vez validadas las tintas en la impresión 2D se procede a su implementación en la impresión 3D, lo cual constituye el núcleo de la tesis. La implementación de materiales magnetocalóricos Heusler para la impresión 3D de estructuras como paso preliminar a la fabricación de intercambiadores de calor magnetocalóricos es el objetivo principal de la tesis. Se presenta la metodología para diseñar e imprimir estos intercambiadores de calor, abordando los desafíos y oportunidades asociados con el proceso.

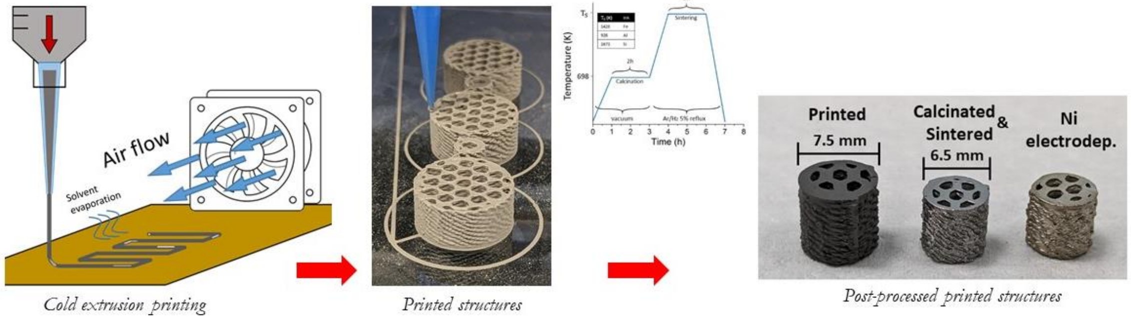

Figure 2: Proceso de impresión 3D implementado a los materiales magnetocalóricos. Tras la impresión se logra eliminar el polímero mediante tratamientos térmicos de calcinación y posteriormente se realiza un proceso de sinterización que le otorga integridad estructural y dureza a la estructura impresa.

El objetivo final de la tesis culmina en la fabricación aditiva de materiales magnetocalóricos, donde se obtienen estructuras 3D magnetocalóricas (ver Figure 2). Después de la impresión, estas estructuras se someten a tratamientos térmicos para eliminar el polímero mediante calcinación seguido de un tratamiento térmico adicional para sinterizar el polvo de la estructura, dando como resultado componentes compactos y funcionales.

Un paso importante a superar consiste en conseguir retener las propiedades magnetocalóricas tras la eliminación del polímero y la posterior sinterización, pues el polímero va en detrimento de las propiedades magnetocalóricas del material impreso. Para ello, se lleva a cabo una exploración exhaustiva de diversas rutas de sinterización, en las que se investiga la influencia de la atmósfera bajo la cual se realizan los tratamientos térmicos y de los gases inertes empleados en dicho proceso, con el objetivo de lograr un equilibrio óptimo entre la integridad mecánica y la eficiencia magnetocalórica.

La tesis culmina con la validación de la técnica de impresión 3D por extrusión a los materiales magnetocalóricos logrando mantener las propiedades magnetocalóricas en cada proceso hasta lograr obtener una estructura 100% magnetocalórica, abriendo las puestas a futuras aplicaciones en el sector de la refrigeración de estado sólido.

Laburpena

Energian eraginkorrak eta iraunkorrak diren hozte-teknologien bilaketan, kaloria-efektuen azterketa etorkizun handiko bide gisa sortu da. Doktorego-tesi hau efektu magnetokalorikoaren esplorazio zabal batean oinarritzen da, ingurumena errespetatzen duten materialak erabiliz egitura magnetokalorikoen 3D inprimaketa errentagarria ahalbidetzeko helburu nagusiarekin. Ikerketak barne hartzen ditu forma-memoria duten Heusler aleazio magnetikoen sintesia, zinten prestaketa, tratamendu termikoak, hautsaren ekoizpena eta material horiek tinta inprimagarri bihurtzea, eta urrats bakoitzean kontserbatutako propietate magnetokalorikoak dituzten 3D egitura konplexuen fabrikazio gehigarria burutzea.

Tesia kaloria-efektuen sarrera sakon batekin hasten da, efektu magnetokalorikoaren ikuspegiarekin. Efektu magnetokalorikoa, eremu magnetikoan izandako aldaketei erantzuteko tenperatura-aldaketek ezaugarritzen dutena, hozte iraunkorreko eta energia-kudeaketa termikoko soluzioetarako bide alternatibo bat da. Efektu magnetokalorikoa erakusten duten materialen artean, tesia Heusler formako memoria-aleazio magnetikoak izeneko material-familia batean zentratzen da, bereziki NiMn-ean oinarritutako materialetan.

Tesiaren lehen urratsa Heusler motako material magnetokalorikoen ikuspegi orokor osoa ematea da, propietate estrukturalak eta magnetikoak kontuan hartuta. Atal honetan, efektu magnetokalorikoaren, fase-trantsizioen eta material horien azpiko printzipioen azterketa xehatua egiten da. Ikerketak aleazio-sistemetan zenbait elementu sartzean sakontzen du, Heusler aleazioen propietateetan duten eragin sakona eta efektu magnetokalorikoaren hobekuntza

saihestuz. Lana ingurumenaren eraginkortasuna eta kontsiderazioak orekatuko dituzten aleazio-konposizio optimoak lortzean oinarritzen da.

Ikerketa literaturaren ikerketan oinarritutako miaketa teorikotik inplementazio praktikora igarotzen da, hainbat teknika erabiliz Heusler aleazio magnetokaloriko ugari fabrikatzen diren heinean. Melt-spinning teknika erabiliz, aleazioak zinta bihurtzen dira, ondoren optimizatzeko bidea erraztuz, estrategikoki diseinatutako tratamendu termikoen bidez. Tratamendu termikoen azterketa sistematikoa egiten da zinten propietate magnetikoak eta magnetokalorikoak doitzeko, propietate optimoak lortze aldera.

Tesiaren aurrerapen berritzaile bat zintak 2D eta 3D inprimaketaren bidez tinta inprimagarri bihurtzearen ingurukoa da. Ehotze mekanikoaren bidez, zintak hauts bihurtzen dira, eta horri tratamendu termikoak egiten zaizkio ehotzeak eragindako materialaren degradazioaren ondorioak indargabetzeko. Hauts hori hainbat polimero biodegradagarrirekin nahasten da, besteak beste, zelulosarekin. Polimero horrek ingurumena errespetatzen du, fabrikazio gehigarriko aplikazioetarako tinta inprimagarriak sortzeko, 3D egiturak egiteko gaitasuna inauguratuz eta zinten propietate magnetokalorikoak zainduz.

Tesiaren muina egiturak 3D inprimatzeko Heusler material magnetokalorikoak inplementatzean datza, bero-trukagailu magnetokalorikoak fabrikatzeko aurretiazko urrats gisa. Bero-trukagailu horiek diseinatzeko eta inprimatzeko metodologia aurkezten da, prozesuarekin lotutako erronkei eta aukerei helduz. 3D inprimaketa-teknikaren estrategia garatzeko, burdinazko, aluminiozko eta siliziozko hauts komertzialak erabiltzen dira, tintaren eta inprimaketaren parametroak optimizatzeko. Teknika ondo garatuta dagoenean, hauts magnetokalorikoaren inprimaketari aplikatzen zaio.

Tesiaren azken helburua material magnetokalorikoen fabrikazio gehigarria da, non 3D egitura magnetokalorikoak lortzen diren. Inprimaketaren ondoren, egitura horiek tratamendu termikoak jasaten dituzte, polimeroa kaltzinazio bidez desagerrarazteko eta sinterizazioari ekiteko; ondorioz, osagai trinkoak eta funtzionalak lortzen dira. Hainbat sinterizazio-ibilbideren azterketa sakona egiten da, osotasun mekanikoaren eta eraginkortasun magnetokalorikoaren arteko oreka optimoa lortzeko.

Abstract

In the quest for sustainable and energy-efficient cooling and refrigeration technologies, the study of caloric effects has emerged as a promising avenue. This doctoral thesis embarks on an extensive exploration of the magnetocaloric effect, with a primary goal of enabling the cost-effective 2D – 3D printing of magnetocaloric structures using environmentally-friendly materials. The research encompasses the synthesis of Heusler magnetic shape memory alloys, ribbon preparation, heat treatments, powder production, and the transformation of these materials into printable inks, culminating in the additive manufacturing of complex 2D – 3D structures with retained magnetocaloric properties at each step.

An in-depth exploration into the magnetocaloric effect inherent in Heusler magnetic shape memory alloys, with a primary focus on elucidating the potential technological applications of this caloric phenomenon is studied. The introductory discourse provides a thorough examination of caloric effects, with specific attention directed towards the magnetocaloric effect and its relevance in diverse technological domains.

The research rigorously investigates the off-stoichiometric NiMn-X (X=Sn, In,Ga) Heusler alloys, elucidating the nuanced impact of the incorporation of dopant elements such as Cobalt, Copper and Iron on their transformation, magnetic and magnetocaloric properties. Employing the melt-spinning technique, ribbons are fabricated and subjected to a systematic heat treatment protocols designed to optimize their transformation, magnetic and magnetocaloric properties.

A route for powder preparation from the ribbons is studied and established. This powder undergoes a refined heat treatment procedure to mitigate the

detrimental effects of grinding, ensuring the preservation of magnetocaloric properties during this material processing.

Characterization of both ribbons and powder serves as the foundational groundwork for the subsequent exploration of additive manufacturing applications. Formulation of printable inks utilizing cellulose as a polymer facilitates the creation of novel 2D-3D structures through additive manufacturing techniques.

Following the printing process, the fabricated structures undergo a meticulous heat treatment regime, involving calcination to remove the polymer and sintering to achieve structural compactness and mechanical integrity. Various sintering routes are systematically investigated to discern the optimal approach that balances mechanical robustness with the preservation of magnetocaloric effects throughout each stage.

The overarching objective of this research is to demonstrate the sustained retention of magnetocaloric properties across the entire spectrum of processes, from alloy fabrication to melt-spinning, heat treatment to grinding, additive manufacturing to sintering and getting 100% magnetocaloric 3D structure. The findings not only contribute nuanced insights into the manipulation of Heusler alloys for practical applications but also pave the way for the development of advanced materials with enhanced magnetocaloric functionalities in the sector of additive manufacturing.

Visual Abstract

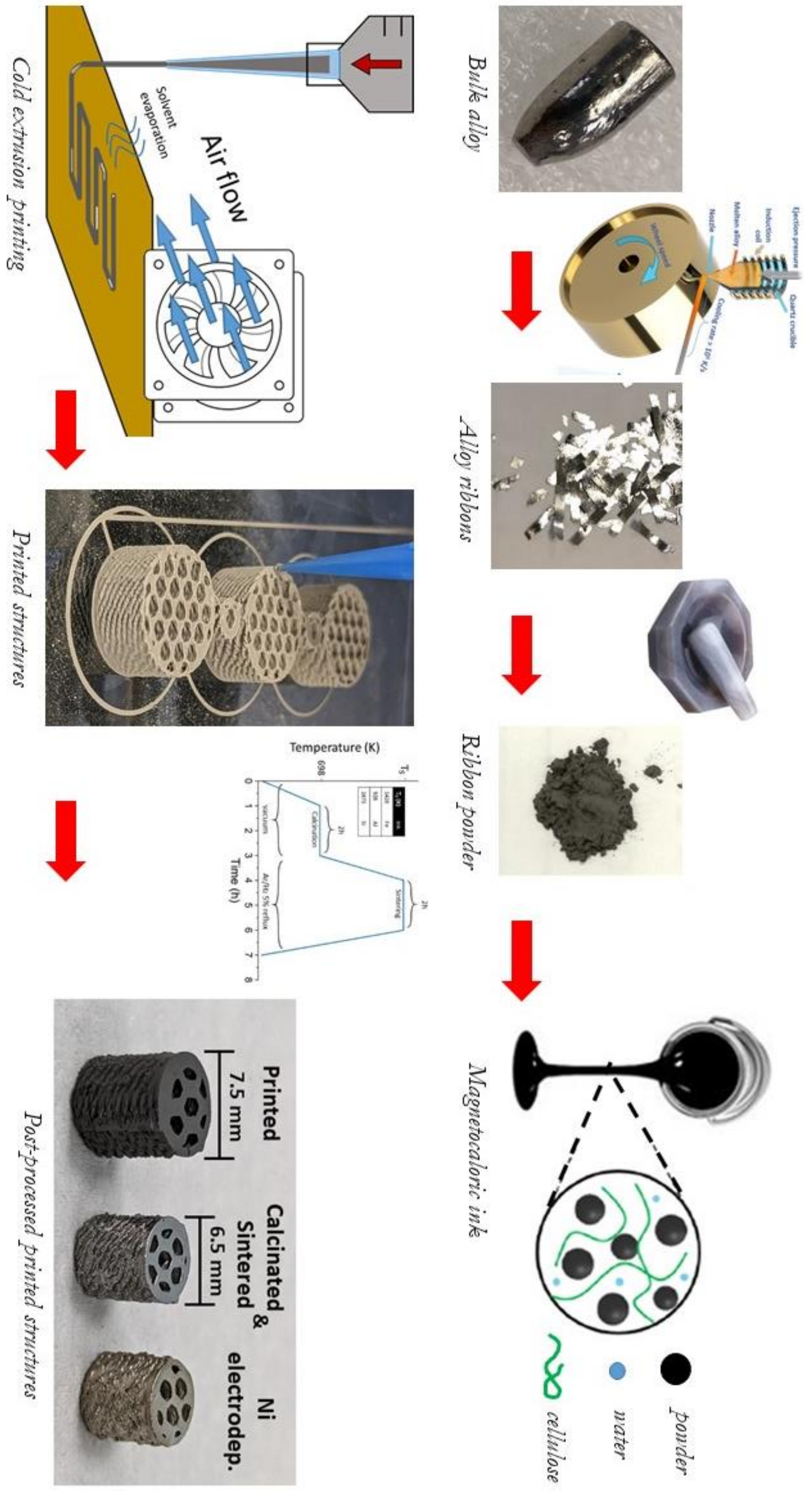

Contents

Chapter 1

Introduction

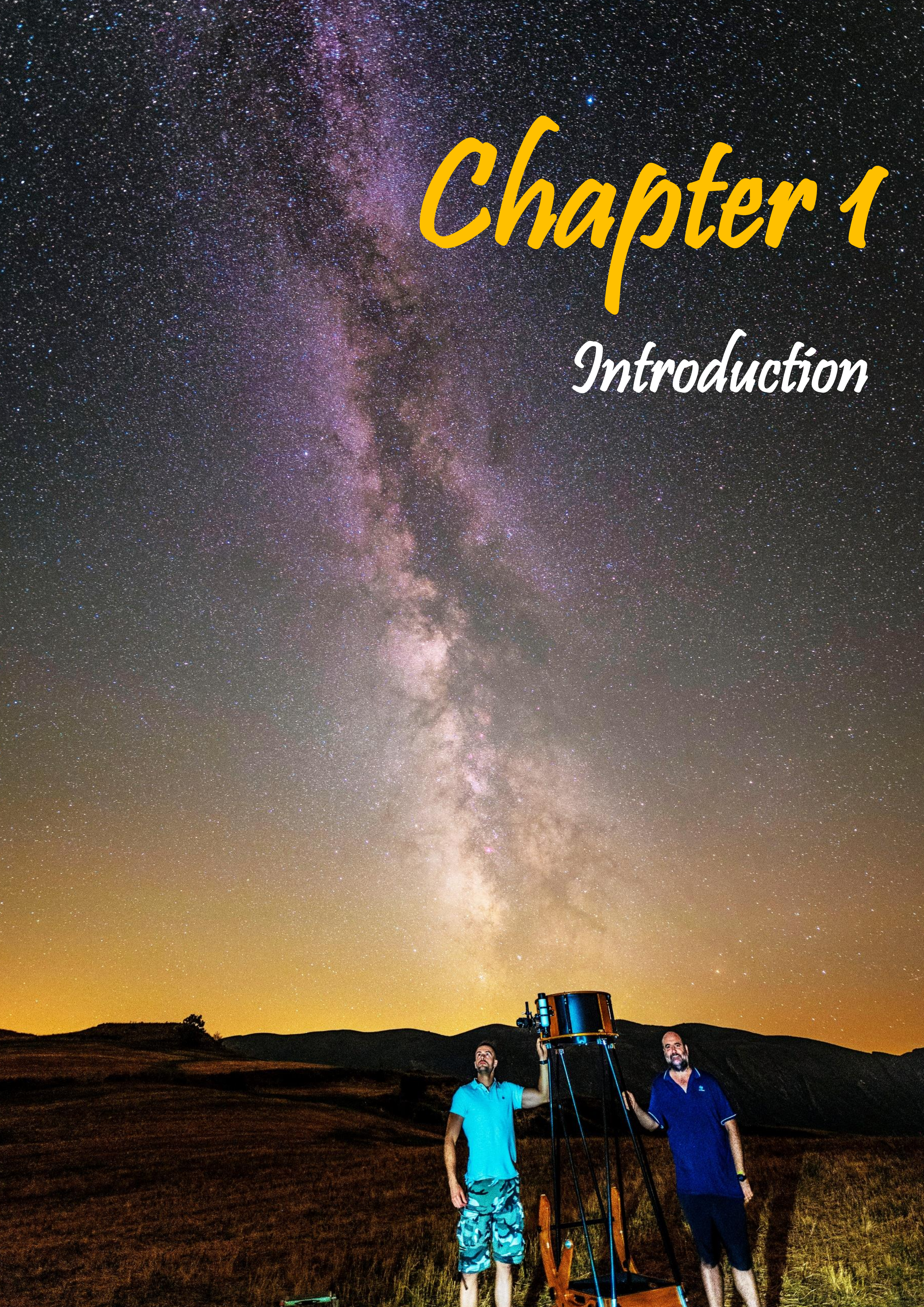

Chapter 1

Introduction

1.1. MOTIVATION

Global warming and growing energy demand are among the most urgent challenges for both the well-being of the Earth's inhabitants and for the world economy. Therefore, science and technology are increasingly searching for new approaches to reduce energy consumption and greenhouse gas emissions. Specifically, the annual tendency of global temperature increase has led to an increase of conditioner air and general refrigeration use, representing nearly 20% of the total electricity used in buildings around the globe today[1]. Current refrigeration is based on gas expansion-compression cycles and is called *conventional refrigeration*. Despite its wide use, the process is not very efficient, with the best available systems having up to 40% of Carnot efficiency. It also uses harmful gases for the atmosphere like CFC's, HCFC's which are up to 4000 times more harmful than CO_2[2]. As a more sustainable alternative, *solid state refrigeration* is considered a promising option that can be about 50% more efficient than conventional methods, while avoiding the use of harmful materials[3][4].

This solid-state refrigeration is based on caloric effects, which are properties of the so-called caloric materials, a family of metallic functional materials that exhibit a thermal response to an external stimulus. Specifically, the magnetocaloric effect (MCE) is currently under world-wide investigation in a family of materials that are promising candidates for room temperature refrigeration. The magnetocaloric material would act as a heat exchanger in a magnetic refrigerator that comprises a heat transfer fluid and a source of a magnetic field.

In order to design a really functional heat exchanger a certain geometry of MC material is needed to optimize refrigeration. For complex geometries, additive manufacturing (AM), a technique that builds 3D structures layer by layer, is a very useful and growing technology providing wide variety of possibilities. However, since current metallic 3D printing technologies involve complex and energy-consuming equipment, it is desirable to explore a more sustainable alternative that uses environmentally-friendly materials.

1.2. CALORIC MATERIALS

Caloric materials can be classified according to the stimulus that generates the thermal response. Depending on this stimulus, the effect that these materials exhibit is called the magnetocaloric (MC) effect (in response to a magnetic field), electrocaloric (EC) effect (due to an electric field), barocaloric (BC) effect (in response to pressure), elastocaloric (eC) effect (due to strain), and more. For the Magnetocaloric Effect (MCE), the mechanism leading to the thermal response is the change in magnetization (M) caused by a magnetic field (H). In the case of the Electrocaloric Effect (ECE), the response is the variation in dipole polarization generated by an electrical field (E). The Barocaloric Effect (BCE) is generated by isotropic stress resulting from hydrostatic pressure that shrinks the material, while the Elastocaloric Effect (eCE) occurs when a material is deformed under uniaxial stress. The properties that characterize caloric materials include adiabatic temperature change (ΔT_{ad}), isothermal entropy change (ΔS_{iso}) and isothermal heat (*Q*). On the other hand, caloric effects can be classified according to the sign of the thermal response upon the external stimulus applied, resulting in either a *conventional* or *inverse* caloric effect:

- *Conventional caloric effect* → $\Delta T_{ad} > 0 \; \& \; \Delta S_{iso} < 0$
- *Inverse caloric effect* → $\Delta T_{ad} < 0 \; \& \; \Delta S_{iso} > 0$

The caloric effect can be measured using both direct and indirect methods to get ΔT_{ad}, ΔS_{iso} and Q values. Direct adiabatic temperature change measurement is the primary method for quantifying the caloric effect. However, achieving ideal conditions for this measurement can be challenging, so the literature often reports ΔS_{iso} values using indirect methods. The thermodynamic relationship that links the theoretical ΔT_{ad} and ΔS_{iso} is:

$$\Delta T_{ad} = \frac{T \cdot \Delta S_{iso}}{C_p} \tag{1}$$

where T represents the temperature at which the transformation happens, and C_p denotes the heat capacity[5]. The entropy change is calculated indirectly using Maxwell's relationships. For a magnetocaloric material, this relationship can be expressed as follows:

$$\left(\frac{\partial M}{\partial T}\right)_H = \left(\frac{\partial S}{\partial H}\right)_T \Rightarrow \Delta S_m = \mu_0 \int_{H_i}^{H_f} \left(\frac{\partial M}{\partial T}\right)_H dH \tag{2}$$

According to Eq.(1), the magnitude of the temperature change is minimal around room temperature and only becomes significant at lower temperatures where the specific heat of the material is reduced. This characteristic has made these materials well-suited for low-temperature cooling [6]. However, since the discovery of magnetocaloric materials with a phase transformation occurring near room temperature [7], research over the last two decades has shifted its focus towards room-temperature cooling. Numerous studies have demonstrated the feasibility of achieving a meaningful room-temperature cooling in a wide range of materials, provided that the right materials are chosen.

1.2.1. Magnetocaloric effect

The magnetocaloric effect is defined as the heating or cooling of a magnetic material upon the application or removal of a magnetic field. It was first theoretically predicted by William Thomson (Lord Kelvin) in 1860[8] and later in 1878[9]. Thomson deduced that iron would warm up when a magnetic field was applied to it and cool down when the field was removed. While some literature claims that E. Warburg was first who has observed the MCE in iron in 1881[10][11], the phenomenon was explicitly demonstrated only in 1917 by Weiss and Piccard. They measured Ni around its Curie temperature at 1.5T and found a temperature change of 0.7 K[11]. In 1933, Giauque and MacDougall achieved sub Kelvin temperature of 0.25 K using a demagnetization of the paramagnetic $Gd_2(SO_4)_3 \times 8H_2O$ salt cooled by liquid helium from 1.5 K [12]. Three decades later, in 1967, Brown constructed a reciprocating magnetic refrigerator to demonstrate the feasibility of room-temperature magnetic refrigeration using Gd metal[13], achieving a temperature span of 47 K after 50 cycles.

After this period, MCE was not extensively investigated until 3 decades later when Pecharsky and Gschneider discovered the giant magnetocaloric effect (GMCE) in $Gd_5Si_2Ge_2$ in 1977[7]. For this alloy, the MCE was enhanced due to a structural transformation that comes with the magnetic transition. Following this discovery, the number of publications on the magnetocaloric effect and magnetic refrigeration was steadily increasing with some recent stabilization trend (Figure 1.1).

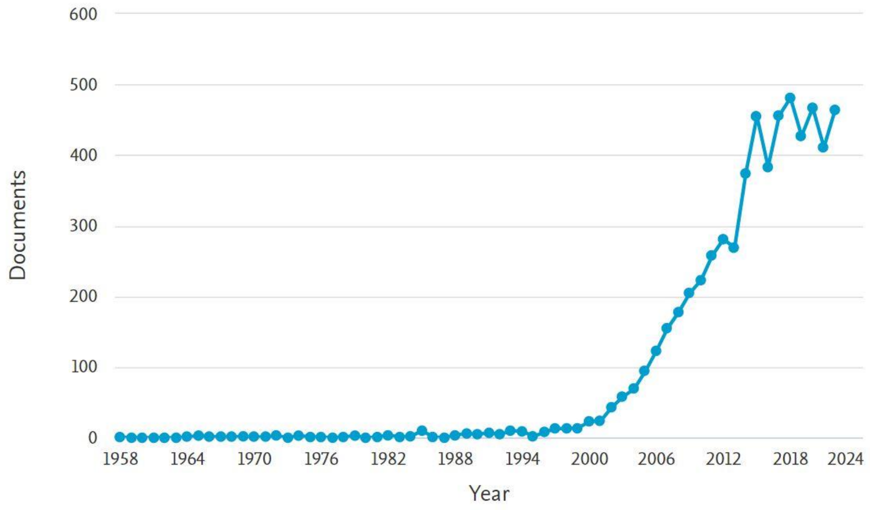

Figure 1.1: Publications about magnetocaloric effect over past decades (SCOPUS).

Enhanced properties of magnetocaloric materials achieved over the last decades have increased the interest in using them for solid-state refrigeration instead of a gas-expansion-compression technology of a *conventional refrigeration*. The replacement of traditional technology by solid state refrigeration, particularly, by MCE cooling, offers several advantages:

- Environmentally-friendliness since it does not use ozone-depleting gases like (CFC's, HCFC's)
- Higher efficiency (60% of Carnot efficiency compared to 40% for conventional refrigeration), requiring less energy and resulting in reduced CO_2 emissions
- Lower costs
- Minimal maintenance and reduced noise

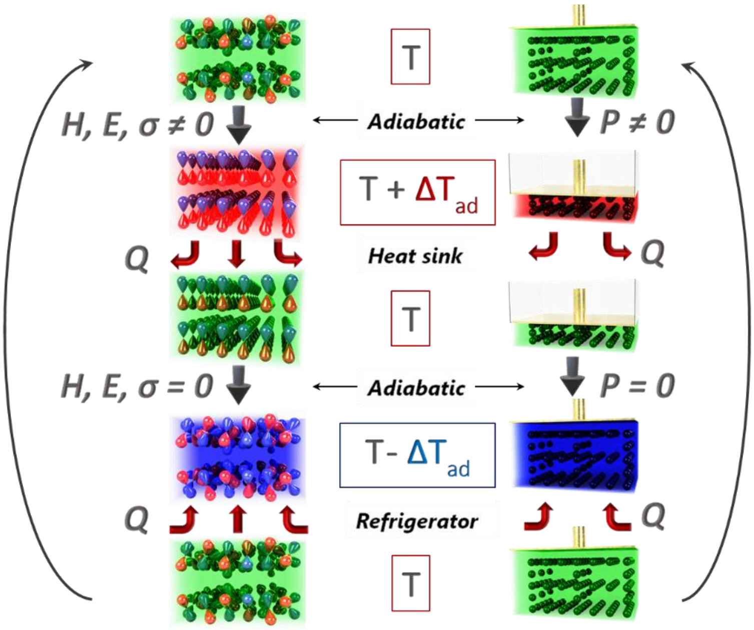

Figure 1.2: Visualization of magnetocaloric cooling in a single cycle versus its analogue for the vapour compression system.

Figure 1.2 illustrates the fundamental working mechanism of magnetic refrigeration in comparison to its vapour expansion-compression refrigerator counterpart. In the case of conventional refrigeration, a gas undergoes adiabatic compression and decompression, resulting in heat generation during compressing and heat dissipation during adiabatic decompression. Analogously, in solid-state refrigeration, the cycle starts with the material at thermal equilibrium, with magnetic moments randomly oriented.When a magnetic field is applied under an adiabatic conditions, the magnetic dipoles align with the magnetic field, causing the sample to experience a temperature increase due to a decrease in its magnetic entropy. After the increased heat dissipates through a radiator, the material returns to its initial temperature. When the magnetic field is removed adiabatically, the material experiences a temperature decrease, reaching a lower temperature than the initial one. This stage can be used for refrigeration. After this, the material thermally stabilizes and the cycle starts again.

Both conventional and inverse magnetocaloric effects are characterized by the isothermal entropy change, Δ*S*m(*T*, H), and/or the adiabatic temperature change, Δ*T*ad(*T*, H), when a magnetic field is applied or removed under isothermal or adiabatic conditions, respectively[14][15]. In the most easiest way, the magnetic field induced entropy change can be estimated using a thermodynamic Maxwell relationship[16], although in the case of the first-order magnetostructural transformations some additional considerations should be taken into account [16][17]. Commonly, thermomagnetic curves measured under the iso-field conditions are used to calculate Δ*S*m(*T*, H) through numerical approximation of the Maxwell relationship:

$$\Delta S_m(T,H) = S_m(T,H) - S_m(T,0) = \int_0^H \left(\frac{\partial M(T,H')}{\partial T}\right) dH' \qquad (3)$$

1.2.1.1. Conventional magnetocaloric effect

In terms of energy, the magnetocaloric effect is characterized as the change of magnetic entropy in an isothermal process or as the change of temperature under adiabatic conditions upon the applications of an external magnetic field (ΔH). The physical process of the MCE is related to the coupling between the external magnetic field and the magnetic moments within the material. First, we will explain the MCE mechanism with a pictorial description and then we will provide a more formal thermodynamic interpretation.

Let us assume a magnetic material is inside and outside a magnetic field (see Figure 1.3). When no magnetic field is applied, the magnetic moments are randomly oriented, giving rise to some entropy, which we will refer to as magnetic entropy, S_M. If we adiabatically apply a magnetic field to the material (Fig 1.3 left), the magnetic moments will become oriented with the field (let us assume fully oriented, for simplicity) and the magnetic entropy becomes zero $(S_M = 0)$, resulting in a negative change in magnetic entropy $(S_M < 0)$. Since the process is adiabatic, the total entropy change is zero $(\Delta S = 0)$. The total entropy change includes lattice (S_L), electronic (S_E) and magnetic (S_M) contributions so:

$$\Delta S = \Delta S_L + \Delta S_M + \Delta S_E = 0 \Rightarrow \Delta S_L + \Delta S_E = -\Delta S_M > 0 \qquad (4)$$

This positive change in electron and lattice entropy implies an increase in temperature of the material. When the magnetic field is adiabatically removed, the magnetic moments becomes disoriented, resulting in the cooling of the material. For MCE measurement, the adiabatic temperature change (ΔT_{ad}) achieved in this process of magnetization/demagnetization is used as a parameter to evaluate the material's cooling efficiency.

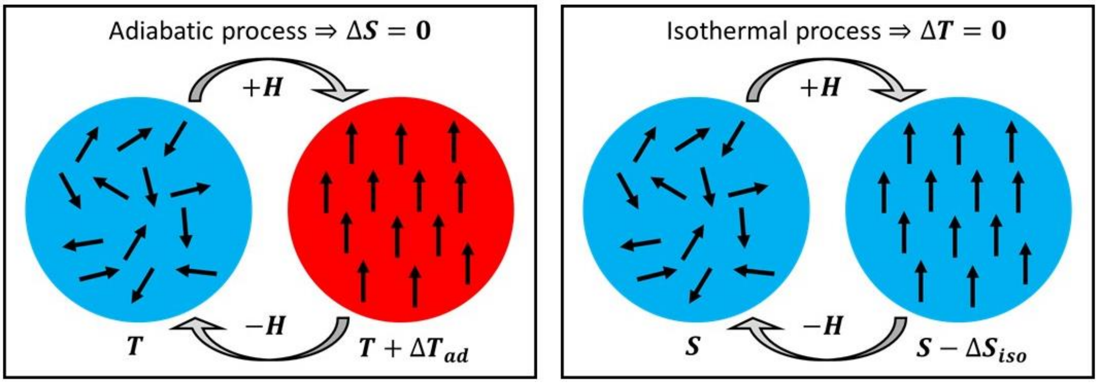

Figure 1.3: Schematic representation of application of an external magnetic field under adiabatic (left) and isothermal (right) conditions.

Apart from the adiabatic temperature change, the MCE can also be represented by the isothermal entropy change, ΔS_{iso}. Figure 1.3 right shows the magnetization process under isothermal conditions. In this case, magnetic entropy reaches zero after the alignment of the magnetic moments with the magnetic field, so the magnetic entropy change is negative ($\Delta S_M < 0$). This magnetic entropy, associated with magnetic moments, is “released” to the environment because the temperature remains constant, making it equals to ΔS_{iso} (assuming there is no coupling between the three contributions to entropy stated above). Unlike adiabatic temperature change, ΔS_{iso} is relatively easy to measure and is the most commonly reported parameter in MCE evaluations.

From these considerations, we can deduce that the largest entropy change and thus the largest adiabatic temperature change will be obtained when magnetic moments become fully disoriented at $H = 0$ and fully aligned at $H \neq 0$. The materials that can satisfy these conditions at ambient temperatures and achievable magnetic fields in practice are ferromagnets. For these materials, the magnetic moments naturally align themselves at the Curie temperature and ferromagnetic ordering can be achieved under relatively small magnetic fields. In the case of paramagnets, spontaneous ferromagnetic ordering does not occur and large magnetic fields are required to induce such order, making ferromagnets the only ones of practical interest.

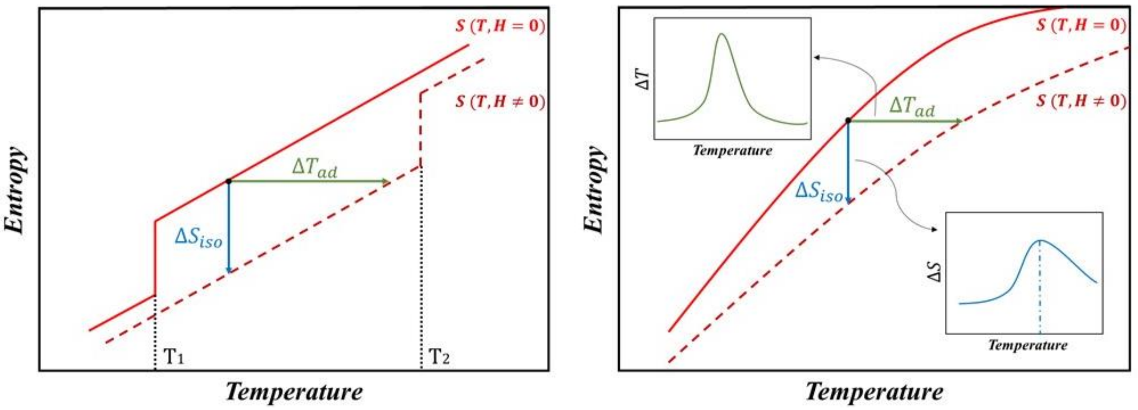

Figure 1.4: Entropy versus temperature behaviour of a magnetic material under no magnetic field and under a magnetic field for a first-order magnetic ordering (left) and a second-order magnetic ordering (right).

The magnetic entropy change depends on both magnetic field and temperature. The temperature evolution at two different magnetic fields is graphically depicted in Figure 1.4, where we can distinguish two processes:

- Isothermal magnetization change (vertical line). The magnetic field is applied isothermally, reducing the entropy by ΔS_{iso}, while lattice and electronic contributions remain constant. Magnetic entropy change is given by:

$$\Delta S_M(T)_{T,\Delta H,P} = [S_M(T)_{H_1} - S_M(T)_{H_0}]_{T,P} = [S_1(T)_{H_1} - S_0(T)_{H_0}]_{T,P} \quad (5),$$

where S_M is the magnetic entropy and S_0, S_1 are the total entropies at different magnetic fields.

- Adiabatic magnetization change (horizontal line): Applying the magnetic field under adiabatic conditions leads to the ordering of magnetic moments. The magnetic entropy decreases whereas the electronic and lattice entropies increase to maintain the total entropy constant. This results in an increase of the temperature in the material by a value ΔT_{ad}, expressed as:

$$\Delta T_{ad}(T)_{T,\Delta H,P} = [T_1(S)_{H_1} - T_0(S)_{H_0}]_{S,P} \quad (6),$$

where T_0 and T_1 are the temperatures in magnetic fields H_0 and H_1, respectively.

The magnetocaloric effect can be treated from a more formal thermodynamic approach. The entropy, which is the first derivative of the Gibbs free energy ($S = -(\partial G/\partial T)_P$), is a continuous function of temperature but changes its slope at the transition temperature. While entropy cannot be measured directly, it can be calculated from an experimentally measurable quantity, namely, the heat capacity, $C(T)_{H,P}$:

$$S(T)_{H,P} = \int_0^T \frac{C(T)_{H,P}}{T} dT \quad (7)$$

The total entropy of the material as a function of temperature is shown in Figure 1.4 left for a first-order magnetic transition. In this case, there is a discontinuous change of entropy at transition temperature T_1. The jump in the entropy comes from the enthalpy of the transition, ΔE, and the entropy increase is $\Delta E/T$. The isothermal entropy change at temperature T ($T_{t1} < T < T_{t2}$) is:

$$\Delta S_{iso}(T)_{\Delta H,P} = \int_0^T \frac{C_l(T)_{H_2,P}}{T} dT - \int_0^{T_{t1}} \frac{C_l(T)_{H_1,P}}{T} dT - \int_{T_{t1}}^T \frac{C_h(T)_{H_1,P}}{T} dT - \frac{\Delta E_{H_1}}{T_{t1}} \qquad (8)$$

where C_l and C_h are the heat capacities at low- (below transition temperature) and high-temperature (above transition temperature) phases. If we assume that $C_l(T)_{H,P} \approx C_h(T)_{H,P}$ as observed in $Gd_5Si_2Ge_2$ for the same magnetic field[18], we get:

$$\Delta S_{iso}(T)_{\Delta H,P} = \int_0^T \frac{C(T)_{H_2,P} - C(T)_{H_1,P}}{T} dT - \frac{\Delta E_{H_1}}{T_1} \qquad (9)$$

From this equation it can be deduced that the larger difference between the heat capacities in two fields gives a larger entropy change. The last term in this equation, called the structural entropy change, ΔS_{str}, is an additional contribution associated with the first-order phase transition and the abrupt atomic rearrangement that happens in this class of transitions. The relation between the entropy change and the adiabatic temperature change is given by[15]:

$$\Delta T_{ad}(T)_{\Delta H,P} \cong -\frac{T}{C(T_0)_{H_2,P}} \Delta S_{iso}(T)_{\Delta H,P} \qquad (10)$$

where $T_0 \in [\,T, T + \Delta T_{ad}(T)_{\Delta H,P}\,]$ and is unknown. In any case, from the above equation we see that ΔT_{ad} is directly proportional to entropy change and inversely proportional to the heat capacity, so it will be lower for materials with a high heat capacity.

When the material undergoes a second-order magnetic transition (Figure 1.4 right), the entropy is a continuous function of temperature and changes its slope at the transition temperature. In this case, the isothermal entropy change is given by:

$$\Delta S_{iso}(T)_{\Delta H,P} = \int_0^T \frac{C(T)_{H_2,P} - C(T)_{H_1,P}}{T} dT \tag{11}$$

From this equation, we can see that the entropy change will be larger when the difference between the heat capacities in two fields is large. The expression for the entropy change, Eqs.(9,11), are the theoretical ones. In reality, only 60-90% of this can be achieved. Moreover, only a small fraction of this entropy (less than 30%) is used in a magnetocaloric process, so experimental values of ΔS_{mag} are significantly smaller than the theoretical ones.

1.2.1.2. Inverse magnetocaloric effect

The inverse magnetocaloric effect is the opposite phenomenon to the conventional one. In this case, the magnetic entropy change is positive when the adiabatic temperature change is negative, and vice versa. The sample cools down when a magnetic field is applied. This effect is found in materials that undergo a reverse martensitic transformation, from paramagnetic/antiferromagnetic martensite to ferromagnetic austenite. It is observed in NiMnX (X=Sn, In, Sb) Heusler-type alloys and has been extensively studied[19][20][21].

1.2.1.3. Refrigeration capacity

MCE is also characterized by a refrigerant capacity (*RC*) which is defined as the amount of heat transferred between hot and cold reservoirs in a single refrigeration cycle. There are three different ways for calculating the *RC,* as reported in literature:

(1) *Relative cooling power (RCP),* determined by the product $|\Delta S_M(H)|^{max} \times \delta T_{FWHM}(H)$ [19]

(2) *Introduced by Gschneidner*, where the area under the peak of ΔS_M within δT_{FWHM} temperature range is calculated[22]:

$$RC = \int_{T_{cold}}^{T_{hot}} |\Delta S_M(T,H)| dT \tag{12}$$

(3) *By Wood and Potter*, where the area of the largest rectangle of ΔS_M is estimated[23]

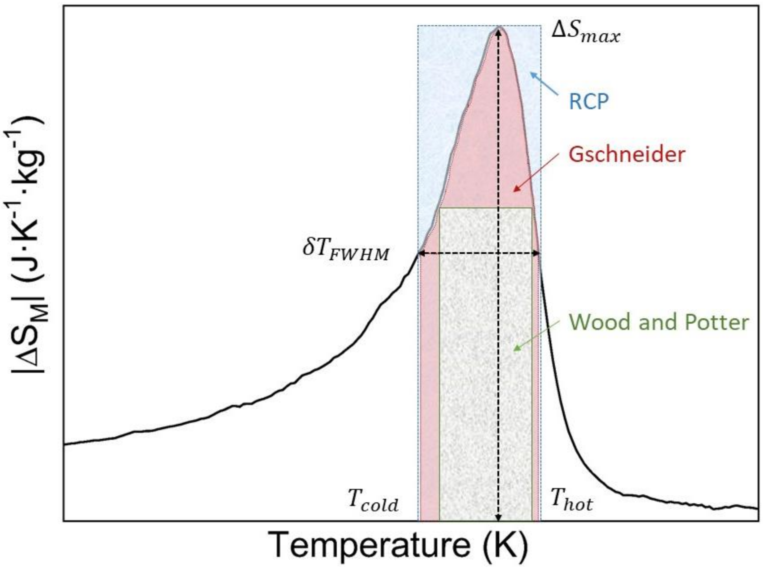

Figure 1.5: Schematic representation of the RC obtained from the magnetic entropy change curve. The RCP blue rectangle has the same width as the Gschneidner area's maximum width.

These three calculations are shown graphically in Figure 1.5. Since both the entropy change and adiabatic temperature change are proportional to the derivative of magnetization with respect to temperature, $|\partial M/\partial T|$, the greater is the variation of magnetization with temperature, the higher values of MCE are achieved. This is expected for both first- and second-order phase transitions. The MCE occurs at the Curie temperature in second-order phase transitions, i.e., transition from paramagnetic to ferromagnetic ordering.

1.2.2. Elastocaloric effect

The elastocaloric effect (*eCE*) is the thermal response to an external mechanical stress. This external stimulus induces a phase transformation, resulting in an entropy change and, consequently, a temperature change in the material. Elastocaloric materials reported for cooling mainly include NiTi-based, Fe-based, Cu-based and ferromagnetic SMAs. Rubber, as an example, increases its temperature when rapidly stretched, as first reported by Gough in 1805, who found out that rubber heats slightly when stretched rapidly[24]. Soon after, Thomson proposed a thermodynamic interpretation [25], and Joule discovered several elastocaloric materials[26]. However, due to the weak caloric effects of common metals and polymers, the elastocaloric effect barely received attention in the next 100 years. In 1980, Rodriguez and Brown, studying the martensitic transformation, occasionally found a significant eCE in $Cu_{69.6}Al_{27.7}Ni_{2.7}$ SMA [27]. In 2004, Quarini and Prince reported large temperature variations of 16K and -14K in the NiTi alloy subjected to a loading-holding-unloading protocol and originally proposed the concept of solid-state cooling[28].

As already mentioned, the elastocaloric effect arises from the absorption or release of latent heat during the martensitic transformation that occurs during cyclic loading and unloading. Figure 1.6 shows one cycle of loading and unloading for a superelastic NiTi alloy. This Brayton cycle consists of four steps:

(i) Adiabatic loading (1 → 2): in this step, an exothermic martensitic transformation from highly-ordered cubic austenitic phase to low-symmetry monoclinic martensite phase occurs, resulting in the heating of the material.

(ii) Heating (2 → 3): The applied stress or strain is maintained at a constant value while the material releases the heat acquired in the first step, thus returning to its initial temperature. This step can be used for heating applications.

(iii) Adiabatic unloading (3 → 4): After adiabatically removing the load, an endothermic reverse martensitic transformation occurs, cooling down the material.

(iv) Cooling (4 → 1): Heat is absorbed from the surrounding by the material, recovering the initial temperature. This step can be used for solid-state refrigeration.

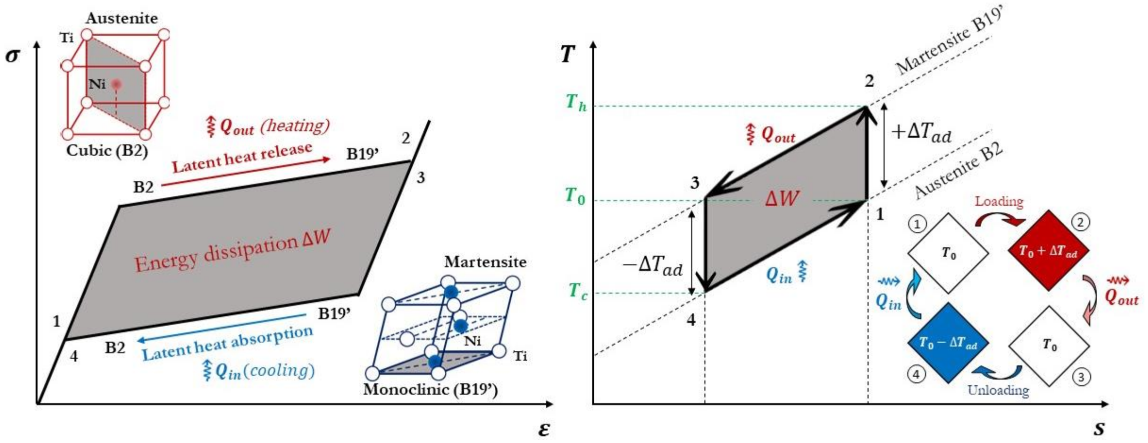

Figure 1.6: Schematic illustration of the elastocaloric response for superelastic NiTi. The stress-strain curve (left) together with the corresponding temperature-entropy (right) diagram.

1.3. MARTENSITIC TRANSFORMATION AND SHAPE MEMORY EFFECT

A Martensitic Transformation (MT) is a first-order phase transition in solid state materials consisting of the regular rearrangement of the crystal lattice. It is a diffusionless and displacive transition, that is, it involves a simultaneous and cooperative movements of atoms at a distances less than one interatomic distance. As a result, the chemical composition is unaltered in both the parent and the product phases. There is a wide variety of materials where this transformation takes place, from steels, nonferrous alloys and metals to polymers and ceramic materials. Starting from the high temperature phase, known as the *austenite phase*, upon cooling the material undergoes a martensitic transformation that starts at T_{m_s} where properties such as, e.g., magnetization and strain experience a drop. This transformation continues until it reaches the temperature where the transformation is fully completed, referred to as the *martensite phase*, at T_{m_f} (see Figure 1.7). When heated, the reverse martensitic transformation occurs, with the austenitic phase starting at T_{a_s} and ending at T_{a_f}, where the initial state is recovered. The thermal hysteresis, denoted as ΔT, is a direct consequence of the first-order nature of the martensitic transformation. Mathematically, the value of the hysteresis is given by:

$$\Delta T = \frac{T_{a\_s} + T_{a\_f}}{2} - \frac{T_{m\_s} + T_{m\_f}}{2}$$

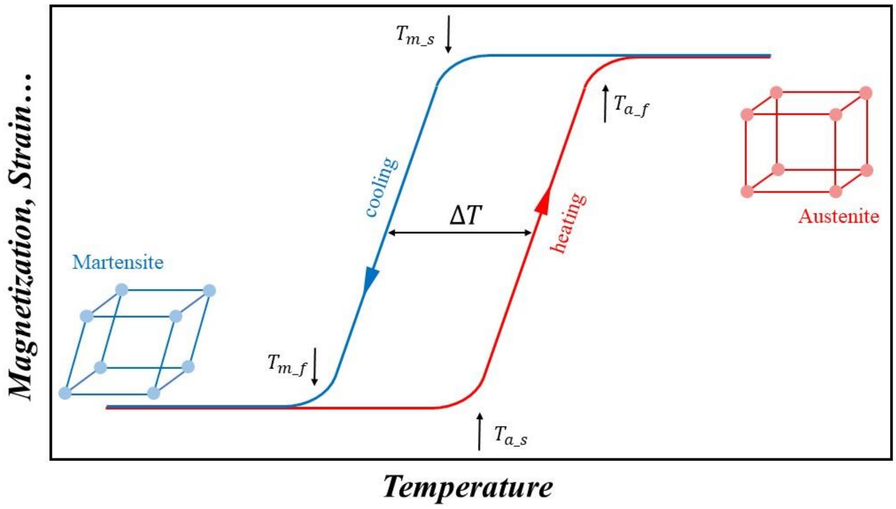

Figure 1.7: Schematic of the temperature-induced martensitic transformation.

At temperatures above T_{a_f}, the martensitic phase can also be induced by straining the material, as illustrated in Figure 1.6. The deformation is fully reversible when deformed above T_{a_f}. However, if deformation occurs above T_{m_s} but below T_{a_f}, some stress-induced martensite will remain stable leading to an incomplete shape restoration.

The critical stress (σ^{p-m}) is the point at which the sample transforms into martensite. This value increases linearly with temperature, starting from zero at the T_{m_s}. From this point until the material is fully transformed, the stress at which the transformation occurs is roughly constant. If more stress is applied, it leads to the elastic loading of the martensite until a material starts deforming in the plastic regime. When the applied stress is released, and the strain is limited to the start of elastic loading of the martensite, the reverse transformation occurs at a lower stress level than during loading, leading to the recovery of the initially induced strain. In this case the material is considered *superelastic*. Compared to the 0.2% elastic strain in conventional metallic materials, SMA materials can achieve reversible strains of up to 20% of the initial length. This effect is called to by various names since it is a result of a phase transformation, such as the pseudo-elasticity, or the superelasticity. The MT exhibits hysteresis since an unloading happens at a lower stress plateau than during loading, in an analogy to the temperature-induced transformation.

Materials exhibiting the shape memory effect undergo a martensitic transformation driven by a shear-like mechanism (also known as invariant plane strain) and have the peculiarity that the product martensitic phase contains many lattice defects such as dislocations, twins and/or staking faults (called by the lattice invariant strain). Shape memory behaviour is present in various alloy systems, but only few of them have been developed to an industrial scale, with NiTi, NiTi-X and Cu-based alloys accounting for 90% of all SMA applications.

In terms of functional properties of SMAs, the temperature-induced transformation plays the main role in the one-way and two-way memory effects, work production and the generation of recovery stresses. The basis of the superelastic effect is the reversible stress-induced transformation. When the material is in the martensite state it is said to be in the cold shape, and when it is in the austenitic state it is said to be in its hot shape. The hot shape always represents the initial shape that the material takes after processing. Accordingly, the defined cold shape is originated from the hot shape after cooling into martensite. The latter shape can now be further deformed to the final cold shape (limited to less than 10% strain deformation of the initial shape) to induce the particular properties as described here.

We are going to give a description of the one-way and two-way memory effects by considering a spring-like model made of SMA:

- *One-way memory effect*: When a material is in the martensitic state, the shape memory element can be easily deformed from a fixed "hot shape" state that is retained after cooling to nearly any "cold shape" (Figure 1.8) . The only restriction is that the deformations may not go beyond a predetermined strain limit (up to 8%). These pseudo-plastic deformations are completely recoverable through heating, yielding the original hot shape state. Because only the hot shape is memorized, this effect is known as the one-way memory effect. The transition temperatures between the cold and hot shape conditions are determined by the alloying and processing parameters, which are adjustable by SMA-suppliers.

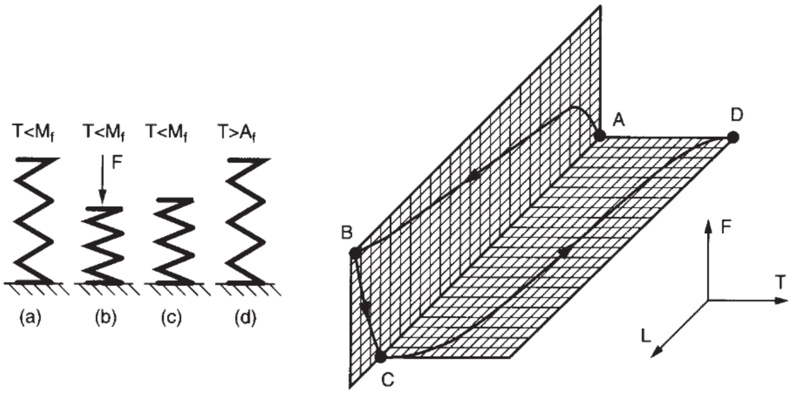

Figure 1.8: One-way memory effect. The sample is deformed (A → B) and unloaded (B → C) at a temperature below M_f. During heating the pseudoplastic deformation is restored at a temperature above A_f (C → D). Load, length change and temperature are indicated by F, L and T, respectively [29].

- *Two-way memory effect*: The two-way memory effect refers to the memorization of two shapes (Figure 1.9). During cooling, a cold shape spontaneously emerges, requiring no external forces to obtain the memorized cold shape, which sets it apart from the one-way memory effect. Subsequent heating restores the original hot shape. However, the two-way memory effect only occurs after a specific thermomechanical procedure known as a "training", which can be provided by the SMA-supplier.

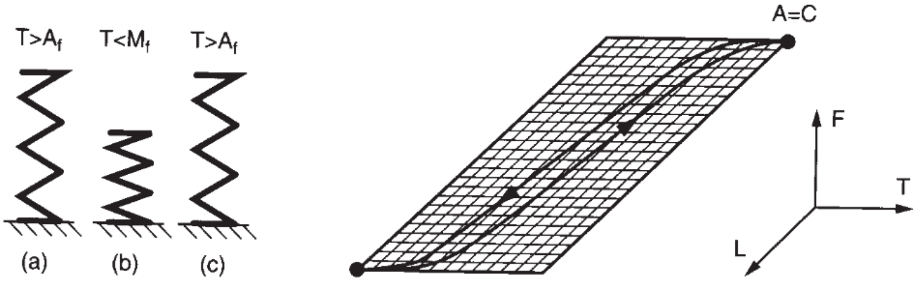

Figure 1.9: Two-way memory effect. During cooling to a temperature below M_f ($A \rightarrow B$) a spontaneous shape change occurs. This shape change is recovered during post heating to a temperature above A_f ($B \rightarrow C$) [29].

1.4. HEUSLER-TYPE NIMN-BASED MAGNETIC SHAPE MEMORY ALLOYS (MSMAs)

Heusler-type alloys are widely studied compounds since their discovery by Fritz Heusler in 1903, starting with the Cu_2MnAl compound, which has ferromagnetism even though none of its individual elements is ferromagnetic [30]. These alloys are a class of intermetallic materials that comprise a vast collection of over 10000 compounds. They can be classified into two groups based on their stoichiometry[31]:

- XYZ or 1:1:1 (Half-Heusler)
- X_2YZ or 2:1:1 (Full-Heusler or just Heusler)

X and Y are mainly 3d metals whereas Z is a group IIIA-VA element. The extensive class of magnetic X_2YZ Heusler compounds shows multifunctional magnetic properties, including magnetocaloric effects(Krenke, Duman, et al. , 2005), magneto-optical behaviour[32] and magnetostructural properties[33]. These properties arise from the reversible spontaneous lattice distortion these compounds undergo, caused by the martensitic transformation that converts them from a high-temperature cubic austenite phase to a low temperature tetragonal, orthorhombic, or monoclinic martensite phase. MT in such alloys is accompanied by a considerable change of magnetic properties or even change of magnetic order (also called as the magnetostructural transformation) and can be induced by the application of a magnetic field, mechanical stress or by a change in temperature. Since MT is displacive and diffusionless, the deformed alloy in the low-temperature phase can recover its original shape by reverse transformation when heated back to the high-symmetry austenitic phase. As described in Sec. 1.1, this effect is known as the shape memory effect (SME) that was observed for the first time in Au-Cd alloys in 1951 and became more popular in 1963 with Ti-Ni compounds[34][35]. Specifically, stoichiometric and non-stoichiometric Heusler-type alloys are known as magnetic shape memory alloys (MSMAs). They have the main advantage over nonmagnetic conventional SMAs owing to their possibility to actuate at high frequencies. Thermally activated devices based on the conventional SMAs are limited to 5Hz[36] due to their slow response originated from a thermal inertia.

As far as the crystal structure is concerned, Heusler compounds crystallize in the $L2_1$ –ordered structure with a cubic space group ($Fm\bar{3}m$, space group no. 225), where three elements occupy non-equivalent positions in the lattice. Here the crystal lattice can be represented by four interpenetrated fcc (face centered cubic) lattices.

On the other hand, in the ordered state, Half-Heusler compounds crystallize in a non-centrosymmetric cubic structure ($F\bar{4}3m$ space group no. 216) which can be derived from the tetrahedral ZnS-type structure by filling the octahedral lattice sites.

1.4.1. NiMn-based Heusler alloys

Ni-Mn-based Heusler-type MetaMagnetic Shape Memory Alloys (MMSMAs), a set of alloys that present the Magnetocaloric Effect (MCE), are of great interest due to their strong potential for a solid-state refrigeration. They undergo a first-order martensitic transformation from a high-symmetry ferromagnetic austenitic phase at high temperature to a low-symmetry weak magnetic or antiferromagnetic martensitic phase at lower temperature, whereby exhibiting a large change of the magnetization[37]. This magnetostructural transformation leads to the so-called magnetic shape memory effect[38]. In addition, the application of an external magnetic field can shift the MT because of the strong magnetostructural coupling[39][40][41], giving rise to the peculiar giant MCE phenomena, making these materials a promising candidates for efficient solid-state refrigeration applications.

The phase stability as well as structural and magnetic properties of Ni-Mn-X (X=In, Sn, Sb, Ga,…) Heusler alloys have been widely studied both theoretically and experimentally in the literature, showing that it is possible to manipulate, in the predictable way, the magnetic exchange interactions in both low-temperature martensite and high-temperature austenite, as well as tune other multifunctional properties, such as shape memory effect or superelasticity, by the doping with many other elements, such as Co, Cu, Fe, Cd, W etc. [42][43][44][45][46][47][48]. Ni-Mn-based Heusler MMSMAs are very attractive candidates for magnetocaloric applications owing to the availability of the raw materials, non-toxicity, easiness-to-be-prepared and a large magnetocaloric effect under a magnetic field of existing permanent magnets[49][50].

Ni-Mn-Sn Heusler alloys family represents one of the intensively studied MMSMAs. This stoichiometric compound, Ni_2MnSn, has a $L2_1$ –ordered cubic structure with four interpenetrating face centered cubic (*fcc*) sublattices[51] (Figure 1.10). In an ideal ordered case, the $(0,0,0)$ and $(^1/_2, ^1/_2, ^1/_2)$ sites are occupied by Ni atoms, leaving the remaining ($^1/_4$,$^1/_4$,$^1/_4$) and ($^3/_4$,$^3/_4$,$^3/_4$) sites being occupied by Sn and Mn atoms. On the other hand, in off-stoichiometric Ni-Mn-Sn Heusler alloys, the excess of Mn atoms occupy the partially vacant Sn sites. Indeed, some percentage of Ni, Mn, Sn atoms may be distributed randomly, forming some degree of disorder present in the crystal structure which can be largely removed by annealing these materials at high temperatures[52][53].

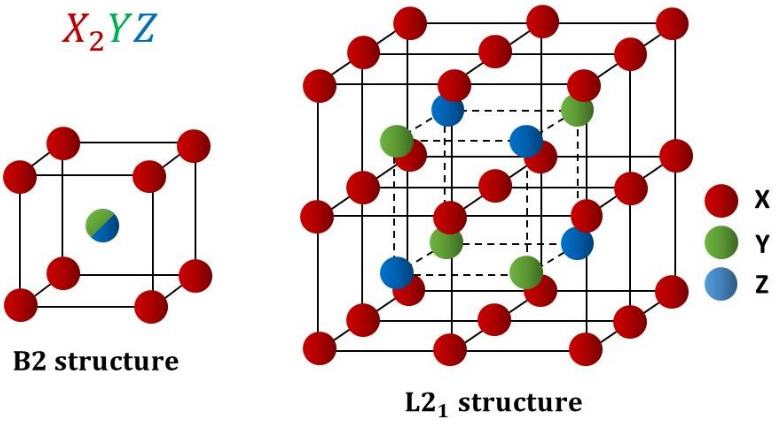

Figure 1.10: B2 vs L21 structures for austenitic phase.

Upon cooling from the melt, Ni-Mn-X (X= Sn, Sb, In, Ga) alloys crystallize first in entirely disordered A2 structure, then exhibit a partially ordered B2 structure, where Ni atoms occupy the corner positions and Mn and Z atoms are randomly located in body-centered (*bcc*) positions. Further cooling produces the disorder-order transition where the crystal structure of alloys transforms from B2 to $L2_1$, in which Ni atoms are located in the corners of the structure, whereas Mn and Z atoms are at alternate body sites. The martensite transformation temperature depends on the atomic order, which can be modified by the chemical composition change and/or by the processing of the alloy.

The Ni-Mn-X alloys exhibit a martensitic transformation into martensites with a non-modulated or modulated crystal lattices. When the concentration of X atoms is low this family of alloys transforms into a non-modulated tetragonal

$L1_0$ –ordered martensite [54]. Figure 1.11 shows the crystallographic lattice relations between $L2_1$ austenite and $L1_0$ martensite. Martensite may have modulated structures apart from $L1_0$ structure (especially for alloys with a high Z concentration). The most common modulated structures are the following ones:

(1) Four-layered 4O structures[55]
(2) Five-layered 10M structure [56][57]
(3) Seven-layered 14M structure[56]

These modulated structures are formed by shearing of the (110) planes along the $[1\bar{1}0]$ crystallographic direction. The fabrication process and chemical composition significantly influence the crystal structure of martensite and the equilibrium martensitic transformation temperature, T_{m0}.

The off-stoichiometric Ni-deficient Ni-Mn-Sn Heusler alloys can be doped with Cobalt, where Cobalt goes to the Ni sites. These Ni(Co)-Mn-Sn Heusler alloys are of great interest since they reportedly have MT near room temperature[58]. Previous works have investigated the crystal structures of martensite phases in these alloys by means of X-ray diffraction (XRD). Umetsu et al. showed that Co-doped Ni-Mn-Sn alloy has an $L2_1$ structure (Figure 1.11) at room temperature[59], with space group *Fm-3m* (Cu_2MnAl prototype). This structure is confirmed in the present work using *Mn*-rich $Ni_{40}Mn_{42.5}Co_8Sn_{9.5}$ alloy at room temperature [60]. Umetsu et al. concluded that in the Ni-Mn-Sn alloy, the Mn moments on 4a and 4b sites are antiferromagnetically coupled, whereas in the Co-doped alloy they are ferromagnetically coupled, attributing the ferromagnetic enhancement to the change in magnetic structure by Co substitution.

On the other hand, melt-spinning is a useful technique for obtaining ready-shaped magnetocaloric materials with a high surface/volume ratio suitable for their implementation in active magnetic regenerators. Thanks to the high cooling rate of melt-spinning (about 10^6 K/s) it can modify the physical characteristics of the alloys. Such high rates induce the stabilization of the high temperature austenite phase in Heuler-type MMSMAs with its corresponding B2 ordered structure instead of the highly ordered $L2_1$ structure. As far as MCE and other functionalities of Ni-Mn-based Heusler alloys are closely related to the crystal structures of constituent phases, a deep understanding of crystal structure is required for exploiting all these functionalities towards property optimization.

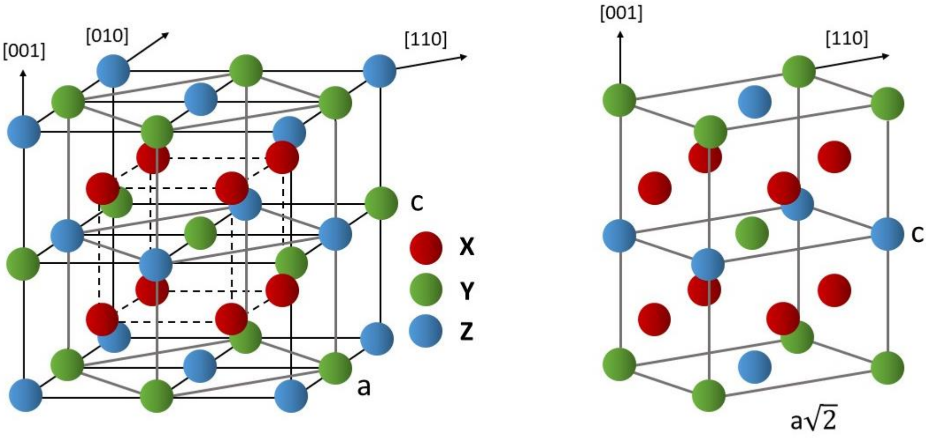

Figure 1.11: Crystallographic relations between $L2_1$ austenite and non-modulated $L1_0$ martensite. For NiMnSn stoichiometric alloys, X are Ni atoms, Y are Mn atoms and Z are Sn atoms.

The Heusler-type MMSMAs are very sensitive to composition in terms of phase transformation temperature[61][62], Curie temperature[63], saturation magnetization[64], which, in turn, are direct consequence of a crystal structure variation[65]. Also, post-annealing and cooling rates have a strong influence on the magnetic properties[66], as phase changes occur due to atomic ordering. Material processing may degrade the magnetic properties of these compounds, but these can be reversed by performing heat treatments[60].

1.4.1.1. Effects of doping

(a) Co addition

The modification of the Ni/Mn/Sn ratio in Heusler NiMn-based alloys influences their magnetocaloric properties and transformation characteristic temperatures. Nevertheless it is difficult to shift the martensitic transformation towards room temperature with just varying that ratio, while simultaneously having a large magnetocaloric effect at low fields. Adding Co to Ni-Mn-Sn alloys allows to obtain suitable materials for magnetic cooling due to the strong influence of Co on magnetic and structural properties. Ni-Co-Mn-Sn system has been widely studied by several groups. Krenke et al. studied the influence of substituting Co for Ni in $Ni_{50-x}Co_xMn_{37}Sn_{13}$ alloys on the magnetocaloric effect[67]. They found that introducing Co led to a decrease in M_s and ΔS but the thermal hysteresis associated with the transition became narrower with Co content from 1 to 3 at.%. Similarly, Cong et al. performed a systematic study of the $Ni_{50-x}Co_xMn_{39}Sn_{11}$ alloys and obtained a phase diagram relating the chemical composition to temperatures of phase transitions and magnetic behaviour[68].

Figure 1.12 shows the relationship between transformation temperatures and the Co content, ranging from 0 to 19 at.%. The martensitic transformation temperature, defined in this study as $(T_{ms}+T_{mf}+T_{as}+T_{af})/4$, shows a roughly linear negative dependence with increasing Co content until 7 at.% of Co and strong negative exponential decrease for more than 7 at.% of Co content. The linear slow decrease of T_M is ascribed to the change of *e/a* ratio. The substitution of Ni (10 valence electron) by Co (9 valence electron) decreases the *e/a* and, as consequence, leads to a decrease of T_M. For higher Co content, the rapid decrease may be due to atomic order, precipitation of other phases, etc. In particular, the formation of the secondary γ phase was observed that has a different composition than the matrix. The austenite Curie temperature increases with increasing Co content and seems to be correlated to the strengthening of the ferromagnetic exchange interactions with Co doping. Based on the diagram, it can be noted that the most interesting range of compositions, from a practical point of view, is between 5 and 8 at.% of Co since in this region MT occurs with large magnetization change that benefits the magnetocaloric effect. The addition of Co also affects the crystal structure with the formation of modulation from 4O to 10M and then to 14M with an increase of Co content.

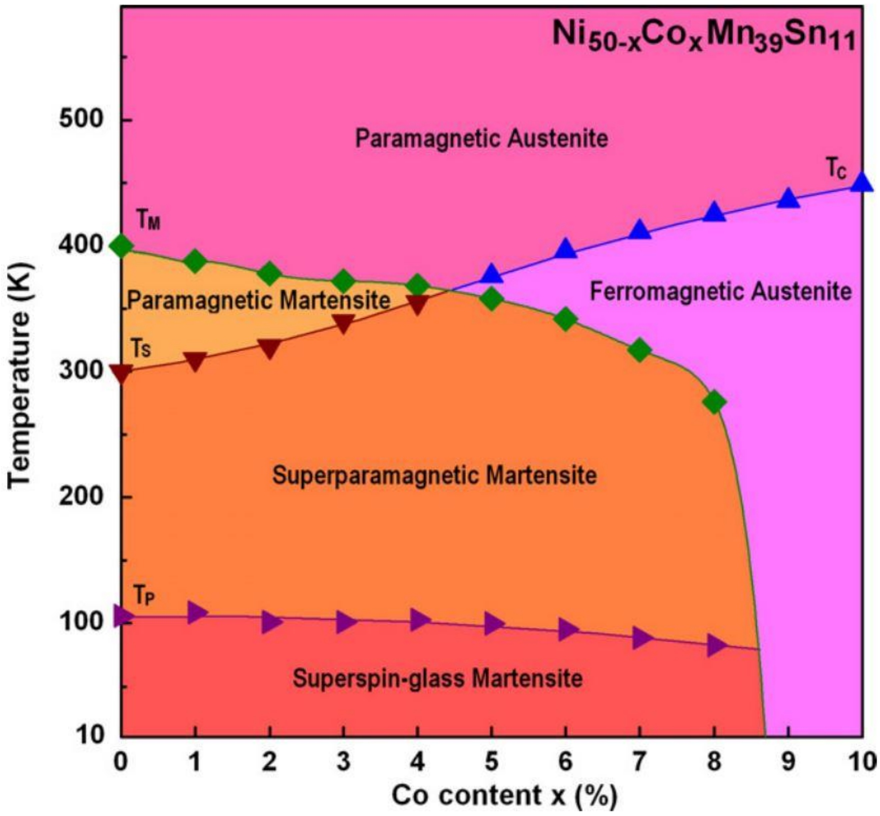

Figure 1.12: Phase diagram for Ni-Co-Mn-Sn system. The evolution of the characteristic transformation temperatures versus the Co content is displayed [68].

(b) Cu addition

Cu addition to the Ni-Mn-Sn Heusler alloys also enhances the magnetocaloric properties and influences the crystal structure and phase transformation temperatures. Das et al. investigated the alloys system of $Ni_{44-x}Z_xMn_{43}Sn_{11}$ (Z = Co, Cu) and the effect of Co versus Cu doping for magnetocaloric properties as well as for transformation temperatures. Cu doping led to a decrease in both martensitic and magnetic transformation temperatures. Substituting Cu for Ni increased ΔS_M significantly, having an even stronger effect than the addition of Co[68]. The decrease of T_{ms} with Cu substitution for Ni is opposite to what would be expected by the *e*/*a* rule. In this case, another factor such as the unit cell volume should be considered. On the other hand, the replacement of Mn by Cu in $Ni_{43}Mn_{46-x}Cu_xSn_{11}$ increases both magnetic and martensitic transition temperatures. In this case, ΔS_M increases with the addition of Cu[69]. The magnetocaloric properties are improved due to a larger magnetization change at martensitic transformation from austenitic to martensitic phases caused by Cu addition. It was demonstrated that Cu enhances ferromagnetic exchange interaction in austenite resulted in the mentioned greater magnetization change at MT[70].

1.4.1.2. Effect of fabrication methods

The fabrication method has a significant effect on the properties of the resulting alloy. For alloy synthesis, the most popular methods are induction casting and arc-melting. In the laboratory conditions, the former technique offers the possibility to prepare alloys in large quantities (several tens of grams), whereas the latter one should not exceed a few grams. The reason is that induction casting uses large crucible in which a large quantity of alloy fits and that can be completely and *simultaneously* melted, giving rise to a rather homogeneous liquid alloy that will maintain its homogeneity when casted at a high quenching rate. In this method, post annealing is required for improving a homogeneity. Another drawback of this technique is that the alloy is susceptible for reaction with the alumina crucible if overheated in a liquid state or keeping liquid too long. On the other hand, arc melting furnace generally provides homogeneous alloy as long as its mass is less than 10 grams since otherwise the arc cannot melt the entire constituents simultaneously, preventing it from becoming a fully homogeneous ingot. Flipping and re-melting the ingot a few times assure the alloy homogeneity.

Melt-spinning is a technique that produces metallic ribbons or flakes which could be a single-phase without chemical segregation. The high cooling rate in normally prevents the formation of unexpected phases[71]. This technique allows to shorten or even avoid a long annealing, leading to lower fabrication cost and the fabrication time. In addition, melt-spinning process influences atomic order, which affects the magnetic properties and martensitic transition temperatures. Generally, MMSMAs ribbons have a lower MT than the bulk alloys, and this is attributed to grain refinement and internal stresses formed during fabrication [72].

1.4.1.3. Heat treatments

The functional properties of a material can be improved by performing specific heat treatments. On the other hand, material processing like melt-spinning, grinding process for powder obtaining, or any post processing may degrade its magnetic properties. This degradation can be partially or completely reverted by performing specific heat treatments to the material. Another property that can be enhanced is the thermal hysteresis reduction since heat treatments have influence on the microstructure, phase transitions, and magnetic properties of these materials. Heat treatments affect in various manners to the material:

1) <u>Phase Transition Stabilization</u>: Heusler magnetocaloric materials typically undergo phase transitions when exposed to varying magnetic fields. These phase transitions are essential for the magnetocaloric effect, but they can introduce hysteresis. Heat treatments can stabilize these phase transitions, making them more reproducible and reducing hysteresis.

2) <u>Microstructural changes</u>: Heat treatments can induce changes in the microstructure of the material. For example, they can promote the growth of specific crystal grains or the elimination of defects. These microstructural changes can result in a more uniform and well-defined response of the material to changes in temperature and magnetic field.

3) Homogenization: Heat treatments can help in the homogenization of the material composition. Inhomogeneities or compositional variations within the material can lead to irregular phase transitions and hysteresis. Heat treatments can even out these variations and improve the material's consistency.

4) Magnetic property optimization: The magnetic properties of Heusler magnetocaloric materials are closely linked to their phase transitions. Heat treatments can help optimize these magnetic properties, such as the Curie temperature and the saturation magnetization.

5) Stress Relief: During the fabrication process, magnetocaloric materials may experience stress or strain, which can affect their magnetic and thermal behaviour. Heat treatments can relieve these internal stresses and restore the material to a more stable and stress-free state.

6) Defect Annealing: Any defects or dislocations in the crystal lattice of the material can disrupt its magnetic and thermal behaviour. Heat treatments can facilitate defect annealing, reducing these disruptions and promoting more predictable phase transitions.

Overall, heat treatments are a valuable tool in optimizing the properties of Heusler magnetocaloric materials. They help achieve more controlled and predictable phase transitions, leading to a reduction in thermal hysteresis and, ultimately, enhancing the efficiency and reliability of these materials for cooling and refrigeration applications.

1.5. APPLIED ASPECTS OF MAGNETOCALORIC MATERIALS

The main potential application of magnetocaloric materials is for magnetic refrigeration. Both first-order magnetocaloric (FOMT) and second-order magnetocaloric (SOMT) materials are generally used for magnetic refrigeration and heat pumping[73]. It is clear that a magnetocaloric material exhibiting a large magnetocaloric effect is desirable for refrigeration. One of the parameters for measuring the utility of a magnetocaloric material is its magnetic field – induced isothermal entropy change, a quantity that is usually reported in every study devoted to a magnetocaloric material. However, this is not only parameter needed to be taken into account since it does not provide information about the usability of the material for a refrigeration device, because heat is not transferred isothermally. The main parameter that must be taken into account is the magnetic field –induced adiabatic temperature change since it provides a basis for establishing the capacity of magnetocaloric material to create the temperature gradient. The largest possible adiabatic temperature change is required to overcome the irreversible heat losses because of the irreversibility of the heat transfer between the material and the heat transferring fluid.

Therefore, it is desirable to have magnetocaloric materials with the largest adiabatic temperature change per magnetic field unit, taking into consideration environmental, geopolitical and resources issues associated with practical applications. Gd-based materials are considered critical in this regard [74], while the chemical elements in NiMn-based Heusler compounds are in a common use, which is one of the reasons for choosing these materials for this thesis.

1.5.1. Active Magnetic Regenerators

The temperature span required for magnetocaloric refrigeration is greater than the one a magnetocaloric material can provide by itself, although it is enough for low temperature adiabatic demagnetization refrigeration due to the fact that the heat capacity decreases with temperature, increasing thus the adiabatic temperature change (see equation (1)). In low-temperature refrigeration, paramagnetic salts are cooled to milli-Kelvin temperatures. Since the aim of this thesis is to study a refrigeration at room temperature, the primary focus will be on this kind of refrigeration.

Regarding a room-temperature refrigeration, the temperature span of the magnetocaloric effect can be increased by two means: the first one involves heat regeneration, whereas the second one uses a cascade system consisting of several interconnected thermodynamic cycles. Most popular technologies use a heat regenerator that consist on an indirect heat exchanger in which the heat transfer occurs by means of a heat transfer fluid that is periodically stored and transferred to the regenerator matrix or material. Thus, the regenerator matrix or heat exchanger is a porous structure through which the working fluid oscillates, as in a Stirling engine[75]. The porous matrix is referred to as an active magnetic regenerator (AMR) when composed of the magnetocaloric material, as it not only absorbs or transfers heat but also actively contributes to the magnetocaloric effect.

1.5.2. Magnetic refrigerator

The magnetocaloric material is the core of a magnetic refrigerator. The refrigerating device is composed of three main elements: (i) a magnetic field source, (ii) a heat transfer fluid and (iii) an active magnetic regenerator (AMR). The AMR is composed of the magnetocaloric material acting as a heat exchanger and is the heart of a magnetocaloric device. Special attention must be given to the processing of the regenerators, the layering with different magnetocaloric materials, and optimization of their performance and geometry. The heat exchanger may have different geometries and some of them can improve refrigeration. In order to have a functional heat exchanger, some considerations must be taken into account to maximize refrigeration performance.

First, a magnetocaloric regenerator must have a very large surface-to-volume ratio to ensure maximum heat transfer to the working fluid. Convective heat transfer is strongly dependent on the scale of heat transferred between a particular body and the working fluid. Thus, the porosity of the regenerator not only depends strongly on the properties of the magnetocaloric material, but also on the viscosity and thermal properties of the working heat transfer fluid and fluid dynamics. One important issue regarding the viability of a magnetocaloric refrigerator is manufacturability and mechanical (cyclic) stability. In terms of shape, magnetocaloric regenerators can be divided into two types: (i) packed-bed structures and (ii) ordered structures (see Figure 1.13).

The first room-temperature magnetocaloric refrigerator consisted of an ordered structure with parallel plates of Gd[13]. Radulov et al. manufactured thin polymer bonded $La(Fe,Mn,Si)_{13}H_x$ plates by cold processing using wire-saw cutting and cold rolling[76]. They investigated the magnetocaloric properties and corrosive behaviour over a period of seven months to evaluate if the device was practical. In 2015 Varga et al. produced magnetocaloric wires from Heulser alloys and successfully produced glass-coated NiMnGa- and NiMnInCo-based microwires. Several processing techniques were studied, each with its own limitations and strengths.

Figure 1.13: Types of magnetocaloric regenerators, image taken from [73].

For complex heat exchanger geometries that would not be feasible to produce by conventional means (molding, extrusion, etc), additive manufacturing is a promising and versatile technique that can provide a wide variety of possible geometries. This thesis will focused on producing magnetocaloric heat exchangers using additive manufacturing.

1.6. ADDITIVE MANUFACTURING

Additive manufacturing (AM), a technique that consists of building 3D structures layer-by-layer, is a cost-effective technique for obtaining complex three-dimensional structures. The versatility of printing complex structures that would not be feasible to be created by conventional techniques has led to increased interest in this technique in every scientific and technological area[77][78]. 3D printing is a polyvalent technique where both polymers and metals can be printed. Thus, the applications of this technique cover a wide range of disciplines, from microelectronics[79][80], robotics[81], sensors and actuators[82][83] to biomedicine, such as medical implants and tissue engineering[84][85][86][87]. The case of metallic AM is of great interest since metallic structures offer more robustness than polymeric ones and offer the possibility to use metallic functional materials, increasing the application areas where these AM technologies can be used. One of the functional materials that can be 3D printed is a magnetocaloric materials itself.

The AM technologies for metals can be divided into three main categories: (i) direct AM printing, where the metal is melted or sintered during the printing process; (ii) indirect AM printing, where partial or no melting happens requiring a post-processing of the printed structure; and (iii) hybrid AM where CNC milling follows the AM process[88].

Among the direct AM techniques used in magnetocalorics, the most popular ones are the followings: selective laser melting (SLM), direct metal laser sintering (DMLS), direct metal deposition (DMD), electron beam melting (EBM), etc. These techniques use an energy source (laser, electron beam) to selectively melt/sinter powdered metal in a powder reservoir, building layer by layer a 3D structure. These techniques provide compact and robust metallic structures but require the use of complex and expensive devices that use high power sources that sinter/melt the metallic powder, requiring a high amount of energy to obtain the structure [88][89][90][91].

On the other hand, in the indirect additive manufacturing process, a metal powder is combined with a polymer, that acts as a binder, and then this mixture is printed. The printing process of this technique requires less energy consumption since there is no full melting/sintering of the material. For pure metallic structures, a post heat treatment is required to first remove the polymer by calcination and then to sinter the metallic powder. This leads to a lower dense printed structures, ranging from 45% to 85% of the theoretical density[92]. The strong point of indirect AM is that the materials for printing can be chosen in order to satisfy environmental-friendliness in a cost-effective way.

1.6.1. Screen-printing

Ink screen printing technology enables the fabrication of different 2D geometrical patterns and shapes[93]. A polyethylene terephthalate (PET) foil is used as a printing substrate since it is flexible, non- porous, and allows easy detachment of the printed ink sample from the substrate once it is dry. Before printing, the surface of the substrate is ionized by a corona treatment to enhance the adherence of the ink[94]. The schematic representation of the screen-printing process used in the present work for the printing of the magnetocaloric multi- layered thin films is shown in Figure 1.14. The printing device and layout of the PET substrate on the printing platform are displayed in Figure 1.14. During ink curing for 24 h, a permanent magnet was placed beneath the substrate to induce a preferable orientation of the particles in the printed layer.

The use of the magnetic field to align the particles along their easy-magnetic axes is an efficient tool[95][96] to enhance the magnetocaloric effect.

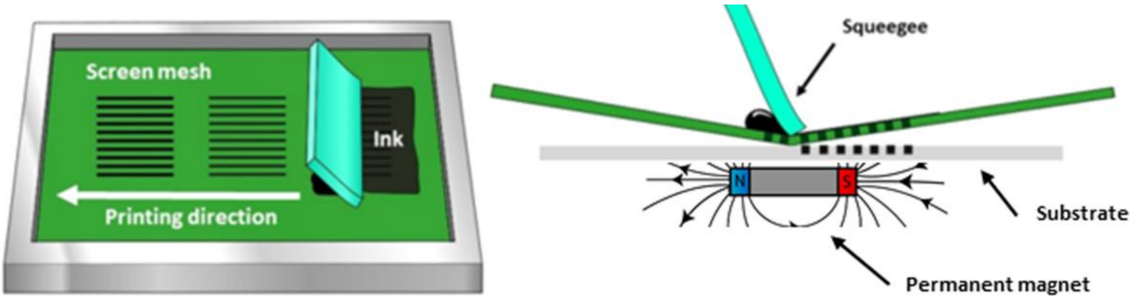

Figure 1.14: Scheme of the screen-printing technique (left) and a detail of ink transfer through the screen mesh into the substrate behind which a permanent magnet is placed for inducing magnetic orientation of the particles (right).

1.6.2. Cold extrusion printing

The next step is a transition from 2D printing to 3D printing. As a cost-effective alternative to the indirect AM technique, solvent-cast cold extrusion 3D printing is an interesting technique that uses a simple printer. In this case, an ink has to be prepared using mainly three components (a) metallic powder, (b) polymeric binder, and (c) solvent. On the other hand, by making the correct choice of polymer and solvent, this technique can also be environmentally-friendly. Previous work done by C. Xu et al. using Chitosan as a binder demonstrated the wide possibilities for producing actual 3D 100% metallic structures by removing the polymer followed by a sintering process through heat treatments[97]. Since vertical layer growth is not straightforward with these printers, another alternative is 4D printing studied by B.Y. Ahn et al., where they printed origami structures by creating 2D grids and then folding them to obtain 3D structures [98]. PVA was used as binder by E. Peng et al. for printing ferrite-based magnetic structures followed by subsequent sintering processes[99]. Thus, this technique is promising for obtaining metallic structures in a simple and cost-effective way. The main challenge with this technique is to develop an optimal ink, since the resulting printed structures depend entirely on ink properties, such as the optimal powder-to-polymer volume ratio and proper viscosity of the ink. The schematic representation of this cold extrusion printer is shown in Figure 1.15.

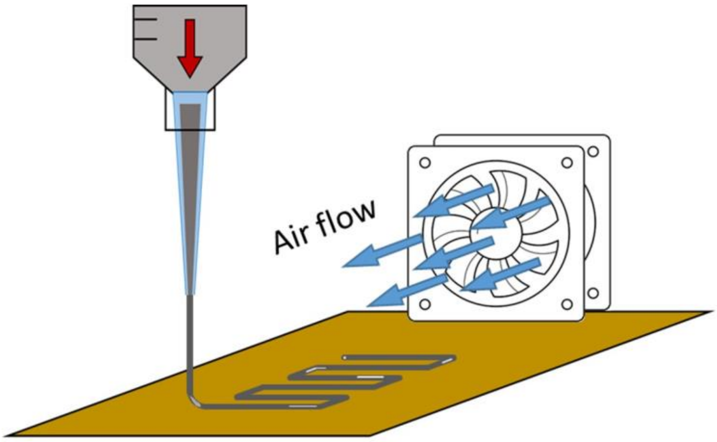

Figure 1.15: Scheme of the cold extrusion printing technique. A cooling fan is used for accelerating the ink drying rate for optimal printing.

1.7. STATE OF THE ART

The state of the art in the field of development of sustainable cost-effective MCE materials, importantly, suitable for AM, which can be deduced from the aforementioned analysis of the literature, shows that the progress in this field is still not enough for the technological breakthroughs. Further R&D is needed to demonstrate a potential and viability of MCE materials for wide-spread applications in a solid state refrigeration.

1.8. OBJECTIVES

A global objective of the present work is to develop practically new functional material such as powdered high efficient Heusler-type MMSMA exhibiting MT and MCE characteristics similar to a bulk homolog and being suitable for additive manufacturing of a heat exchanger prototype. We will pursue the next less scoped objectives:

1. Exploring transformation behaviour of the representatives of the main families of Heusler-type NiMn-based MMSMAs in order to select a prospective alloy which will serve, at the end, as prototype MCE powder component of printing ink.
2. Preparation and all-round study of MMSMA ribbons as the precursors for fabrication of the MCE functional powder
3. All-round investigations of MMSMAs powders prepared from ribbons
4. Elucidating conditions needed to create metallic printable inks
5. 2D and 3D printing of MCE prototype devices using a developed MMSMA/polymer inks and unveiling their characteristics.

1.9. REFERENCES

[1] International Energy Agency (IEA), The Future of Cooling Opportunities for energy-efficient air conditioning, (2018) 92. https://iea.blob.core.windows.net/assets/0bb45525-277f-4c9c-8d0c-9c0cb5e7d525/The_Future_of_Cooling.pdf.

[2] O. Sari, M. Balli, From conventional to magnetic refrigerator technology, Int. J. Refrig. 37 (2014) 8–15. https://doi.org/10.1016/j.ijrefrig.2013.09.027.

[3] Zimm et al., DESCRIPTION AND PERFORMANCE OF A NEAR-ROOM TEMPERATURE MAGNETIC REFRIGERATOR, 43 (n.d.) 1759–1760.

[4] C.R.H. Bahl, T.F. Petersen, N. Pryds, A. Smith, A versatile magnetic refrigeration test device, Rev. Sci. Instrum. 79 (2008). https://doi.org/10.1063/1.2981692.

[5] Y. Mozharivskyj, Magnetocaloric Effect and Magnetocaloric Materials, Elsevier Inc., 2016. https://doi.org/10.1016/b978-0-12-409547-2.11643-9.

[6] L. Mañosa, A. Planes, M. Acet, Advanced materials for solid-state refrigeration, J. Mater. Chem. A. 1 (2013) 4925–4936. https://doi.org/10.1039/c3ta01289a.

[7] V.K. Pecharsky, J. Gschneidner K. A., Giant Magnetocaloric Effect in Gd5Si2Ge2, Phys. Rev. Lett. 78 (1997) 4494–4497. https://doi.org/10.1103/PhysRevLett.78.4494.

[8] Thomson, W. In Cyclopedia of the Physical Sciences; Nichol, J. P., Ed.; 2nd ed.; Richard Green and Company: London; p 838., (1860).

[9] W. Thomson, On the thermoelastic, thermomagnetic, and pyroelectric properties of matter, London, Edinburgh, Dublin Philos. Mag. J. Sci. 5 (1878) 4–27. https://doi.org/10.1080/14786447808639378.

[10] E. Warburg, ., E. Ann. Phys. Chem. (1881) 141. https://doi.org/10.1093/benz/9780199773787.article.b00194542.

[11] A. Smith, Who discovered the magnetocaloric effect? Warburg, Weiss, and the connection between magnetism and heat, Eur. Phys. J. H. 38 (2013) 507–517. https://doi.org/10.1140/epjh/e2013-40001-9.

[12] W.F. Giauque, D.P. MacDougall, Attainment of temperatures below 1°absolute by demagnetization of Gd2(SO4)38H2O [12], Phys. Rev. 43 (1933) 768. https://doi.org/10.1103/PhysRev.43.768.

[13] G. V. Brown, Magnetic heat pumping near room temperature, J. Appl. Phys. 47 (1976) 3673–3680. https://doi.org/10.1063/1.323176.

[14] T. Krenke, E. Duman, M. Acet, E.F. Wassermann, X. Moya, L. Manosa, A. Planes, Inverse magnetocaloric effect in ferromagnetic Ni-Mn-Sn alloys, Nat. Mater. 4 (2005) 450–454. https://doi.org/10.1038/nmat1395.

[15] V.K. Pecharsky, K.A. Gschneidner, A.O. Pecharsky, A.M. Tishin, Thermodynamics of the magnetocaloric effect, Phys. Rev. B. 64 (2001) 144406. https://doi.org/10.1103/PhysRevB.64.144406.

[16] V.K. Pecharsky, K.A. Gschneidner, Magnetocaloric effect from indirect measurements: Magnetization and heat capacity, J. Appl. Phys. 86 (1999) 565–575.

https://doi.org/10.1063/1.370767.

[17] V.A. Chernenko, V.A. L'vov, E. Cesari, J.M. Barandiaran, Fundamentals of magnetocaloric effect in magnetic shape memory alloys, 1st ed., Elsevier B.V., 2019. https://doi.org/10.1016/bs.hmm.2019.03.001.

[18] V.K. Pecharsky, K.A. Gschneidner, Heat capacity near first order phase transitions and the magnetocaloric effect: An analysis of the errors, and a case study of Gd5(Si2Ge2) and Dy, J. Appl. Phys. 86 (1999) 6315–6321. https://doi.org/10.1063/1.371734.

[19] K.A. Gschneidner, V.K. Pecharsky, Magnetocaloric materials, (2000) 387–429.

[20] A. You, M.A.Y. Be, I. In, Hysteresis effects in the inverse magnetocaloric effect in martensitic Ni-Mn- In and Ni-Mn-Sn, 073914 (2015) 5–10.

[21] J.A. Phys, T. Krenke, E. Duman, M. Acet, Effect of Co and Fe on the inverse magnetocaloric properties of Ni-Mn-Sn, 033903 (2015) 1–6. https://doi.org/10.1063/1.2761853.

[22] K.A. Gschneider, Recent develompents in magnetic refrigeration, 317 (1999) 69–76. https://doi.org/10.4028/www.scientific.net/MSF.315-317.69.

[23] D. Salazar-Jaramillo, P. Álvarez-Alonso, P. Lázpita, J.L. Sánchez Llamazares, P. Gorría, J.A. Blanco, V.A. Chernenko, Magnetocaloric Effect in Specially Designed Materials, Elsevier Inc., 2018. https://doi.org/10.1016/B978-0-12-813904-2.00007-3.

[24] J. Gough, No Title, Mem. Lit. Phil. Soc. Manchester. 1 (2nd Ser (1805) 288.

[25] W. Thomson, On the thermoelastic and thermomagnetic properties of matter, in: Quart. J. Pure Appl. Math., 1857: pp. 57–77.

[26] J.P. Joule, On some thermo-dynamic properties of solids, in: Philos. Trans. R. Soc. L., 1859: pp. 91–131.

[27] C. Rodriguez, L.C. Brown, The thermal effect due to stress-induced martensite formation in B-CuAlNi single crystals, Metall. Mater. Trans. A. 11 (1980) 147–150. https://doi.org/10.1007/BF02700450.

[28] J. Quarini, A. Prince, Solid state refrigeration: Cooling and refrigeration using crystalline phase changes in metal alloys, Proc. Inst. Mech. Eng. Part C J. Mech. Eng. Sci. 218 (2004) 1175–1179. https://doi.org/10.1243/0954406042369062.

[29] J. Van Humbeeck, Shape memory alloys: A material and a technology, Adv. Eng. Mater. 3 (2001) 837–850. https://doi.org/10.1002/1527-2648(200111)3:11<837::AID-ADEM837>3.0.CO;2-0.

[30] P.J. Webster, Heusler alloys, Contemp. Phys. 10 (1969) 559–577. https://doi.org/10.1080/00107516908204800.

[31] T. Graf, C. Felser, S.S.P. Parkin, Simple rules for the understanding of Heusler compounds, Prog. Solid State Chem. 39 (2011) 1–50. https://doi.org/10.1016/j.progsolidstchem.2011.02.001.

[32] N. V. Uvarov, Y. V. Kudryavtsev, A.F. Kravets, A.Y. Vovk, R.P. Borges, M. Godinho, V. Korenivski, Electronic structure, optical and magnetic properties of Co 2FeGe Heusler alloy films, J. Appl. Phys. 112 (2012). https://doi.org/10.1063/1.4752870.

[33] M. Khan, I. Dubenko, S. Stadler, N. Ali, Magnetostructural phase transitions in Ni50Mn 25+xSb25-x Heusler alloys, J. Phys. Condens. Matter. 20 (2008). https://doi.org/10.1088/0953-8984/20/23/235204.

[34] W.J. Buehler, J. V. Gilfrich, R.C. Wiley, Effect of Low-Temperature Phase Changes on the Mechanical Properties of Alloys near Composition TiNi, J. Appl. Phys. 34 (1963) 1475–1477. https://doi.org/10.1063/1.1729603.

[35] M. Kelansth, A. Dunbar, ELrgonne Rational daboratoq!, (1962).

[36] T. Gottschall, K.P. Skokov, M. Fries, A. Taubel, I. Radulov, F. Scheibel, D. Benke, S. Riegg, O. Gutfleisch, Making a Cool Choice: The Materials Library of Magnetic Refrigeration, Adv. Energy Mater. 9 (2019). https://doi.org/10.1002/aenm.201901322.

[37] Y. Wang, D. Salas, T.C. Duong, B. Medasani, A. Talapatra, Y. Ren, Y.I. Chumlyakov, I. Karaman, R. Arróyave, On the fast kinetics of B2–L21 ordering in Ni-Co-Mn-In metamagnetic shape memory alloys, J. Alloys Compd. 781 (2019) 479–489. https://doi.org/10.1016/j.jallcom.2018.12.034.

[38] R. Kainuma, Y. Imano, W. Ito, Y. Sutou, H. Morito, S. Okamoto, O. Kitakami, K. Oikawa, a Fujita, T. Kanomata, K. Ishida, Magnetic-field-induced shape recovery by reverse phase transformation., Nature. 439 (2006) 957–60. https://doi.org/10.1038/nature04493.

[39] K. Ullakko, J.K. Huang, C. Kantner, R.C.O. Handley, Large magnetic-field-induced strains in Ni2MnGa single crystals Large magnetic-field-induced strains in Ni 2 MnGa single crystals, Appl. Phys. Lett. 69 (2013) 1966–1998.

[40] R.Y. Umetsu, W. Ito, K. Ito, K. Koyama, A. Fujita, K. Oikawa, T. Kanomata, R. Kainuma, K. Ishida, Anomaly in entropy change between parent and martensite phases in the Ni50Mn34In16 Heusler alloy, Scr. Mater. 60 (2009) 25–28. https://doi.org/10.1016/j.scriptamat.2008.08.022.

[41] J.A. Monroe, I. Karaman, B. Basaran, W. Ito, R.Y. Umetsu, R. Kainuma, K. Koyama, Y.I. Chumlyakov, Direct measurement of large reversible magnetic-field-induced strain in Ni-Co-Mn-In metamagnetic shape memory alloys, Acta Mater. 60 (2012) 6883–6891. https://doi.org/10.1016/j.actamat.2012.07.040.

[42] D.Y. Cong, S. Roth, L. Schultz, Magnetic properties and structural transformations in Ni-Co-Mn-Sn multifunctional alloys, Acta Mater. 60 (2012) 5335–5351. https://doi.org/10.1016/j.actamat.2012.06.034.

[43] J. Liu, N. Scheerbaum, S. Kauffmann-Weiss, O. Gutfleisch, NiMn-based alloys and composites for magnetically controlled dampers and actuators, Adv. Eng. Mater. 14 (2012) 653–667. https://doi.org/10.1002/adem.201200038.

[44] V. Sokolovskiy, A. Grünebohm, V. Buchelnikov, P. Entel, Ab initio and Monte Carlo approaches for the magnetocaloric effect in Co- and in-doped Ni-Mn-Ga Heusler alloys, Entropy. 16 (2014) 4992–5019. https://doi.org/10.3390/e16094992.

[45] H.B. Luo, C.M. Li, Q.M. Hu, S.E. Kulkova, B. Johansson, L. Vitos, R. Yang, First-principles investigations of the five-layer modulated martensitic structure in Ni2Mn(AlxGa1-x) alloys, Acta Mater. 59 (2011) 5938–5945. https://doi.org/10.1016/j.actamat.2011.06.002.

[46] D. Soto, F.A. Hernández, H. Flores-Zúñiga, X. Moya, L. Mañosa, A. Planes, S. Aksoy, M. Acet, T. Krenke, Phase diagram of Fe-doped Ni-Mn-Ga ferromagnetic shape-memory alloys, Phys. Rev. B - Condens. Matter Mater. Phys. 77 (2008) 1–7. https://doi.org/10.1103/PhysRevB.77.184103.

[47] H.B. Xiao, C.P. Yang, R.L. Wang, V. V. Marchenkov, K. Bärner, Effect of alloying element Al substitution on Ni-Mn-Sn shape memory alloy by first-principle calculations, J. Appl. Phys. 112 (2012). https://doi.org/10.1063/1.4772618.

[48] T. Kihara, X. Xu, W. Ito, R. Kainuma, M. Tokunaga, Direct measurements of inverse magnetocaloric effects in metamagnetic shape-memory alloy NiCoMnIn, Phys. Rev. B - Condens. Matter Mater. Phys. 90 (2014) 1–6. https://doi.org/10.1103/PhysRevB.90.214409.

[49] T. Krenke, M. Acet, E.F. Wassermann, X. Moya, L. Mañosa, A. Planes, Martensitic transitions and the nature of ferromagnetism in the austenitic and martensitic states of Ni-Mn-Sn alloys, Phys. Rev. B - Condens. Matter Mater. Phys. 72 (2005) 1–9. https://doi.org/10.1103/PhysRevB.72.014412.

[50] R.B. Helmholdt, K.H.J. Buschow, Crystallographic and magnetic structure of Ni2MnSn and NiMn2Sn, J. Less-Common Met. 128 (1987) 167–171.

[51] A. Ayuela, J. Enkovaara, K. Ullakko, R.M. Nieminen, Structural properties of magnetic Heusler alloys, J. Phys. Condens. Matter. 11 (1999) 2017–2026. https://doi.org/10.1088/0953-8984/11/8/014.

[52] V. Sánchez-Alarcos, V. Recarte, J.I. Pérez-Landazábal, G.J. Cuello, Correlation between atomic order and the characteristics of the structural and magnetic transformations in Ni-Mn-Ga shape memory alloys, Acta Mater. 55 (2007) 3883–3889. https://doi.org/10.1016/j.actamat.2007.03.001.

[53] A. Ghosh, K. Mandal, Effect of structural disorder on the magnetocaloric properties of Ni-Mn-Sn alloy, Appl. Phys. Lett. 104 (2014). https://doi.org/10.1063/1.4862431.

[54] T. Krenke, M. Acet, E.F. Wassermann, Ferromagnetism in the austenitic and martensitic states of Ni-Mn-In alloys, (2006) 1–10. https://doi.org/10.1103/PhysRevB.73.174413.

[55] A.G. Varzaneh, P. Kameli, F. Karimzadeh, H. Salamati, Effect of Heat Treatment on Martensitic Transformation of Ni47Mn40Sn13 Ferromagnetic Shape Memory Alloy Prepared by Mechanical Alloying Effect of Heat Treatment on Martensitic Transformation of Ni 47 Mn 40 Sn 13 Ferromagnetic Shape Memory Alloy Prepared b, 3 (2015). https://doi.org/10.1007/s12540-015-4537-0.

[56] J. Pons, R. Santamarta, V.A. Chernenko, E. Cesari, Structure of the layered martensitic phases of Ni – Mn – Ga alloys Structure of the layered martensitic phases of Ni – Mn – Ga alloys, (2006). https://doi.org/10.1016/j.msea.2006.02.179.

[57] S.L. Taylor, R.N. Shah, D.C. Dunand, Ni-Mn-Ga micro-trusses via sintering of 3D-printed inks containing elemental powders, Acta Mater. 143 (2018) 20–29. https://doi.org/10.1016/j.actamat.2017.10.002.

[58] A. You, M.A.Y. Be, I. In, Metamagnetic shape memory effect in a polycrystalline alloy, 192513 (2006) 10–13. https://doi.org/10.1063/1.2203211.

[59] R.Y. Umetsu, A. Sheikh, W. Ito, B. Ouladdiaf, K.R.A. Ziebeck, T. Kanomata, R.

Kainuma, The effect of Co substitution on the magnetic properties of the Heusler alloy Ni50Mn33Sn17, Appl. Phys. Lett. 98 (2011) 10–13. https://doi.org/10.1063/1.3548558.

[60] B. Rodríguez-Crespo, D. Salazar, S. Lanceros-Méndez, V. Chernenko, Development and magnetocaloric properties of Ni(Co)-Mn-Sn printing ink, J. Alloys Compd. 917 (2022) 165521. https://doi.org/10.1016/j.jallcom.2022.165521.

[61] S.S. Nambiar, B.R.N. Murthy, S. Sharma, A.A. Prasanna, A.J. Chelvane, Microstructure and Mechanical Properties of Annealed Quinary Ni-Mn-Sn-Fe-In Heusler Alloy, Eng. Sci. 17 (2022) 303–308. https://doi.org/10.30919/es8d632.

[62] S. Esakki Muthu, N. V. Rama Rao, M. Manivel Raja, D.M. Raj Kumar, D. Mohan Radheep, S. Arumugam, Influence of Ni/Mn concentration on the structural, magnetic and magnetocaloric properties in Ni50-xMn37+xSn13 Heusler alloys, J. Phys. D. Appl. Phys. 43 (2010). https://doi.org/10.1088/0022-3727/43/42/425002.

[63] V. Zhukova, M. Ipatov, A. Granovsky, A. Zhukov, Magnetic properties of Ni-Mn-In-Co Heusler-type glass-coated microwires, J. Appl. Phys. 115 (2014) 10–13. https://doi.org/10.1063/1.4868919.

[64] W. Maziarz, P. Czaja, M.J. Szczerba, L. Lityńska-Dobrzyńska, T. Czeppe, J. Dutkiewicz, Influence of Ni/Mn concentration ratio on microstructure and martensitic transformation in melt spun Ni-Mn-Sn Heusler alloy ribbons, J. Alloys Compd. 615 (2015) S173–S177. https://doi.org/10.1016/j.jallcom.2013.12.164.

[65] H. Zheng, W. Wang, S. Xue, Q. Zhai, J. Frenzel, Z. Luo, Composition-dependent crystal structure and martensitic transformation in Heusler Ni-Mn-Sn alloys, Acta Mater. 61 (2013) 4648–4656. https://doi.org/10.1016/j.actamat.2013.04.035.

[66] A.S. Kalbfleisch, G. Matthews, P.J. Jacques, On the influence of the cooling rate on the martensitic transformation of Ni-Mn-Sn Heusler alloys, Scr. Mater. 114 (2016) 121–124. https://doi.org/10.1016/j.scriptamat.2015.12.005.

[67] T. Krenke, M. Acet, X. Moya, A. Planes, Effect of Co and Fe on the inverse magnetocaloric properties of Ni-Mn-Sn □, 033903 (2007). https://doi.org/10.1063/1.2761853.

[68] D.Y. Cong, S. Roth, L. Schultz, Magnetic properties and structural transformations in Ni – Co – Mn – Sn multifunctional alloys, ACTA Mater. 60 (2012) 5335–5351. https://doi.org/10.1016/j.actamat.2012.06.034.

[69] D.H. Wang, C.L. Zhang, H.C. Xuan, Z.D. Han, J.R. Zhang, S.L. Tang, B.X. Gu, Y.W. Du, The study of low-field positive and negative magnetic entropy changes in, 013909 (2007). https://doi.org/10.1063/1.2752140.

[70] R. Das, S. Sarma, A. Perumal, A. Srinivasan, Effect of Co and Cu substitution on the magnetic entropy change in Ni 46 Mn 43 Sn 11 alloy □, 901 (2011). https://doi.org/10.1063/1.3540327.

[71] F. Chen, Y.X. Tong, Y.J. Huang, B. Tian, L. Li, Y.F. Zheng, Intermetallics Suppression of g phase in Ni 38 Co 12 Mn 41 Sn 9 alloy by melt spinning and its effect on martensitic transformation and magnetic properties, 36 (2013) 81–85. https://doi.org/10.1016/j.intermet.2013.01.004.

[72] H. Zheng, D. Wu, S. Xue, J. Frenzel, G. Eggeler, Martensitic transformation in rapidly

solidified Heusler, Acta Mater. 59 (2011) 5692–5699. https://doi.org/10.1016/j.actamat.2011.05.044.

[73] A. Kitanovski, Energy Applications of Magnetocaloric Materials, Adv. Energy Mater. 10 (2020). https://doi.org/10.1002/aenm.201903741.

[74] R. Gauß, G. Homm, O. Gutfleisch, The Resource Basis of Magnetic Refrigeration, 21 (2016). https://doi.org/10.1111/jiec.12488.

[75] S. Zare, Free piston Stirling engines : A review, (2019). https://doi.org/10.1002/er.4533.

[76] I.A. Radulov, D.Y. Karpenkov, M. Specht, T. Braun, A.Y. Karpenkov, K.P. Skokov, O. Gutfleisch, T.U. Darmstadt, A. Characterization, Heat Exchangers From Metal-Bonded La (Fe , Mn , Si) 13 H x Powder, 53 (2017) 1–7.

[77] A. Haleem, M. Javaid, Additive Manufacturing Applications in Industry 4.0: A Review, J. Ind. Integr. Manag. 04 (2019) 1930001. https://doi.org/10.1142/s2424862219300011.

[78] L. Chen, Y. He, Y. Yang, S. Niu, H. Ren, The research status and development trend of additive manufacturing technology, Int. J. Adv. Manuf. Technol. 89 (2017) 3651–3660. https://doi.org/10.1007/s00170-016-9335-4.

[79] R.D. Sochol, E. Sweet, C.C. Glick, S.Y. Wu, C. Yang, M. Restaino, L. Lin, 3D printed microfluidics and microelectronics, Microelectron. Eng. 189 (2018) 52–68. https://doi.org/10.1016/j.mee.2017.12.010.

[80] R.C.Y. Auyeung, H. Kim, S. Mathews, N. Charipar, A. Piqué, Laser additive manufacturing of embedded electronics, Elsevier Ltd, 2017. https://doi.org/10.1016/B978-0-08-100433-3.00012-9.

[81] E. Sachyani Keneth, A. Kamyshny, M. Totaro, L. Beccai, S. Magdassi, 3D Printing Materials for Soft Robotics, Adv. Mater. 33 (2021) 1–17. https://doi.org/10.1002/adma.202003387.

[82] S.Y. Wu, C. Yang, W. Hsu, L. Lin, 3D-printed microelectronics for integrated circuitry and passive wireless sensors, Microsystems Nanoeng. 1 (2015) 1–9. https://doi.org/10.1038/micronano.2015.13.

[83] J. Hoerber, J. Glasschroeder, M. Pfeffer, J. Schilp, M. Zaeh, J. Franke, Approaches for additive manufacturing of 3D electronic applications, Procedia CIRP. 17 (2014) 806–811. https://doi.org/10.1016/j.procir.2014.01.090.

[84] S.F.S. Shirazi, S. Gharehkhani, M. Mehrali, H. Yarmand, H.S.C. Metselaar, N. Adib Kadri, N.A.A. Osman, A review on powder-based additive manufacturing for tissue engineering: Selective laser sintering and inkjet 3D printing, Sci. Technol. Adv. Mater. 16 (2015). https://doi.org/10.1088/1468-6996/16/3/033502.

[85] Y. Wu, Y. Lu, M. Zhao, S. Bosiakov, L. Li, A Critical Review of Additive Manufacturing Techniques and Associated Biomaterials Used in Bone Tissue Engineering, Polymers (Basel). 14 (2022) 1–24. https://doi.org/10.3390/polym14102117.

[86] X. Wang, S. Xu, S. Zhou, W. Xu, M. Leary, P. Choong, M. Qian, M. Brandt, Y.M. Xie, Topological design and additive manufacturing of porous metals for bone scaffolds and orthopaedic implants: A review, Biomaterials. 83 (2016) 127–141.

https://doi.org/10.1016/j.biomaterials.2016.01.012.

[87] D. Barba, E. Alabort, R.C. Reed, Synthetic bone: Design by additive manufacturing, Acta Biomater. 97 (2019) 637–656. https://doi.org/10.1016/j.actbio.2019.07.049.

[88] Razvan Udroiu, Powder bed additive manufacturing systems and its applications, Acad. J. Manuf. Eng. 10 (2012) 122–129.

[89] J.P. Kruth, L. Froyen, J. Van Vaerenbergh, P. Mercelis, M. Rombouts, B. Lauwers, Selective laser melting of iron-based powder, J. Mater. Process. Technol. 149 (2004) 616–622. https://doi.org/10.1016/j.jmatprotec.2003.11.051.

[90] A. Simchi, F. Petzoldt, H. Pohl, On the development of direct metal laser sintering for rapid tooling, J. Mater. Process. Technol. 141 (2003) 319–328. https://doi.org/10.1016/S0924-0136(03)00283-8.

[91] B. Dutta, S. Palaniswamy, J. Choi, L.J. Song, J. Mazumder, Additive manufacturing by direct metal deposition, Adv. Mater. Process. 169 (2011) 33–36.

[92] E.C. Santos, M. Shiomi, K. Osakada, T. Laoui, Rapid manufacturing of metal components by laser forming, Int. J. Mach. Tools Manuf. 46 (2006) 1459–1468. https://doi.org/10.1016/j.ijmachtools.2005.09.005.

[93] M. Rincón-iglesias, A. Delgado, N. Peřinka, E. Lizundia, S. Lanceros-méndez, Water-based 2D printing of magnetically active cellulose derivative nanocomposites, Carbohydr. Polym. 233 (2020) 115855. https://doi.org/10.1016/j.carbpol.2020.115855.

[94] L. Dai, D. Xu, Polyethylene surface enhancement by corona and chemical, 60 (2019) 1005–1010. https://doi.org/10.1016/j.tetlet.2019.03.013.

[95] K.N. Al-milaji, S. Gupta, V.K. Pecharsky, R. Barua, H. Zhao, R.L. Hadimani, Differential effect of magnetic alignment on additive manufacturing of magnetocaloric particles, (2020). https://doi.org/10.1063/1.5130028.

[96] K.N. Al-Milaji, R.L. Hadimani, S. Gupta, V.K. Pecharsky, H. Zhao, Inkjet Printing of Magnetic Particles Toward Anisotropic Magnetic Properties, Sci. Rep. 9 (2019) 1–9. https://doi.org/10.1038/s41598-019-52699-0.

[97] C. Xu, Q. Wu, G. L'Espérance, L.L. Lebel, D. Therriault, Environment-friendly and reusable ink for 3D printing of metallic structures, Mater. Des. 160 (2018) 262–269. https://doi.org/10.1016/j.matdes.2018.09.024.

[98] B.Y. Ahn, D. Shoji, C.J. Hansen, E. Hong, D.C. Dunand, J.A. Lewis, Printed origami structures, Adv. Mater. 22 (2010) 2251–2254. https://doi.org/10.1002/adma.200904232.

[99] E. Peng, X. Wei, T.S. Herng, U. Garbe, D. Yu, J. Ding, Ferrite-based soft and hard magnetic structures by extrusion free-forming, RSC Adv. 7 (2017) 27128–27138. https://doi.org/10.1039/c7ra03251j.

Chapter 2

Experimental Methods

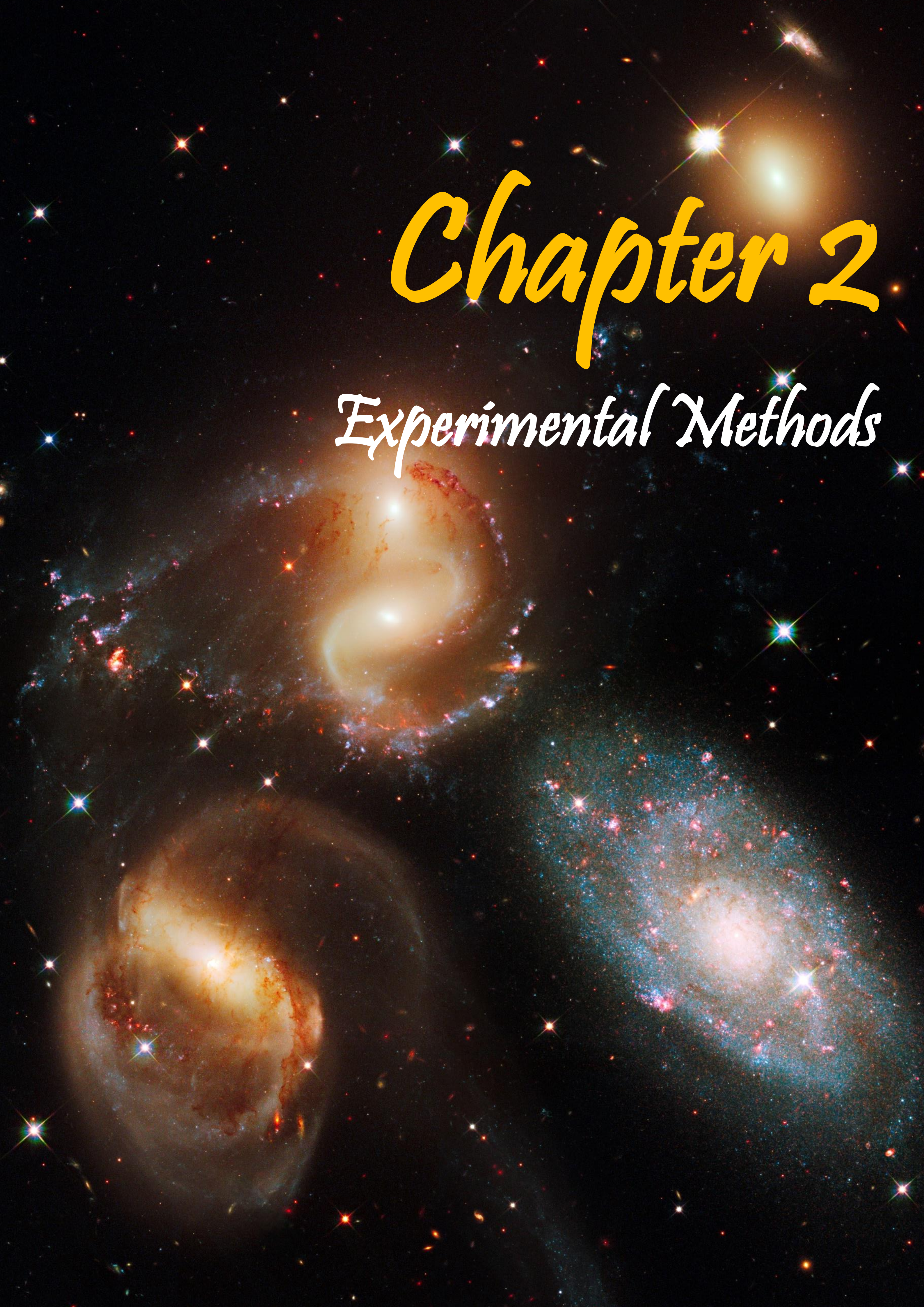

Chapter 2

Experimental Methods

2.1. CHOOSING ALLOY COMPOSITION

The first step of the experimental procedure is to choose the composition of the alloy and calculate the amount of each element required for the synthesis. Given a specific composition in atomic percentage, the mass percentage of each element (*E*) is given by:

$$\%E = \frac{n_E * m_E}{\sum_i n_i * m_i} \times 100$$

where n_E is the stoichiometric index and m_E is the atomic mass of the element *E*.

According to the goals of the thesis, different compositions series in the Heusler-type NiMn-based alloys system were selected to be prepared for studies. One of the main criteria for selection was that these materials should exhibit a martensitic transformation around room-temperature. The alloys were prepared by two methods: (i) induction melting and (ii) arc-melting. In both methods the pure constituent elements (with purity of 99.99%+) and Ar atmosphere were used. Appropriate alloys were used for re-melting and subsequent melt-spinning.

2.2. ALLOYS FABRICATION

2.2.1. Induction casting

The first method used for the fabrication of alloys is the induction melting technique (Reitel induret mini, Figure 2.1). The elements were placed in an alumina crucible and the mixture was melted using an induction coil until all the pieces were completely melted in an inert Argon atmosphere to avoid any oxidation. The liquid alloy was then casted into a copper mold for fast and homogeneous solidification. The weight of ingots was usually 40 g.

Figure 2.1: Induction melting furnace (left). Arc-melting furnace (right).

2.2.2. Arc-melting

Another technique used for the fabrication of alloys is the arc-melting (Edmund Bühler Compact Arc Melter MAM-1), where the elements are placed in a profiled copper substrate and an electric arc is generated by inducing a high voltage between it and a Tungsten tip under an inert Argon-purged atmosphere. The electric arc furnace is capable of melting pieces of materials up to 3273K (3000°C) in few seconds. The arc has to be moved along the area where all the metallic pieces are placed so they all melt and form a single bulk piece. After the first melting, the alloy is not homogeneous and to obtain homogeneity, the sample must be re-melted 4 to 6 times, turning it each time.

Some elements are susceptible to evaporation during the melting process. This leads to a reduction in the mass of this element which slightly changes the composition during melting compared to the nominal one. This issue can be avoided or reduced by adding a small percentage to the nominal mass of this element (3 – 5 wt. %) and melting the alloy several times, weighing it after each melt, until the mass of the molten alloy equals the nominal mass.

The arc-melting furnace used for the present work has the capacity to melt up to 20 grams of alloy but experimentally the maximum amount that can be melted to have homogeneity is about 10 grams since larger samples cannot be melted entirely at the same time preventing a good homogeneity of the ingot.

2.3. MELT-SPINNING

The melt-spinning process of the bulk samples was used to prepare polycrystalline ribbons. This technique provides easy processability to the metallic materials. A melt-spinner Edmund Bühler Melt Spinner MSP10 is shown in Figure 2.2, left. Figure 2.2 right schematically illustrates the working principle of melt-spinning technique. Here, the alloy is placed into a quartz tube with an ejection orifice at the bottom of about 0.75mm diameter. Then, it is induction melted and ejected into a copper wheel that has a certain linear speed (10 – 40 m/s). This produces a high quenching rate ($10^5 – 10^6$ K/s) facilitating retaining high temperature metastable phases at room temperature and preventing the formation of precipitates. As a result the magnetic properties could be improved.

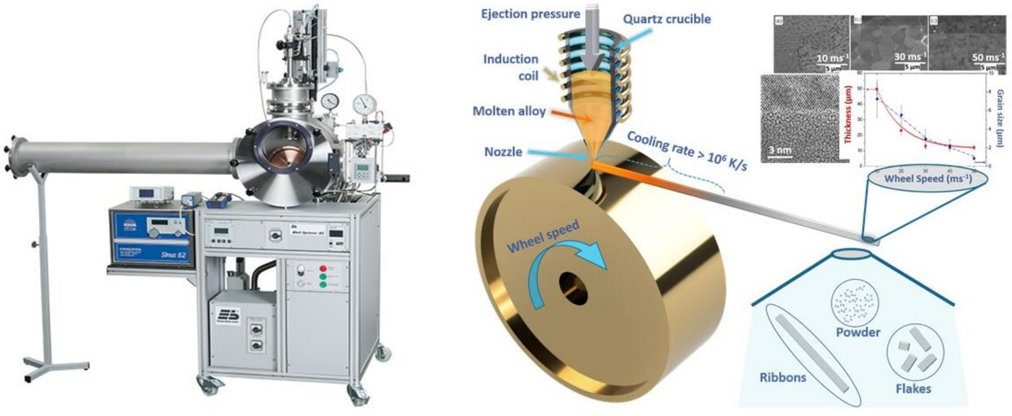

Figure 2.2: Melt-spinner used for ribbon fabrication (left) and schematic of the working principle of the technique (right) [1].

The wheel speed affects the quenching rate of the material. The higher is the wheel speed, the higher is the quenching rate since less material per unit of length is deposited on the copper wheel. Therefore increasing the wheel speed results in the ribbons with reduced thickness. It affects the crystallization process of the material, making the grains smaller which, e.g., in the case of permanent magnets gives rise to the enhanced coercivity as schematically shown here:

$$\nearrow wheel\ speed \ \Rightarrow \nearrow quenching\ rate \ \Rightarrow \searrow grain\ size \ \Longrightarrow \nearrow coercivity$$

2.4. POWDER PREPARATION

2.4.1. Manual grinding

Most of the powder obtained in the present work was prepared by a manual grinding ribbons using an agate mortar and pestle tool and then sieving the powder to the desired size fraction (20 – 106 μm). The grinding process degrades the material by inducing surface strains. This effect can be reversed by performing heat treatments. Another way of reducing the impact of the grinding process is using liquid nitrogen during grinding process, when the powder is in the pure martensitic phase.

2.4.2. Hammer milling

Hammer milling was used for preparing powder in larger quantity than that being prepared by manual grinding. The device used for that was Hosokawa Alpine PICOLINE and the working principle of this technique is basically a steel drum containing a horizontal or vertical rotating shaft or drum on which hammers are mounted. The hammers are fixed to a central rotor and can have some mobility or even move freely. The rotor spins at a high speed inside the drum while material (less than 1mm in diameter) is fed into a feed hopper. The material is impacted by the hammer bars and expelled into a container once the size is less than a certain value.

2.4.3. Gas atomization

Some powder used for this thesis was prepared by gas atomization which is a process where a molten metal is disintegrated into droplets that then solidify. This technique provides metal powder in quantities of kgs.

2.5. HEAT TREATMENTS

Heat treatments are useful for alloys homogenization and for enhancing their properties after performing any process that may degrade them. Heat treatments must be done under an inert atmosphere to avoid any oxidation. For ribbons and tiny samples, the procedure is to introduce them in quartz tubes to which three flushes are applied, each of those consists of performing a vacuum for five minutes and then introducing high purity Argon (99.999%). After flushes, the quartz tube with the sample is sealed using a propane plus oxygen torch under vacuum or under a specific pressure below 1 bar. Some of the furnaces used have a system that allows controlling the atmosphere during the heat treatment by using a large quartz tube inside which the sample to be treated is placed (maximum diameter 4.5cm) and which can be sealed at both ends.

In the furnace working setup, one end is connected to a desired inert gas source and the other end is connected to a vacuum pump. Continuous vacuum or gas reflux can be applied to this large quartz tube depending on the experiment requirements. The furnaces used for these atmosphere-controlled experiments are the Mini Rotary Tube Furnace from NBD (NBD-O1200-50ICR) and the Carbolite VST 12/200. For samples encapsulated in quartz tubes, the Nabertherm RHTC 80-230/15, ThermConcept KL 15/11 and the Carbolite furnaces were used.

2.6. INK PREPARATION

Once a proper powder is obtained it is then used for the ink manufacture. The goal is to make an environmentally-friendly approach and for that the polymers selected for ink fabrication were those that satisfy environmentally-friendliness, to be bio-based, water soluble and to be widely available cost-effective raw materials. Specifically, the HPC was selected for having a high processability and good film forming capacity. Specifically, the inks consist of three elements:

- ✓ Metallic powder: Commercial Fe, Al and Si powder and fabricated powder of NiMn-based Heusler alloy
- ✓ Matrix: a polymer that acts as a binder ⇒ Hydroxypropyl Cellulose (HPC), Collagen and Silk.
- ✓ Dissolvent: Deionized H_2O

2.6.1. Collagen-based ink

The source of collagen for ink preparation was a salmon skin which provides a good quality collagen with good mechanical properties. The first step is to separate the collagen from the skin. For that, the scales and muscles were removed, and skin piece was further washed with water and cut into pieces of about 2 x 2 cm. Then, for fat removal from the skin, the pieces are immersed in 10% ethanol for 48h, under stirring (the solution is replaced twice a day). In order to remove non-collagenous proteins the skins are then treated with 0.1M NaOH (1:10 w/v), during 3 x 2 h. After thorough washing with water, salmon skins are dissolved in 0.5M acetic acid (1:10 w/v) during 72h, under stirring. Then the resulting mixture is centrifuged and the supernatant, containing the acid soluble collagen is further vacuum filtered to remove non-soluble impurities. Now, salmon skin collagen is recovered by salting out and after centrifugation is suspended in 0.5 M of acetic acid, dialyzed against 0.1 M acetic acid. Then it is freeze-dried until further use. All the extraction procedure is conducted at 4 ºC.

2.6.2. Silk-based ink

For silk-based ink preparation we start from Bombyx mori silkworm cocoons by a standard method, named soap degumming[2]. Each cocoon is cut in half, and the internal surface is cleaned mechanically. Then, several small pieces of 1 cm^2 are cut. The silk cocoon is basically composed by two elements: (i) Silk fibroin, which is the polymer we are interested in; and (ii) sericin, that acts as a glue joining the fibres. For separating the sericin from the fibroin, the pieces of cocoons are introduced in an alkaline solution of 0.05 wt%. Na_2CO_3 (see Figure 2.3) and is heated up to 95ºC (above 100ºC the chains starts to break but we want to avoid this) and left 10 minutes, repeating this *Degumming* process one more time. In this process the Hydrogen bridges of the polymer are broken. After this process white neat fibres are obtained and they are left drying overnight.

The second part of this ink preparation process consists on dissolving the silk fibroine (SF) to obtain a gel. To accomplish this task the dried fibres are introduced in a solution that is prepared with [4g $CaCl_2$ x $2H_2O$ + 4mL H_2O + 1.5 ml EtOH] per 0.5g of fibroine. The ethanol helps breaking Hydrogen bridges. The solution is heated up to 80ºC and magnetically mixed at 400 rpm. This produces a solution of 8% of fibroin in water. Then the mix is introduced in a dialysis cassette (cut-off: 30kDa) and is left for 6 hours. After the salt removal the final product is a solution of water and fibroin with 2% of concentration. This solution is metastable and may have two phases: Dissolved and Precipitated. The solution is centrifuged 5min at 7500 rpm to remove any solid residue that could be in it (Figure 2.3).

The dried silk is semi-crystalline and during further processing the Hydrogen bridges are broken, giving rise to an amorphous material, which will be dried.

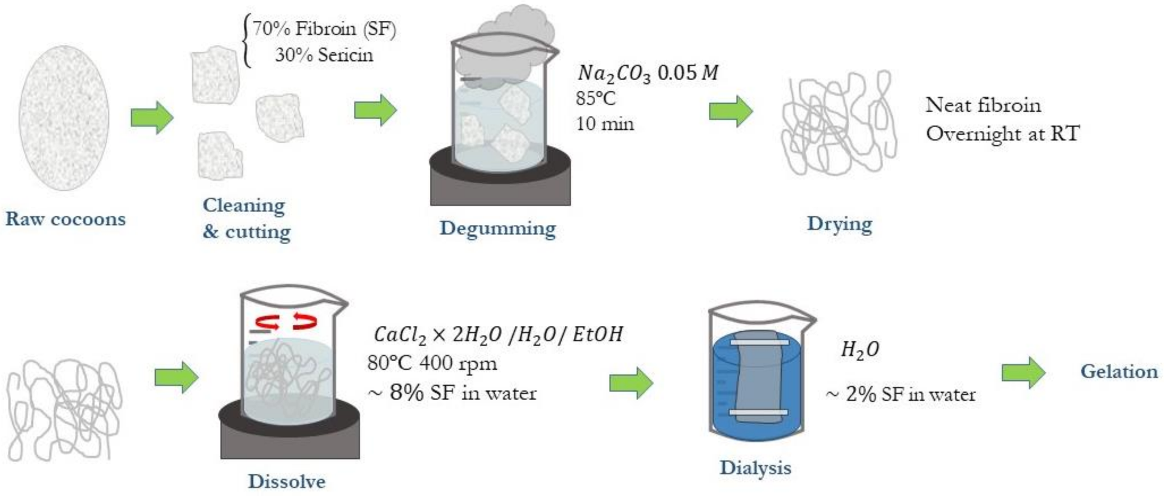

Figure 2.3: Schematic of the route for silk preparation.

The metallic ink is prepared by mixing metallic powder with SF and formic acid that improves the viscosity in order to well-distribute the metallic particles within the ink.

2.6.3. Cellulose-based ink

The flow chart for cellulose-based ink preparation is schematically shown in Figure 2.4. The preparation of the ink consists on dissolving the HPC in distilled water by manual stirring and leaving for 24 hours at room temperature until air bubbles are removed and the HPC is completely dissolved. Then the metallic powder is added and the mix is manually stirred during 5 minutes until homogenization.

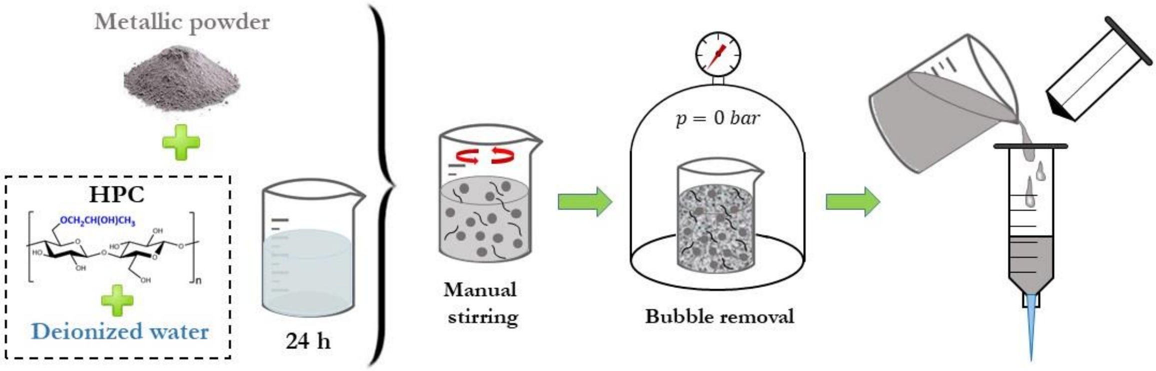

Figure 2.4: The flow chart of the experimental procedure for ink preparation and bubble removal.

The process of manual stirring introduces air bubbles within the viscous ink leaving it for non-optimal printing. Introducing the ink in a vacuum chamber removes air bubbles after 2-3 cycles of vacuuming. The water evaporation in this process is minimal (less than 5%) so the water reduction can be neglected. After vacuuming the ink is introduced into a 10mL syringe for being stored and/or to start printing. In some cases the syringe is vacuumed during 2 minutes for removing completely remaining bubbles that may be introduced in the process of filling it.

2.7. 2D PRINTING

2.7.1. Doctor Blade

The first step for ink testing was done by Doctor Blade, a technique that consists on depositing a drop of ink in a substrate and then passing a sharp blade at a certain height (in our case 0.5mm). This technique provides a homogeneous film that is left drying at room temperature overnight. Figure 2.5 shows the scheme of the working principle[3].

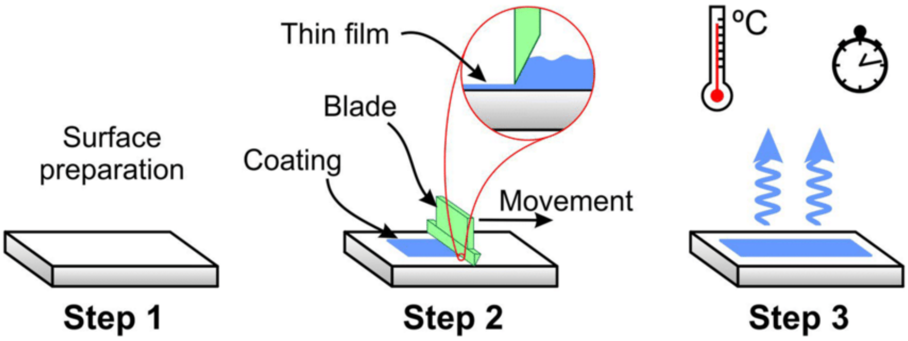

Figure 2.5: Generic scheme for film preparation by doctor blade technique. In our case the drying temperature was room-temperature.

2.7.2. Screen-printing

After doctor blade tests, the first printing tests of the prepared inks were done by 2D printing using the screen-printing method (Figure 2.6). The device used for this tests is the Wenzhou Zhengchang Machinery ZH3040H. The ink is deposited in the form of chips on the screen mesh and, using a manual scrapper, is directed to the printing pattern under which a PET substrate is placed, where the ink is deposited. Since metallic inks are magnetic, placing a permanent magnet under the substrate can orientate the particles with their magnetic easy axis along the magnetic field. To increase the amount of magnetic material, 10 layers are printed one on top of the other.

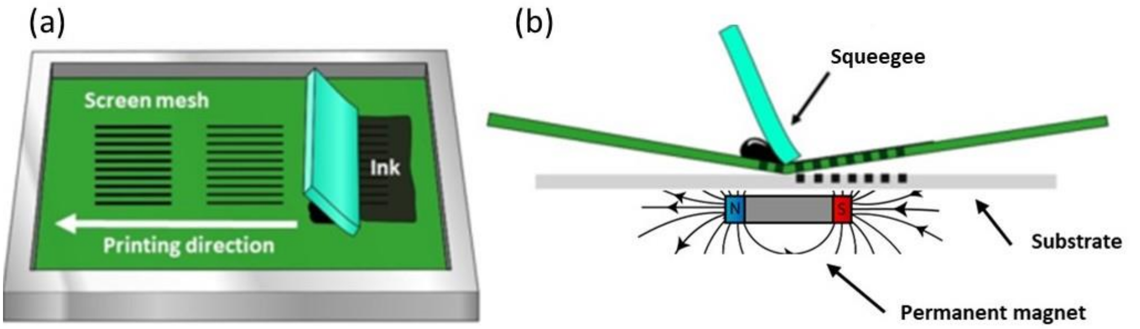

Figure 2.5: Screen-printing setup (left) and detail of the ink deposition in the substrate in the printing process, where it is oriented by the permanent magnet placed below the substrate (right).

2.8. 3D PRINTING

3D structures are printed using the cold-extrusion technique (also known as solvent-cast printing) using Tissue Scribble printer (3dcultures). The scheme of cold-extrusion technique is shown in Figure 2.7. The metallic ink, which now presents rather viscous paste, is loaded into a 10 mL syringe attached with a tapered nozzle with exit inner diameter of 410μm. The structures are printed in a PET (Polyethylene Terephthalate) foil substrate that is stuck into a levelled glass surface. In order to ensure proper PET substrate adhesion to the glass surface small drops of water are deposited at the corners of PET substrate so a thin layer of water enters by capillarity between the substrate and the glass surface. The printing speed in this work varies from 200 mm/min to 300 mm/min, depending on the ink viscosity. The syringe extrusion rate is of 1.15 ml/hour. These values of printing speed and extrusion rate were chosen to get a balance between the extrusion rate with nozzle translation speed (printing speed). To accelerate the drying rate, a cooling fan (DC 5.5V, 0.55W, 250mm from the printer nozzle) is used so there is a continuous airflow. This ensures that the printed layer is going to be deposited into a dried previous layer since otherwise the layer-to-layer adhesion is not optimal.

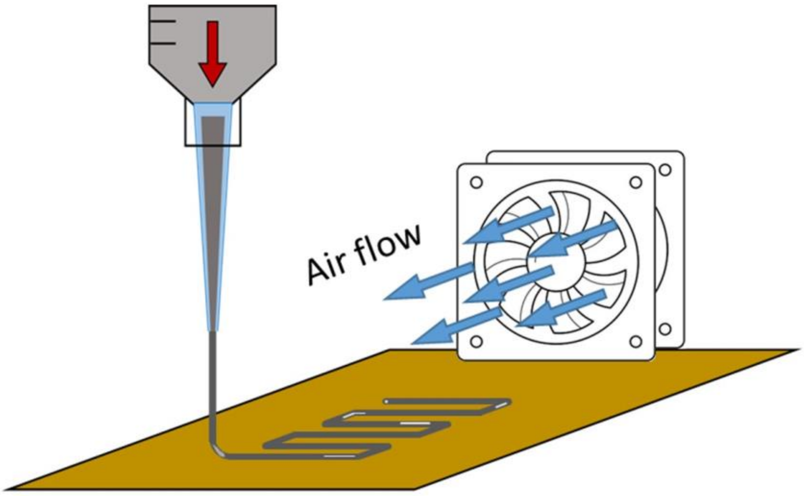

Figure 2.6: Schematic model for extrusion 3D printing technique used.

2.9. CHARACTERIZATION METHODS

2.9.1. Vibrating Sample Magnetometer (VSM)

The magnetic and transformation characterization were performed by using the vibrating sample magnetometer (VSM) from MicroSense Inc. (the magnetic field and temperature ranges are 0-2 T and 100-500 K, respectively). With this characterization technique the temperature and magnetic field induced phase transformations can be revealed by performing magnetization versus temperature and magnetization versus magnetic field measurements. The working scheme of the VSM is shown in Figure 2.8. The sample is placed within a uniform magnetic field (up to 2 T) and the sample holder vibrates in the Z-axis at a given frequency and the coils placed in the ends of the electromagnets measure the signal change by a magnetic induction principle. The temperature is controlled by a continuous air flux that passes through a resistor that heats it by applying a certain voltage. For the measurements below room temperature the copper tube where the air goes to the furnace is submerged into a liquid nitrogen so the air is cooled down.

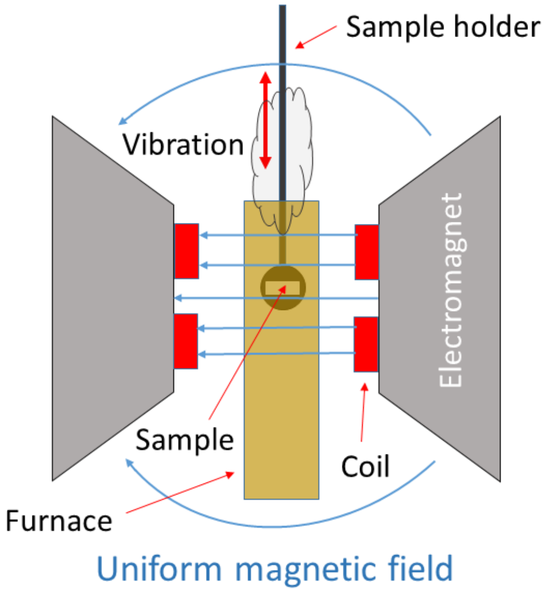

Figure 2.7: Scheme of the working principle of the VSM.

2.9.2. Superconducting Quantum Interference Device (SQUID)

For high magnetic field measurements (up to 7 T) a SQUID-VSM magnetometer from Quantum Design Inc. was used. This device allows to measure smaller samples than the VSM since its sensitivity is far higher than the VSM one. The measurement temperature range is from 5K to 400K.

2.9.3. Differential Scanning Calorimetry (DSC)

Differential scanning calorimetry is a thermoanalytical technique where the amount of heat required to increase the temperature of a sample and a reference is measured as a function of temperature. During the measurement a reference sample with a well-defined heat capacity over the range of the temperatures to be scanned is maintained at roughly the same temperature as the measuring sample. With this technique temperature induced phase transformations can be detected and characterized. In the present work a Mettler-Toledo DSC822e calorimeter (ramp 20 K/min), under N_2 atmosphere was used.

2.9.4. Scanning Electron Microscopy (SEM)

For microstructure analysis a scanning electron microscope (SEM) was used (Hitachi TM 3000). It was equipped with an energy-dispersive X-ray spectroscopy (EDS, or also known as EDX) for composition measurements. The sample to be measured is placed in the sample holder using carbon tape, to ensure electrical conductivity between them. The grains size, ribbon thickness, morphology etc. can be studied with this technique. Composition mapping was done with the EDX measurements.

2.9.5. Magnetic field-induced adiabatic temperature change

A customary developed technique of direct measurements of adiabatic temperature change was used for magnetocaloric characterization of the samples. The schematic of the device is shown in Figure 2.9 [4]. MCE measurements must be performed under adiabatic conditions which mean that the sample must be thermally insulated by: (i) covering the sample with Teflon tape to ensure thermal insulation by conduction, (ii) the chamber where the sample holder is going to be mounted is kept at constant vacuum to ensure thermal insulation by convection and (iii) the shield that has the capsule where the sample is placed is made out of Copper avoiding thermal losses by infrared radiation.

For making the measurement the sample is divided in two pieces and is mounted in the sample holder so the thermocouple is embedded between the two pieces of the sample. For proper heat transfer to the thermocouple a silver paste is used. Then the sample is put in contact with the heater which is integrated in the alumina-based sample holder and insulated with Teflon tape. The sample holder is then mounted in the system between two poles of a electromagnet that provides a constant magnetic field.

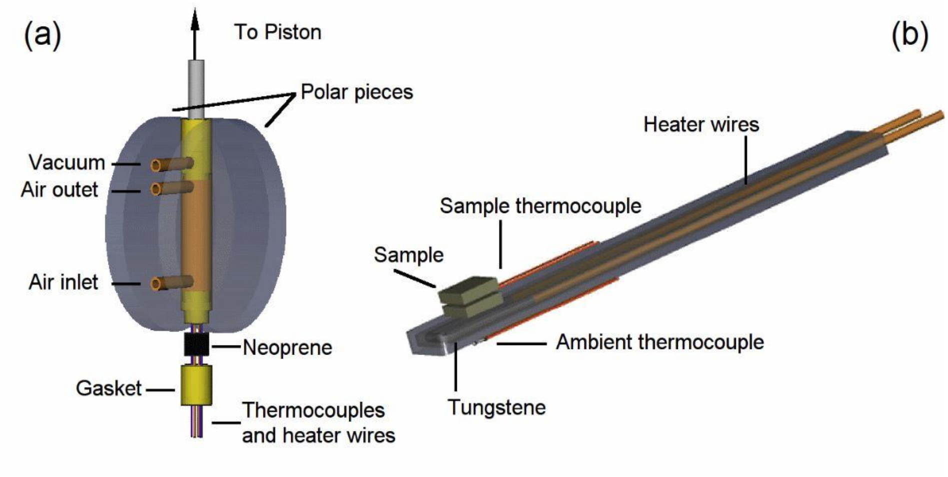

Figure 2.8: Sketch of the experimental setup (a). The sample holder with heater assembly (b) [4].

The temperature is controlled by a heater attached to the sample holder that heats the sample by thermal contact. For cooling below the room temperature a flux of air, cooled down by liquid nitrogen, is passed through an external cavity close to the cavity where the sample holder is placed. The procedure for the measurement is to heat up the sample until full austenitic phase is reached and then cooling down to the selected temperature of measurement. Then the sample is removed from the magnetic field by a hydraulic system and the value of the temperature change is measured by the thermocouple.

3.9.5. Mechanical characterization

Mechanical characterization was performed to the printed structures under compression at 1 mm/min speed using Shimadzu AGS-J 500M device.

3.9.6. X-Ray Diffraction (XRD)

X-ray diffraction patterns (XRDP) are obtained using a Bruker D8 Advance diffractometer (30 kV and 20 mA, λCu = 1.5418 Å) and the FullProf suite for the refinement.

2.9.7. Magnetic field induced entropy change calculation

As explained in the introduction, the magnetic entropy change can be calculated by integrating the magnetization versus temperature curves by the Maxwell thermodynamic relationship

$$\Delta S_m(T,H) = S_m(T,H) - S_m(T,0) = \int_0^H \left(\frac{\partial M(T,H')}{\partial T}\right) dH'$$

The calculations were done using Scilab ® software and the data obtained from the SQUID isomagnetic magnetization versus temperature measurements.

2.10. REFERENCES

[1] D.S. Et.al., Lightweight, multifunctional materials based on magnetic shape memory alloys, in: Elsevier, 2020: pp. 187–238.

[2] A. Reizabal, S. Gonçalves, R. Brito-Pereira, P. Costa, C.M. Costa, L. Pérez-Álvarez, J.L. Vilas-Vilela, S. Lanceros-Méndez, Optimized silk fibroin piezoresistive nanocomposites for pressure sensing applications based on natural polymers, Nanoscale Adv. 1 (2019) 2284–2292. https://doi.org/10.1039/c8na00417j.

[3] D. Frederichi, M.H.N.O. Scaliante, R. Bergamasco, Structured photocatalytic systems: photocatalytic coatings on low-cost structures for treatment of water contaminated with micropollutants—a short review, Environ. Sci. Pollut. Res. 28 (2021) 23610–23633. https://doi.org/10.1007/s11356-020-10022-9.

[4] P. Álvarez-Alonso, J. López-García, G. Daniel-Perez, D. Salazar, P. Lázpita, J.P. Camarillo, H. Flores-Zuñiga, D. Rios-Jara, J.L. Sánchez-Llamazares, V.A. Chernenko, Simple Set-Up for Adiabatic Measurements of Magnetocaloric Effect, Key Eng. Mater. 644 (2015) 215–218. https://doi.org/10.4028/www.scientific.net/kem.644.215.

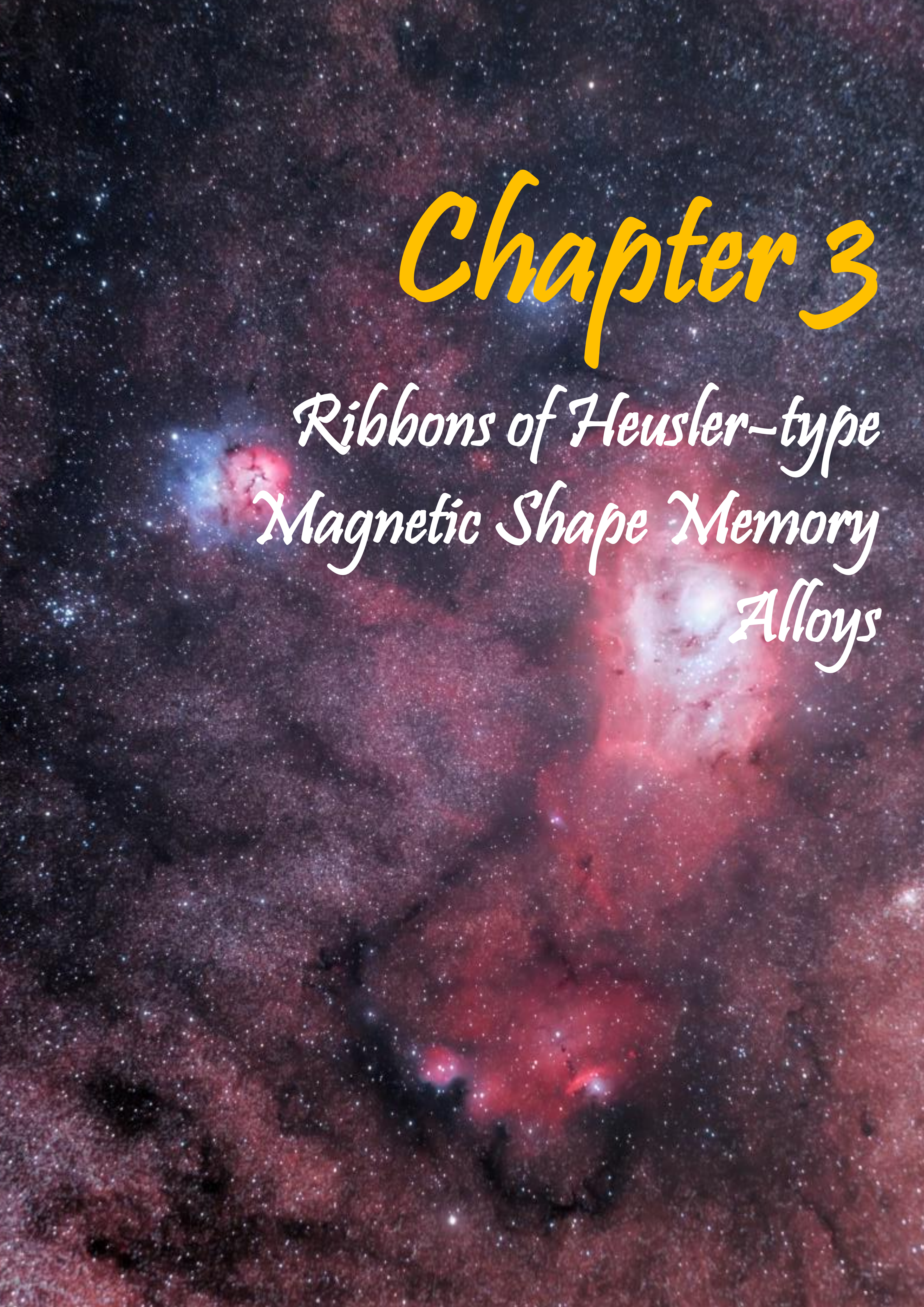

Chapter 3

Ribbons of Heusler-type Magnetic Shape Memory Alloys

Chapter 3

Search for NiMn-based MSMAs in ribbon form with potentially enhanced MCE performance

3.1. INTRODUCTION

This Chapter is concerned about the results obtained during fulfilling the objectives 1 and 2 of the present work, as it deals with a search for the optimal Heusler-type MMSMAs satisfying a range of requirements including enhanced MCE in its ribbon and subsequently in its powder forms, the latter one is in need for additive manufacturing applications. We are looking for materials in the ribbon form with a martensitic transformation near room temperature exhibiting the largest possible magnetic field induced adiabatic temperature change. Also, low hysteresis of MT is desirable to minimize energy loss. As explained in the introduction, the materials selected for this thesis are the Heusler-type NiMnX (X=In, Sn, Ga...) MMSMA compounds. The martensitic transformation temperature is highly sensitive to the composition, and even slight changes in it can have a significant impact on its characteristics.

The literature has shown that these NiMnX alloy systems are cost-effective materials suitable for room temperature cooling applications while maintaining a noncritical material content[1]. The rather well studied non-stoichiometric Heusler-type MMSMAs systems are:

(1) NiMnSn
(2) NiMnGa
(3) NiMnIn

These sets of alloys can exhibit a transformation near room temperature, especially, when doped with small amounts of other elements. The most common dopants include Copper, Iron and Cobalt, as explained in the introduction. The use of Cobalt as a dopant element shifts the martensitic transformation towards lower temperatures, making it possible to achieve the transformation close to room temperature when used in the proper proportions [2].

Iron addition to NiMnSn compounds results in the substitution of Mn with Fe atoms. This addition leads to a slight increase in the Curie temperature and the saturation magnetization [3].

The current chapter describes the results obtained in the present work on the representatives in each of the aforementioned alloy systems. Compositional, structural and transformation characteristics are studied for each compound. A suitability of each alloy for the subsequent powdering step through ribbon intermediate stage is assessed by thermomagnetization measurements. So, the first step was a preparation of different Heusler alloys, studying their magnetic properties in ribbon form and investigating the effect of heat treatments on the martensitic transformation. Our goal was to achieve MT close to room temperature with a minimum MT thermal hysteresis which is accompanied by an abrupt change in magnetization, with the maximum possible drop in magnetization (that is, a close to zero magnetization in the martensitic state just after finish of the forward MT is desirable). In the following subsections the results on Heusler-type MMSMAs in the ribbon form, as-spun and heat treated, are presented.

It should be emphasized that heat treatment is a valuable tool in optimizing the properties of Heusler MCE materials. It helps achieving more controlled and predictable phase transitions, leading to a reduction in thermal hysteresis and, ultimately, enhancing the efficiency and reliability of these materials for cooling and refrigeration applications.

3.2. NiMnSn MSMA SYSTEM

3.2.1. $Mn_{42.5}Ni_{40}Co_{8}Sn_{9.5}$

3.2.1.1. Composition and microstructure

The first representative alloy of this MMSMAs system was the Cobalt-doped NiMnSn with a nominal composition of $Ni_{40}Mn_{42.5}Co_{8}Sn_{9.5}$. The actual composition of the melt-spun ribbons made of this alloy was determined by EDS and the results are shown in Table 3.1 for both the as-spun state and after heat treatment (HT). The instrumental uncertainty of the composition determination by our EDS analysis was ±0.5 at. %. Table 3.1 evidences that within indicated uncertainty the ribbon barely changes composition after the heat treatment.

Table 3.1: Composition of the NiCoMnSn ribbons in as-spun state and after heat treatment (HT).

Sample	***Mn (at %)***	***Ni (at %)***	***Co (at %)***	***Sn (at %)***
As-spun ribbons	40.5	42.3	8.4	8.8
HT ribbons	40.2	43.1	8.3	8.5

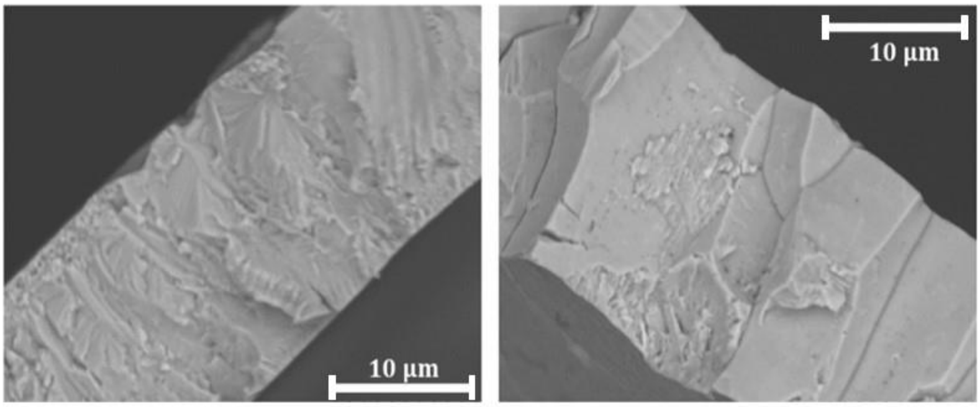

Figure 3.1: Cross-sectional SEM images of the as-spun (left) and after heat treatment (right) ribbons.

The morphology of the ribbon cross-section after its fracture was observed by a SEM imaging. Figure 3.1 shows the SEM cross-sectional images of the ribbon in the as-spun and after heat treatment states. The images show a columnar grows of the crystal grains with the essential increase of the grain thickness after HT. The fracture surface in right figure looks smoother than on the left panel which can indicate on a much more degree of brittle failure of the HT sample compared to the as-spun counterpart.

3.2.1.2. Transformation characteristics

The measurement of the temperature dependences of low-field magnetization, *M*(*T*), is a common tool to investigate the transformation behaviour, magnetic state and determine the MT and Curie temperatures in MMSMAs [4–6]. As discussed in the section 3.1 and Ref. 3, three heat treatments were performed on as-spun ribbons in order to find the optimal one[7]:

(1) 723 K 30' + q
(2) 1173 K 60' + q
(3) 1173 K 60' + q & 723K 30' + q

The q stands for "quenching" which means a very rapid cooling the sample down to 273 K by immersing it in iced water immediately after the heat treatment. This is done in order to retain the high temperature phase state. It was found that each heat treatment has a different effect on the alloy. The first one (1) improves the chemical order in the crystal structure, whereas the second one (2) improves the structural order and reduces the surface micro-strains produced during the melt-spinning technique. The third heat treatment (3) is a combination of the two previous ones resulting in being the optimal one.

Figure 3.2 depicts the low-field thermomagnetization curves for both the as-spun and heat-treated ribbons samples, which were used to select the optimal heat treatment regime. When cooling from the high temperature paramagnetic austenite, the magnetization exhibits a rapid increase due to the ferromagnetic ordering of the austenitic phase at the Curie temperature. At the martensitic transformation, which also represents a magnetic transition from the ferromagnetic austenite to the antiferromagnetic martensite [8], the magnetization rapidly drops to almost zero. This strong change in the magnetic state characterizes a magnetostructural first-order transformation that can be easily induced by a magnetic field, resulting in several remarkable properties, particularly a significant inverse magnetocaloric effect [6,9–11].

The thermomagnetization curves for ribbons in the as-spun and heat-treated conditions at 723 K show reduced MT temperatures and enhanced temperature hysteresis (Figure 3.2). These behaviours reflect the inhomogeneous state of the samples, including composition gradients, internal stresses, defects etc., caused by the fabrication techniques, such as rapid solidification during melt-spinning.

Experiments demonstrate that the compositional and structural imperfections could not be eliminated by the heat treatment at 723 K for 30 min. Figure 3.2 shows considerably better MT parameters of the samples treated at 1173 K and quenched, without additional aging or aged at 723 K. Samples in these states exhibit nearly rectangular shape M(T) loops with reduced hysteresis, approximately 30 K. In this case, the heat treatments produce a much more homogeneous state in the samples, which are also relaxed from internal stresses and exhibit fewer structural defects, as evidenced by the XRD results (see chapter 4, section 4.2.1.2.).

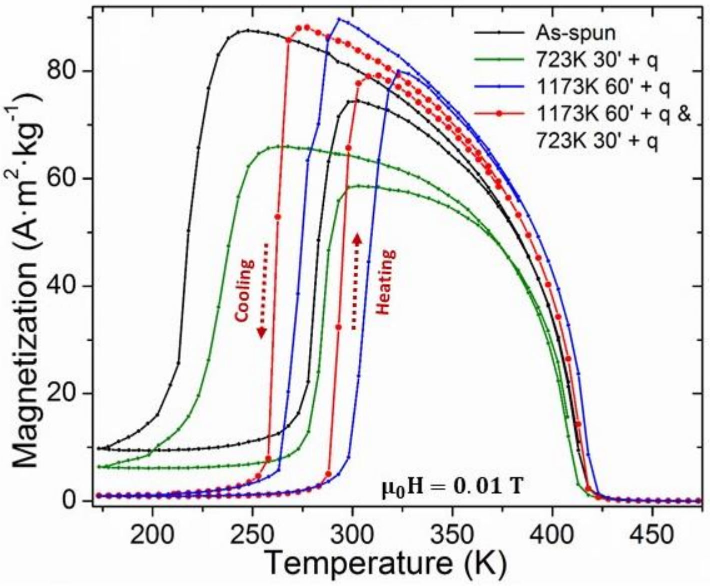

Figure 3.2: Thermomagnetization curves for $Ni_{40}Mn_{42.5}Co_8Sn_{9.5}$ ribbons with different heat treatments.

These ribbons are suitable for powder production since the transformation after heat treatments occurs near room temperature, making this alloy suitable for (near) room-temperature cooling. The suitability of this alloy in powder form for printing is discussed in chapter 4.

3.2.2. $Mn_{48}Ni_{35.5}Sn_8Co_{6.5}Fe_2$

3.2.2.1. Composition and microstructure

With the intention to increase MT temperature and increase a jump of M(T) at MT we have fabricated Ni(Co)MnSn ribbon with reduced Sn and Co and increased Ni contents and added Fe atoms, whereby the nominal composition of this MMSMA became $Mn_{48}Ni_{35.5}Sn_8Co_{6.5}Fe_2$. The actual composition of this ribbon was evaluated by EDS. Table 3.2 summarize the ribbon composition, which is an average of the measurements on 10 ribbon pieces.

Table 3.2: Actual compositions of the as-spun and heat treated ribbons determined by EDS analysis.

Sample	***Mn (at %)***	***Ni (at %)***	***Sn (at %)***	***Co (at %)***	***Fe (at %)***
As-spun ribbons	48.2	35.2	7.5	6.5	2.8
HT ribbons	42.3	34.0	15.0	6.3	2.3

The Table 3.2 shows that content of all elements in as-spun ribbon varies within ± 1 at% from the nominal one, which corresponds to the instrumental uncertainty of the composition determination by our EDS analysis, whereas the content of Mn and Sn in HT ribbon is modified. It is known that both a Mn reduction and increasing Sn favour a shifting the MT temperatures towards low temperatures.

The cross-sectional view of ribbon is documented by SEM imaging shown in Figure 3.3(left). It reveals a ribbon thickness of about 20μm and does not show a well-pronounced columnar structure. Fig. 3.3(right) shows rather globular than well-crystalized grain microstructure with the uniform size of the individual grains equal to about 1 μm in diameter.

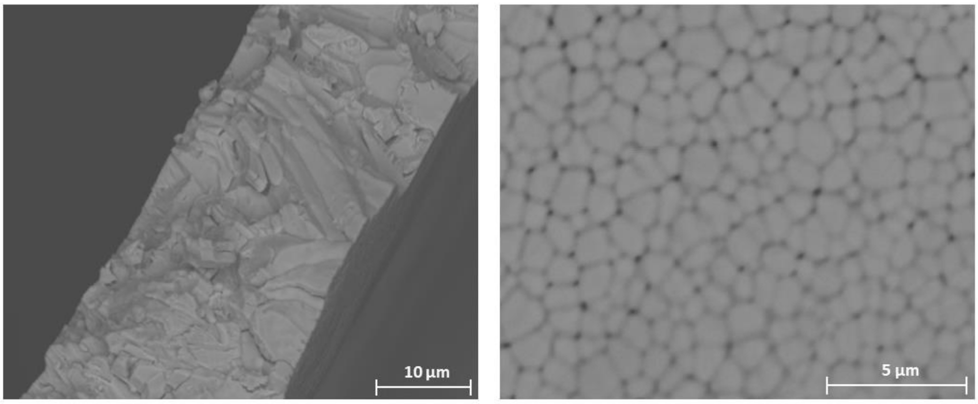

Figure 3.3: SEM cross-sectional view image of the ribbon (left) and grain structure observed in the shiny surface of the ribbon, which was in contact with coper wheel (right).

3.2.2.2. Transformation characteristics

The first measurement that gives an insight on the transformation behaviour, the Curie temperature, and MT temperature is the low-field magnetization versus temperature curve[12][13]. Figure 3.4 shows magnetization versus temperature dependences for the as-spun and heat-treated ribbons at low magnetic field. Previous works have shown that performing special heat treatments may improve phase transformation and reduce hysteresis in Heusler MMSMAs[14]. However, the heat treatments that usually work well for the alloys in Ref.[16] go detrimental with the alloy studied here, as Figure 3.4 shows. In this case, the martensitic transformation is less abrupt, and the transformation front is not smooth indicating that heat treatment results in some inhomogeneities in the sample. The latter ones are responsible for a decrease of the magnetic susceptibility of alloy. All these effects are in agreement with the composition changes outlined in Table 3.2. Mn is susceptible to evaporation and since this alloy has a high manganese content, the heat treatments can have a greater impact on the alloy stoichiometry, particularly, causing a decrease of the MT temperatures, as this trend was already mentioned.

On the other hand, the room temperature transformation characteristics and magnetic properties in the as-spun ribbon are satisfactory. Therefore, the advantage of this alloy lies in the fact that no further treatment is necessary, reducing production costs and energy consumption. Thus, this alloy is going to be studied in its as-spun ribbon form from this point of view. The values of martensitic and austenitic transformation temperatures, T_M and T_A respectively, are listed in Table 3.3.

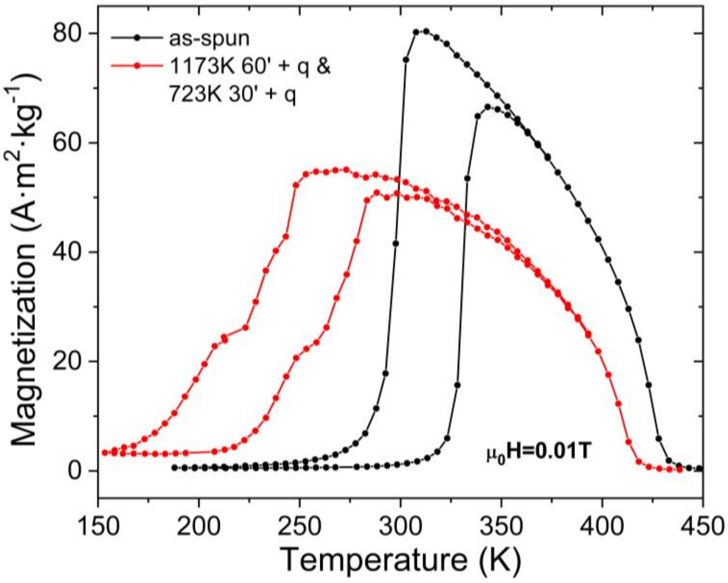

Figure 3.4: Thermomagnetization curves for as-spun and heat treated ribbons.

Table 3.3: Curie temperature and austenitic and martensitic transformation temperatures extracted from the thermomagnetization curves for as-spun and heat treated ribbons.

Sample	T_{CA} (K)	T_M (K)	T_A (K)
As-spun ribbons	423	298	331
HT ribbons	408	225	265

3.2.2.3. “Magnetic field – temperature” phase diagrams of martensitic transformation

The thermomagnetization curves, M(T,H), for the as-spun ribbons recorded under different magnetic fields are shown in Figure 3.5. In this figure, the magnetic field effect on MT is seen as a displacement of the MT hysteretic loop towards lower temperatures, which is a typical behaviour for MMSMAs and attributed to the magnetic field induced stabilization of the austenitic phase[13]. The values of martensitic temperature (T_M) and austenitic temperature (T_A) are extracted from M(T,H) curves using the derivative method. They are plotted as a function of magnetic field representing quasi-equilibrium phase diagram of MT shown in the inset of Figure 3.5. The data in Figure 3.5 can be approximated by almost parallel to each other straight lines having negative slope of (-2.4±0.2) K/T for T_A and (-1.8±0.3) K/T for T_M, determined by linear fitting.

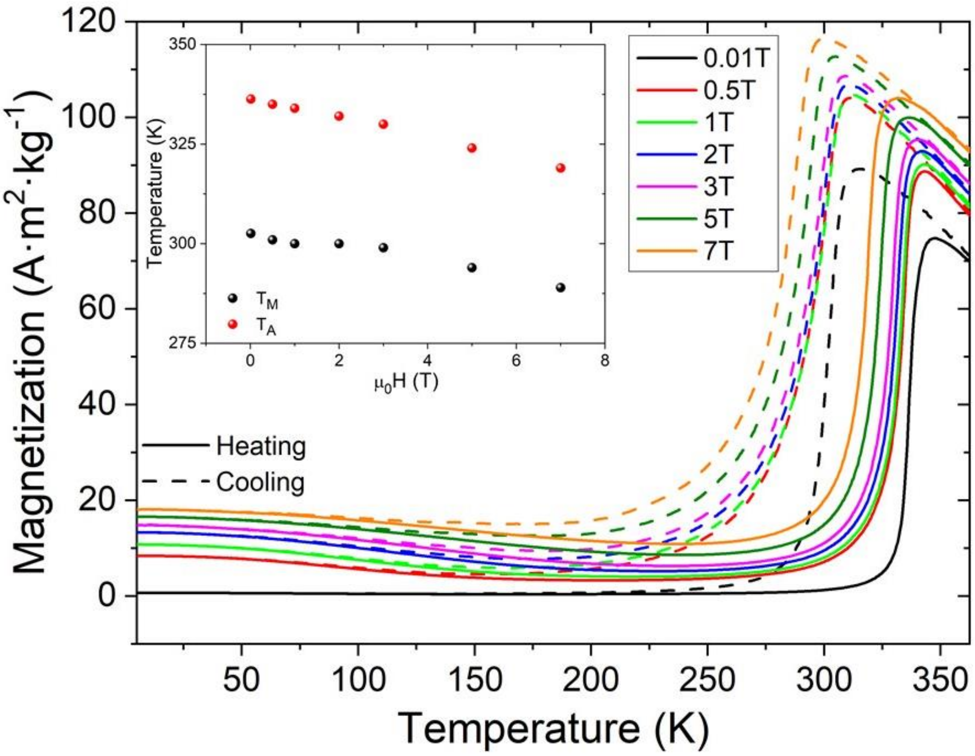

Figure 3.5: Thermomagnetization curves at different applied magnetic fields. Inset shows temperature-magnetic field phase diagram of MT.

3.2.2.4. Magnetic field induced entropy change

Conventional and inverse magnetocaloric effects are characterized by the isothermal entropy change, $\Delta S_m(T,H)$, and/or adiabatic temperature change, $\Delta T_{ad}(T,H)$, when a magnetic field is applied or removed in isothermal conditions. By means of Maxwell thermodynamic relationships the magnetic field induced entropy change can be estimated [15]. It is a common practice that Maxwell relationship is applied for the first-order phase transitions. From the thermomagnetization curves at different magnetic fields (Figure 3.5) the calculation of $\Delta S_m(T,H)$ can be done by numerical approximation of the Maxwell relationships, as explained in chapter 2:

$$\Delta S_m(T,H) = S_m(T,H) - S_m(T,0) = \mu_0 \int_0^H \left(\frac{\partial M(T,H')}{\partial T}\right) dH'$$

Figure 3.6 shows the $\Delta S_m(T,\mathrm{H})$ plots calculated by using cooling and heating data from Figure 3.5 for as-spun ribbon. The curves show high maximums at both the forward and reverse MT. Figure 3.7(left) in the next subsection shows field dependence of the $\Delta S_m(T,\mathrm{H})$ maximums.

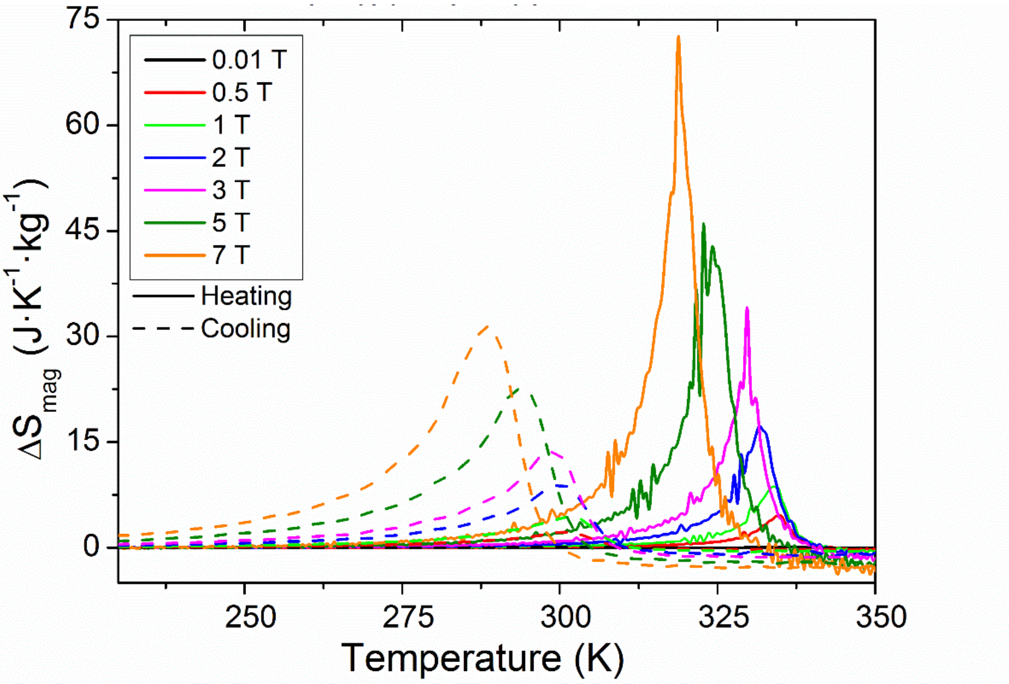

Figure 3.6: Magnetic entropy change at MT under different magnetic fields derived from M(T) curves for as-spun ribbon.

3.2.2.5. Refrigerant capacity

The refrigerant capacity is the amount of heat transferred between hot and cold reservoirs in a single refrigeration cycle. It can be calculated by integrating the curve of $\Delta S_m(T,H)$ at FWHM:

$$RC \approx \int_{T_{cold}}^{T_{hot}} |\Delta S_M(T,H)| dT$$

Integrating the curves from Figure 3.6 yields the refrigeration capacity versus magnetic field dependences for cooling and heating cycles depicted in Figure 3.7(right). This integration procedure is referred to as a Gschneidner refrigerant capacity (RC) calculation[16]. It is worth noting that field dependencies of the maximum of $\Delta S_m(T,H)$ and RC are very similar.

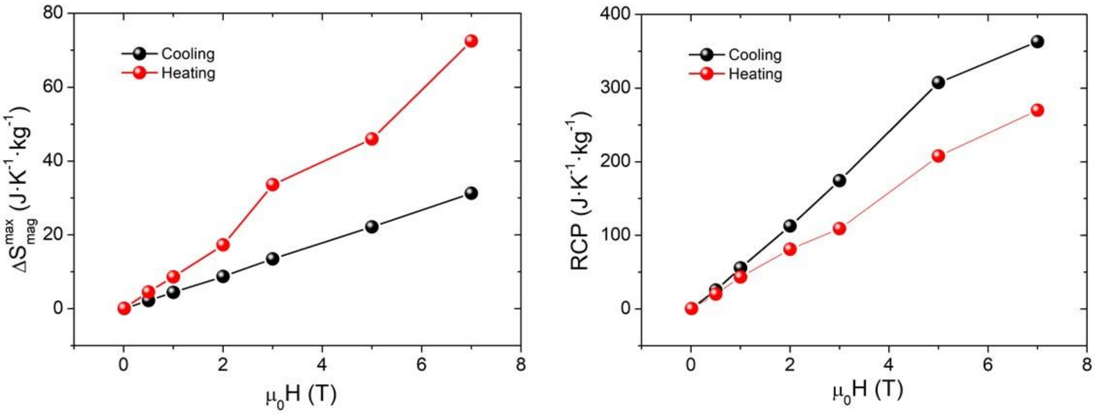

Figure 3.7: Maximum magnetic entropy (left) and refrigerant capacity (right) as a function of the magnetic field.

3.1.2.6. Adiabatic magnetocaloric effect

The adiabatic temperature change, Δ*T*ad, was measured by rapid inserting and removing the samples from a constant magnetic field of 2 T produced by the electromagnet. These measurements have been performed at constant temperatures during step-wise heating/cooling ramps ranging between 260 K and 390 K. The results are presented in Figure 3.8, which shows that the peak position is observed close to 330 K for the as-spun ribbon, reaching a maximum value of Δ*T*ad = $|1.9|$ K. The ribbon exhibits a defined peak of the inverse magnetocaloric effect (negative Δ*T*ad(*T*) values resulting from the application of the magnetic field) in the vicinity of the reverse MT. This transformation corresponds to the phase change from a weakly magnetic martensitic phase to a ferromagnetic austenite.

From Figure 3.8 it can be inferred that contrary to the occurrence of the considerable peak of adiabatic temperature change at the reverse MT, no peak is observed at the forward MT during cooling ramp, only one can see a positive Δ*T*ad signal exhibiting a step-like anomaly at the forward MT. The heating peak is highly prominent because the structural transformation is induced by applied field, where a relatively large volume fraction of transformed material is involved. On the other hand, in the cooling process, it would be necessary to induce the reverse transformation under applied magnetic field from some portion of martensite overcoming the MT hysteresis. Therefore no peak was observed under applied magnetic field when the sample was step-wise cooled across the forward MT. Note, that in order to observe a peak of Δ*T*ad at the forward MT, one need to do measurements under field removal. That is during cooling the system has to be magnetically ordered in partial austenitic state (with applied magnetic field) and in the moment of performing the measurement the systems should go to the disordered state of martensitic phase (with no applied field), inducing the transformation from martensite to austenite.

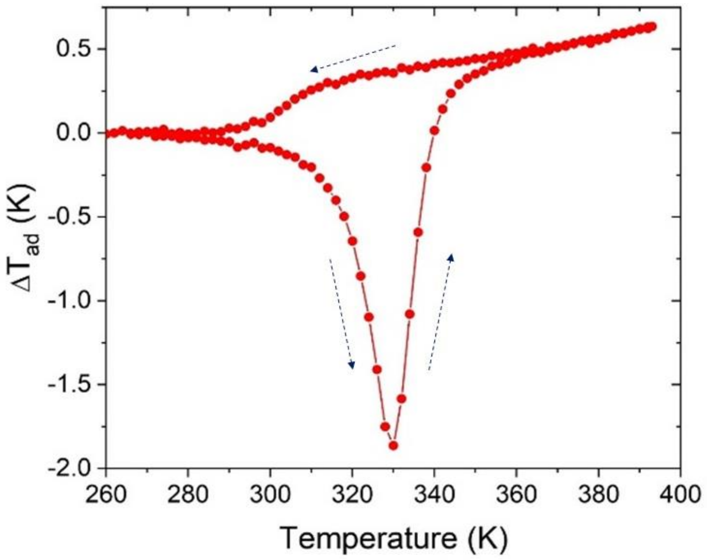

Figure 3.8: Cooling-heating dependences of adiabatic temperature change measured under 2T for as-spun ribbon.

3.2.3. $Ni_{43}Mn_{39}Co_7Sn_{11}$

3.2.3.1. Composition analysis

The third alloy studied was the compound with a nominal composition of $Ni_{43}Mn_{39}Co_7Sn_{11}$. With this alloy composition we conducted a study of the influence of the same-regime melt-spinning processing on reproducibility of the composition content of resulting ribbons. Experimentally, we have seen that it is almost impossible to obtain two or more identical ribbon compositions due to factors such as the introduction of weight errors during the preparation of precursors and the duration of alloy melting, which leads to the subsequent evaporation of some of its constituents during the melt-spinning process. The results presented in Table 3.4 indicate that some variations in the ribbons compositions occur.

Table 3.4: Actual compositions for each prepared ribbon measured by EDS.

Sample	*Ni (at %)*	*Mn (at %)*	*Co (at %)*	*Sn (at %)*
V0	43.1	39.5	7.2	10.4
V1	43.3	39.8	6.6	10.3
V2	44.7	37.8	7.3	10.2
V3	43.3	39.2	7.4	10.1
V6	43.6	38.6	7.5	10.4

3.2.3.2. Transformation characteristics

As far as these types of alloys are highly sensitive to such changes, a notable alteration in the magnetic response is observed, as evident from the thermomagnetization curves shown in Figure 3.9. Taking into account the results of the transformation behaviour shown in Figure 3.9, we selected several ribbons from Table 3.4 and performed their heat treatment. The results of the thermomagnetization measurements are shown in Figure 3.10. According to Figure 3.10, the transformation and magnetic behaviour of the heat treated ribbon V3 corresponds to the most desirable characteristics of the present work.

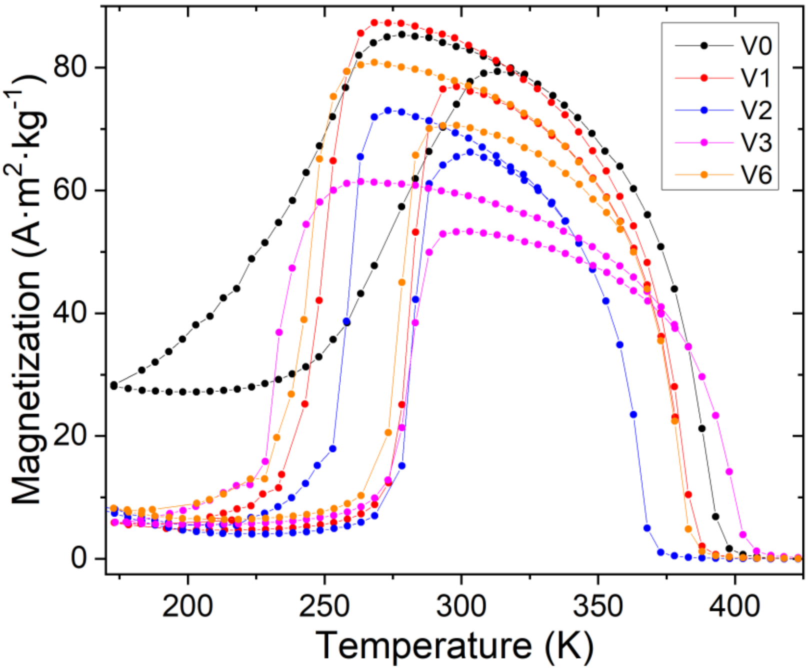

Figure 3.9: Low-field thermomagnetization curves for the set of as-spun ribbons fabricated based on the same nominal $Ni_{43}Mn_{39}Co_{7}Sn_{11}$ *alloy composition.*

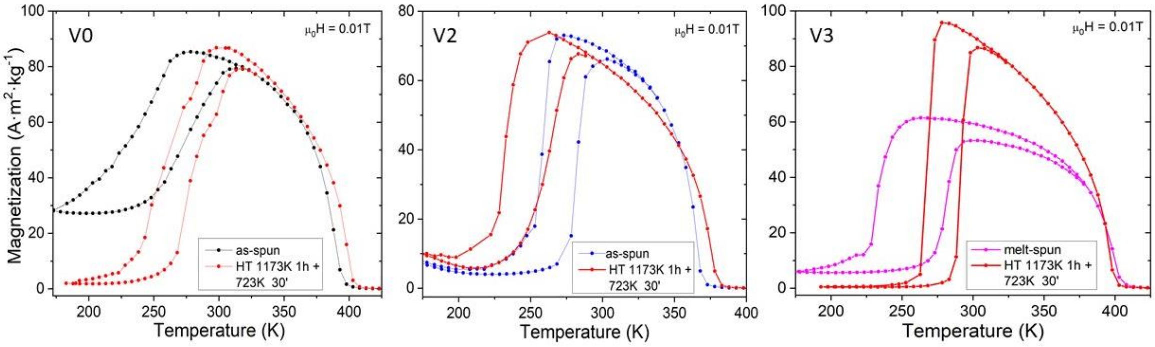

Figure 3.10: Thermomagnetization curves for as-spun and heat treated ribbons selected from Table 3.4 at low magnetic field.

Comparatively the as- spun counterpart, an enhancement of the maximum magnetization value is about 60%, and a reduction in hysteresis is about 50%, mirroring the improvements observed in the first alloy described in this chapter. This particular ribbon V3 is chosen for a systematic study since its transformation is not far away from room temperature, and it demonstrates the most desirable magnetic behaviour for our purposes. As a result, a comprehensive characterization of this ribbon in its powdered form is carried out in the following chapter.

3.3. NiMnGa MSMA SYSTEM

The Heusler NiMnGa-based MSMAs were studied using Cu, Fe and Co dopants. The idea with designing of this type of alloys was two-fold: (i) to get a compositions exhibiting a merged martensitic transformation and a ferromagnetic ordering from the ferromagnetic martensite-to-paramagnetic austenite. Fe was added in attempt to increase a magnetization jump at MT; and (ii) the Mn-excess and cobalt doping in more than 5 at.% could change the magnetic nature of MT, from FerroMSMA to a desired MetaMSMA.

3.3.1. $Ni_{49}Mn_{20}Cu_6Ga_{23}Fe_2$

3.3.1.1. Composition and microstructure

With intention to achieve the materials corresponding to the case (i), two ribbons with different compositions were prepared. For the first one we used a nominal composition $Ni_{49}Mn_{20}Cu_6Ga_{23}Fe_2$ and for a second one we added to this alloy an additional +5.2 at.% of gallium, whereby changing a relative proportions of the other elements in the alloy. The same compositional analysis that was conducted for the previous NiMnSn-based MMSMAs is performed on this type of alloys, as well. Table 3.5 shows actual compositions of the ribbons measured by EDS.

Table 3.5: Actual compositions of two as-spun ribbons measured by EDS.

Sample (as-spun)	***Ni (at %)***	***Mn (at %)***	***Cu (at %)***	***Ga (at %)***	***Fe (at %)***
Nominal 30 m/s	48.1	21.6	5.8	21.8	2.8
+5.2at.% Ga 30 m/s	48.1	20.7	6.1	22.6	2.4

SEM images shown in Figure 3.11 reveal the grain structure of the ribbons with the ribbons thicknesses measuring approximately 15µm. Fig. 3.11 shows that the preferable orientation of the long axes of grains is across ribbon thicknesses.

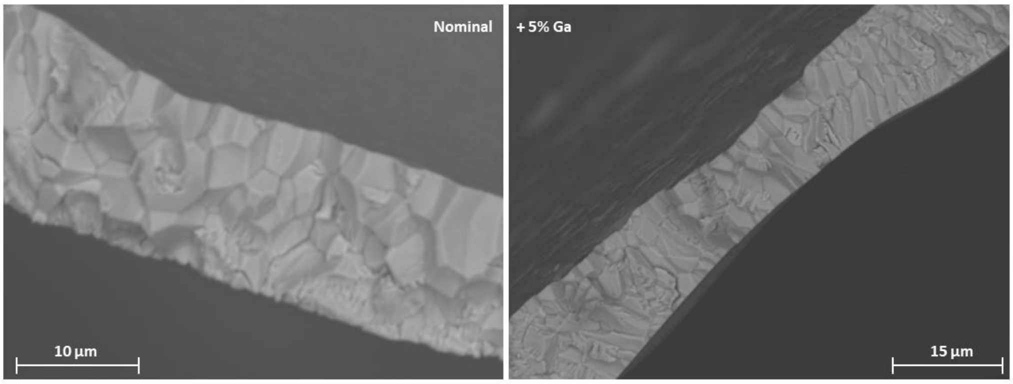

Figure 3.11: Cross-sectional SEM view of two ribbons with a nominal composition (left) and with nominal+added galium composition (right).

3.3.1.2. Transformation characteristics

Table 3.5 shows different compositions of the two ribbons which gives rise to the shifting the martensitic transformation and Curie temperature variations as thermomagnetization curves evidence in Figure 3.12. Figure 3.12 depicts also the curves for these ribbons after heat treatment. The graphs in this figure show a strong influence of Ga content on the MT temperatures and little influence on Curie temperature. Heat treatment does not change too much the positions of MT and Tc. Thus, the dependences in Fig. 3.12 show that neither composition nor heat treatment were successful in getting merged MT and Curie temperatures. As a final conclusion, these two alloys are not suitable for the objectives of this thesis.

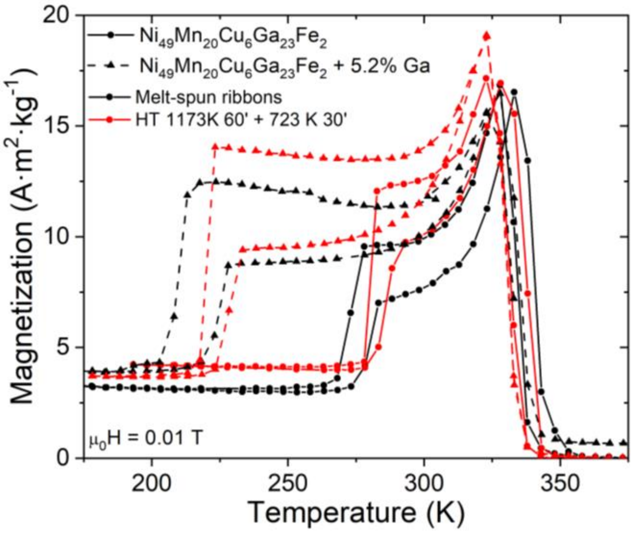

Figure 3.12: Thermomagnetization curves for the two compositions in as-spun and heat treated ribbon form.

3.3.2. $Ni_{46}Mn_{30}Co_5Ga_{20}$

3.3.2.1 Composition and microstructure

This $Ni_{46}Mn_{30}Co_5Ga_{20}$ alloy was fabricated in the intention to achieve a material corresponding to the case (ii). It was prepared by induction furnace and then two sets of ribbons were fabricated with two different wheel speeds: 25 m/s and 40 m/s. The effect of wheel speed on ribbon thickness is evaluated by SEM imaging (Figure 3.13) and the composition is analysed via EDS measurement (Table 3.6).

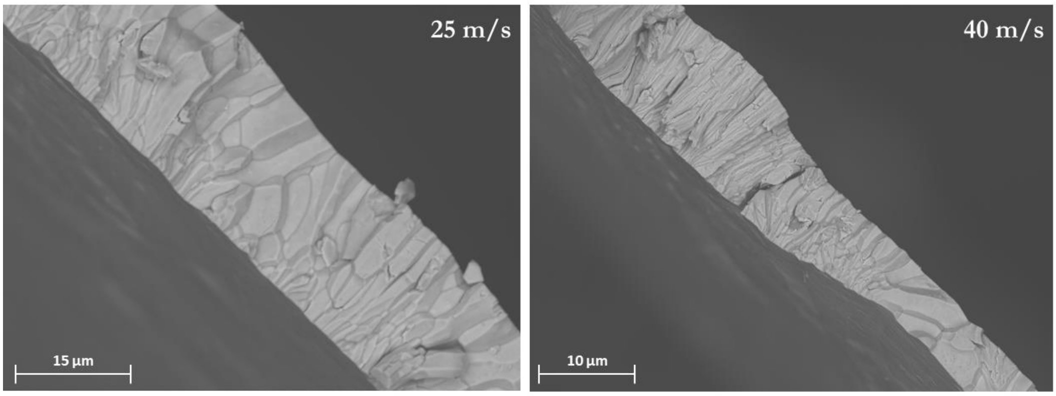

Figure 3.13: Cross-sectional view of $Ni_{46}Mn_{30}Co_5Ga_{20}$ ribbons melt-spun with the wheal speed of 25 m/s (left) and 40 m/s (right).

Table 3.6: Actual compositions of the two sets of ribbons measured by EDS.

Sample	*Ni (at %)*	*Mn (at %)*	*Co (at %)*	*Ga (at %)*
As-spun 25 m/s	46.2	29.2	5.3	19.4
As-spun 40 m/s	45.4	29.9	5.0	19.7

Figure 3.13 shows that the higher is a wheel speed the thinned is a ribbon obtained. Although the ribbons thickness is irregular, it is clear that while the low-speed ribbon thickness is varied between 17 and 20 µm, the high-speed one has a thickness between 7 and 13µm. Increasing of the wheel speed resulted in very thin grain columnar structure (Figure 3.13).

3.3.2.2. Transformation characteristics

The effect of heat treatments on the transformation and magnetization behaviours was studied by thermomagnetization measurements. The results are shown in Figure 3.14. From Figure 3.14, the optimal wheel can be inferred to be 25 m/s since it has about 50% higher maximum magnetization compared to the 40 m/s ribbon. To assess whether a magnetocaloric material is suitable for any refrigeration application, it is important to analyse its performance under achievable magnetic fields generated by permanent magnets (about 2 T). Figure 3.15 shows two thermomagnetization curves for the as- spun ribbon obtained at the optimal wheel speed measured under high and low magnetic fields. The magnetic field behaviour of *M*(H) anomalies at MT in Figure 3.15 provides an indirect evidence about the nature of the magnetic state change at MT material, which is obtained as a result of the ferromagnetic martensite –to- ferromagnetic austenite transformation. Consequently, this alloy is not suitable for the objectives of this thesis.

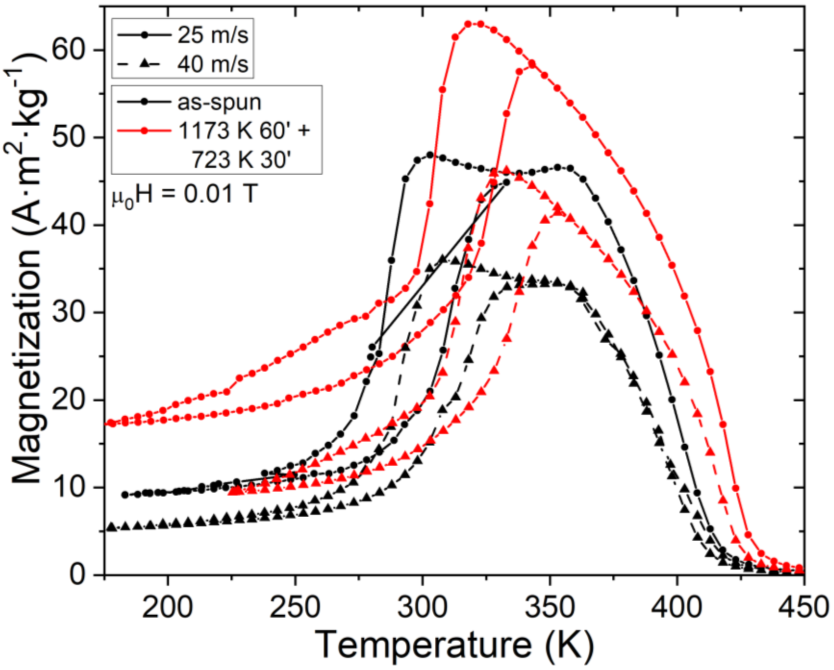

Figure 3.14: Thermomagnetization curves for the as-spun and heat treated ribbons melt-spun at the wheel speeds of 25 m/s and 40 m/s.

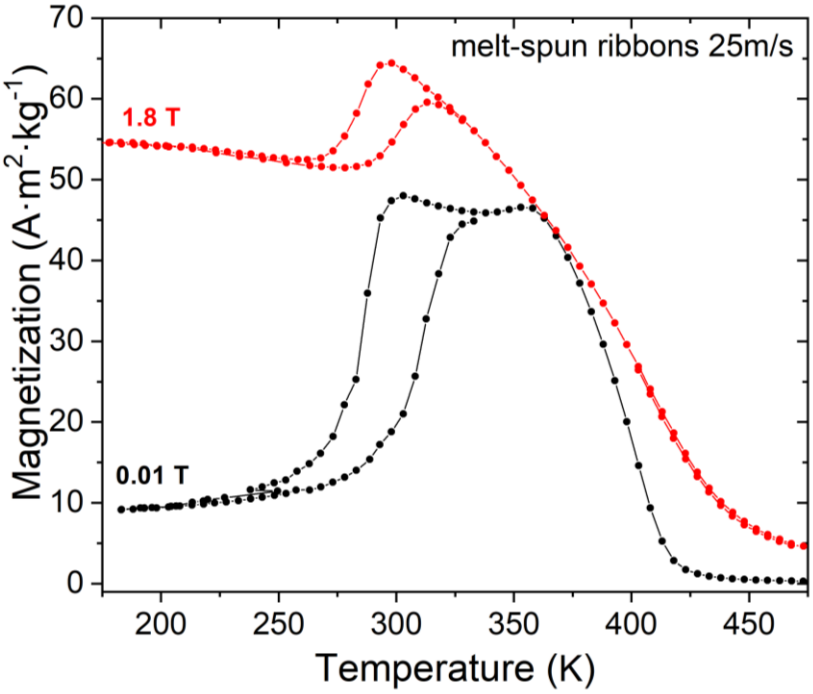

Figure 3.15: Thermomagnetization curves for as-spun ribbon melt-spun at the wheel speed of 25 m/s measured under high and low magnetic fields.

3.3.3. $Ni_{46}Mn_{31}Co_5Ga_{17}Fe_1$

3.3.3.1. Composition and microstructure

In a further attempt to achieve ferromagnetic SMA which exhibits merged MT and Curie temperatures we have prepared a ribbon with nominal composition of $Ni_{46}Mn_{31}Co_5Ga_{17}Fe_1$. For the actual compositional determination, eight pieces of ribbon were measured using energy-dispersive X-ray spectroscopy. The averaged results are shown in Table 3.7 evidencing a good agreement with the nominal content. The SEM cross-sectional and ribbon surface views are depicted in Figure 3.16. The observations indicate a globular microstructure of the ribbon where it can be found several grains with martensitic twins.

Table 3.7: Actual composition of the as-spun ribbon.

Sample (as-spun)	*Ni (at %)*	*Mn (at %)*	*Co (at %)*	*Ga (at %)*	*Fe (at %)*
30 m/s	46.6	31.0	5.0	15.8	1.7

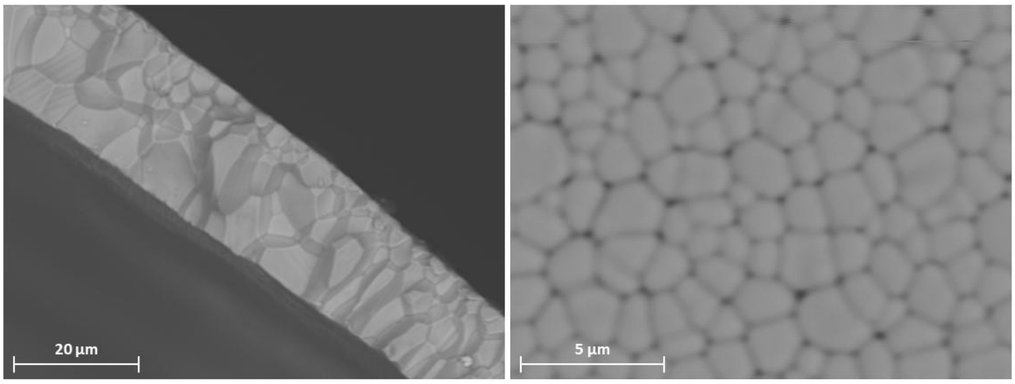

Figure 3.16: SEM cross-sectional view of as-spun $Ni_{46}Mn_{31}Co_{5}Ga_{17}Fe_{1}$ *(left) and SEM surface image of the ribbon shiny face which was in contact with Cu wheel (right).*

3.3.3.2. Transformation characteristics

Figures 3.17 and 3.18 show the thermomagnetization curves for both as-spun and heat-treated ribbons under low and high magnetic fields. All curves in these two figures indicate *M*(H) anomaly typical for a second order magnetic transition from the paramagnetic to the ferromagnetic states in the martensitic phase, which means that the Curie temperature (at about 238 K) is below a martensitic transformation. Note a well-pronounced Hopkinson peak at low magnetic field. This material would not yield a substantial magnetic entropy change (see equation (3)) since the magnitude of this change depends on the character of the magnetization drop which is very smeared in Figure 3.17. Thus, this alloy is not suitable for the objectives of this thesis.

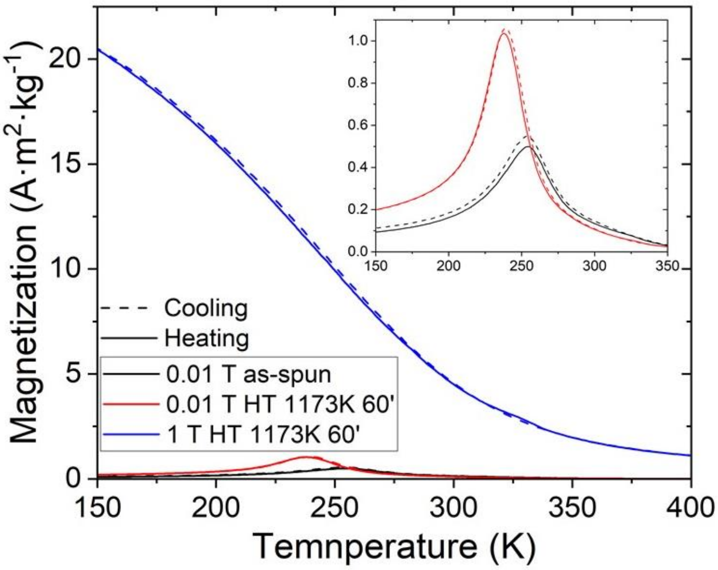

Figure 3.17: Thermomagnetization curves for $Ni_{46}Mn_{31}Co_5Ga_{17}Fe_1$ ribbons in the as-spun and heat treated states. Low magnetic field curves are shown in more detail in the inset.

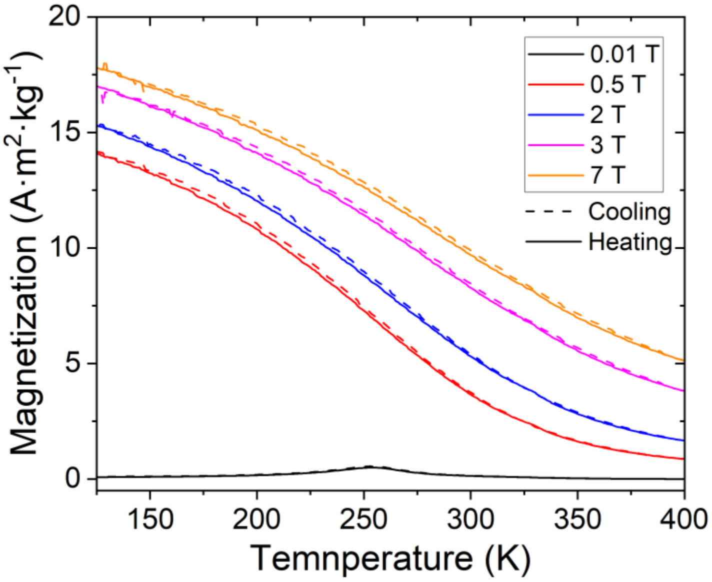

Figure 3.18: Thermomagnetization curves for $Ni_{46}Mn_{31}Co_5Ga_{17}Fe_1$ as-spun ribbons at different magnetic field.

3.3.4. $Ni_{50}Mn_{18.7}Cu_{6.25}Ga_{25}$

3.3.4.1. Composition and microstructure

A nominal composition of $Ni_{50}Mn_{18.7}Cu_{6.25}Ga_{25}$ was also checked to get the ribbon exhibiting merged MT and Curie temperatures. The ribbon with a thickness of around 20µm was fabricated at 30 m/s of wheel speed. EDS analysis revealed actual compositions for the as-spun ribbon and heat treated one which are shown in Table 3.8. Although the compositions of as-spun and

HT ribbons are quite similar, both of them are different from the nominal composition.

Table 3.8: Actual composition for as-spun and heat treated ribbons.

Sample	*Ni (at %)*	*Mn (at %)*	*Cu (at %)*	*Ga (at %)*
As-spun 30 m/s	51.1	15.9	6.7	26.3
HT ribbons	52.2	15.8	6.8	25.2

The cross-sectional microstructures of both ribbons are depicted in Figure 3.19 showing irregular shaped grains. The fracture surface in the left image reflects more ductile nature of the fracture than the one on the right image.

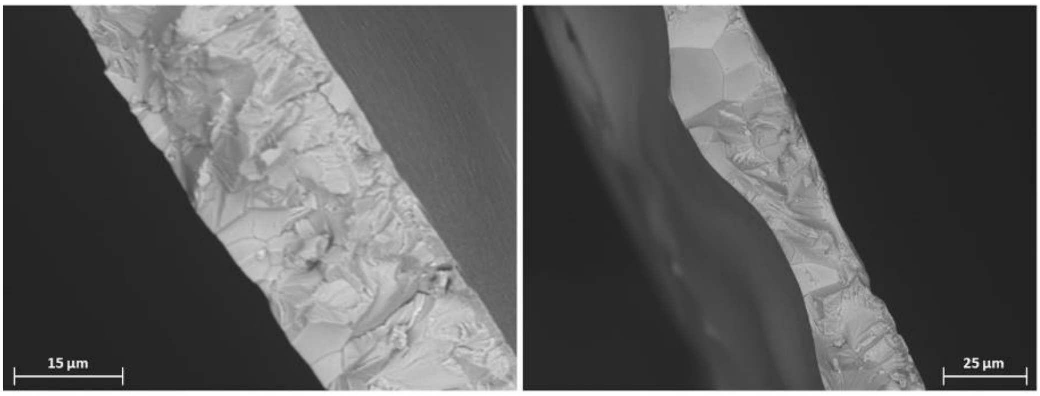

Figure 3.19: Cross-sectional microstructure of as-spun (left) and heat treated ribbons (right).

3.3.4.2. Transformation characteristics

The results of thermomagnetization behaviour for the as-spun and heat treated ribbons at low and high magnetic field are shown in Figure 3.20. The effect of heat treatment on the curves presented in Figure 3.20 is almost negligible. Like in the case of ribbon from subsection 3.2.2.1, the dependences reflect an ordinary ferromagnetic transition in the martensitic state with Curie temperature of about 229 K, which means that MT occurs at high temperatures in the paramagnetic state. Note Hopkinson peaks at a low magnetic field. The second-order nature of this magnetic transition and a very smeared character of the M(T) curves mean that magnetocaloric performance of material should be low, making this ribbons not suitable for the aim of the thesis.

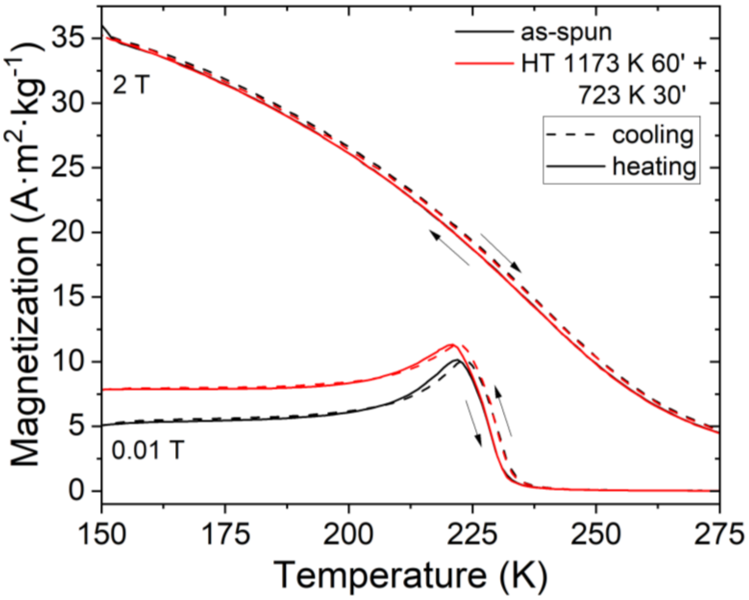

Figure 3.20: Thermomagnetization curves for as-spun and heat treated ribbons.

3.3.5. $Ni_{50}Mn_{18}Cu_5Ga_{25}Fe_2$

3.3.5.1. Composition analysis

In order to decrease MT temperature and increase T_{CA}, the ribbon with a nominal composition of $Ni_{50}Mn_{18}Cu_5Ga_{25}Fe_2$ was designed using the data for alloy from Subsection 3.2.2. The actual composition was determined as shown in Table 3.9.

Table 3.9: Actual composition for as-spun ribbon.

Sample	*Ni (at %)*	*Mn (at %)*	*Cu (at %)*	*Ga (at %)*	*Fe (at %)*
As-spun 30 m/s	49.0	19.3	5.9	23.7	2.3

3.3.5.2. Transformation characteristics

Thermomagnetization curves at different magnetic fields are shown in Figure 3.21. The *M*(T) dependence when cooling from high temperature exhibits first anomaly produced by Curie temperature in the austenite (at about 323 K), then during further cooling it shows a hysteretic loop due to MT (at about 238 K) which shifts to the higher temperatures under magnetic field. These features are typical for the ferromagnetic Ni-Mn-Ga (FSMAs), exactly opposite to the behaviors of MT in MMSMAs. Therefore this alloy does not fit to the objectives of the present work.

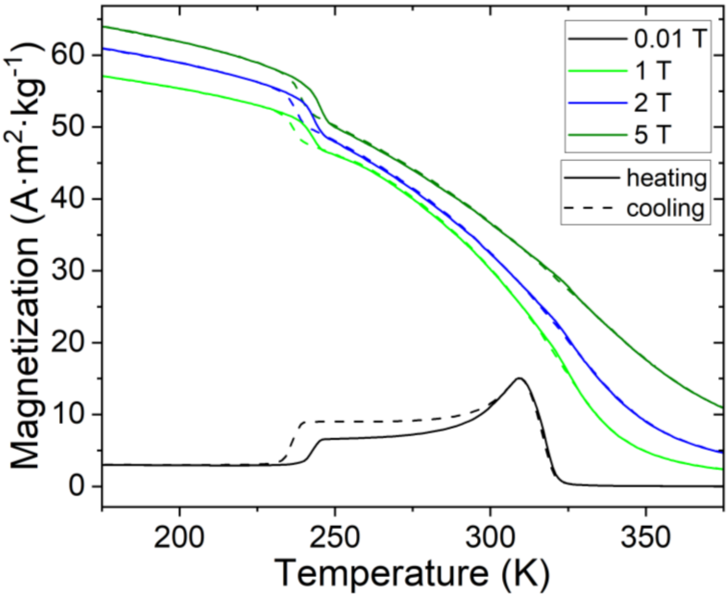

Figure 3.21: Thermomagnetization curves at different magnetic fields.

3.4. NiMnIn MSMA SYSTEM

3.4.1. $Ni_{45.2}Mn_{36.7}Co_{5.1}In_{13.0}$

3.4.1.1. Composition analysis

It is well-known that the MT and magnetic characteristics of NiMnIn-based Heusler-type off-stoichiometric MMSMAs are very difficult to reproduce due to extremely high sensitivity to the composition variation and to degree of atomic order. In the present work, we selected nominal composition of such type of alloy $Ni_{45.2}Mn_{36.7}Co_{5.1}In_{13.0}$ and prepared ribbon, which actual composition is presented in Table 3.10.

Table 3.10: Actual composition for as-spun ribbon.

Sample	*Ni (at %)*	*Mn (at %)*	*Co (at %)*	*In (at %)*
As-spun ribbon	46.8	35.5	5.5	12.2

3.4.1.2. Transformation characteristics

The low-field thermomagnetization curve of the as-spun ribbon, presented in Figure 3.22, shows a well-pronounced MT and Curie temperature for the ferromagnetic transition. MT occurs well below room temperature with thermal hysteresis of about 50 K. The *M*(*T*) dependence of the HT ribbon in this figure shows a reduced MT hysteresis, of about 30 K, but still it is too large. Moreover, MT is shifted to low temperatures, to about 100 K. All these factors are not in line with objectives of the present work so this material is discarded for the further investigations.

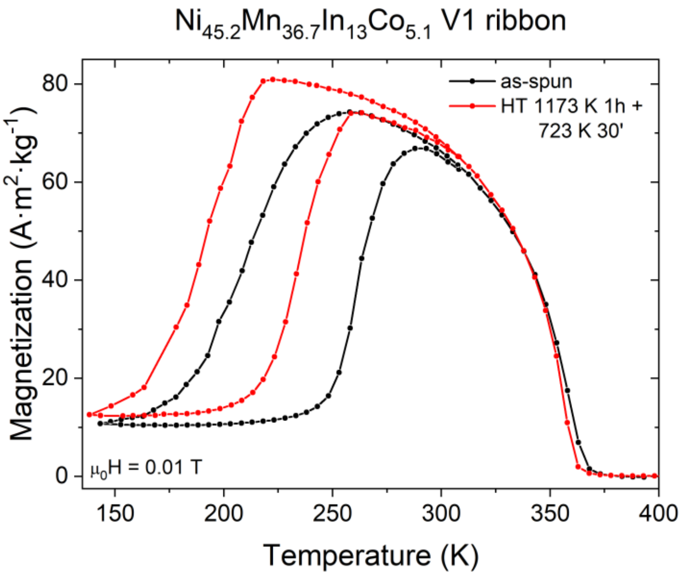

Figure 3.22: Thermomagnetization curves of the as-spun and HT ribbons.

3.5. CONCLUSIONS

In this Chapter we have prepared a number of the ribbons featuring three main classes of the Heusler-type MSMAs. Their basic characterization (transformation behaviour and magnetic properties) was mostly performed by thermomagnetization measurements. Based on the results obtained, the following ribbons were selected for the preparation of MMSMA powders and their all-round studies: $Mn_{42.5}Ni_{40}Co_{8}Sn_{9.5}$, $Mn_{48}Ni_{35.5}Sn_{8}Co_{6.5}Fe_{2}$, $Ni_{43}Mn_{39}Co_{7}Sn_{11}$, $Ni_{50}Mn_{18.7}Cu_{6.25}Ga_{25}$.

3.6. REFERENCES

[1] I. Dubenko, T. Samanta, A. Kumar Pathak, A. Kazakov, V. Prudnikov, S. Stadler, A. Granovsky, A. Zhukov, N. Ali, Magnetocaloric effect and multifunctional properties of Ni-Mn-based Heusler alloys, J. Magn. Magn. Mater. 324 (2012) 3530–3534. https://doi.org/10.1016/j.jmmm.2012.02.082.

[2] D.Y. Cong, S. Roth, L. Schultz, Magnetic properties and structural transformations in Ni – Co – Mn – Sn multifunctional alloys, ACTA Mater. 60 (2012) 5335–5351. https://doi.org/10.1016/j.actamat.2012.06.034.

[3] E.C. Passamani, F. Xavier, E. Favre-Nicolin, C. Larica, A.Y. Takeuchi, I.L. Castro, J.R. Proveti, Magnetic properties of NiMn-based Heusler alloys influenced by Fe atoms replacing Mn, J. Appl. Phys. 105 (2009). https://doi.org/10.1063/1.3075835.

[4] C.O. Aguilar-Ortiz, J.P. Camarillo-García, J. Vergara, P. Álvarez-Alonso, D. Salazar, V.A. Chernenko, H. Flores-Zúñiga, Effect of solidification rate on martensitic transformation behavior and adiabatic magnetocaloric effect of Ni 50 Mn 35 In 15 ribbons, J. Alloys Compd. 748 (2018) 464–472. https://doi.org/10.1016/j.jallcom.2018.03.074.

[5] C.O. Aguilar-Ortiz, D. Soto-Parra, P. Álvarez-Alonso, P. Lázpita, D. Salazar, P.O. Castillo-Villa, H. Flores-Zúñiga, V.A. Chernenko, Influence of Fe doping and magnetic field on martensitic transition in Ni–Mn–Sn melt-spun ribbons, Acta Mater. 107 (2016) 9–16. https://doi.org/10.1016/J.ACTAMAT.2016.01.041.

[6] P. Lázpita, M. Sasmaz, E. Cesari, J.M. Barandiarán, J. Gutiérrez, V.A. Chernenko, Martensitic transformation and magnetic field induced effects in Ni42Co8Mn39Sn11 metamagnetic shape memory alloy, Acta Mater. 109 (2016) 170–176. https://doi.org/10.1016/J.ACTAMAT.2016.02.046.

[7] Y. Wang, D. Salas, T.C. Duong, B. Medasani, A. Talapatra, On the fast kinetics of B2 e L2 1 ordering in Ni-Co-Mn-In metamagnetic shape memory alloys, 781 (2019). https://doi.org/10.1016/j.jallcom.2018.12.034.

[8] V. Golub, V.A. L'vov, O. Salyuk, J.M. Barandiaran, V.A. Chernenko, Magnetism of nanotwinned martensite in magnetic shape memory alloys, J. Phys. Condens. Matter. 32 (2020) 313001. https://doi.org/10.1088/1361-648X/ab7f69.

[9] R. Kainuma, Y. Imano, W. Ito, Y. Sutou, H. Morito, S. Okamoto, O. Kitakami, K. Oikawa, a Fujita, T. Kanomata, K. Ishida, Magnetic-field-induced shape recovery by reverse phase transformation., Nature. 439 (2006) 957–60. https://doi.org/10.1038/nature04493.

[10] T. Krenke, E. Duman, M. Acet, E.F. Wassermann, X. Moya, L. Manosa, A. Planes, Inverse magnetocaloric effect in ferromagnetic Ni-Mn-Sn alloys, Nat. Mater. 4 (2005) 450–454. https://doi.org/10.1038/nmat1395.

[11] V.A. Chernenko, V.A. L'vov, E. Cesari, J.M. Barandiaran, Fundamentals of magnetocaloric effect in magnetic shape memory alloys, 1st ed., Elsevier B.V., 2019. https://doi.org/10.1016/bs.hmm.2019.03.001.

[12] C.O. Aguilar-Ortiz, D. Soto-Parra, P. Álvarez-Alonso, P. Lázpita, D. Salazar, P.O. Castillo-Villa, H. Flores-Zúñiga, V.A. Chernenko, Influence of Fe doping and magnetic field on martensitic transition in Ni-Mn-Sn melt-spun ribbons, Acta Mater. 107 (2016) 9–16. https://doi.org/10.1016/j.actamat.2016.01.041.

[13] P. Lázpita, M. Sasmaz, E. Cesari, J.M. Barandiarán, J. Gutiérrez, V.A. Chernenko, Martensitic transformation and magnetic field induced effects in Ni42Co8Mn39Sn11 metamagnetic shape memory alloy, Acta Mater. 109 (2016) 170–176. https://doi.org/10.1016/j.actamat.2016.02.046.

[14] B. Rodríguez-Crespo, D. Salazar, S. Lanceros-Méndez, V. Chernenko, Development and magnetocaloric properties of Ni(Co)-Mn-Sn printing ink, J. Alloys Compd. 917 (2022) 165521. https://doi.org/10.1016/j.jallcom.2022.165521.

[15] V.K. Pecharsky, K.A. Gschneidner, Magnetocaloric effect from indirect measurements: Magnetization and heat capacity, J. Appl. Phys. 86 (1999) 565–575. https://doi.org/10.1063/1.370767.

[16] K.A. Gschneider, Recent develompents in magnetic refrigeration, 317 (1999) 69–76. https://doi.org/10.4028/www.scientific.net/MSF.315-317.69.

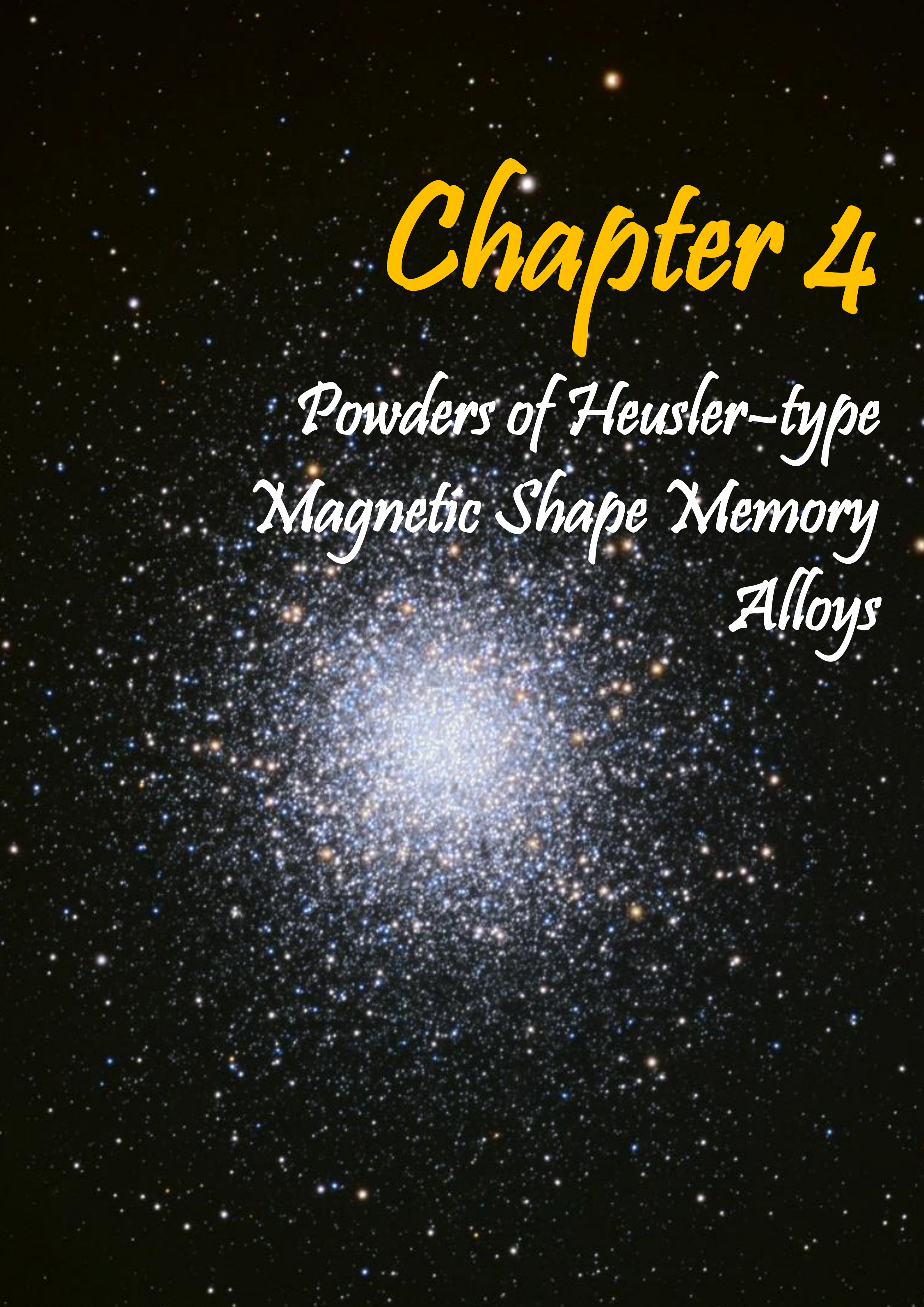

Chapter 4

Powders of Heusler-type Magnetic Shape Memory Alloys

Chapter 4

Production and Investigation of NiMn-Based MSMAs Powders with Enhanced MCE Properties

This chapter is dedicated to the production and investigation of powders obtained from selected ribbons that currently meet the objectives of the thesis and are potentially suitable for 2D and 3D printing. So, the next step is to produce powders from these ribbons and assess to which extent they meet the thesis objectives. The powders with the best appropriate properties will be considered for implementation in the next chapter, which focuses on the printing process.

4.1 Powder productions from ribbons and by gas atomization

From the ribbons prepared and characterized in the previous chapter, the most suitable ones for the thesis objectives were selected to produce powders. The chosen samples, as already mentioned in Chapter 3, included three NiMnSn-based Heusler MMSMAs and one NiMnGa-based ferromagnetic SMA, since they exhibit a martensitic transformation near room temperature accompanied by an abrupt change in magnetization. Additionally, a fourth NiMnSn powder, produced via gas atomization and obtained in the framework of collaboration with FM group from Darmstadt Technische Universität (TU) was used for further characterization.

The procedure for obtaining powders from the ribbons involves manually grinding them in an agate mortar and sieving them to the desired size (see section 2.4.1.). The grinding process introduces some micro-strains that can degrade the magnetic and magnetocaloric properties of the materials. However, this effect can be minimized through two means. First, if the ribbons intended for grinding exhibit MT below room temperature, the grinding should take place in the martensitic state, whereby minimizing the impact of the grinding process on the ordered state of metallic powder. If MT takes place at around room temperature, the grinding should be done within a region, where the alloys exhibit a mixture of the austenite and martensite phases, resulting in a similar effect as in the previous case. If MT occurs above room temperature, the grinding should be obviously done at room temperature, i.e., in martensitic state. Thus, when the MT is at room temperature or below it, the grinding process is done in the present work by using cooling with liquid nitrogen, to ensure it takes place in the low-symmetry martensitic phase. This procedure was found to enhance the magnetic behaviour, probably, due to avoiding the formation of structural micro-strains (Figure 4.1).

In the previous chapter, it was demonstrated that special heat treatments could enhance the magnetic properties of our ribbons. As the grinding process may degrade the material's magnetic behaviour, the same heat treatments as for the ribbons are performed to recover the magnetic properties of powders.

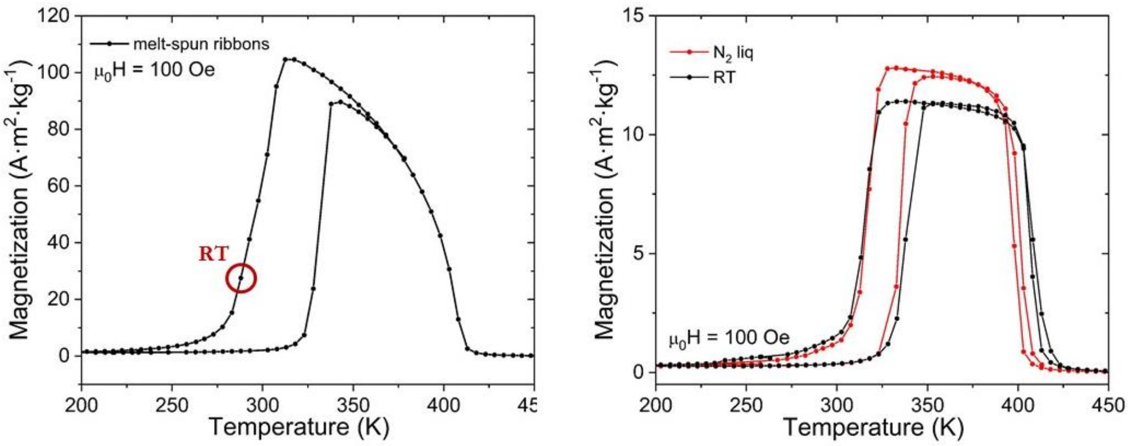

Figure 4.1: Magnetization versus temperature curve for $Ni_{40}Mn_{42.5}Co_8Sn_{9.5}$ *as-spun ribbons (left). At room temperature, there is some coexistence of high symmetry phase austenite and low symmetry martensite. The comparison of powdered ribbons done at room temperature versus the same powderization carried out using liquid nitrogen (at 77K, where there is full martensite phase) is reflected in the thermomagnetization curves (right).*

4.2. NiMnSn MSMA SYSTEM

4.2.1. $Mn_{42.5}Ni_{40}Co_8Sn_{9.5}$

4.2.1.1. Composition and microstructure

$Mn_{42.5}Ni_{40}Co_8Sn_{9.5}$ powder was obtained by manual grinding from the corresponding ribbon described in the previous Chapter. SEM image of the heat-treated particles is presented in Figure 4.2. The actual compositions of the as-grinded and heat treated powders are shown in Table 4.1. The results in Table 4.1 indicate that heat treatment has a slight impact on the composition. Nevertheless, even slight change of the composition may affect the transformation behaviour of MMSMAs.

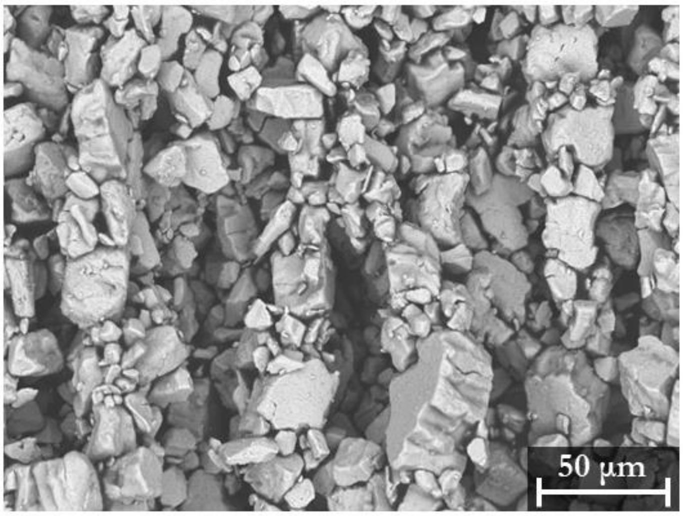

Figure 4.2: SEM image of the particles obtained by manual grinding the ribbons with a subsequent heat treatment.

Table 4.1: Actual compositions of the as-ground and heat treatment powders.

Sample	*Mn (at %)*	*Ni (at %)*	*Co (at %)*	*Sn (at %)*
As-ground powder	40.9	42.6	7.6	8.9
HT powder	39.0	44.0	7.6	9.0

4.2.1.2. X-ray diffraction

Room temperature X-ray diffraction patterns for both the as-spun and heat-treated ribbons, as well as for the as-ground and heat-treated powders, are shown in Figure 4.3. The FullProf analysis results, shown in Figure 4.4 upper left for the as-spun ribbon as a typical example, reveal that all samples, except of the as-ground powder, exhibit a single austenitic phase with the cubic $L2_1$–ordered Heusler structure with the Fm-3m space group. In this structure, the ideal intensity ratio of the fundamental peaks for a randomly oriented powdered state is $I_{400}/I_{220} = 0.15$ (ICSD card #103803). Therefore, different values of this ratio obtained from the bulk samples are indicative of their texture. Specifically, this ratio calculated using the patterns in Figure 4.4 is equal to 0.30 and 0.27 for the as-spun and heat-treated ribbons, respectively, and 0.16 for the heat-treated powder. These values reflect the highest out-of-plane texture degree in the case of the as-spun ribbon, which is slightly reduced after heat treatment and finally disappears for the heat-treated powder.

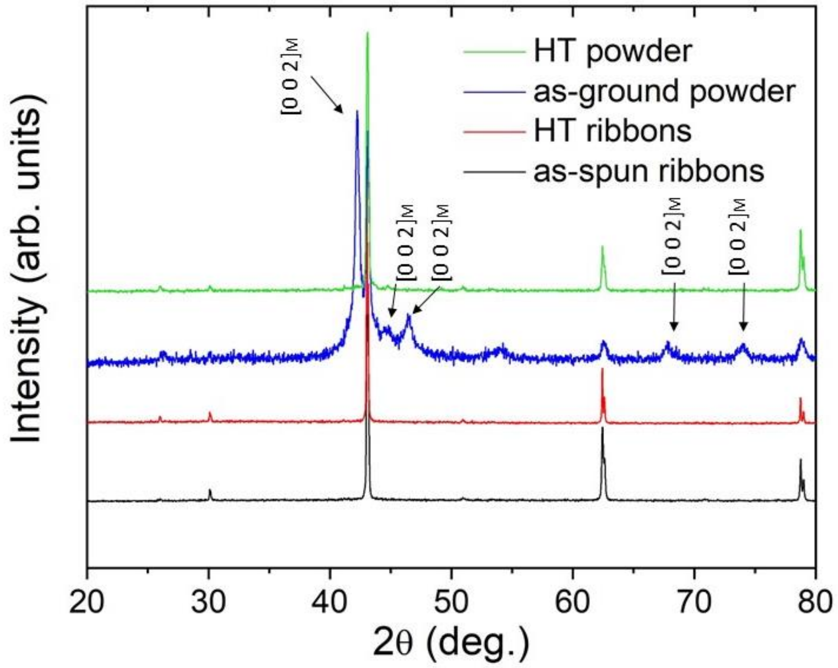

Figure 4.3: Room temperature XRD patterns of the ribbons and powders before and after heat treatment. The materials exhibit one-phase austenitic cubic structure; the second phase for the as-ground powder is indexed in terms of the orthorhombic martensitic phase.

Notably, the XRD pattern for the as-ground powder in Figure 4.4 contains additional reflections alongside the austenitic phase peaks. These extra reflections are a result of the presence of the martensitic phase, which can be indexed in terms of an orthorhombic structure, as indicated in Figure 4.4, with the unit cell parameters of $a = 4.40$ Å, $b = 5.35$ Å and $c = 4.29$ Å.

Table 4.2 summarizes the results of the XRD pattern analysis for the austenitic phase exhibited by all samples at room temperature, namely the values of the austenite lattice parameter, full width at half maximum of the X-ray peak at 2θ=62.3 deg. and residual strain estimated by the Williamson-Hall plot [1]. Whereas the cubic lattice parameter is not sensitive to the type of sample, the line profile appears to depend on the sample preparation. The line width is related to the residual strains and sizes of sub-micrometric crystallites. Thus, the significant broadening of the X-ray peaks in the case of the as-ground powder is not surprising, as this fact reflects the influence of the aforementioned parameters. In this case, the presence of the martensitic phase is attributed to the influence of high residual stresses. However, the applied heat treatment, conducted at 1173 K for 1 h + quenching, causes recrystallization of the powder and relaxes the residual stresses, which agrees with the observed trends shown in Table 4.2 and the disappearance of the two-phase state at room temperature. Furthermore, the presence of the 111 and 200 superstructure reflections at about 26 deg. and 30 deg., respectively, reveals the $L2_1$-atomic ordering in all samples, which is a particular feature for Ni-Mn-Sn-based Heusler alloys [2].

Table 4.2: XRDP results for the as-received and heat-treated (*HT*) ribbon and powder samples of the alloy with nominal composition of $Ni_{40}Co_8Mn_{42.5}Sn_{9.5}$ (at.%). *a* is the lattice parameter of cubic austenite; FWHM is a full width at half maximum of the X-ray peak at 2θ=62.3 deg., ε is the microstrain estimated from the Williamson-Hall plot [1].

Sample	*a (Å)*	*FWHM (deg.)*	*ε (%)*
As-spun ribbon	5.955	0.59	7.2
HT ribbon	5.955	0.82	2.8
As-ground powder	5.953	1.00	40.7
HT powder	5.953	0.45	9.5

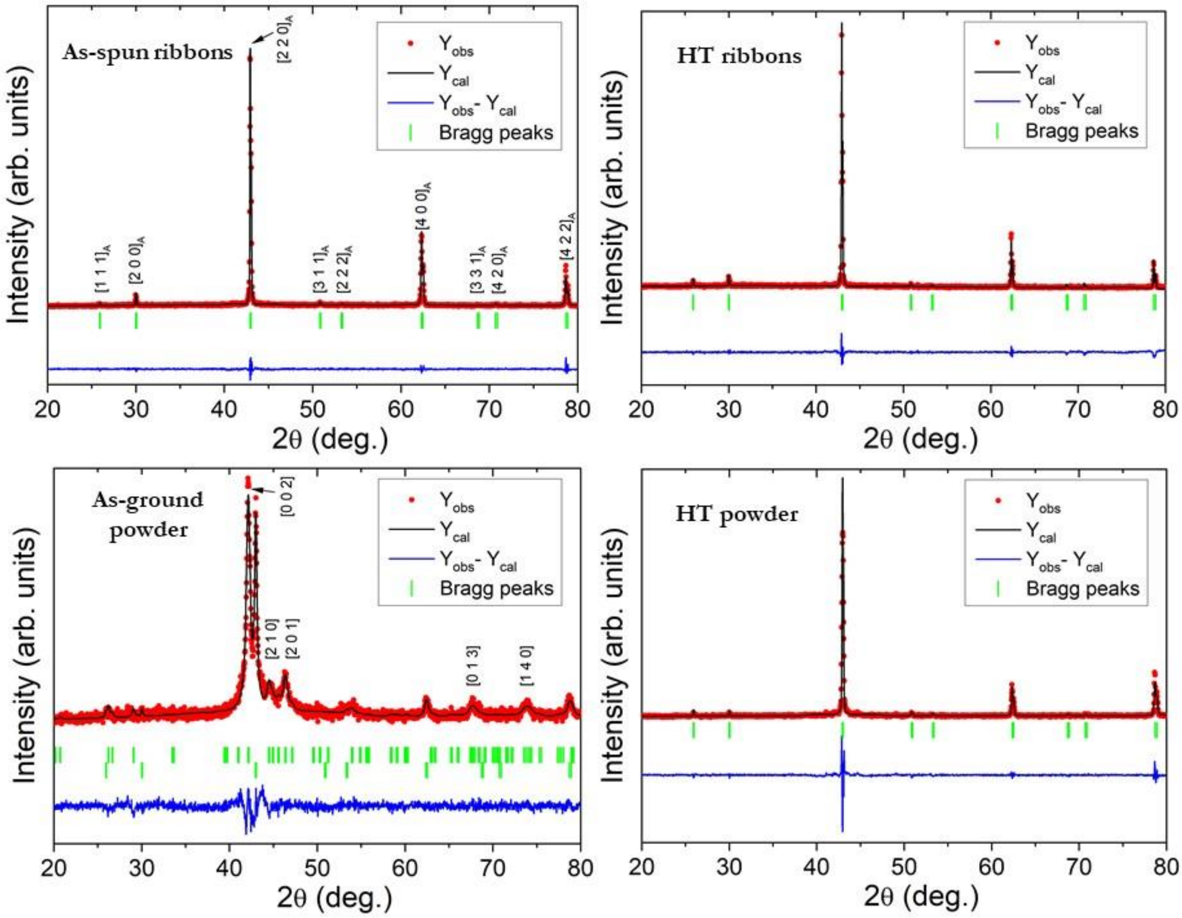

Figure 4.4: Rietveld refinement of the X-rays diffractograms for cubic austenite in the as-spun ribbon (upper left), heat-treated ribbons (upper right), as-ground powder (lower left) and heat-treated powder (lower right).

4.2.1.3. Transformation characteristics

Figure 4.5 shows the thermomagnetization curves for the as-ground and heat treated powders. It is evident that the heat treated ribbon grinding process for obtaining the powder significantly degrades the martensitic transformation (red curve in Figure 3.2 versus black curve in Figure 4.5). In the Chapter 3, it was demonstrated that special heat treatments can significantly improve the magnetic properties. Consequently, the same heat treatment route is followed for the powder, as shown in Figure 4.5, where the abrupt martensitic transformation is successfully achieved.

In summary, the *M*(*T*) dependencies enable us to determine the optimal heat treatment regime for both ribbons (as discussed in chapter 3) and powder.

Additionally, it has been experimentally demonstrated that by using a heat treatment at 1173 K for 60’ + quenching, it is feasible to recover the transformation characteristics for the manually ground thin ribbon in the form of powder with particle sizes well below 38 μm. This finding is highly significant since, as previously mentioned, it is challenging to replicate transformation characteristics from bulk MMSMA into its powder form. In the next chapter, this finding will be validated through a detailed comparative study of the ribbon and printed powder as the ink filler.

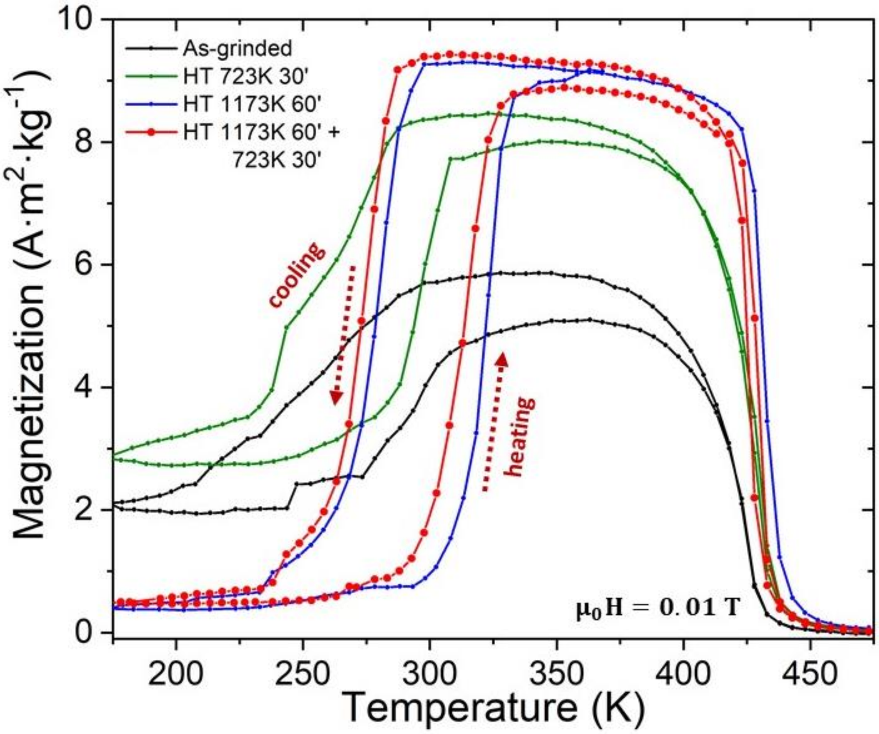

Figure 4.5: Thermomagnetization curves for $Ni_{40}Mn_{42.5}Co_{8}Sn_{9.5}$ powder with different heat treatments.

4.2.2. $Mn_{48}Ni_{35.5}Sn_{8}Co_{6.5}Fe_{2}$

4.2.2.1. Transformation characteristics

The grinding process of this ribbon resulted in a very dramatic effect on the martensitic transformation of the powder. According to the thermomagnetization dependences, shown in Figure 4.6, both the as-received and heat-treated powders show a very smeared MT and the reduced value of

M(*T*) change at MT, factors which impeded us to consider this powder as candidate for printing.

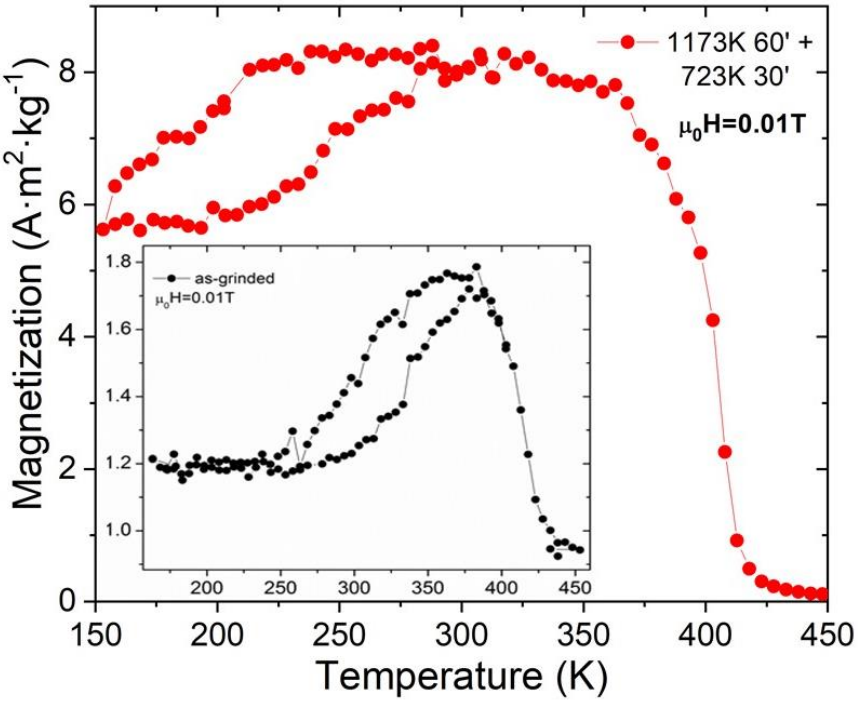

Figure 4.6: Thermomagnetization dependence for the $Mn_{48}Ni_{35.5}Sn_8Co_{6.5}Fe_2$ *heat-treated powder. Inset shows the results for as-ground powder.*

4.2.3. $Ni_{43}Mn_{39}Co_7Sn_{11}$

4.2.3.1. Composition and microstructure

From the set of ribbons prepared with this nominal composition, two alloys were chosen. The first one, V3(A1), was selected for a systematic study of the effects of heat treatments, and the second one, V1(A2), was chosen to investigate the composition's effect on magnetocaloric properties. Table 4.3 shows the results on actual compositions (obtained by EDS with an instrumental uncertainty of ± 0.5 at.%).

Table 4.3: Actual compositions for the two alloys studied.

Sample	*Ni (at %)*	*Mn (at %)*	*Co (at %)*	*Sn (at %)*
A1 (V3)	43.3	39.2	7.4	10.1
A2 (V1)	43.3	39.8	6.6	10.3

4.2.3.2. Transformation characteristics

The temperature dependences of low-field magnetization, *M(T),* as well as calorimetric curves, presented in Figure 4.7 and Figure 4.8, respectively, were used to determine characteristic transformation temperatures, hysteresis of MT and the Curie temperature of the studied powders. Both figures show well-pronounced effects of heat treatments on the transformation behaviour, where it can be observed that heat treatments produced shifts in characteristic temperatures and a reduction of the thermal hysteresis of MT. The martensitic transformations and Curie temperatures were verified by DSC measurements, where MT from the high-temperature austenitic to low-temperature martensitic phases and vice versa are accompanied by exothermal and endothermal effects, respectively (Figure 4.8). Notably, sample A2 presents about twice larger maximum saturation magnetization value than A1, meaning that the former alloy saturates at lower field than A1, possibly, due to anisotropic effects induced by the fabrication method of powders (crystal texture or shape anisotropy). At high magnetic fields, both samples show similar values of the maximum magnetization.

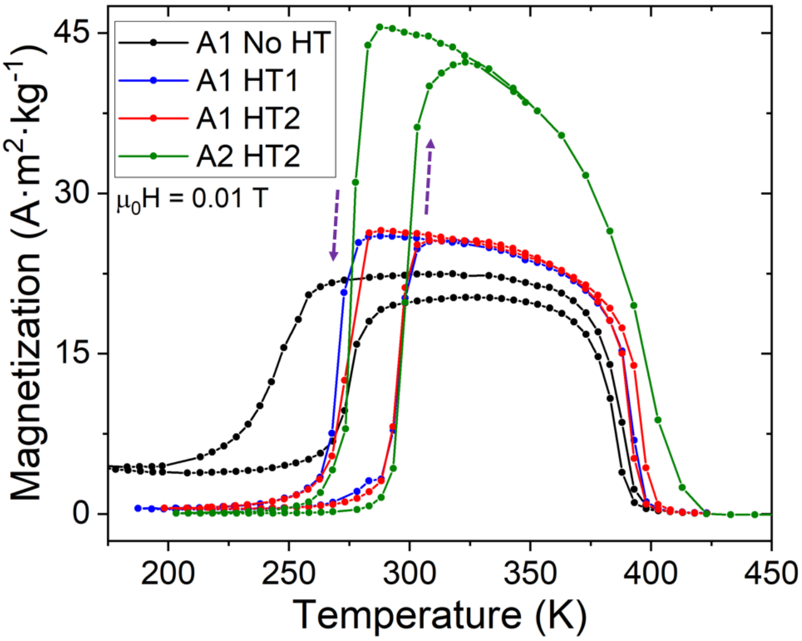

Figure 4.7: Magnetization versus temperature dependences for the heat-treated and as-received powders at low magnetic field.

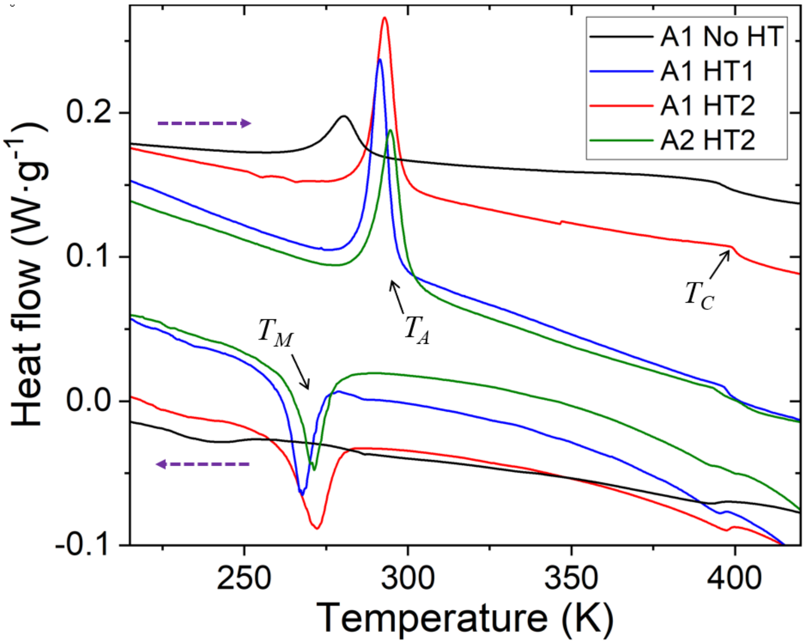

Figure 4.8: DSC curves for the heat-treated and as-received powders.

Martensitic and austenitic transformation temperatures and the Curie point, were extracted from both *M(T)* and DSC curves. They are summarized in Table 4.4. It is evident from Table 4.4 that all the transformation temperatures measured by DSC curves correlated with those obtained from the *M(T)* data.

Table 4.4: Transformation temperatures obtained from the low magnetic field magnetization curves by the derivative method / and from the positions of extremums on DSC curves for heat-treated and no-heat-treated powders.

Powder	T_C, ***K***	T_A, ***K***	T_M, ***K***
A1 No HT	*388 / 395*	*275 / 280*	*248 /242*
A1 HT1	*393 / 396*	*296 / 291*	*270 / 268*
A1 HT2	*391 / 398*	*296 / 293*	*273 / 272*
A2 HT2	*397 / 403*	*298 / 295*	*277 / 271*

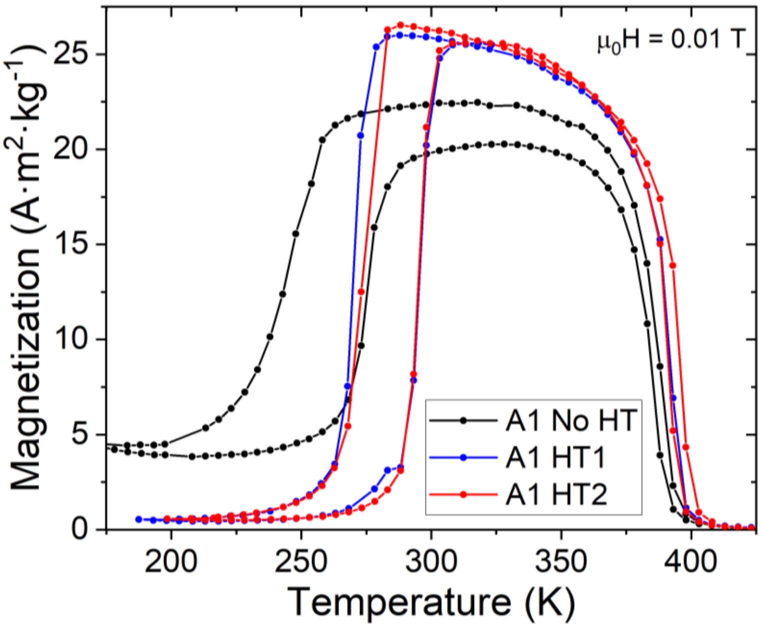

Figure 4.9: Magnetization versus temperature dependences showing the martensitic transformation evolution with the different heat treatments performed for the powder A1.

4.2.3.3. "Magnetic field – temperature" phase diagrams of martensitic transformation

The magnetisation behaviour of materials at high magnetic fields is required to evaluate their magnetocaloric performance. It is also important to check the magnetization behaviour under magnetic fields achievable by the permanent magnets, such as 1.5 T [3]. Figure 4.10 shows the magnetisation versus temperature dependences for the four powders at a field of 1.5 T. As can be noticed in this figure that the magnetisation jump at MT, denoted as ΔM, is critically affected by heat treatments, being doubled for the alloys that underwent a heat treatment with respect to the non-heat-treated one. As a result, ΔM equal to 110 Am^2kg^{-1} was recorded for H2HT2 powder, which is, to our knowledge, a record-breaking value for any MMSMAs powders yet described in the literature. It is worth noting that the size of ΔM directly relates to the magnetocaloric performance of materials. A more direct analysis of the magnetocaloric performance of the alloys can be obtained from the analysis of thermomagnetisation, $M(T)$, curves measured under different constant magnetic fields up to 5 T, which are presented in Figure 4.11.

Following to the magnetic field–induced shift of anomalies on $M(T)$ curves (these anomalies are produced by MT), one can obtain phase diagrams for "martensitic and austenitic transformation temperatures" as a function of the magnetic field, represented in Figure 4.12 for all the samples. In all cases, there is a negative linear dependence of the MT temperatures with increasing magnetic field. The slope of this dependence for the heat-treated powders was calculated to be –(5.0±0.2) K/T, whereas T_M slope for the sample A1 without heat-treatment shows a slope of –(6.3±0.1) K/T.

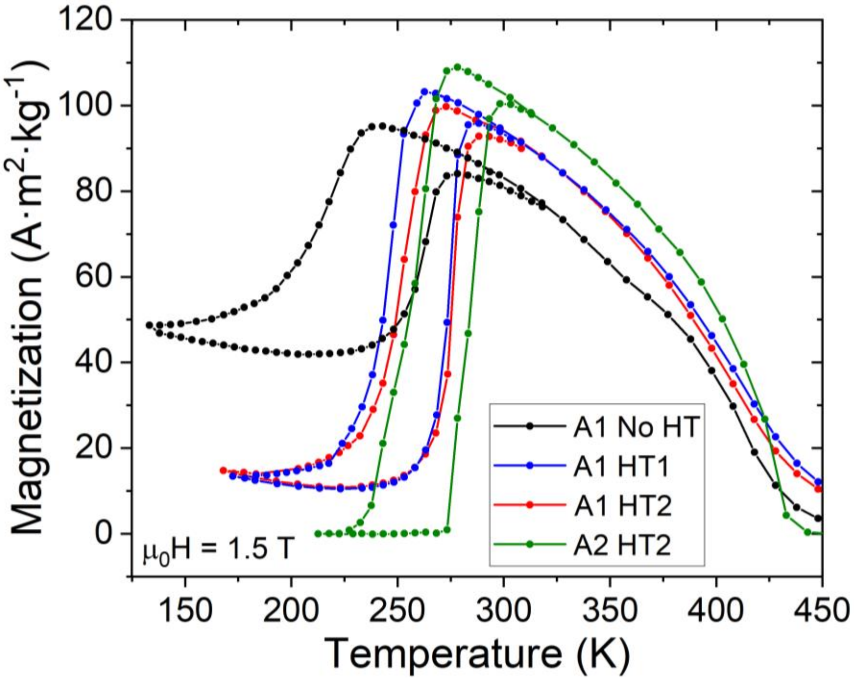

Figure 4.10: Magnetization versus temperature dependences for the studied powders measured under 1.5 T magnetic field.

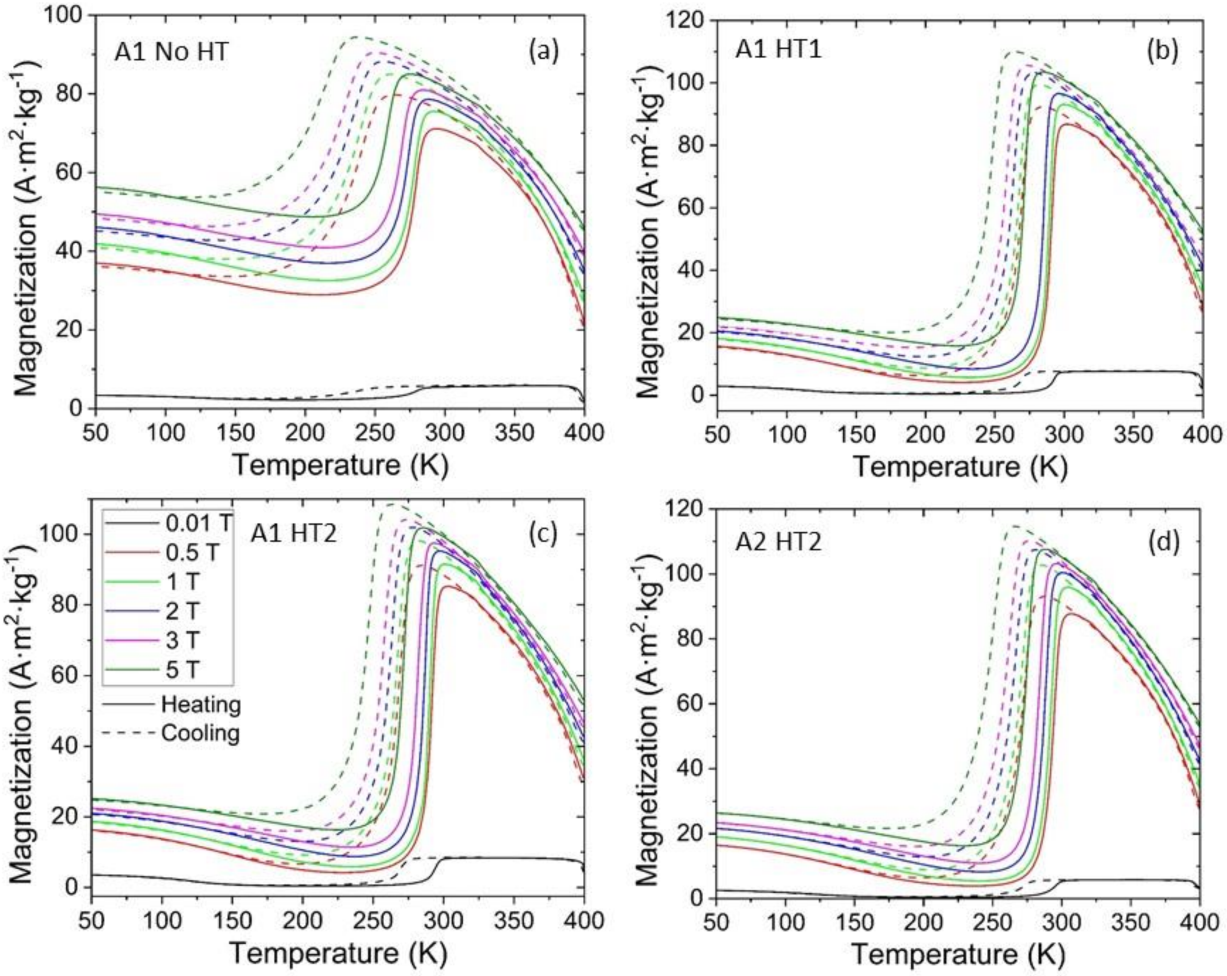

Figure 4.11: Thermomagnetization curves at different magnetic fields for the studied powders.

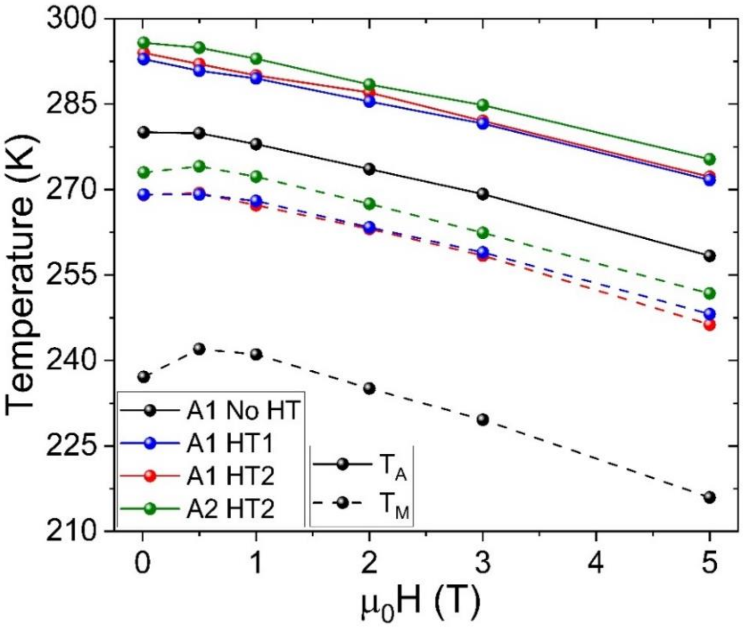

Figure 4.12: Phase diagrams "MT transformation temperatures versus magnetic field" for all the powders.

4.2.3.4. Magnetocaloric effect

4.2.3.4.1. Magnetic field-induced entropy change

Conventional and inverse magnetocaloric effects are characterized by the isothermal entropy change, $\Delta S_m(T,H)$, and/or adiabatic temperature change, $\Delta T_{ad}(T,H)$ when a magnetic field is applied or removed in the isothermal conditions. A magnetic field induced entropy change can be estimated using Maxwell thermodynamic relationships [4]. From the measured $M(T)$ curves at different magnetic fields (Figure 4.11), one can calculate the isothermal entropy change $\Delta S_m(T,\mathrm{H})$ as follows:

$$\Delta S_m(T,H) = S_m(T,H) - S_m(T,0) = \mu_0 \int_0^H \left(\frac{\partial M(T,H')}{\partial T}\right) dH' \qquad (1)$$

Figure 4.13 shows the $\Delta S_m(T,\mathrm{H})$ plots calculated by using cooling and heating data from Figure 4.11 for the four powders studied.

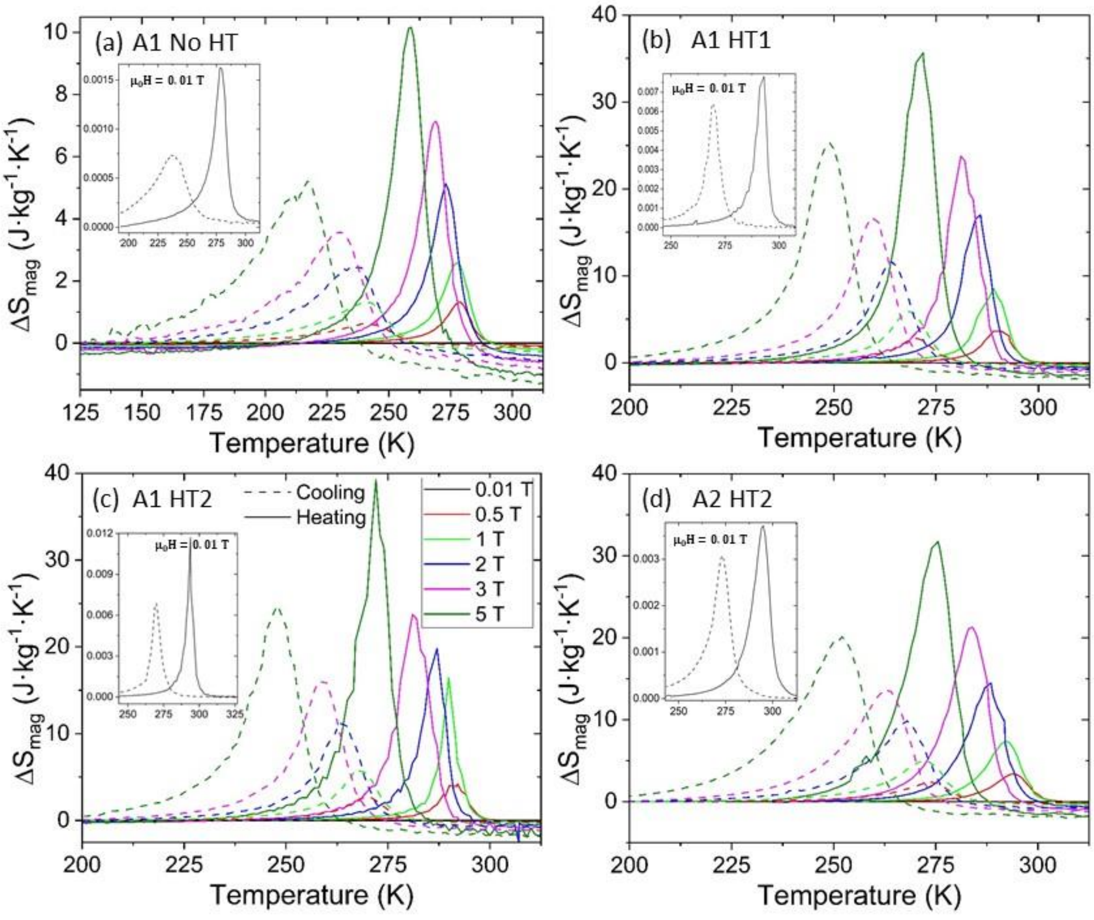

Figure 4.13: Magnetic entropy change at different magnetic fields as a function of temperature derived from cooling/heating M(T) dependences shown in Figure 4.11.

Figure 4.13 shows that the heat-treated powders exhibit values of $\Delta S_{m,max} \approx 35\ \mathrm{J \cdot kg^{-1} \cdot K^{-1}}$ as derived from the analysis of heating *M*(*T*,H) curves at $\mu_0 \Delta H = 7\ T$, whereas for the non-heat-treated sample $\Delta S_{m,max} \approx 10\ \mathrm{J \cdot kg^{-1} \cdot K^{-1}}$.

The $\Delta S_{m,max}$ values obtained from the cooling *M*(*T*) curves are lower than those obtained from the heating ones due to a more smeared character of the forward MT in comparison with the reverse MT. For example, heating curves at $\mu_0 \Delta H = 2$ T yield $\Delta S_{m,max} \approx 20\ \mathrm{J \cdot kg^{-1} \cdot K^{-1}}$ for the heat treated powder A1; this value falls down to 12 $\mathrm{J \cdot kg^{-1} \cdot K^{-1}}$ for cooling curves at the same field. Noteworthy, the values of $\Delta S_{m,max}$ for the heat treated samples obtained in the present work are comparable to those of well-known magnetocaloric materials under similar applied fields, e.g., ~18.5 $\mathrm{J \cdot kg^{-1} \cdot K^{-1}}$ for $Gd_5(Si_2Ge_2)$[5], for $LaFe_{11.4}Si_{1.6}$ ~19.4 $\mathrm{J \cdot kg^{-1} \cdot K^{-1}}$ [6], or ~25.0 $\mathrm{J \cdot kg^{-1} \cdot K^{-1}}$ for $Ni_{40}Co_8Mn_{42.5}Sn_{9.5}$ [7].

There is a remarkable difference in entropy change between the heat-treated and non-heat-treated powders, as expected from the less abrupt *M*(*T*) curve with a much smaller Δ*M* for the non-heat-treated powder in Figure 4.13(a). For A1, there is almost no difference in entropy change between HT1 and HT2, as well as between HT2 for both A1 and A2.

Figure 4.14 shows a comparison of ΔS_m(*T*) dependences of the four samples under field of 1.5 T. As previously mentioned, the difference between the two heat treatments for the A1 powder is negligible in the heating curves, whereas in the cooling curves, the HTA1 sample has a slightly higher $\Delta S_{m,max}$ than HT2. For the non-heat-treated alloy $\Delta S_{m,max}$ is about three times smaller than the rest of the samples.

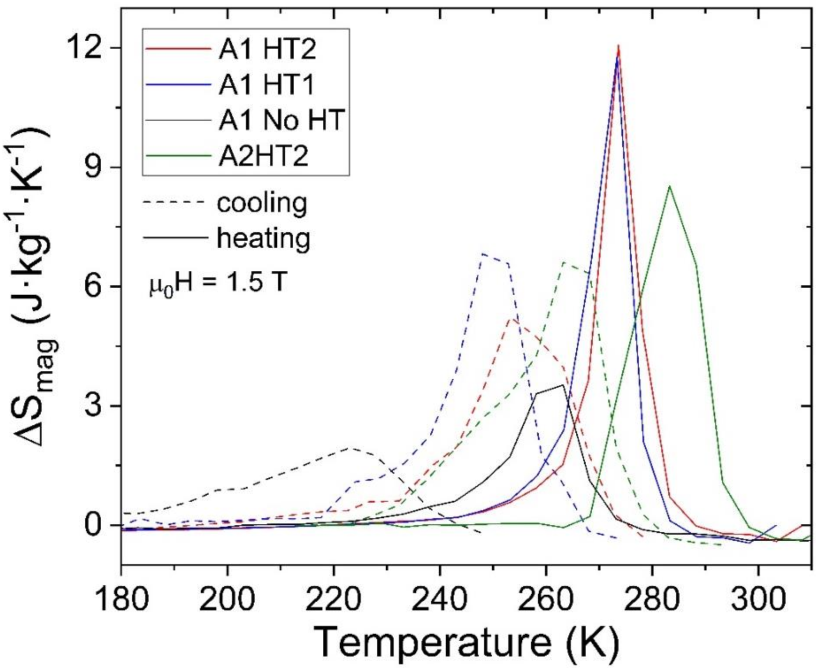

Figure 4.14: Magnetic entropy change at 1.5 T for the four powders studied.

4.2.3.4.2. Refrigeration capacity

The refrigeration capacity, denoted as *RC*, is the amount of heat transferred between hot and cold reservoirs in a single refrigeration cycle. It can be calculated by integrating the maximum of ΔS(*T*) at FWHM:

$$RC \approx \int_{T_{cold}}^{T_{hot}} |\Delta S_M(T,H)| dT \tag{2}$$

The value of the integrated area is known as a Gschneidner´s calculation [8].The refrigeration capacity versus magnetic field dependencies for cooling and heating ramps, calculated by Eq.(2) using the data from Figure 4.13, are shown in Figure 4.15. This figure demonstrates that the RC(*H*) dependencies are affected by the heat treatments, where one can see that the refrigerant capacity is minimal for the non-heat-treated sample and it increases with the application of heat treatments. It is worth noting that, although the A2HT2 powder has slightly smaller maximums of entropy than A1HT2, it boasts the largest refrigeration capacity due to a wider entropy peak.

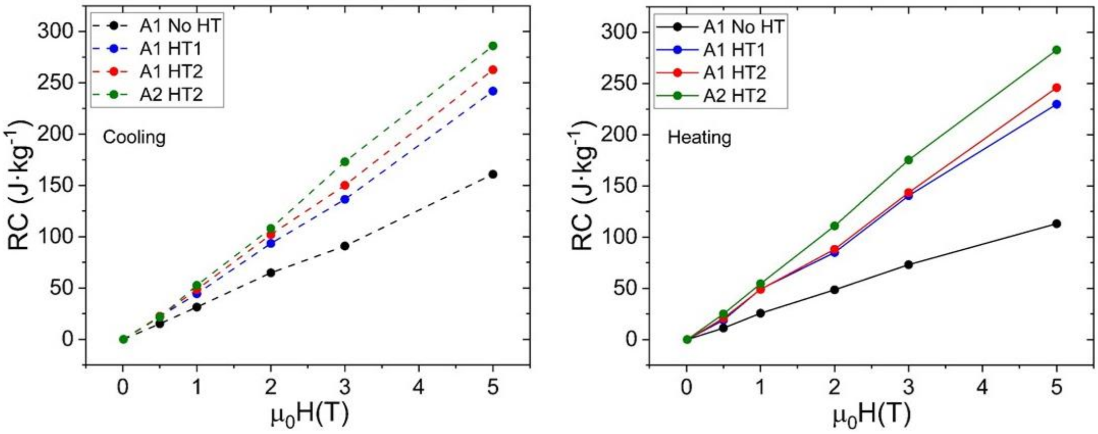

Figure 4.15: Refrigeration capacity as a function of magnetic field for cooling (left) and heating (right) process.

4.2.4. $Ni_{49.8}Mn_{36.6}Sn_{13.6}$

4.2.4.1. Composition and microstructure

The $Ni_{49.8}Mn_{36.6}Sn_{13.6}$ powder was obtained from FM group from Darmstadt TU, in the framework of collaboration. It was prepared by gas atomization and the resulting powder was sieved to a size of 20µm and below. The particle shapes are spherical as the SEM image shows in Figure 4.16. A compositional analysis was done by EDS (see Table 4.5).

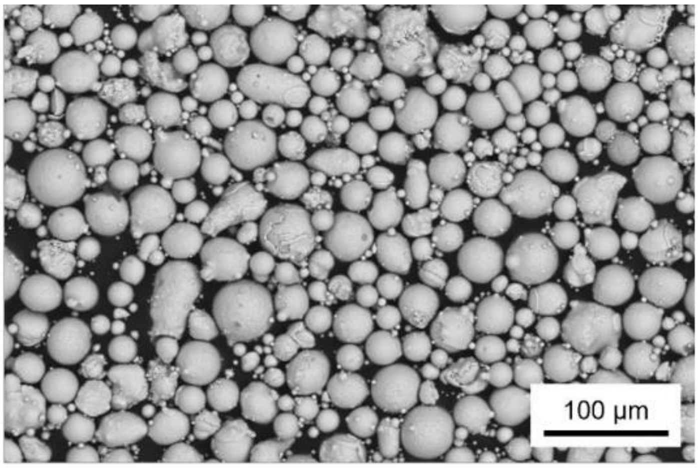

Figure 4.16: SEM image of atomized powder[9].

Table 4.5: Composition of as-atomized and heat treated powders.

Sample	*Ni (at %)*	*Mn (at %)*	*Sn (at %)*
As-atomized	48.6	37.5	13.9
HT powder	49.0	37.3	13.7

4.2.4.2. Transformation characteristics

The effect of heat treatments is revealed in thermomagnetization curves under 1T shown in Figure 4.17, highlighting a significant improvement of the behaviour of martensitic transformation after heat treatment, especially transformation front and a total anomaly shape.

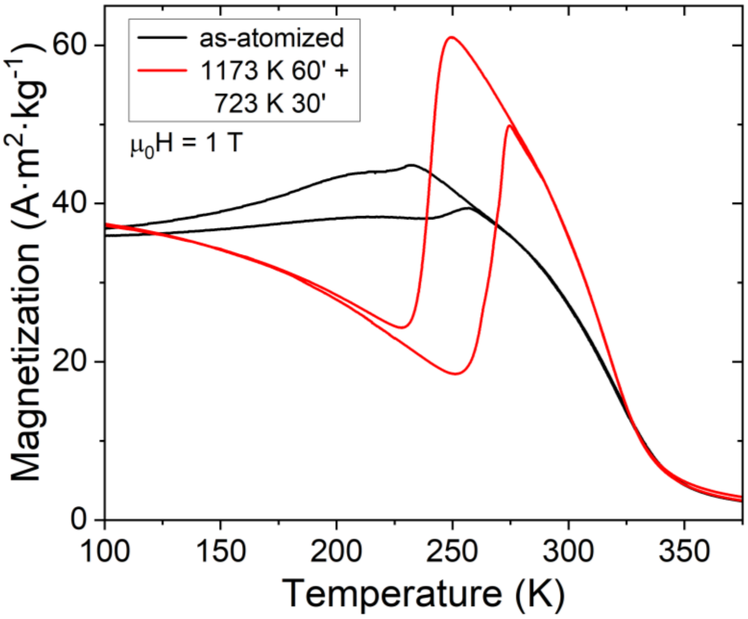

Figure 4.17: Effect of heat treatment on Ni-Mn-Sn atomized powder.

4.2.4.3. "Magnetic field – temperature" phase diagrams of martensitic transformation

The thermomagnetization curves, *M*(*T,H*), for the heat treated powder recorded under different magnetic fields are shown in Figure 4.18 (left). Here, alike the previous alloys, the magnetic field effect on MT is seen as a displacement of the MT hysteresis loop towards low temperatures, a typical behaviour for MetaMSMAs[10] due to the magnetic field induced stabilization of the austenitic phase. The values of martensitic temperature (T_M) and austenitic temperature (T_A) have been extracted from the *M*(T,H) dependences using the derivative method. These temperatures are plotted as a function of the magnetic field in the phase diagram shown in Figure 4.18 (right). The data in Figure 4.18 can be approximated by almost parallel to each other straight lines having negative slope of (-1.68±0.18) K/T for T_A and (-1.82±0.03) K/T for T_M, determined by linear fitting.

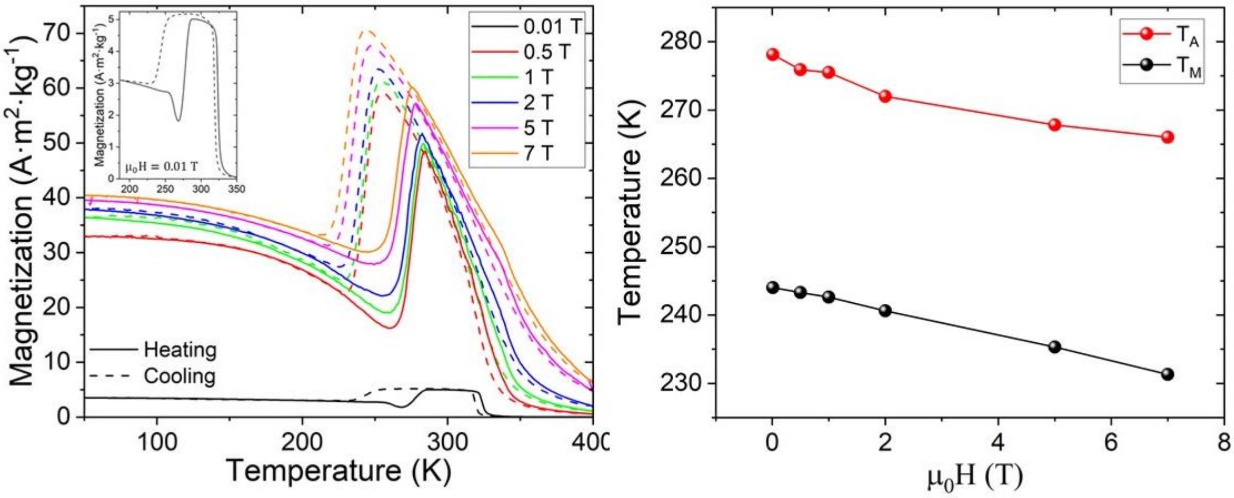

Figure 4.18 Cooling/heating thermomagnetization curves at different applied magnetic fields (left). Phase diagram "MT temperatures versus magnetic field" (right).

4.2.4.4. Magnetocaloric effect

4.2.4.4.1. Magnetic field-induced entropy change

Using the same methodology as previously described, the temperature dependences of the isofield magnetic entropy change are obtained by implementing the Maxwell relationships to the M(T,H) curves presented in Figure 4.18 right (see Figure 4.19). The linear correlation between the maximum entropy change and the magnetic field is confirmed in Figure 4.20 left. With all these data, it becomes possible to calculate the refrigeration capacity (see Figure 4.20 right). Considering the magnetic and magnetocaloric properties of this powdered alloy, together with the fact that it is readily available in high quantities due to the gas atomization process and is in spherical shape, this powder emerges as the most suitable choice for implementation in 3D printing in the next chapter.

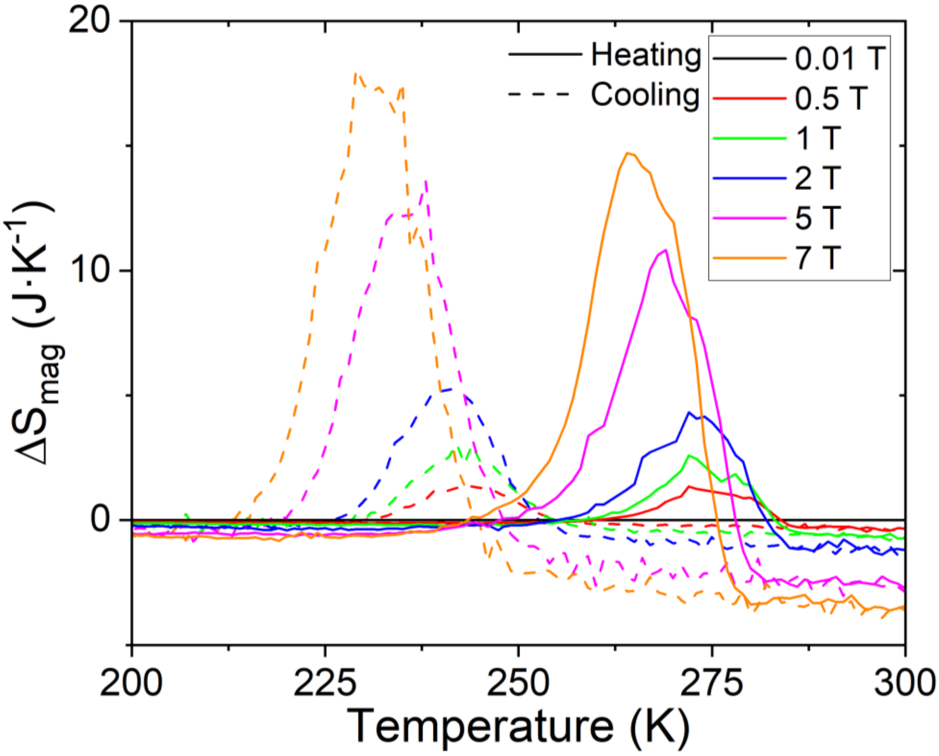

Figure 4.19: Magnetic entropy versus temperature curves obtained from implementing the Maxwell relationship to the data from Figure 4.18(left) for heat treated powders.

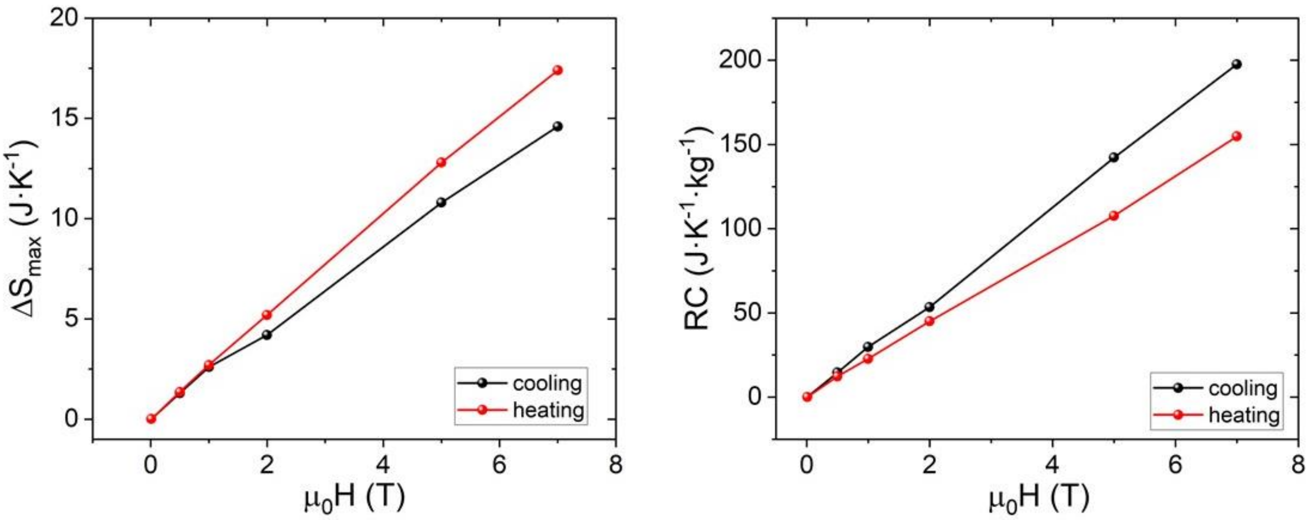

Figure 4.20: Maximum entropy change (left) and refrigeration capacity (right) as a function of magnetic field.

4.3. NiMnGa MSMA SYSTEM

4.3.1. $Ni_{50}Mn_{18.7}Cu_{6.25}Ga_{25}$

4.3.1.1. Composition and microstructure

A bulk $Ni_{50}Mn_{18.7}Cu_{6.25}Ga_{25}$ alloy was prepared by induction furnace. One part of the ingot was used to prepare thin ribbons, which were studied in section 3.3.2. In this subsection we made an attempt to use another part of ingot to prepare a powder with a hammer milling. SEM image of the particles is shown in Figure 4.21. The powder composition, determined by EDS, is presented in Table 4.6.

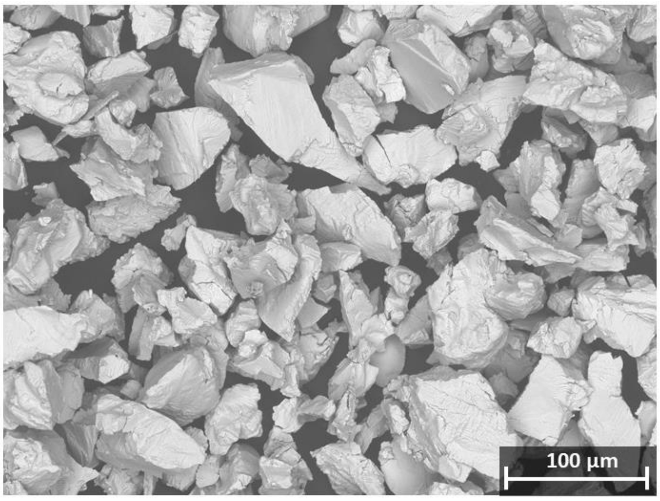

Figure 4.21: Hammer-milled powder sieved below 68µm.

Table 4.6: Actual averaged composition of the milled powder.

Sample	*Ni (at %)*	*Mn (at %)*	*Cu (at %)*	*Ga (at %)*
As-milled	53.4	17.6	8.6	20.5

4.3.1.2. Transformation characteristics

Since the heat treatment had no substantial effect on the ribbons (see subsection 3.3.2), we anticipated that it will also have no effect on the powder. The transformation behaviour of this powder under different magnetic field is shown in Figure 4.22. It is reminiscent to that one shown in Figure 3.18 with a difference that in the curves in Figure 4.22 there exists a tiny smeared anomaly at 170 K which could be attributed to the MT occurring in the ferromagnetically ordered austenite. A tiny *M*(*T*) anomaly fully discards observation of any essential MCE response at MT. Therefore, this powder is not suitable for the goal of the thesis and will not be implemented for printing.

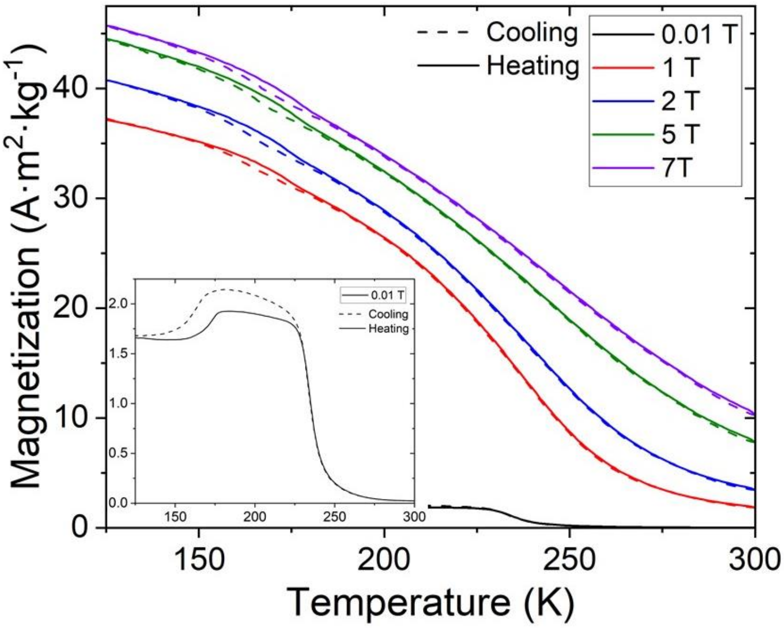

Figure 4.22: Thermomagnetization curves under different magnetic fields for the as-milled powder. The zoomed-in low field curve is shown in the inset.

4.4. CONCLUSIONS

In this chapter we have prepared powder from the ribbons that were selected in the previous chapter. The basic characterization (composition, transformation behaviour and magnetocaloric effect) was mostly performed by thermomagnetization measurements. Apart from the powdered ribbons, another powder made by gas atomization was studied and characterized. Based on the results obtained, the following powders were selected for the printable magnetocaloric ink preparation: $Mn_{42.5}Ni_{40}Co_8Sn_{9.5}$ powdered ribbons and gas-atomized $Ni_{49.8}Mn_{36.6}Sn_{13.6}$ powder.

4.5. REFERENCES

[1] D. Nath, F. Singh, R. Das, X-ray diffraction analysis by Williamson-Hall, Halder-Wagner and size-strain plot methods of CdSe nanoparticles- a comparative study, Mater. Chem. Phys. 239 (2020) 122021. https://doi.org/10.1016/J.MATCHEMPHYS.2019.122021.

[2] V. Sánchez-Alarcos, J.I. Pérez-Landazábal, V. Recarte, I. Lucia, J. Vélez, J.A. Rodríguez-Velamazán, Effect of high-temperature quenching on the magnetostructural transformations and the long-range atomic order of Ni–Mn–Sn and Ni–Mn–Sb metamagnetic shape memory alloys, Acta Mater. 61 (2013) 4676–4682. https://doi.org/10.1016/J.ACTAMAT.2013.04.040.

[3] T. Gottschall, K.P. Skokov, M. Fries, A. Taubel, I. Radulov, F. Scheibel, D. Benke, S. Riegg, O. Gutfleisch, Making a Cool Choice: The Materials Library of Magnetic Refrigeration, Adv. Energy Mater. 9 (2019). https://doi.org/10.1002/aenm.201901322.

[4] V.K. Pecharsky, K.A. Gschneidner, Magnetocaloric effect from indirect measurements: Magnetization and heat capacity, J. Appl. Phys. 86 (1999) 565–575. https://doi.org/10.1063/1.370767.

[5] V.K. Pecharsky, J. Gschneidner K. A., Giant Magnetocaloric Effect in Gd5Si2Ge2, Phys. Rev. Lett. 78 (1997) 4494–4497. https://doi.org/10.1103/PhysRevLett.78.4494.

[6] F.X. Hu, B.G. Shen, J.R. Sun, Z.H. Cheng, G.H. Rao, X.X. Zhang, Influence of negative lattice expansion and metamagnetic transition on magnetic entropy change in the compound LaFe11.4Si1.6, Appl. Phys. Lett. 78 (2001) 3675–3677. https://doi.org/10.1063/1.1375836.

[7] B. Rodríguez-Crespo, D. Salazar, S. Lanceros-Méndez, V. Chernenko, Development and magnetocaloric properties of Ni(Co)-Mn-Sn printing ink, J. Alloys Compd. 917 (2022) 165521. https://doi.org/10.1016/j.jallcom.2022.165521.

[8] K.A. Gschneider, Recent develompents in magnetic refrigeration, 317 (1999) 69–76. https://doi.org/10.4028/www.scientific.net/MSF.315-317.69.

[9] F. Scheibel, C. Lauhoff, P. Krooß, S. Riegg, N. Sommer, D. Koch, K. Opelt, H. Gutte, O. Volkova, S. Böhm, T. Niendorf, O. Gutfleisch, Additive manufacturing of Ni-Mn-Sn shape memory Heusler alloy – Microstructure and magnetic properties from powder to printed parts, Materialia. 29 (2023). https://doi.org/10.1016/j.mtla.2023.101783.

[10] P. Lázpita, M. Sasmaz, E. Cesari, J.M. Barandiarán, J. Gutiérrez, V.A. Chernenko, Martensitic transformation and magnetic field induced effects in Ni42Co8Mn39Sn11 metamagnetic shape memory alloy, Acta Mater. 109 (2016) 170–176. https://doi.org/10.1016/j.actamat.2016.02.046.

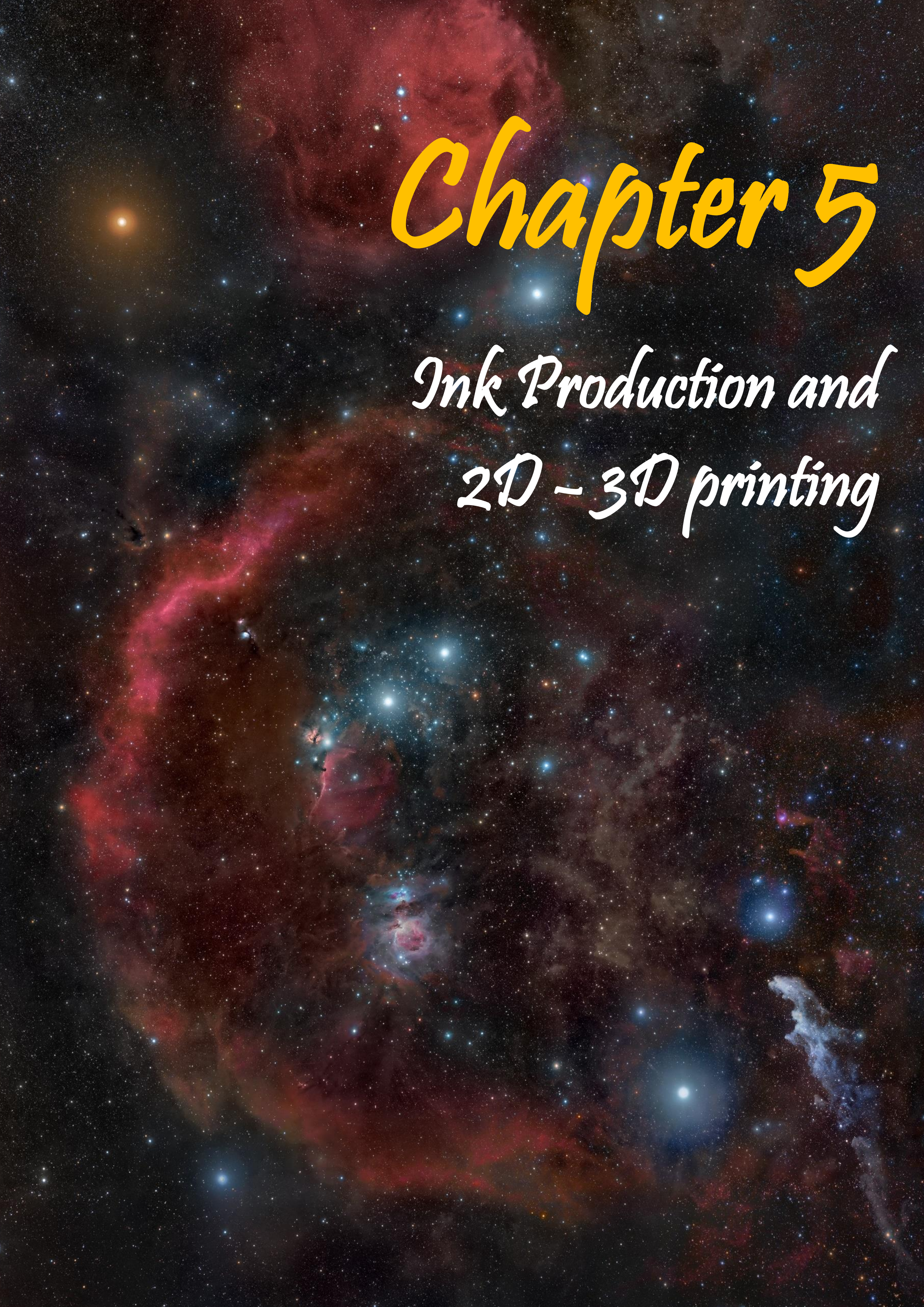

Chapter 5

Ink Production and 2D - 3D printing

Chapter 5

Design and Fabrication of Novel Metallic Printable Materials

5.1. 2D AND 3D PRINTING OF COMMERCIAL POWDERS

5.1.1. Technique validation

This is the last chapter of the thesis and the one that contains its global objective: To develop a new 2D-3D printing technique and the implementation of the selected powders to print actual magnetocaloric 2D-3D structures.

The first step for metallic 2D-3D printing is to elaborate a route for developing proper inks that are suitable for printing high-quality structures with good mechanical properties, uniform layer growth and high number of printable layers. For developing such route, commercial powders were used as the first step, since they are widely available in the laboratory allowing to make a systematic study of the printing limitations, optimization, etc. Then, after establishing the route for printing quality structures, the technique will be implemented to the prepared magnetocaloric powders, available in lower quantity.

The main challenge for both 2D screen-printing and 3D extrusion printing techniques is to develop a proper ink so the printing result is successful. The ink is made of three elements:

1) Metallic filler
2) Matrix
3) Dissolvent

The main parameter that controls the printing quality is the viscosity. For screen 2D printing the requirements of the ink are not that strict, whereas for extrusion 3D printing the requirements are more sensitive and, apart from proper viscosity, the filler/matrix volumetric proportion is also crucial.

5.1.2. Searching for a binder and solvents for eco-friendly approach using metallic powder as filler

Current polymer printing methods involve the use of chemical solvents and synthetic polymers. Also, high printing temperature is required (220°C for PLA). Since our aim is to find eco-friendly approach, we need to replace those materials by environmentally friendly alternatives. In our case, the synthetic polymer is going to be replaced by three alternatives: (i) Silk, (ii) Collagen, and (iii) Cellulose derivative. All of these alternatives are found in nature so they are widely available natural source of raw materials. The chemical solvent is going to be replaced by deionized water.

5.1.2.1. Silk-based ink

Once the silk is dissolved in water, the proportion of water is about 95% so the polymer content is too low for sustaining the powder to be printed. The printing tests resulted in a spread of the filament extruded losing its original shape seconds after the deposition in the substrate, making this polymer not suitable for 3D printing.

5.1.2.2. Collagen-based ink

Similarly to the silk-based ink, the collagen content after it is dissolved is quite low for being able to print metallic powders, resulting in a spread of the filament in the same manner as silk inks.

5.1.2.3. Cellulose-based ink

The Cellulose derivative that we are going to use is the Hydroxypropil Cellulose since it has a good processability and has been proven to have a good film forming capacity. In this case the polymer proportion, once is dissolved in water, can be tuned by increasing to high percentage. Printing tests revealed a consistent deposited filaments that allow to print uniform layers, making this polymer the best option for the aim of the thesis.

5.1.3. Commercial powders and ink parameters

For metallic filler, various powders available in the laboratory were used. The first approach was to use a powder that is widely available and that has very similar density compared to the magnetocaloric powders (near 8 g/cm^3) in order to implement the route for magnetocaloric powders. Hence, an iron powder was selected for this purpose. In addition, various tests were performed using Aluminium (Al) and Silicon (Si) powders. Although these powders have roughly 1/3 of Iron density the printing of these materials may provide a better refinement of the printing technique.

Several inks were prepared for testing, first with the screen-printer and then in the extrusion printer. The metallic/cellulose weight percentage varied from 85% to 95% and the viscosity is controlled entirely by the water content of the ink, that is, for a fixed metallic percentage the water content was varied in a search for the best printing result. The weight percentage cannot be increased arbitrarily for all the powders used since the volumetric percentage of the polymer needs to be above certain value to sustain the entire powder.

In the case of Iron 85% wt. the water quantity was varied from 45% to 80% in volume (25% to 40% in weight) and the best result was 48%Vol. or 28%wt (Table 5.1). For Iron 92.5% wt. the water quantity was varied from 40% to 60% in volume (15% to 30% in weight) having the best results corresponding to 51%Vol. or 22%wt.

Aluminium ink was found to be optimal with water content of 23%Vol. or 40%wt., a proportion that was optimized after varying the water content from 15% to 35% in volume (or 30% to 55% in weight). For Silicon ink, the water quantity was varied from 35% to 55%Vol. (27% to 52% in weight) and the optimal proportion was found to be 47%Vol. or 37%wt (Table 5.1).

Table 5.1: Selected inks prepared for printing using commercial powders. The proportion of each constituent is listed both in mass fraction and in volume fraction.

Ink	Constituent	Density (g/ml)	Mass fraction (%)	Volume fraction (%)
Ink 1 **Fe 85% wt.**	Fe powder ($\phi \leq 10\ \mu m$)	7.9	62	14
	Deionized water	1.0	28	48
	HPC	0.5	10	38
	Total	1.7	100	100
Ink 2 **Fe 92.5% wt.**	Fe powder ($\phi \leq 10\ \mu m$)	7.9	72	21
	Deionized water	1.0	22	51
	HPC	0.5	6	28
	Total	2.4	100	100
Ink 3 **Al 85% wt.**	Al powder ($\phi \leq 45\ \mu m$)	2.7	51	24
	Deionized water	1.0	40	52
	HPC	0.5	9	23
	Total	1.3	100	100
Ink 4 **Si 85% wt.**	Si powder ($\phi \leq 106\ \mu m$)	2.3	54	29
	Deionized water	1.0	37	47
	HPC	0.5	9	24
	Total	1.3	100	100

Table 5.2: Dried ink percentages.

Ink	Constituent	Density (g/ml)	Mass fraction (%)	Volume fraction (%)
Ink 1 **Fe 85% wt.**	Fe powder ($\phi \leq 10\ \mu m$)	7.9	85	27
	HPC	0.5	15	73
	Total	2.5	100	100
Ink 4 **Fe 92.5% wt.**	Fe powder ($\phi \leq 10\ \mu m$)	7.9	92.5	45
	HPC	0.5	7.5	55
	Total	3.7	100	100
Ink 3 **Al 85% wt.**	Al powder ($\phi \leq 45\ \mu m$)	2.7	85	51
	HPC	0.5	15	49
	Total	1.6	100	100
Ink 2 **Si 85% wt.**	Si powder ($\phi \leq 106\ \mu m$)	2.3	85	55
	HPC	0.5	15	45
	Total	1.5	100	100

Table 5.1 shows the selected inks from commercial powders with the proportions of each constituent in mass and volume percentage but the printed structure will contain only the polymer and the metallic powder, so it is of great interest to know the mass and volumetric proportion of polymer versus metallic powder in the dried inks, see Table 5.2.

5.1.4. Printing commercial powders

5.1.4.1. Screen-printing

The first approach for ink testing was done by 2D screen-printing. In this technique 16 x 8 mm rectangle shaped chips were printed by applying 1 and 10 layers of material to increase the magnetic content and for comparison (see Figure 5.2). To modify the surface tension of the ink and improve its wettability, the surface active agent BYK-348 was added in a proportion of 3 - 5 µl/ml. Several inks were prepared for screen-printing by varying the proportions of filler material, binder and water. Three weight fractions of metallic powder, namely, 60 wt%, 75 wt% and 85 wt% were evaluated. For the ink with the 85 wt% of filler the amount of water was varied in order to get optimal viscosity maintaining the highest possible quantity of the metallic powder. It was found that the best-working ink should contain 85 wt% of powder and 15 wt% of HPC, corresponding to the powder/dissolvent proportion of 1 g/0.45 mL. This proportion resulted in an optimal ink viscosity for the screen-printing (1000–10,000 cP).

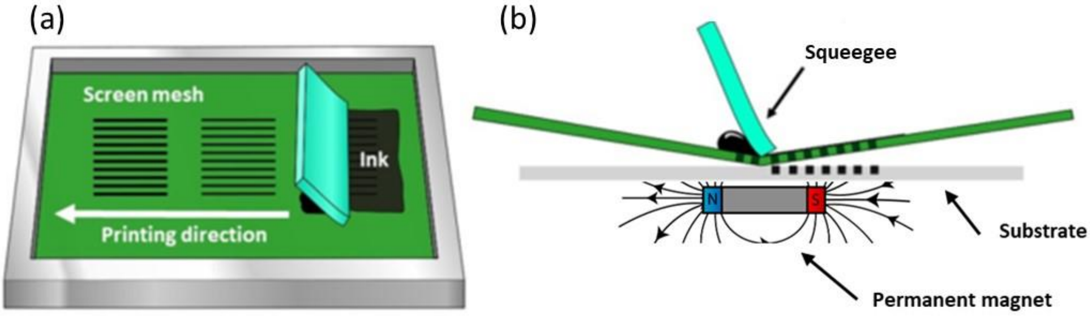

Figure 5.1: Schematic representation of screen-printing setup.

A polyethylene terephthalate (PET) foil was used as a printing substrate since it is flexible, non-porous, and it allows easy detachment of the ink sample from the substrate once it is dry. Before printing, the surface of substrate is ionized by a corona treatment to enhance the adherence of the ink [1]. The printing device and layout of the PET substrate on the printing platform are displayed schematically in Figure 5.1(a,b). During ink curing for 24 h, a permanent magnet was placed beneath the substrate to induce a preferable orientation of the particles in the printed layer. Once the layered composite consisting of the printed pattern of 85 wt% powder embedded into polymer binder is dry, up to nine further layers of the same material were printed following the same procedure. Finally, the obtained multi-layered samples depicted in Figure 5.2 were analysed for material homogeneity and density to select the optimal one which resulted to be the one with the highest amount of surfactant.

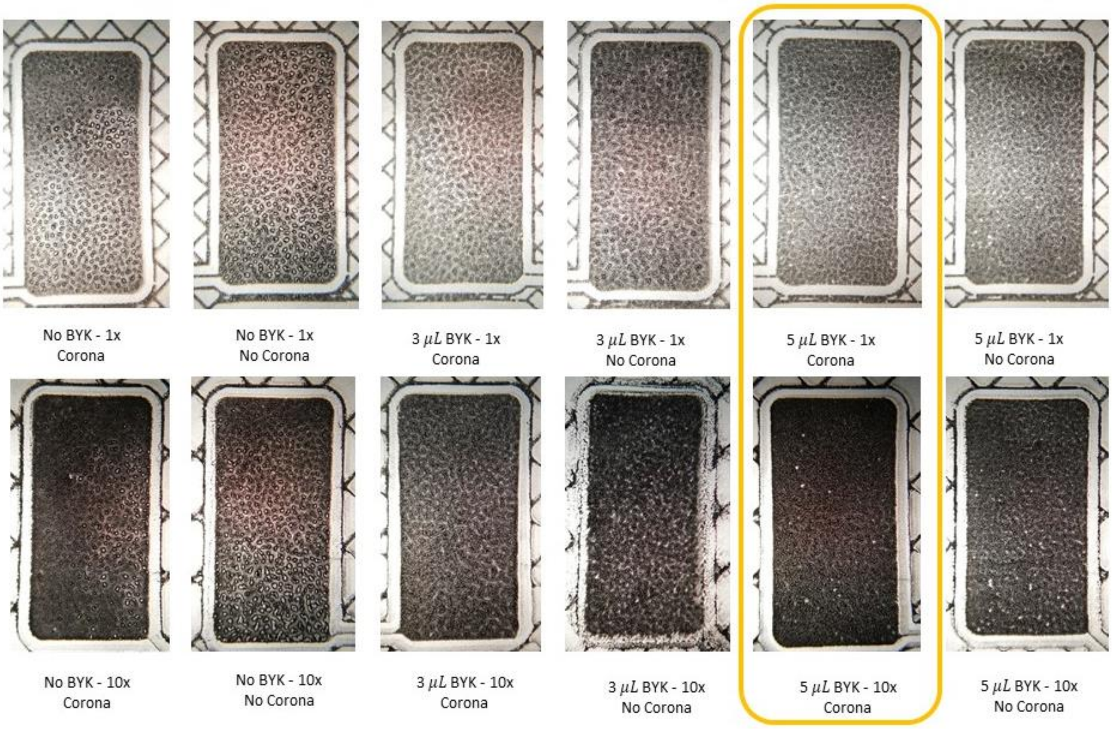

Figure 5.2: Screen printing tests for iron ink at 85% wt. 1 layer (upper images) versus 10 layer (bottom images) are compared with different concentration of surfactant.

5.1.4.2. Cold-extrusion printing

For cold-extrusion 3D printing (Figure 5.3) several geometries were designed for printing to validate the ink and the printing technique. This process consists in two steps: First, to find a correct proportion of ink constituents to achieve the viscosity, internal frictional forces, etc. which would lead to good printing quality and high maximum number of printable layers. Second, to find printed structure design limitations and then improve it with the aim of getting uniform layers and their high number.

The used powder size (varying from 10µm to 100µm) with suitable water quantity prevents the 400µm diameter nozzle from clogging. Viscosity is entirely controlled by water proportion, so the printing quality depends mainly on this parameter and on the absence of air bubbles within the ink. Also, the metal/polymer ratio in volume plays a crucial role in the maximum number of printable layers. Water proportion also controls the rate of drying and this has to be fast enough to allow the lower layer surface to be dried before printing the next layer. An equilibrium of these two parameters has to be found so the printing quality is optimal: suitable viscosity and fast drying rate. This drying rate can be increased using an air fan producing a continuous air flux and reducing in half the time needed for drying. A water-rich ink will result on the low viscosity leading to a spread of the printed filament giving rise to a less precision and also to a reduction of the resolution of minimum printable dimension. Also, the drying rate will be slow, leading to a poor layer-to-layer adhesion and limiting the maximum printable layers. On the other hand, a water-poor ink will be too viscous and the extruding rate will be low, leading to thin printed filament and to discontinuous layers, leaving holes in the printed layer in some cases. These holes generally propagate in Z out-of-plane direction so it is very important to avoid them.

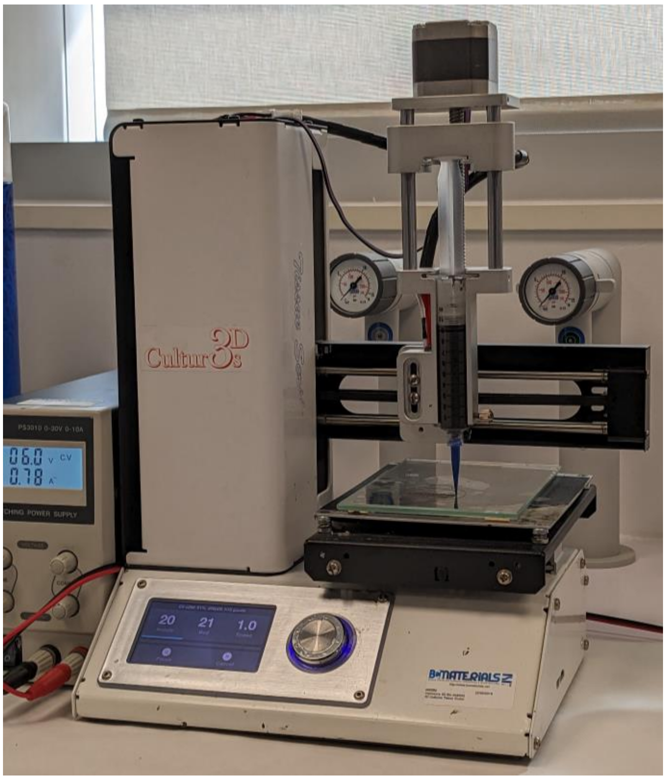

Figure 5.3: Cold-extrusion 3D printing setup.

5.1.4.2.1. Iron ink

For the printing validation, a set of Iron-based inks were prepared with different water mass fractions in order to find the optimal viscosity. The optimal viscosity corresponds to Ink 1 (Table 5.1) and this ink was used for printing. The parameters ensuring such a viscosity behaviour were pursued in the other inks providing similar and better results during 3D structures printing.

Although the inks are labelled with the weight fraction, the important factor is the volume fraction since once printed and sintered, the sample internal porosity will depend on the volume previously occupied by the polymeric matrix. Among prepared inks, all of them share about the same volume fraction of metallic powder except in the Iron-based ink, due to its higher density, so it requires less polymer percentage to maintain its structure. This suggests that the quantity of HPC for this ink could be lowered, increasing the weight fraction of Iron and this was verified experimentally. On the other hand, the other inks revealed to have the maximum fraction of HPC capable of giving a quality ink due to the fact of having not enough polymer for the powder. If HPC fraction was lowered with these inks, the printing quality was affected negatively.

Once an optimal viscosity is obtained, the next step consists on testing the inks printing different designs, and finding which designs lead to solid structures and a high number of printable layers (Figure 5.4). After printing different kind of structures designs we found that in order to get good printing quality the design should have non-intersecting lines, because otherwise in the intersection points the ink accumulates producing a non-uniform layer (see Figure 5.4a and b). This effect propagates in Z direction giving rise to a bad quality 3D piece and, thus, limiting the maximum printable layers to few tens. Since the perimeter for this kind of designs was well printed (Figures 5.4a and 5.4b), the next attempt was to print closed circuits and the results were good (Figures 5.4c and 5.4d). As far as a closed circuit had no great structural integrity, another design was proposed replacing intersecting lines with tangent ones (Figure 5.4f). This honeycomb-like structure has high structural integrity upon compression in a vertical Z direction. Such useful designs were used to print the Si-based and Al-based inks, this time starting from spiral-like designs (see Figures 5.5 and 5.6).

The Ink 1 (iron ink at 85%wt. from Tables 5.1 and 5.2) was tested. After finding the best printable geometries, several high quality layers were printed. However, even with the optimization of the viscosity, it was not possible to print more than 50 layers with uniform layer growth, unlike the case of Aluminium and Silicon inks, where more than 200 layers were possible to be printed (see next section). This suggests that the powder/polymer volume fraction could play a significant role in printing quality together with an optimal viscosity. Since the iron 85%wt. ink has 25% of iron in volume, increasing this fraction to near 50% could give better results. Thus, Iron based ink at 92.5%wt. was used, and the printing quality was improved significantly (Figs. 5.4e vs 5.4f).

The maximum number of layers reached with this ink was more than 200, so the improvement of increasing the powder/polymer volume percentage close to 50/50 was significant. With this ink the water quantity was varied from 40% to 60% in volume (15% to 30% in weight) and the best result was obtained for 51%Vol. or 22%wt. (see Tables 1 and 2). In both iron inks, the optimal nozzle translation speed, or printing speed, was 200 mm/min.

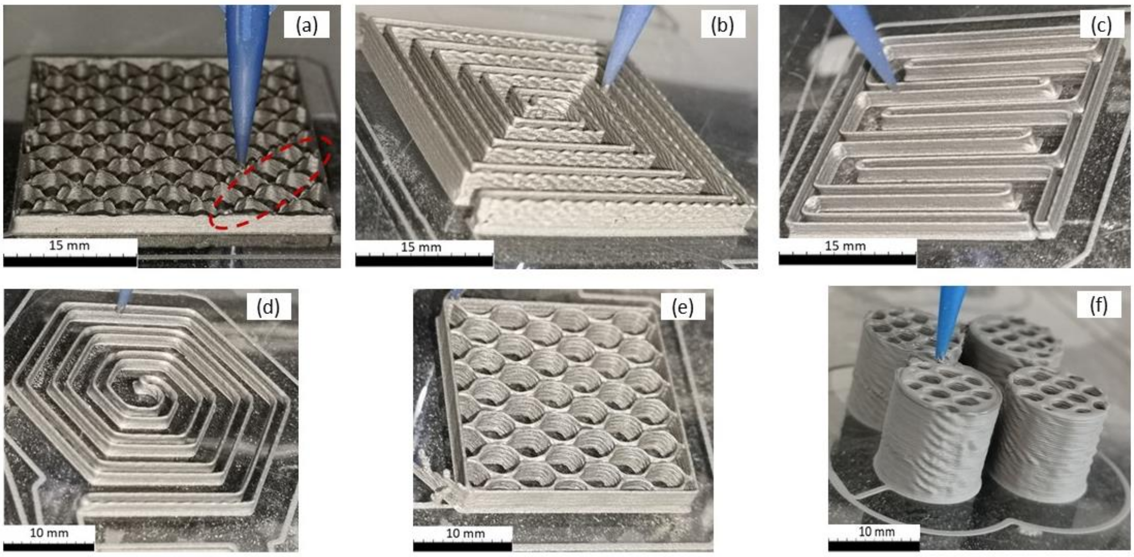

Figure 5.4: Different tested geometries for Fe-based ink validation. (a), (b), (c), (d) and (e) correspond to 85%wt. ink and (f) corresponds to 95%wt. ink. (a) Shows defect propagation through Z axis due to intersected lines that overlap material in specific zones, leading to non-uniform accumulation of material in each layer. The perimeter has no intersecting lines and the growth is uniform so closed circuits were next approach to attempt an increase on maximum number of layers (b) (c) and (d). Honeycomb-like structure which combines uniform layers together with solid structure for 85%wt. ink (e) and 95%wt. ink (f).

5.3.2.2. Aluminium ink

The second ink system explored was the aluminium-based ink. Aluminium ink at 85%wt. was prepared. With this ink the printing quality showed a notorious improvement compared to the Iron 85% wt. ink and was very similar to the iron 92.5% wt. ink. With this ink the maximum printable layers was limited by the volume of the ink loadable in the syringe (10 mL) and not by the ink itself so 200 layers limit was overcame with uniform growth and almost no defects. The optimal printing speed for this ink resulted to be 300 mm/min (Figure 5.5).

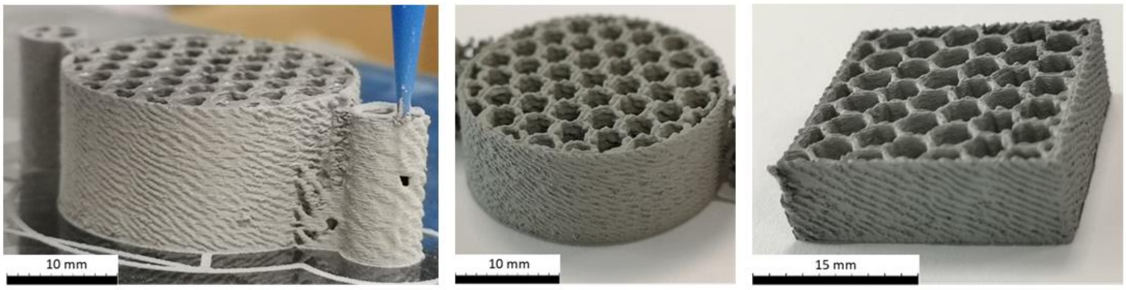

Figure 5.5: Printed Aluminium structures.

5.3.3.3. Silicon ink

Since the Silicon and the Aluminium have very similar densities, the parameters used for the previous ink preparation were implemented so the printing quality was at the same level. Unlike the aluminium powder, the silicon powder is irregular shaped and has a particle size of 160 µm so the structure is more porous than the spherical 20 µm aluminium particles. The amount of the printable layers were also more than 200, and the optimal printing speed resulted to be 300 mm/min too (Figure 5.6).

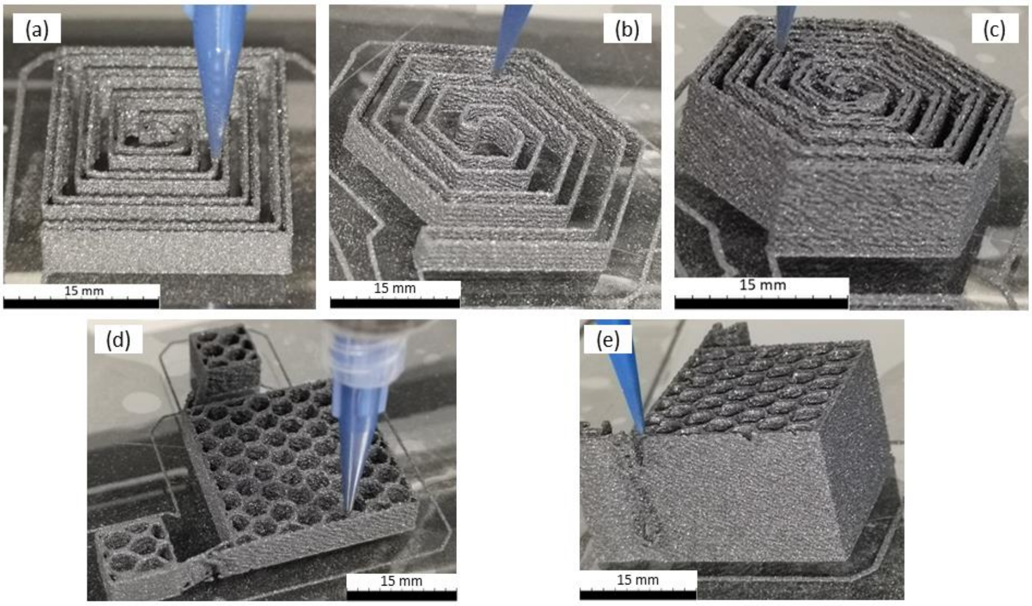

Figure 5.6: Printing capabilities test with silicon-based ink. (a), (b) and (c) correspond to closed circuits and (d) and (e) to honeycomb cubes.

5.1.5 Heat treatments: Calcination and sintering

Once a 3D structure is obtained and dryed overnigh, the resulting piece is composed of the metallic filler and the polymeric matrix. Since the polymers used are water soluble, the structure would dissolve in a magnetic refrigerator that uses water as a heat transfer fluid. Also, the polymer goes in detriment with the refrigeration performance since part of the structure has no functional material and the polymer reduces the thermal conductivity, decreasing the thermal transport between the structure and the heat transfer fluid. Thus, a complete 100% metallic structure is desirable and for that the polymer must be removed and the resulting structure needs to be mechanically strenghtened since removing the polymer would leave brittle structure. To achieve this, a couple of heat treatments should be done with the printed structure. First, a calcination will be performed slighlty above the calcination temperature of the polymer (425°C for HPC [2]) and then a sintering will be performed to compact the structure. The calcination time is 2 hours and the sintering one varied form 1h to 3h depending on the structure size and material (see Figure 5.7).

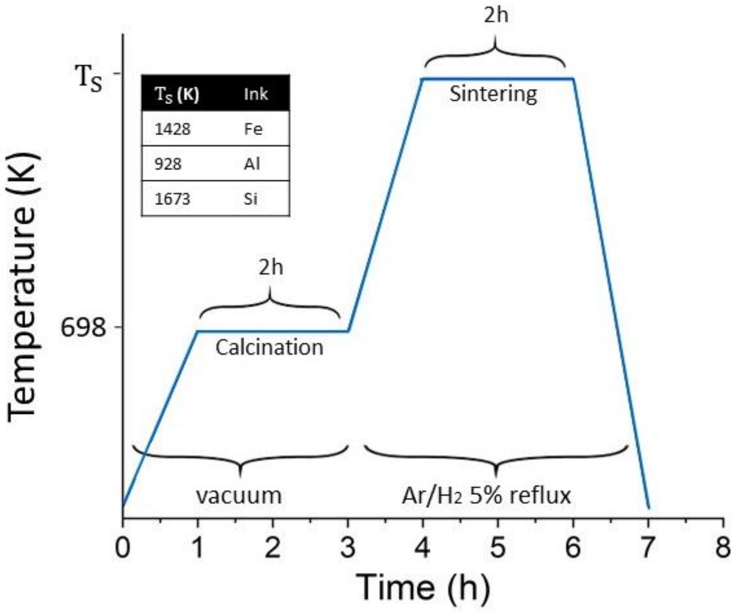

Figure 5.7: Calcination and sintering route used for the printed structures.

To avoid oxidation, the heat treatment is performed in a controlled atmosphere using Ar/H_2(5% H_2 gas). The calcination is carried out under vacuum atmosphere that was previously purged three times by filling with 1 bar of Ar/H_2 gas and then evacuation for 5 min. After the calcination process, a continuous reflux of Ar/H_2 is set to prevent oxidation and the temperature is increased until a sintering temperature (Figure 5.8). After the sintering the furnace is turned off and left cooling down to room temperature. The samples show a layer of surface oxide that can be removed by manual polishing until revealing a pure metallic and shiny surface (confirmed by SEM and EDS).

Figure 5.8: Furnace used for the heat treatments with the reflux system installed.

Figure 5.9 shows the Iron, Aluminium and Silicon printed structures in their as-printed and sintered forms. A successfully sintered Iron structure shows after slight polishing a shiny surface with a perfect structural integrity. The polymer removal makes the structure to shrink reducing its volume around 50%. On the other hand, aluminium and silicon structures were not successfully sintered. In the case of aluminium after the calcination the structure appeared metallic and shiny but after sintering it darkened and aluminium microspheres emerged on the surface. The structural integrity was not appropriate since applying small pressure damaged the structure. This was attributed to the reaction of the aluminium with some remaining carbon content that could be still within the structure. Something similar happened to Silicon structure since, in this case, the equipment available in the laboratory was not capable of reaching the required temperature for silicon sintering. However, since the aim of printing and sintering commercial powders was only to validate the technique and to check the post-heat treatment results, no further work was done.

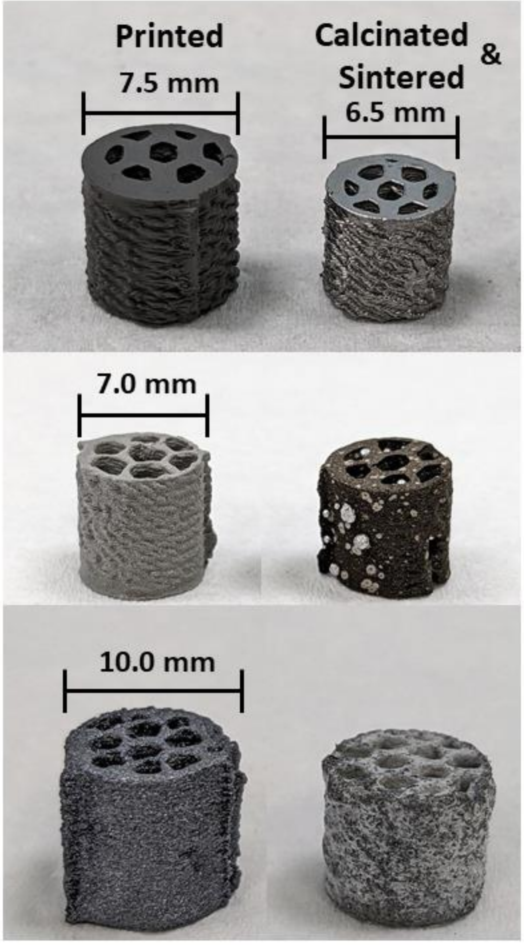

Figure 5.9: Printed and dried structures compared to the same structure after the calcination and sintering route for iron (upper), aluminium (middle) and silicon (lower).

5.1.6. Nickel electrodeposition

Since the metals here engaged in printing are susceptible to oxidation a protection against any corrosion is desirable. To achieve this aim, a coating with a metal may give that chemical stability towards corrosion. The metal to be coated has to be soft magnetic in order to not alter any magnetic properties of the printed metal. Nickel electrodeposition is an easy and useful way of coating the sintered structures. The procedure for this electrodeposition is shown schematically in Figure 5.10.

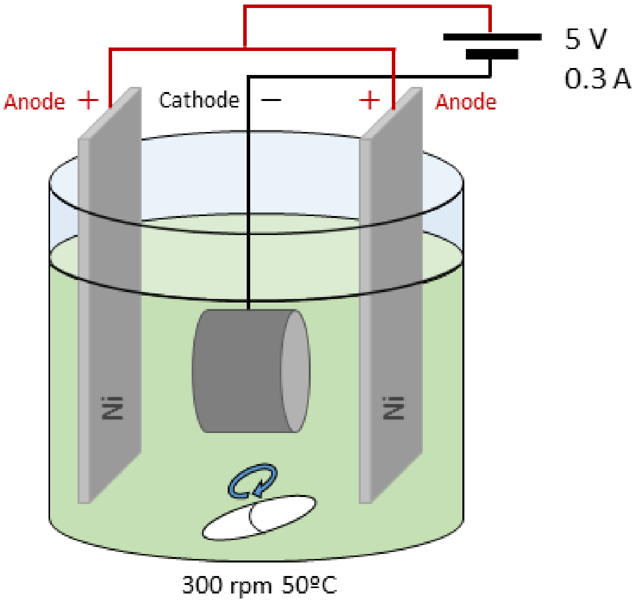

Figure 5.10: Nickel electrodeposition scheme.

Figure 5.11 shows the compasiron for Iron structure in as-printed, sintered and after Nickel electrodeposition to the sintered sample. The calcination and sinetring produces a shrink in the structure, reducing its volume by half, approximately.

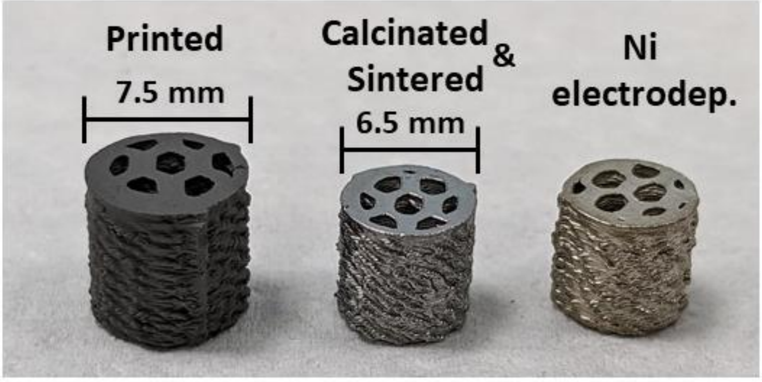

Figure 5.11: Comparison of the printed, sintered and Nickel electrodeposited printed structure with iron-based ink. A shrink occurs after the sintering since the polymer is removed.

5.1.7. SEM characterization: Composition topography

The microstructure and composition of the printed and heat treated samples can be studied by SEM and EDS analyses. First, the polymer removal can be checked by comparing the as-printed structure with the sintered one (Figure 5.12).

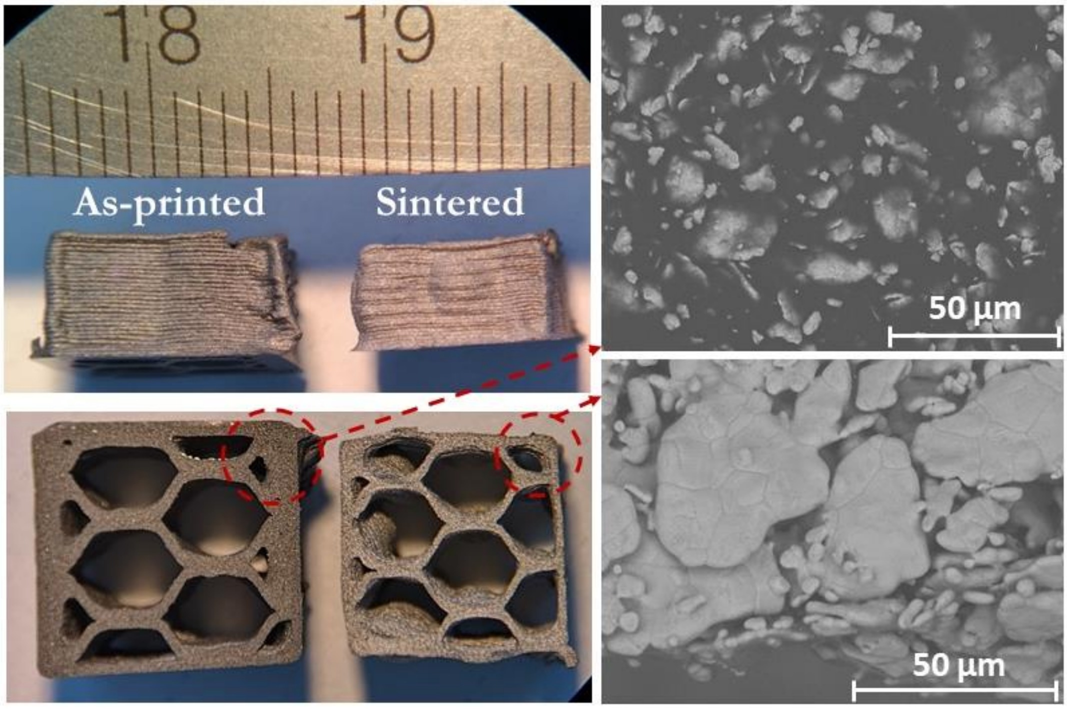

Figure 5.12: Printed and sintered iron structures. SEM images reveal that the as-printed structure has the powder embedded in the polymeric matrix whereas in the sintered state there is no longer polymer and the powder is sintered.

After heat treatments the samples have a thin layer of oxide on the surface that can be removed by polishing. For iron structures, the sintered structure is strong and compact, and after polishing a shiny metallic surface is revealed. Aluminium structures show a clear and shiny surface after the calcination too, but when increasing the temperature to the sintering temperature, the surface turns out darker and the small shiny metallic aluminium spheres appear on the surface. The Silicon structures were not possible to sinter since the higher temperature required for the sintering (around 1680K) resulted in violent explosions of the quartz tubes that the structures were encapsuled in for the heat treatments. Nevertheless, the aim for aluminium and silicon printing was to validate the printing of the low density metals and the sintering route, although those metals are not exactly relevant for the aim of the thesis. For a suface oxide examination, the sintered structures were partially polished and by

EDS analysis the two zones (Zone 1: Not polished, Zone 2: polished) were compared to examinate if the oxide was successfully removed. The compositional map of SEM images is shown for iron, aluminium and silicon in figure 5.13, 5.14 and 5.15, respectively.

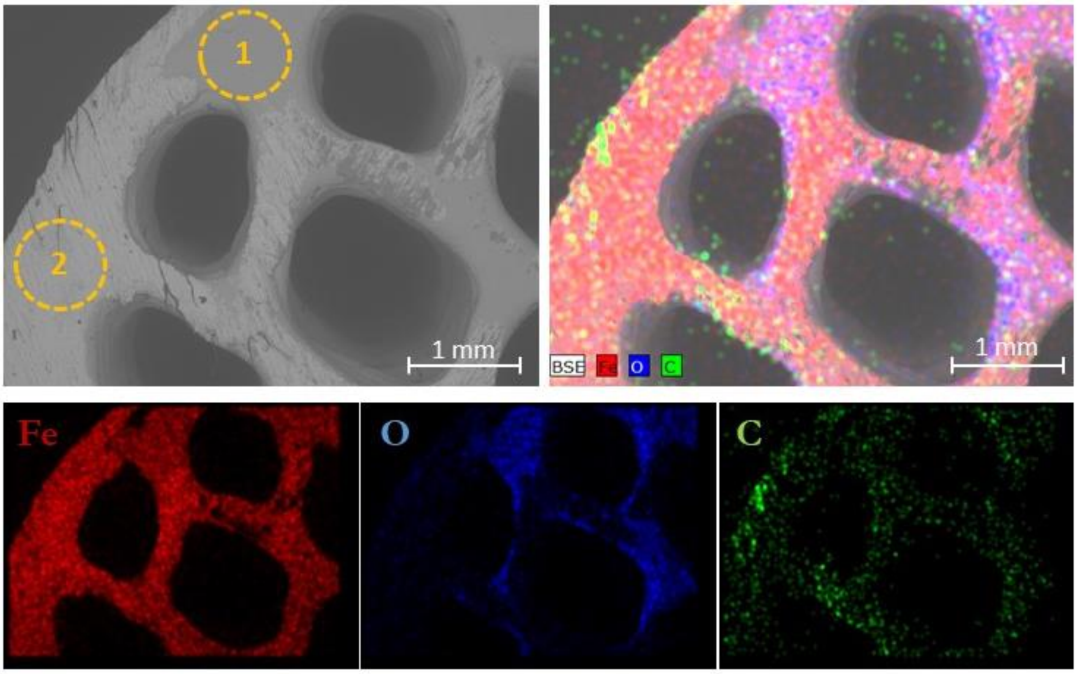

Figure 5.13: Compositional map for iron printed structure. The zone 1 is without any polishing and the zone 2 is after polishing. The compositional map for each element is displayed in the bottom.

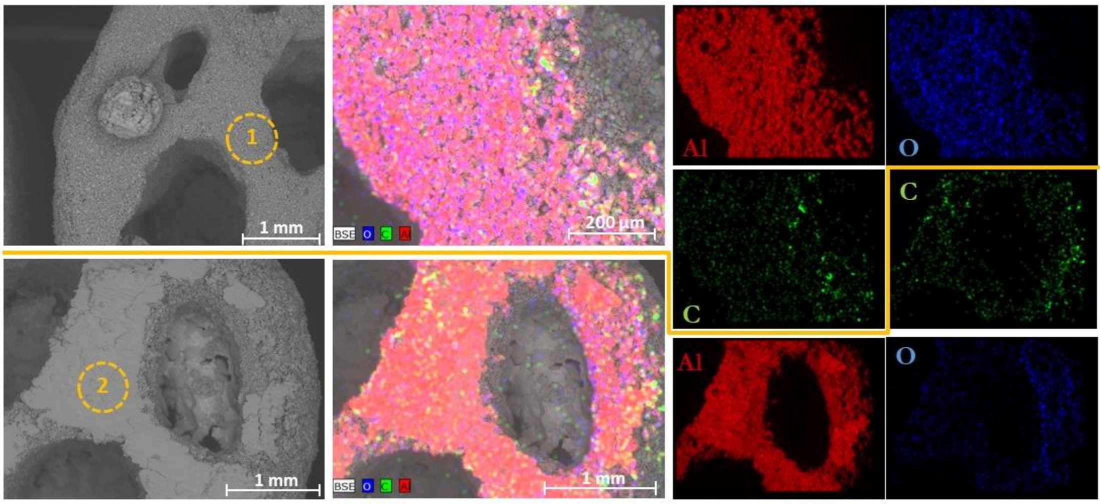

Figure 5.14: Compositional map for aluminium printed and sintered structures with the individual composition map for each element.

Although the Silicon structures were not able to be fully sintered, the EDX analysis was done to a printed piece treated at 1673K for 2h. In this sample (Figure 5.15) the polymer is succesfully removed and the powder is packed together and partially sintered.

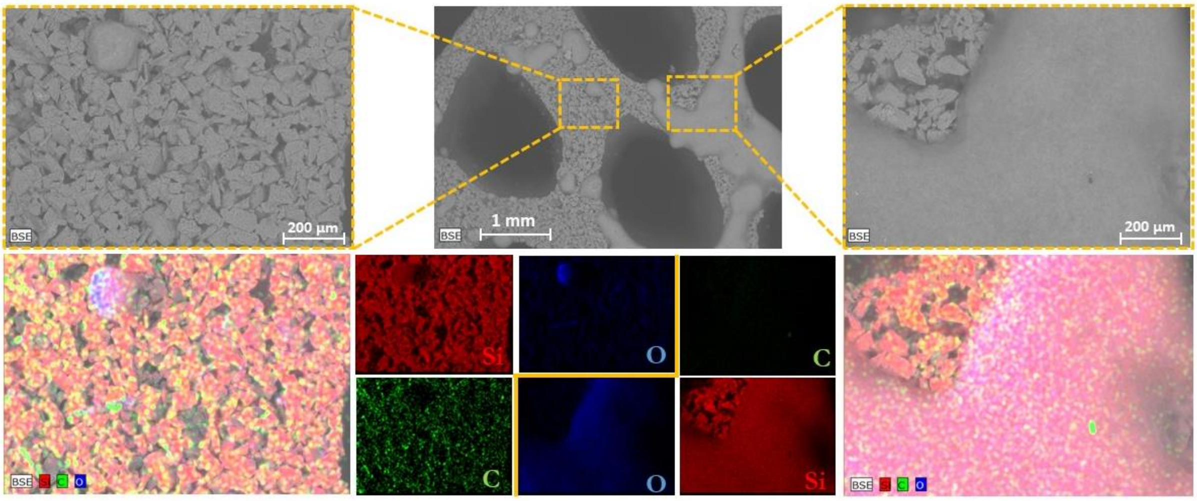

Figure 5.15: Compositional map for silicon printed and half-sintered structures with the individual composition map for each element.

The composition difference between the two zones is shown in table 3. The zone 1 corresponds to the unpolished zone and the Oxygen percentage is high in the three samples confirming that there is an oxide layer after the sintering. However, after some surface polishing the true composition appears with significantly lower percentage of Oxygen confirmng thus that the structures are made of pure metal.

Table 5.3: Composition average for unpolished (zone 1) and polished (zone 2) regions for iron, aluminium and silicon printed and sintered structures.

Material	**Constituent**	**Metal (at.%)**	**C**	**O**
Fe	Zone 1	37	8	55
	Zone 2	75	15	10
Al	Zone 1	37	8	55
	Zone 2	75	15	10
Si	Zone 1	50	7	43
	Zone 2	62	19	19

5.1.8. Mechanical characterization

The printed structures were tested mechanically under compression until failure (compression rate 3×10-4m·s-1) (see Figure 5.16). It is difficult to calculate the stress values, since the structures are not solid and the pores are filling with material during the compression producing the changes in a surface area. For that reason, the force is plotted in Figure 5.17 instead of the stress. Thus, the compression curves can serve only for a qualitative analysis.

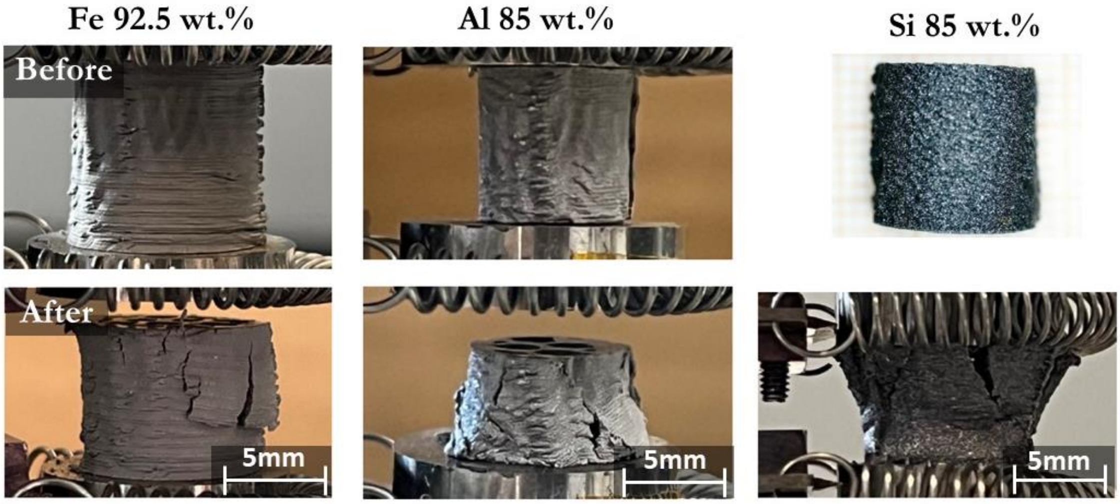

Figure 5.16: Before and after compression in the mechanical test for as-sprinted Iron, Aluminium and Silicon structures.

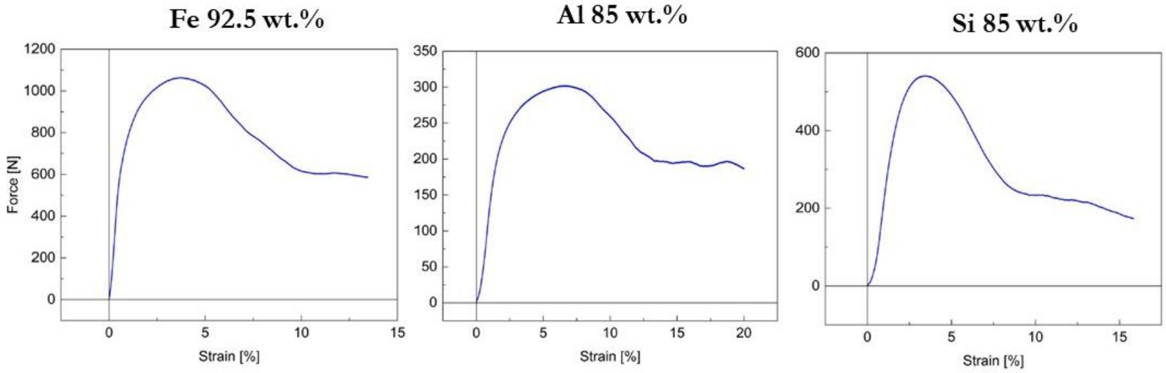

Figure 5.17: Force versus strain curves for each compressed as-printed structure.

Figure 5.17 shows that the Iron structure exhibits the highest ultimate strength of the three samples since its maximum force is 1050N followed by Silicon with 300N and Aluminium with 550N. The sintered Iron structure appreared to be the most strong one, needing around 500kg of weight for reaching the yield point (Figure 5.18).

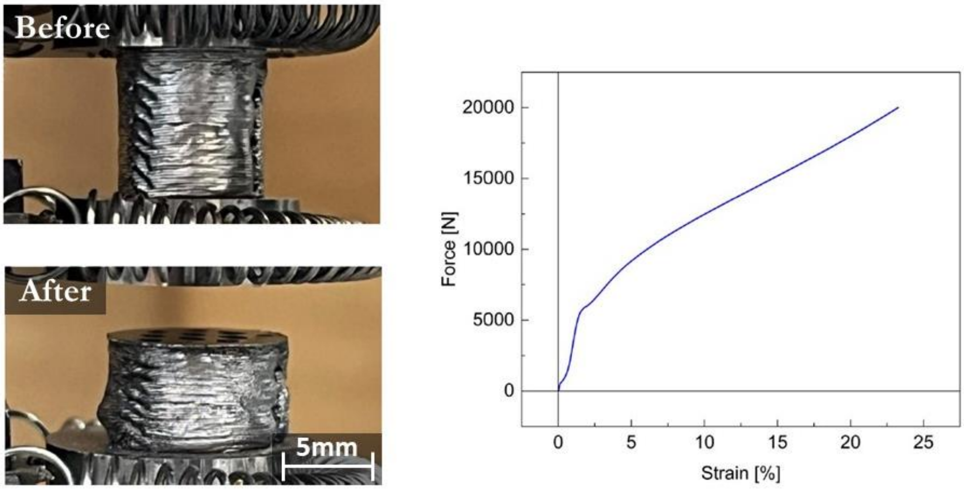

Figure 5.18: Sintered Iron sample before and after mechanical compression until failure (left) and force versus strain curve (right).

5.2. 2D AND 3D PRINTING OF MAGNETOCALORIC HEUSLER-TYPE MMSMAs

5.2.1. Silk-based MCE ink

5.2.1.1.1. Ink preparation and printing tests

A preliminary silk-based ink was prepared to see wheter it was an usable polymer for printing. For this test a 85%wt. ink was prepared using $Ni_{40}Mn_{42.5}Co_7Sn_{9.5}$ powder (see Sec 2.6.2) and mixing it with silk fibroin (dissolved in water at 15% wt.) and adding formic acid. 125mg of powder were mixed with 25mg of fibroin and 0.3ml of formic acid as dissolvent. The components were mixed manually and with the resulting ink a 0.5mm thickness film was prepared using the Doctor Blade ® technique. A PET substrate was used and the film was left drying for 24h at room temperature (Figure 5.19).

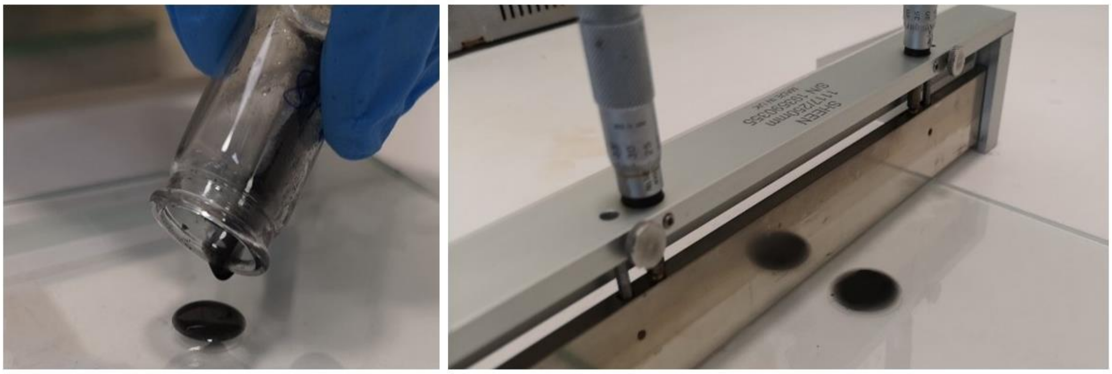

Figure 5.19: Prepared silk-based ink (left) and resulting film prepared by Doctor Blade (right).

5.2.1.1.2. Transformation characteristics and magnetocaloric effect

The as-printed ink was characterized by thermomagetization curves and the magnetocaloric performance was calculated by means of integration the magnetization versus temperature curves using the Maxwell relationship in the same manner as previously (Figure 5.20). Although thermomagnetization curves show maximum magnetization values equivalent to the ones corresponding to the same powder with cellulose ink (see Figure 5.23 right), the magnetic entropy change is about the half that the one corresponding to the cellulose ink (see Figure 5.24 upper right). This detriment of properties is attributed to the formic acid and toghether with the fact that the silk ink is very aqueous, making it not suitable for reaching the viscosity required for 3D printing makes this polymer not suitable for further investigation.

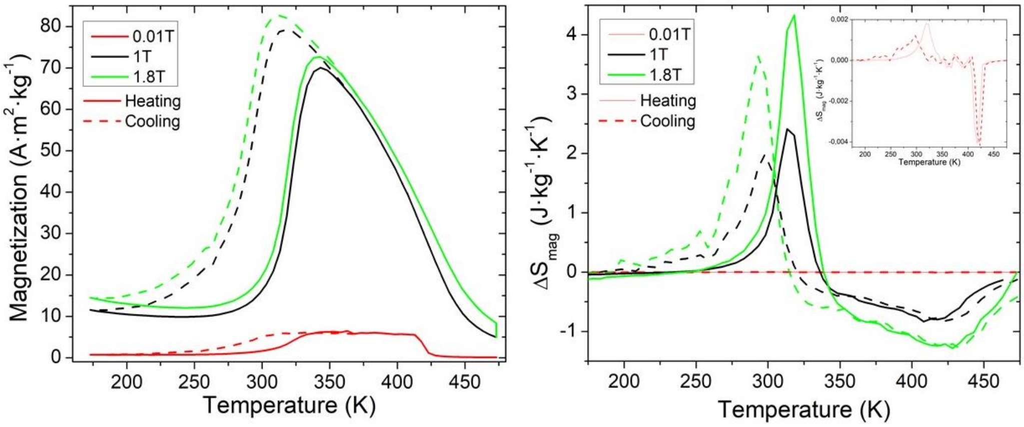

Figure 5.20: Thermomagnetization curves at low and high magnetic fields (left) and magnetic entropy change calculated from thermomagnetization curves (right).

5.2.2. Cellulose-based MCE inks

5.2.1.2.1. Ink parameters

The ink preparation procedure for magnetocaloric powders is the same as in the case of the commercial powders, explained in chapter 2. The cellulose was used also as a polymeric binder for eco-friendliness and for its high processability. In order to avoid any irreversible effects which can occur due to the possible instability of MetaMSMAs at elevated temperatures, the ink must be not overheated above a certain temperature. Being fixed the powder/polymer weight percentage (% wt.) the optimal water quantity has to be find so the viscosity and dryability are the best for printing results. After several inks prepared, the optimal ones are listed in Table 5.4. Table 5.5 shows the results for dried inks.

Table 5.4: Selected magnetocaloric inks for printing, with the proportion of each constituent in mass and volume percentage.

Ink	Constituent	Density (g/ml)	Mass fraction (%)	Volume fraction (%)
Ink 1 NiMnCoSn 85% wt.	$Ni_{40}Mn_{42.5}Co_7Sn_{9.5}$ powder ($\phi \leq 38\ \mu m$)	8.0	62	14
	Deionized water	1.0	22	48
	HPC	0.5	6	38
	Total	2.4	100	100
Ink 2 NiMnCoSn 92.5% wt.	$Ni_{40}Mn_{42.5}Co_7Sn_{9.5}$ powder ($\phi \leq 106\ \mu m$)	8.0	72	21
	Deionized water	1.0	22	51
	HPC	0.5	6	28
	Total	2.6	100	100
Comments:				
Ink 3 NiMnSn 95% wt.	$Ni_{49.8}Mn_{36.6}Sn_{13.6}$ powder ($\phi \leq 20\ \mu m$)	8.0	82	34
	Deionized water	1.0	14	43
	HPC	0.5	4	28
	Total	2.8	100	100

Table 5.5: Selected magnetocaloric inks in dried form with the proportion of polymer/powder in mass and in volume.

Ink	Constituent	Density (g/ml)	Mass fraction (%)	Volume fraction (%)
Ink 1 NiMnCoSn 85% wt.	$Ni_{40}Mn_{42.5}Co_{7}Sn_{9.5}$ powder ($\phi \leq 38\ \mu m$)	8.0	85	27
	HPC	0.5	15	73
	Total	2.4	100	100
Ink 2 NiMnCoSn 92.5% wt.	$Ni_{40}Mn_{42.5}Co_{7}Sn_{9.5}$ powder ($\phi \leq 106\ \mu m$)	8.0	92.5	44
	HPC	0.5	7.5	56
	Total	2.4	100	100
Ink 3 NiMnSn 95% wt.	$Ni_{49.8}Mn_{36.6}Sn_{13.6}$ powder ($\phi \leq 20\ \mu m$)	8.0	95	55
	HPC	0.5	5	45
	Total	2.4	100	100

5.2.3. Screen-printing of $Ni_{40}Mn_{42.5}Co_{7}Sn_{9.5}$ magnetocaloric ink

5.2.3.1. Printing tests

Cellulose-based magnetocaloric inks were first tested with screen-printing technique, once a route was already elaborated previously with commercial inks. The same 18 x 6 mm chips were printed applying 10 layers of material into the PET substrate with corona treatment, in the same way as in the case of iron ink, to increase the magnetic content. To modify the surface tension of the ink and improve its wettability, the surface active agent BYK-348 was added in a proportion of 5 µl/ml. The ink used for this test was the first ink of Table 5.4 with 85 wt% of metallic content. Magnetic orientation was induced placing a permanent magnet beneath the substrate so the powder within the ink orients with the magnetic field before the ink is dried (Figure 5.1). The use of the magnetic field to align the particles along the easy-axis was shown in Refs. [3] [4] to be an efficient tool to enhance the magnetocaloric effect.

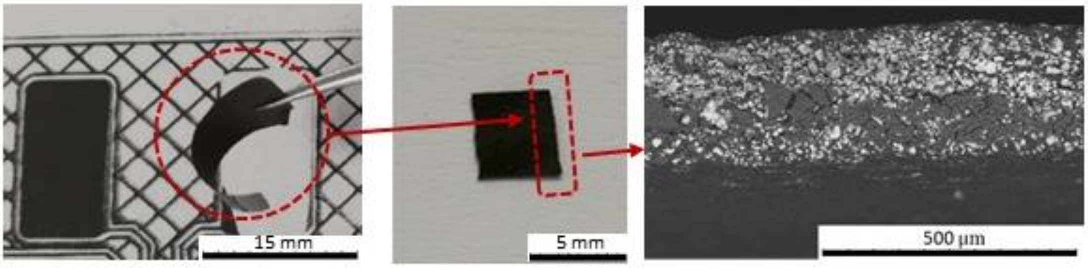

Figure 5.21: Printed magnetocaloric chips, cut in square shape and SEM image of the edge of the square.

Finally, the obtained multi-layered samples with dimensions of 16 mm × 8 mm x 250 µm, depicted in Figure 5.21, were separated from the substrate and cut into square-like or round-shaped samples for magnetic and magnetocaloric measurements. Scanning electron microscopy (SEM) image of the sample cross-section is shown in Figure 5.21(right) demonstrating the homogeneous distribution of the particles.

5.2.3.2. Magnetic anysotropy in printed samples

The printed chip-like samples were cured under applied magnetic field (Figure 5.1 right), preventing a random agglomeration of particles and resulting in their chain-like oriented distribution in the sample, as it can be observed in Figure 5.22, left. Evaluating the influence of the external magnetic field on the printed ink during drying process, it can be observed a remarkable magnetic anisotropy effect revealed by M(H) curves in Figure 5.22 (right) measured at the room temperature with the field applied along the particles orientation direction (red circles) and perpendicular to it (black circles). When the magnetic field is applied in parallel to the particles orientation direction, the saturation state is reached at ~0.34 T, this value increases up to ~0.56 T when the field is applied perpendicularly, indicating that the external field applied during the fabrication of the printed samples favors the saturation magnetization at lower magnetic fields. However, since the powder is oriented at the room temperature, i.e., in the cubic austenitic phase with a small magnetocrystalline anisotropy, the anisotropy effect in Figure 5.22(right) can be attributed to the magnetic shape anisotropy. Thus, the chain-like configuration of particles gives rise to the shape anisotropy effect in the printed ink

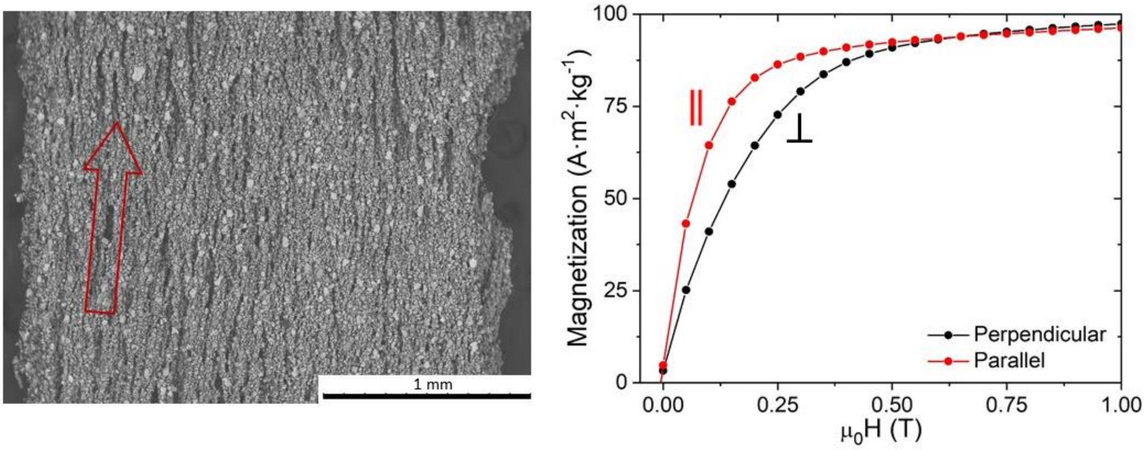

Figure 5.22: Detail of the surface of the printed chip where consistent orientation with the magnetic field (red arrow) can be seen (left) and magnetization versus magnetic field curves.

5.2.3.3. "Magnetic field – temperature" phase diagrams of martensitic transformation

The thermomagnetization curves, M(*T*,H), for the printed samples recorded under different magnetic fields are shown in Figure 5.23 together with the data for the ribbons from which this powder was prepared from. Figure 5.23 shows magnetic field effect on MT, typical for MetaMSMAs, which manifests itself in a displacement of the MT hysteresis loop towards low temperatures (Ref. [5] and references therein) owing to the stabilization of the high magnetization austenitic phase. A thermal hysteresis of MT slowly increases with the applied magnetic field. The values of T_M and T_A, extracted from the M(T,H) curves by the derivative method, are plotted in the inset of Figure 5.19 as a function of the magnetic field. The dependences $T_M(H)$ and $T_A(H)$ in the inset can be well approximated by the linear fits representing the phase diagrams of MT for both samples. Using these data, the magnetic field induced shift of the MT temperature has been estimated according to expression $dT_0/d(\mu_0H)$, where $T_0 = (T_M + T_A)/2$ is defined as an equilibrium temperature of MT. The values of this shift are collected in Table 5.6 for both HT ribbon and printed samples.

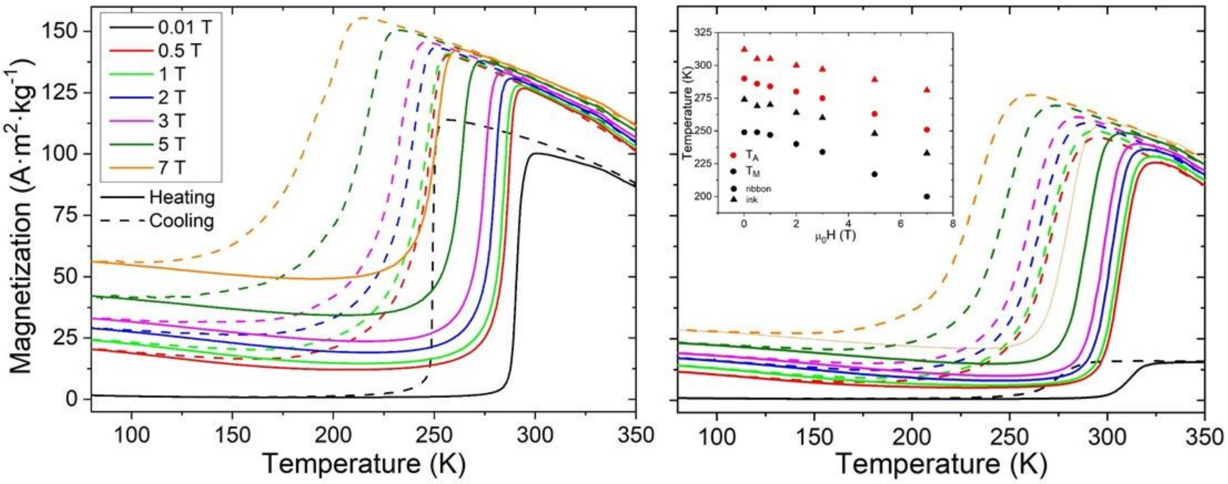

Figure 5.23 Thermomagnetization curves at different applied magnetic fields for HT ribbon (left) and printed sample (right). The inset depicts the dependences of the transformation temperatures as a function of the magnetic field.

Table 5.6: Characteristic temperatures of the forward, T_M, and reverse, T_A, MT and Curie temperature of austenite, T_{CA}, obtained by the derivative method using the M(T) curves in Figure 3.3 and 4.3. The values of magnetic field induced shift of the equilibrium MT temperature, $T_0 = (T_M + T_A)/2$, are also shown.

Sample	**T_{CA} (K)**	**T_M (K)**	**T_A (K)**	**$dT_0/d(\mu_0H)$ K/T**
As-spun ibbon	408	218	284	-
HT ribbon	413	263	293	-6.3 (0.2)
As-ground powder	423	291	309	-
Printed ink	-	274	312	-4.8 (0.2)

According to the M(T,H) curves in Figure 5.23, the maximum magnetization values obtained for the printed samples are lower than the ones observed in the HT ribbon. This is because the printed sample is a composite consisting of the magnetocaloric powder (85 wt%) and the polymer binder (15 wt%), resulting in a magnetization value proportional to the magnetic powder content (150 A·m²/kg versus 124 A·m²/kg at highest field, see Figure 5.23).

It can be noticed in Figure 5.23 a somewhat different character of MT and the magnetic field influence on it in the ribbon and printed samples, which is reminiscent to the difference in the behaviour of MT in $Ni_{45}Mn_{36.7}In_{13.3}Co_{5}$ (at%) MetaMSMA prepared in as-quenched and slow cooled states (Ref. [6] and references therein). According to Ref.[6] this variation can be explained by the different degree of atomic order driving different mechanisms of MT, such as the magnetoelastic or pure magnetic ones. Due to the existence of these mechanisms, the shift of T_0 under magnetic field in the case of pure magnetic nature of MT should be essentially larger than in the case of the magnetoelastic MT [6], which is explicitly observed in the present work (see Table 5.6) leading to a conclusion that the quenching rate used in the present work is faster for the powder (less ordered atomic state) than for the ribbon (more ordered state). The aforementioned difference in the behaviour of MT in the ribbon and powder, including under magnetic field, is an interesting result found for the first time in NiMnSn-type MetaMSMA which needs to be further explored.

The value of the field induced shift of MT temperature for printed samples, equal to -4.8 K/T (Table 5.6), is comparable with the highest values known for MetaMSMAs from the literature (Ref. [7] and references therein). Large value of $dT_0/d(\mu_0 H)$ is one of the parameters facilitating a large magnetocaloric effect at lower values of the magnetic field.

5.2.3.4. Magnetocaloric effect

5.2.2.3.1. Magnetic field induced entropy change

Conventional and inverse magnetocaloric effects are characterized by the isothermal entropy change, $\Delta S_m(T, H)$, and/or by the adiabatic temperature change, $\Delta T_{ad}(T, H)$, when a magnetic field is applied or removed in isothermal or adiabatic conditions, respectively [8,9]. In the most easiest way, the magnetic field induced entropy change can be estimated from a thermodynamic Maxwell relationship [10], although in the case of the first-order magnetostructural transformations some issues should be taken into account [7,11]. Commonly, the thermomagnetic curves measured in the isofield condition, such as shown in Figure 5.23, are used for the calculation of $\Delta S_m(T, H)$ by numerical approximation of the Maxwell relationship (see, e.g., Refs. [9,10,12]):

$$\Delta S_m(T,H) = S_m(T,H) - S_m(T,0) = \int_0^H \left(\frac{\partial M(T,H')}{\partial T}\right) dH'$$

Figure 5.24 (upper left and right) depicts the ΔS_m(T, H) plots calculated by using heating and cooling data from Figure 5.24 for both HT ribbon and printed ink. The curves exhibit a maximum, $\Delta S_{m,max}$, associated to the inverse MCE due to the magnetic field-induced MT. The shifts of maximums to lower temperatures under increasing magnetic field corroborate the dependences of T_A(H) (see the inset of Figure 5.23, right).

The value of $\Delta S_{m,max} \approx$ 50 J/kgK for the HT ribbon is obtained from the analysis of heating M(T,H) curves at $\mu_0\Delta H$ = 5 T and 7 T, whereas for the printed ink under same conditions this value is about 25 J/ kgK and 30 J/kgK, respectively (Figure 5.24 (upper left, right)). As expected, the printed samples show lower values due to the dilution of the magnetocaloric material in the HPC polymer matrix, resulting in the smaller difference in magnetization between the martensite and austenite phases at MT and less sharp transformation front if compared with the ribbon. Also, the $\Delta S_{m,max}$ values obtained from the cooling M(T) curves are lower than those obtained from the heating ones due to the more smeared character of the forward MT in comparison with the reverse MT. For example, heating curves at $\mu_0\Delta H$= 2 T yield the $\Delta S_{m,max} \approx$ 25 J/kgK for the ribbon and 10 J/kgK for the printed samples. These values fall down to 11 J/kgK and 7 J/kgK, respectively, for cooling curves at the same field.

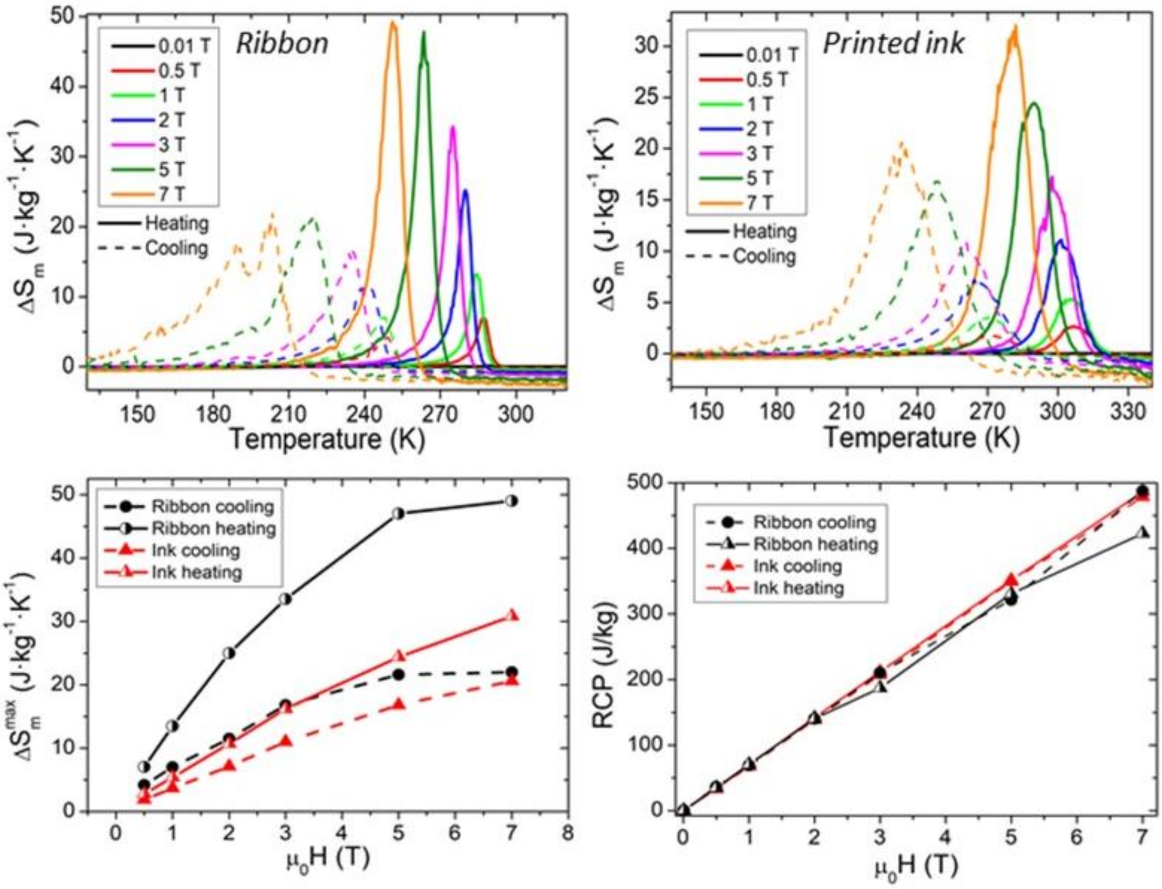

Figure 5.24 Temperature dependence of the magnetic entropy change under different applied magnetic fields in the HT ribbon (upper left) and in the printed ink (upper right). Magnetic field dependence of the maximum entropy change (bottom left); and the relative cooling power associated with the magnetic field induced reverse MT (bottom right).

Noteworthy, the values of $\Delta S_{m,max}$ for the printed samples obtained in the present work are comparable to those for the well-known magnetocaloric materials under the same field change, e.g., ~18.5 J/kgK for $Gd_5(Si_2Ge_2)$ [13],~19.4 J/kgK for $LaFe_{11.4}Si_{1.6}$[14], ~25.0 J/kgK for $Ni_{36.5}Co_{13.5}Mn_{35}Ti_{15}$ [15] or ~25.0 J/ kgK for $Ni_2Mn_{1.4}Sn_{0.6}$ [16].

Figure 5.24 bottom left shows dependences of $\Delta S_{m,max}$ as a function of the applied field. These dependences demonstrate a well pronounced convex character for the ribbon and a slight convex behavior for the ink indicating in both cases a trend towards an existence of maximum at higher fields, in agreement with Ref. [17]. Another parameter characterizing MCE is a relative cooling power (RCP), which is associated to the heat exchange efficiency between the material and its environment. The RCP was estimated by the numerical integration of the area under the ΔS_{mag} (T) curves with integration limits at a full half width maximum by the method proposed by Gschneidner et.al. [18]. The magnetic field dependence of RCP is represented in Figure 5.24 bottom right. Interestingly, this dependence shows a linear behavior coincident for all the data in Figure 5.24 upper left and right, which is a result of the broadening of the ΔS_m(T) peaks for the printed inks, compensating a reduction of their maximums. The values of RCP obtained in this work are in line with those reported for Ni(Co)MnSn ribbons [18]. To summarize, the analysis of the M(T,H) and ΔS_m(T,H) dependences reveals that the printed magnetocaloric ink shows a comparable performance with the HT ribbon, if the dilution and interface effects in the printed sample is taken into account. In terms of RCP, both ribbon and ink show almost identical behavior. Further characterization of MCE is provided in the next section.

5.2.2.3.2. Adiabatic magnetocaloric effect

The adiabatic temperature change, ΔT_{ad}, was measured by the instant removal of a samples from the constant magnetic field of 1.96 T produced by the electromagnet. These measurements have been performed at constant temperatures during step-wise cooling from 310 K to 240 K. The results are presented in Figure 5.25. Figure 5.25 shows that the position of the peak is observed close to 268 K for the HT ribbon and at about 273 K for the printed ink with the maximum values of ΔT_{ad} = 1.1 K and 1.0 K, respectively. The peak positions in both cases are very close to the T_M values from Table 5.6. The ribbon and ink show a defined peak of the inverse magnetocaloric effect (positive ΔT_{ad}(T) values resulting from the removal of the magnetic field) in the vicinity of the forward MT when the material transforms from a ferromagnetic austenite to a weak magnetic martensitic phase.

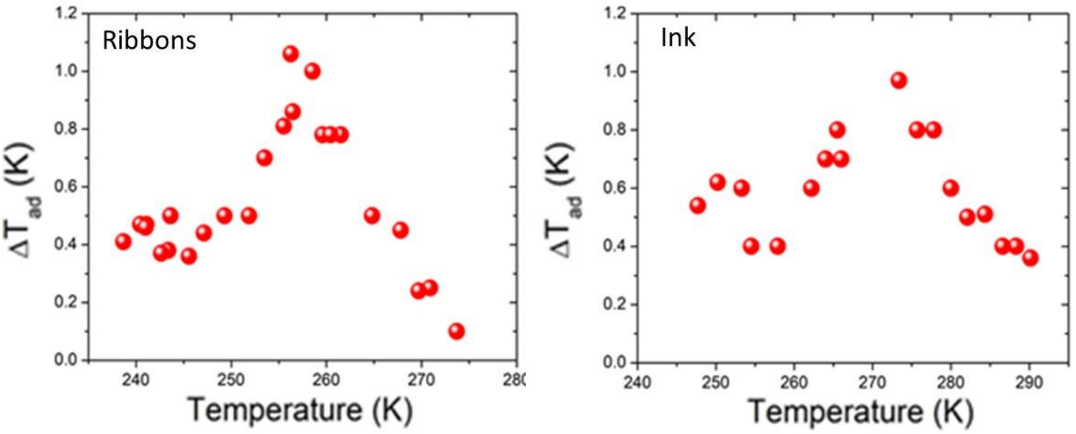

Figure 5.25: Adiabatic temperature change as function of temperature for HT ribbon (left) and printed ink (right) directly measured after rapid removal of a sample from the magnetic field of 1.96 T.

The results of Section 5.2.3.4. show that the net parameters of the MCE behaviour of the MetaMSMA observed in its ribbon form can be reproduced in the ink, which is one of the most remarkable outcomes of the first test of printing magnetocaloric powdered material.

5.2.4. 3D extrusion printing of magnetocaloric inks

5.2.4.1. $Mn_{42.5}Ni_{40}Co_{7}Sn_{9.5}$

5.2.3.1.1. Printing

Having validated that the magnetocaloroic powders are suitable for additive manufactuirng printing, retaining the magnetocaloric properties in the previous section, the next step is to 3D-print magnetocaloric structures with the extrusion printer used for before commercial powders, now with the technique refined. Since we learned that powder/polymer volume fraction has to be near 50/50, the ink used for screen-prinitng was modified by increasing the powder weight fraction from 85% wt. to 92.5% wt. (Table 5.4 and 5.5, Ink 2). Since the maximum quantity that can be prepared using the route for obtaining powder from grinding ribbons is few grams, with this material we are limited to print small structures, which are enough for validating the technique (see Figure 5.26).

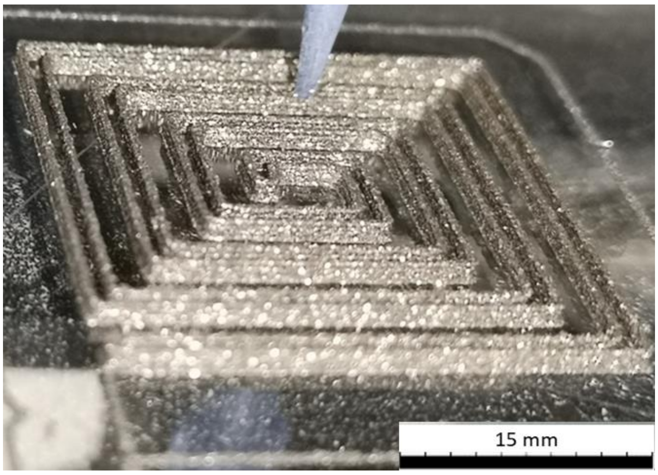

Figure 5.26: Printed structure using the magnetocaloric ink.

5.2.4.1.2. Microstructure and composition analysis

The printed structure is analyzed with the SEM for checking its homogeneity and the composition map is obtained by EDX measurement (Figure 5.27). SEM image for the as-printed structure shows the powder embedded in the polymeric matrix (dark colour). The compositional analysis for the polymer shows that the Carbon and Oxygen concentration is high, confirming this is the polymer. For the powder different element concentration can be seen corresponding to the stoichiometry of the alloy.

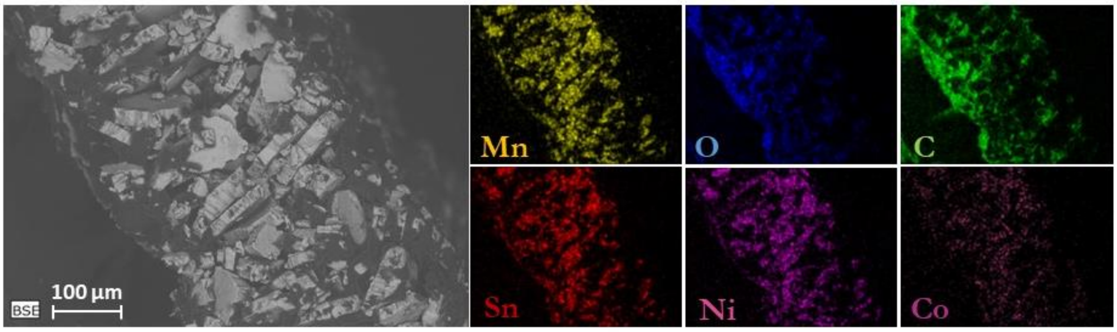

Figure 5.27: Edge of the printed structure showing how the powder is homogeneously distributed and embedded into the polymeric matrix along the thickness (left) and composition map for each element (right).

5.2.4.1.3. Calcination and sintering: Transformation characteristics

A systematic study of the magnetic properties of the printed structure is performed in each processing step and compared one to each other. Figure 5.28 shows various magnetization versus temperature curves where the evolution of magnetic properties is displayed. The as-printed structure shows around 15% less maximum magnetization than the powder itself (12.8 $A·m^2·kg^{-1}$ vs 10.7 $A·m^2·kg^{-1}$, in Figure 5.28) since the printed structure contains polymer resulting in a magnetization value proportional to the magnetic powder content. After the calcination at 698 K for 2 h the hysteresis increases but the maximum magnetization remains almost unaltered. However, after the calcination the martensitic tranformation is lost. A systematic study of magnetic properties was performed at various sintering temperatures from 1173 K to 1323 K, with same conditions combining vacuum for calcination and Ar/H_2 5% reflux during the sintering. However, the martesitic tranformation was lost in every sintering trial (Figures 5.28, 5.29).

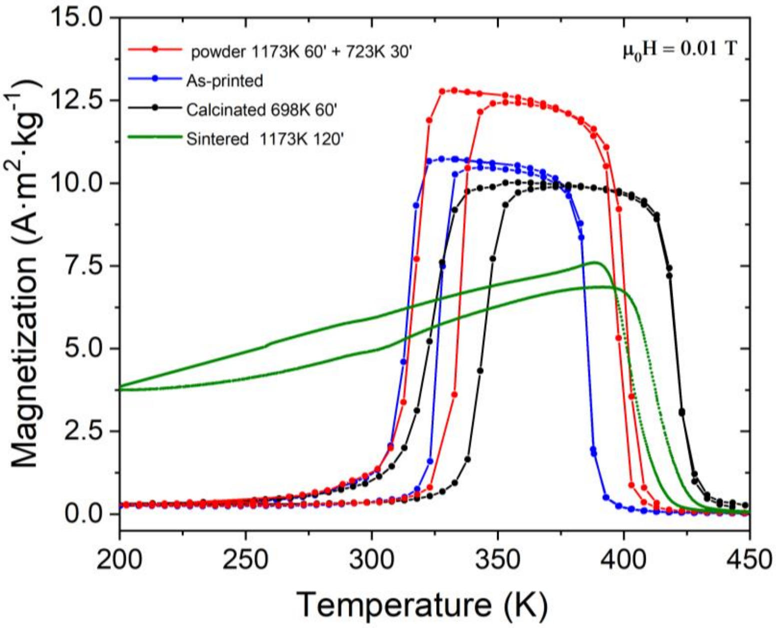

Figure 5.28: Magnetization versus temperature curves for each printing and processing step.

Sintered sample was analyzed by EDX to the sintered sample of Figure 5.27 (see Figure 5.30). The SEM image shows the polymer is no longer in the structure and that in the edge there are segregated filaments of material. EDX analysis reveals these filaments are made of Manganese oxide that is also fund in every surface of the structure (Table 5.7), confirming that the alloy stoichiometry is changed. There is manganese oxide difussion on the surface. On the other hand, the sintering was not complete due to the absense of bottleneck formation between powder particles. The bigger the powder the less full sintering.

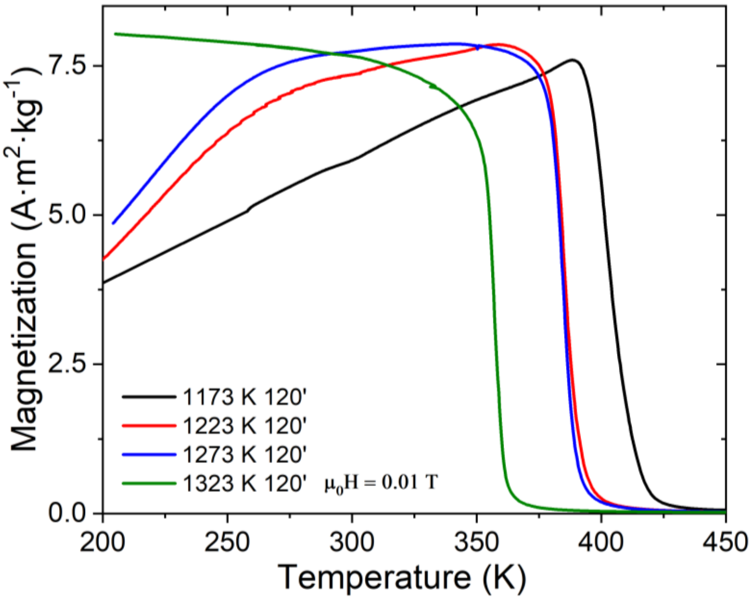

Figure 5.29: Sintering temperature effect to magnetic properties. The martensitic transformation is lost after sintering for all the temperatures tested.

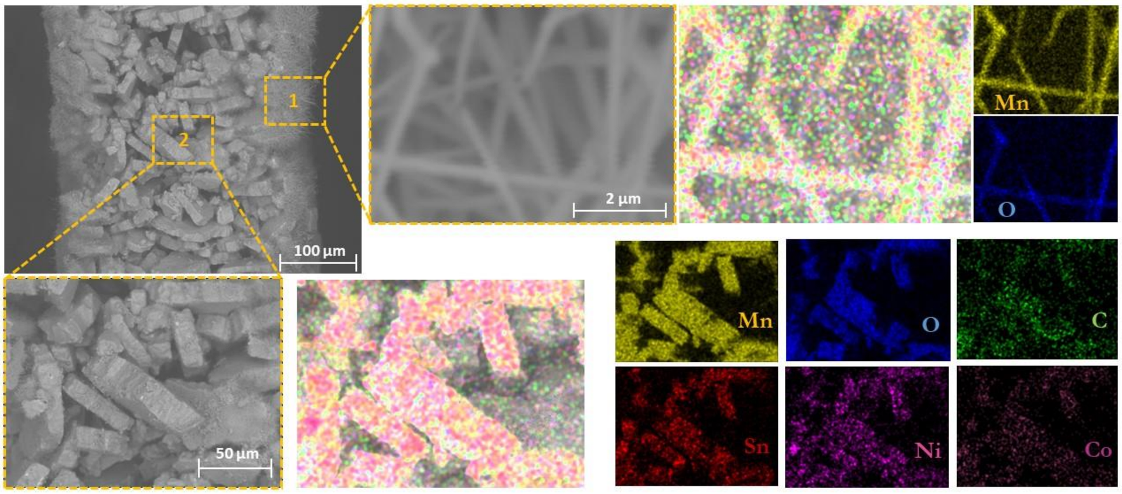

Figure 5.30: Printed piece calcinated / sintered at 1273 K for 120 minutes under Argon plus Hydrogen at 5%. Some filaments are formed in the surface of the structure and compositional map reveals that these filaments are composed by the Manganese oxide.

Table 5.7: Compositional analysis of sintered sample in the outer edge and inner part of it.

Zone	Ni (at%.)	Mn(at%.)	Co (at%.)	Sn (at%.)	C (at%.)	O (at%.)
1	0	45	0	0	15	40
2	3	38	0	1	10	49

We conclude that for this material it is difficult to retain the magnetocaloric properties after the sintering. The main reason, which we assume, is because a high surface to volume ratio of the printed structure had a significant effect in favoring the magnanese oxidation which changes significantly the composition. Nevertheless, the printing technique can be validated from a magnetocaloric point of view, without taking into account the sintering. For this purpose, as-printed sampel was taken and the magnetocaloric performance was evaluated in the same manner as it was done fot the screen-printed chips.

5.2.3.1.4. Magnetocaloric effect

The real performance of a magnetoicaloric material has to be examined at high magnetic field (around 2 T). The thermomagnetization curves for each printing stage is shown in Figure 5.31.

The magentic entropy was calculated with the Maxwell relationship and direct adiabatic temperature change measurement was performed to the as-spun ribbon and the printed material.

Thermomagnetization curves show that the maximum magnetization is reduced in each printing step and the hysteresis increases slightly. Nevertheless, since the as-printed sample contains heat treated powder, the magnetic entropy change and the adiabatic temperature change are higher for the as-printed samples compared to the as-spun ribbons as Figures 5.32 and 5.33 show.

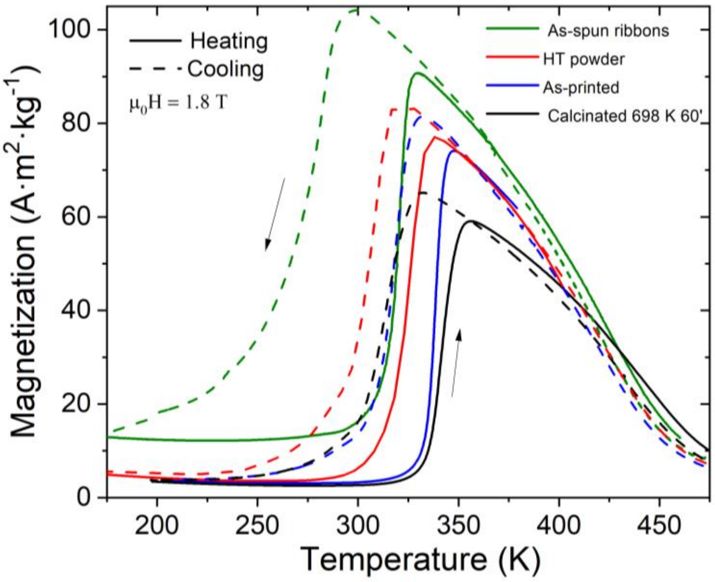

Figure 5.31: Thermomagnetization curves at 1.8 T for as-spun ribbons, heat treated powder, as-printed structure and calcinated structure.

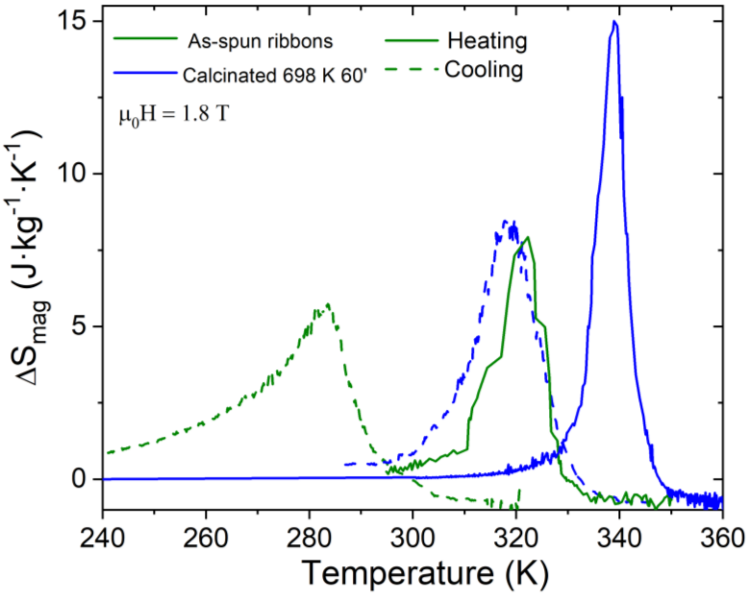

Figure 5.32: Entropy versus temperature calculated from thermomagnetization curves.

From these results we can conclude that printing the powder obtained from ribbons provide printed structures that keep well the magnetocaloric properties. However, it was not posible to get around 100% metallic structures since the sintering process degrades the material significantly due to the high surface-to-volume ratio of the structures that could be printed with the small amount of the material available.

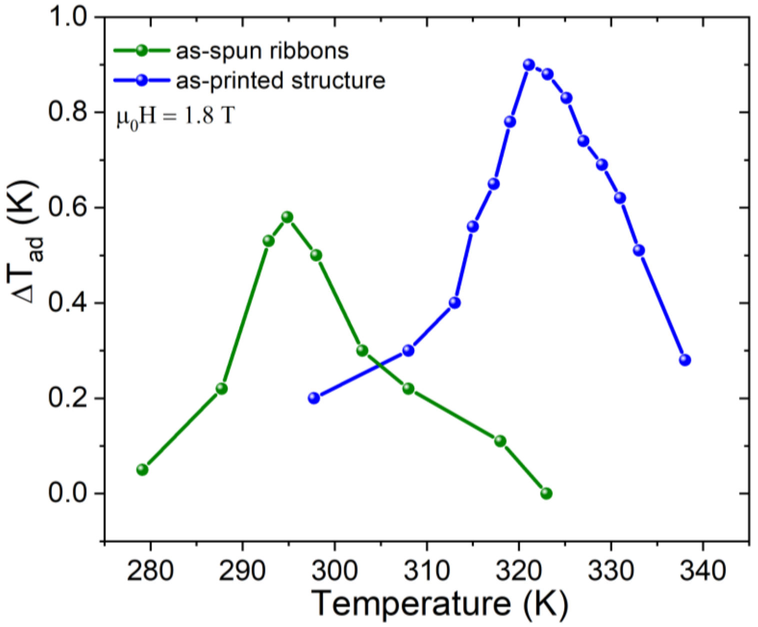

Figure 5.33: Adiabatic temperature change measurement for as-spun ribbons and as-printed sample.

The low scale at which this kind of powder is obtained in the laboratory (few grams) does not allow to make a lot of printing tests neither to print solid enough structures. Nevertheless, the next powder used for printing was available in hundreds of grams and with that one we could further develop a pritinting technique and perform characterization.

5.2.4.2. $Ni_{49.8}Mn_{36.6}Sn_{13.6}$

5.2.4.2.1. Printing tests

The second 3D-printed alloy was the NiMnSn powder obtained by gas atomization as described in Sec 2.4.3. In this case, the quantity of powder available was few hundreds grams, so a lot of tests were possible to be done and large pieces were printed. Also, since the powder size is below 20µm, better results after sintering treatment could be expected. Various inks were prepared at 95% wt. and the selected one for being the optimal one was the one shown in tables 5.4 and 5.5. The water quantity was varied from 8%wt. to 20%wt. (35%Vol. to 55%Vol.) and the optimal one was found out to be 14% wt. or 43%Vol. The honeycomb-like structures that were printed with the commerical powder (Figures 5.4, 5.5 and 5.6) were printed with this ink and the results are shown in Figure 5.34.

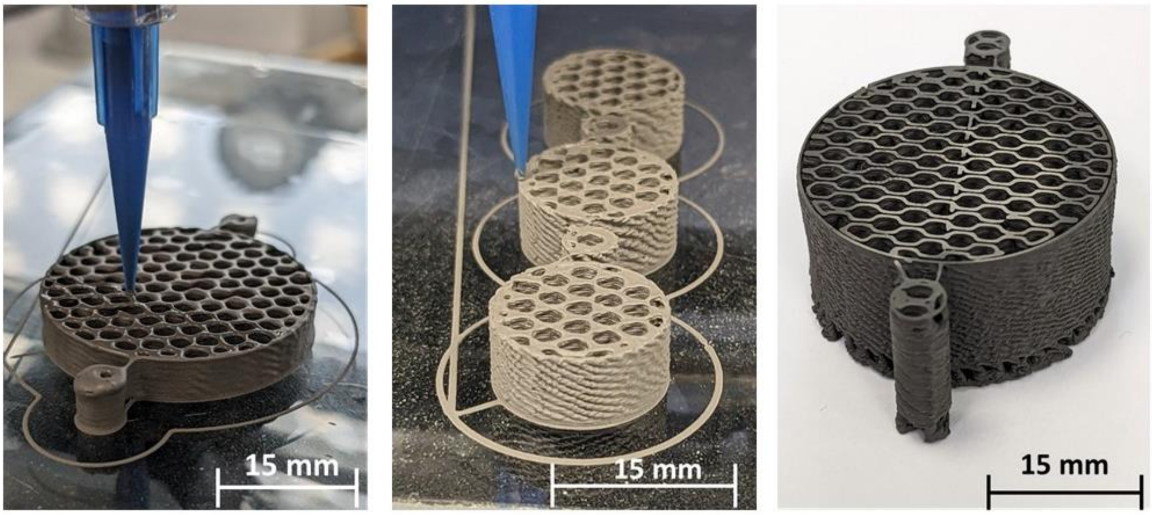

Figure 5.34: Ni-Mn-Sn Printed structures. The printing quality and resolution is the best among all the printings.

5.2.4.2.2. Calcination and sintering

The calcination and sintering route followed was the same as the one performed previously. The calcination was done for 2 hours under continous vaccum, with the vacuum pump connected to the chamber where the sample is placed. For sintering, a continous reflux is set, using a mix of Argon and Hydrogen at 5% of H_2. The sintering time was bewteen 2 and 2.5 hours, depending on the temperature. The same systematic study of sintering temperature effect followed by in the previous material was used here, in a search for a balance between magnetic properties and mechanical integrity. Good mechanical properties were pursued while keeping the magnetocaloric properties or at least minimising any possible degradation.

5.2.3.2.3. Microstructure analysis

By SEM analysis, the heat treatment effect can be seen to check whether the sintering was succesful or not. By visual inspection, samples treated below 1273K (1000ºC) were not completely sintered, since applying some pressure by hand damaged the sample. SEM analysis revealed that bottle neck formation between powder particles was not achieved for treatments below 1273K (Figure 5.35 and 5.36).

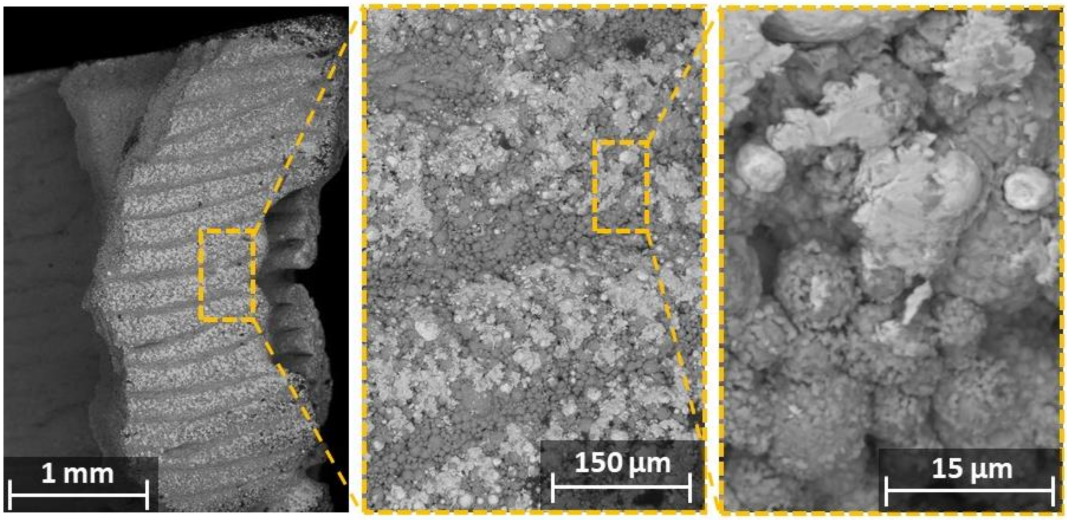

Figure 5.35: Morphology of the Printed sample sintered at 1198K (925°C). The bottle neck formation is not complete resulting in a poor structural integrity.

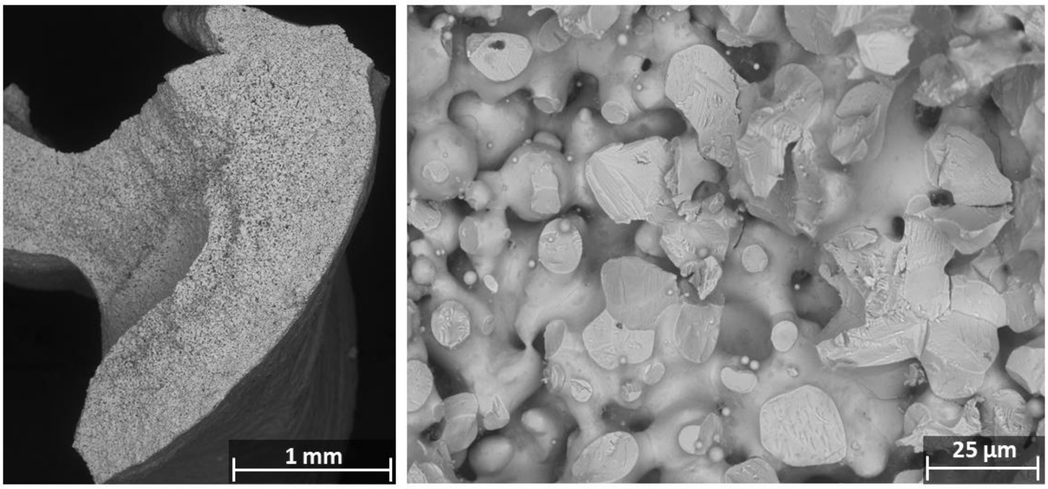

Figure 5.36: Printed structure sintered at 1273K (1000°C) revealed in detail by SEM imaging. The bottleneck formation is complete and the structural integrity is high.

5.2.3.2.4. Transformation characteristics

Thermomagnetization curves gives the first sight of how heat treatments affect the magnetic properties of the material. The magnetic field suitable for any application is around 2T so the analysis will be done at this magnetic field (see Figure 5.37). From Figure 5.37 it can be seen that the maximum magnetization decreases with increasing sintering temperature. Nevertheless, since the goal is to have a balance between structural integrity and magnetic properties, the minimum temperature for which the structural integrity is appropriate is 1273K.

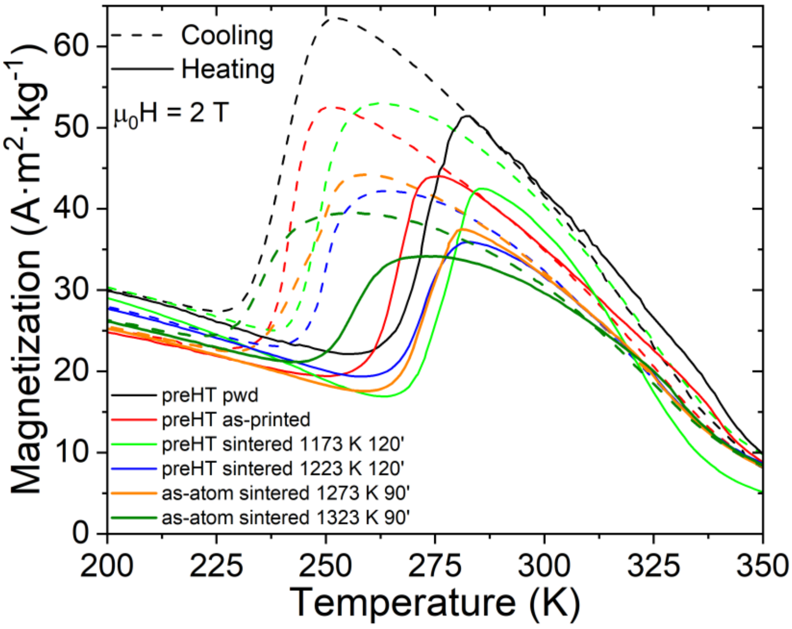

Figure 5.37: Thermomagnetization curves at 2T of magnetic field for different sintering temperatures.

5.2.3.2.5. Magnetocaloric effect: Magnetic entropy change

In the same manner as done previously, the magnetic entropy is calculated by integrating numerically the thermomagnetization curves from Figure 5.34. Figure 5.38 shows de magnetic entropy change for each sintered sample at different temperature, compared to the heat treated powder and as-printed structure at 2T of magentic field. In accordance with Figure 5.33, the magnetic entropy in figure 5.34 is lower for increasing sintering temperature in cooling ramp. However, for heating ramp, this difference is not as much accentuated.

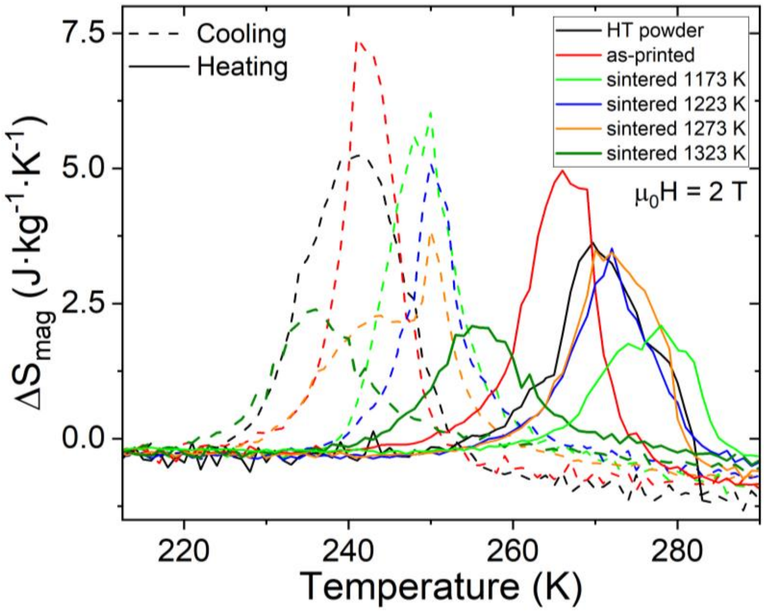

Figure 5.38: Magnetic entropy change at 2 T calculated from thermomagnetization curves.

5.2.3.2.6. Mechanical characterization

The same mechanical characterization under compression that was performed to the commercial powder printed strcutures is performed for the magnetocaloric NiMnSn as-printed and sintered structures (Figure 5.39). The sintering process produced some cracks in the NiMnSn structure as can be seen in Figure 5.39 right, resulting in the noise observed after the yield point in the force vs strain curve (Figure 5.40 right).

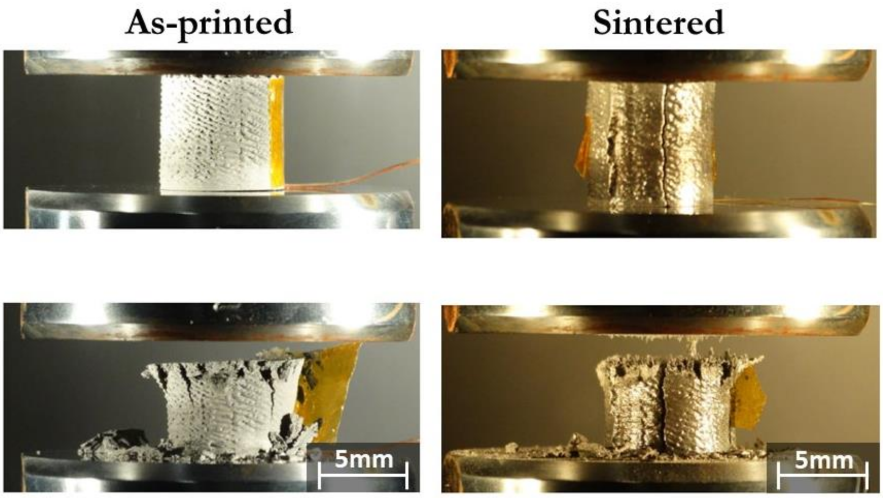

Figure 5.39: Compression tests for as-printed NiMnSn structure (left) and sintered one (right).

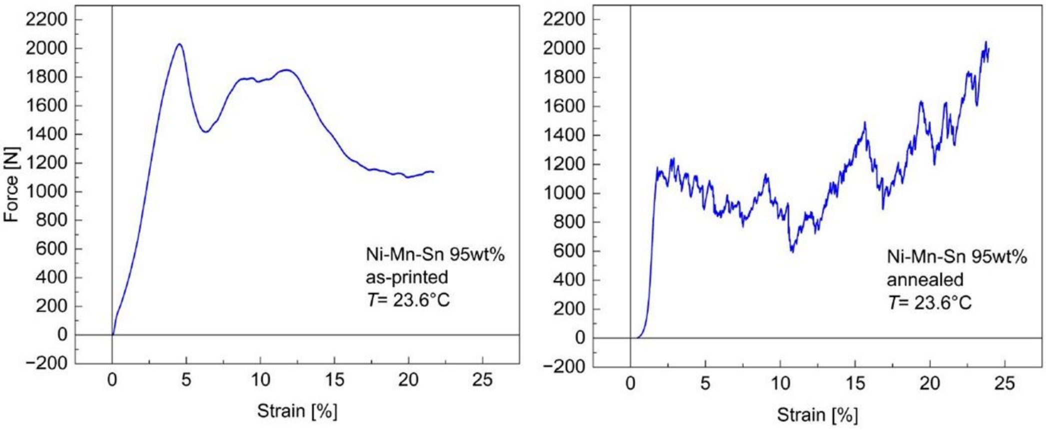

Figure 5.40: Force versus strain curves for as-printed (left) and sintered (right) Ni-Mn-Sn samples.

5.3. CONCLUSIONS

In this chapter we have developed the technological routes for printable metallic ink preparation. The first approach with 2D screen-printing technique showed the magnetocaloric properties are kept in each step from ribbon production to printing. On the other hand, using commercial powders a novel cold-extrusion printing technique was implemented and optimized. 3D structures were printed reaching more than 200 layers. In order to get about 100% metallicity and high structural integrity, post-heat treatment routes were sistematically explored for calcination and sintering stages. Then, the same steps were applied to the selected magnetocaloric powders. As a result, the magnetocaloric powder obtained from ribbon grinding retained the magnetocaloroic properties after the calcination heat treatment but not after the sintering, due to a very high surface to volume ratio. In the case of gas-atomized magnetocaloroic powder, the MCE properties were retained with slight degradation after the sintering while keeping high structural integrity, whereby validating the 3D printing technique for getting about 100% metallic magnetocaloric structures. These structures can serve as experimental samples of the heat exchangers.

5.4. REFERENCES

[1] L. Dai, D. Xu, Polyethylene surface enhancement by corona and chemical co-treatment, Tetrahedron Lett. 60 (2019) 1005–1010. https://doi.org/10.1016/j.tetlet.2019.03.013.

[2] E. Östmark, S. Harrison, K.L. Wooley, E.E. Malmström, Comb polymers prepared by ATRP from hydroxypropyl cellulose, Biomacromolecules. 8 (2007) 1138–1148. https://doi.org/10.1021/bm061043w.

[3] K.N. Al-Milaji, S. Gupta, V.K. Pecharsky, R. Barua, H. Zhao, R.L. Hadimani, Differential effect of magnetic alignment on additive manufacturing of magnetocaloric particles, AIP Adv. 10 (2020). https://doi.org/10.1063/1.5130028.

[4] K.N. Al-Milaji, R.L. Hadimani, S. Gupta, V.K. Pecharsky, H. Zhao, Inkjet Printing of Magnetic Particles Toward Anisotropic Magnetic Properties, Sci. Rep. 9 (2019) 1–9. https://doi.org/10.1038/s41598-019-52699-0.

[5] P. Lázpita, M. Sasmaz, E. Cesari, J.M. Barandiarán, J. Gutiérrez, V.A. Chernenko, Martensitic transformation and magnetic field induced effects in Ni42Co8Mn39Sn11 metamagnetic shape memory alloy, Acta Mater. 109 (2016) 170–176. https://doi.org/10.1016/J.ACTAMAT.2016.02.046.

[6] A.G. Danilevich, V.A. L'vov, Elastically driven metamagnetic-like phase transformations of shape memory alloys, J. Phys. D. Appl. Phys. 49 (2016) 105001. https://doi.org/10.1088/0022-3727/49/10/105001.

[7] V.A. Chernenko, V.A. L'vov, E. Cesari, J.M. Barandiaran, Fundamentals of magnetocaloric effect in magnetic shape memory alloys, 1st ed., Elsevier B.V., 2019. https://doi.org/10.1016/bs.hmm.2019.03.001.

[8] V.K. Pecharsky, K.A. Gschneidner, A.O. Pecharsky, A.M. Tishin, Thermodynamics of the magnetocaloric effect, Phys. Rev. B. 64 (2001) 144406. https://doi.org/10.1103/PhysRevB.64.144406.

[9] T. Krenke, E. Duman, M. Acet, E.F. Wassermann, X. Moya, L. Manosa, A. Planes, Inverse magnetocaloric effect in ferromagnetic Ni-Mn-Sn alloys, Nat. Mater. 4 (2005) 450–454. https://doi.org/10.1038/nmat1395.

[10] V.K. Pecharsky, K.A. Gschneidner, Magnetocaloric effect from indirect measurements: Magnetization and heat capacity, J. Appl. Phys. 86 (1999) 565–575. https://doi.org/10.1063/1.370767.

[11] N.A. De Oliveira, P.J. Von Ranke, Magnetocaloric effect around a magnetic phase transition, Phys. Rev. B - Condens. Matter Mater. Phys. 77 (2008) 1–8. https://doi.org/10.1103/PhysRevB.77.214439.

[12] A.M.G. Carvalho, A.A. Coelho, P.J. Von Ranke, C.S. Alves, The isothermal variation of the entropy (ΔST) may be miscalculated from magnetization isotherms in some cases: MnAs and Gd5Ge2Si2 compounds as examples, J. Alloys Compd. 509 (2011)

3452–3456. https://doi.org/10.1016/J.JALLCOM.2010.12.088.

[13] V.K. Pecharsky, J. Gschneidner K. A., Giant Magnetocaloric Effect in Gd5Si2Ge2, Phys. Rev. Lett. 78 (1997) 4494–4497. https://doi.org/10.1103/PhysRevLett.78.4494.

[14] F. Hu, B. Shen, J. Sun, Z. Cheng, G. Rao, X. Zhang, Influence of negative lattice expansion and metamagnetic transition on magnetic entropy change in the compound LaFe11.4Si1.6, Appl. Phys. Lett. 78 (2001) 3675–3677. https://doi.org/10.1063/1.1375836.

[15] K. Liu, S. Ma, C. Ma, X. Han, K. Yu, S. Yang, Z. Zhang, Y. Song, X. Luo, C. Chen, S.U. Rehman, Z. Zhong, Martensitic transformation and giant magneto-functional properties in all-d-metal Ni-Co-Mn-Ti alloy ribbons, J. Alloys Compd. 790 (2019) 78–92. https://doi.org/10.1016/J.JALLCOM.2019.03.173.

[16] V. a. Chernenko, J.M. Barandiarán, J. Rodriguez Fernández, D.P. Rojas, J. Gutiérrez, P. Lázpita, I. Orue, Magnetic and magnetocaloric properties of martensitic Ni2Mn1.4Sn0.6 Heusler alloy, J. Magn. Magn. Mater. 324 (2012) 3519–3523. https://doi.org/10.1016/j.jmmm.2012.02.080.

[17] D. Bourgault, L. Porcar, S. Rivoirard, P. Courtois, V. Hardy, Entropy change of a Ni45.5Co4.5Mn37In13 single crystal studied by scanning calorimetry in high magnetic fields: Field dependence of the magnetocaloric effect, Appl. Phys. Lett. 107 (2015) 92403. https://doi.org/10.1063/1.4929950.

[18] D. Salazar-Jaramillo, P. Álvarez-Alonso, P. Lázpita, J.L. Sánchez Llamazares, P. Gorría, J.A. Blanco, V.A. Chernenko, Magnetocaloric Effect in Specially Designed Materials, Magn. Nanostructured Mater. From Lab to Fab. (2018) 199–244. https://doi.org/10.1016/B978-0-12-813904-2.00007-3.

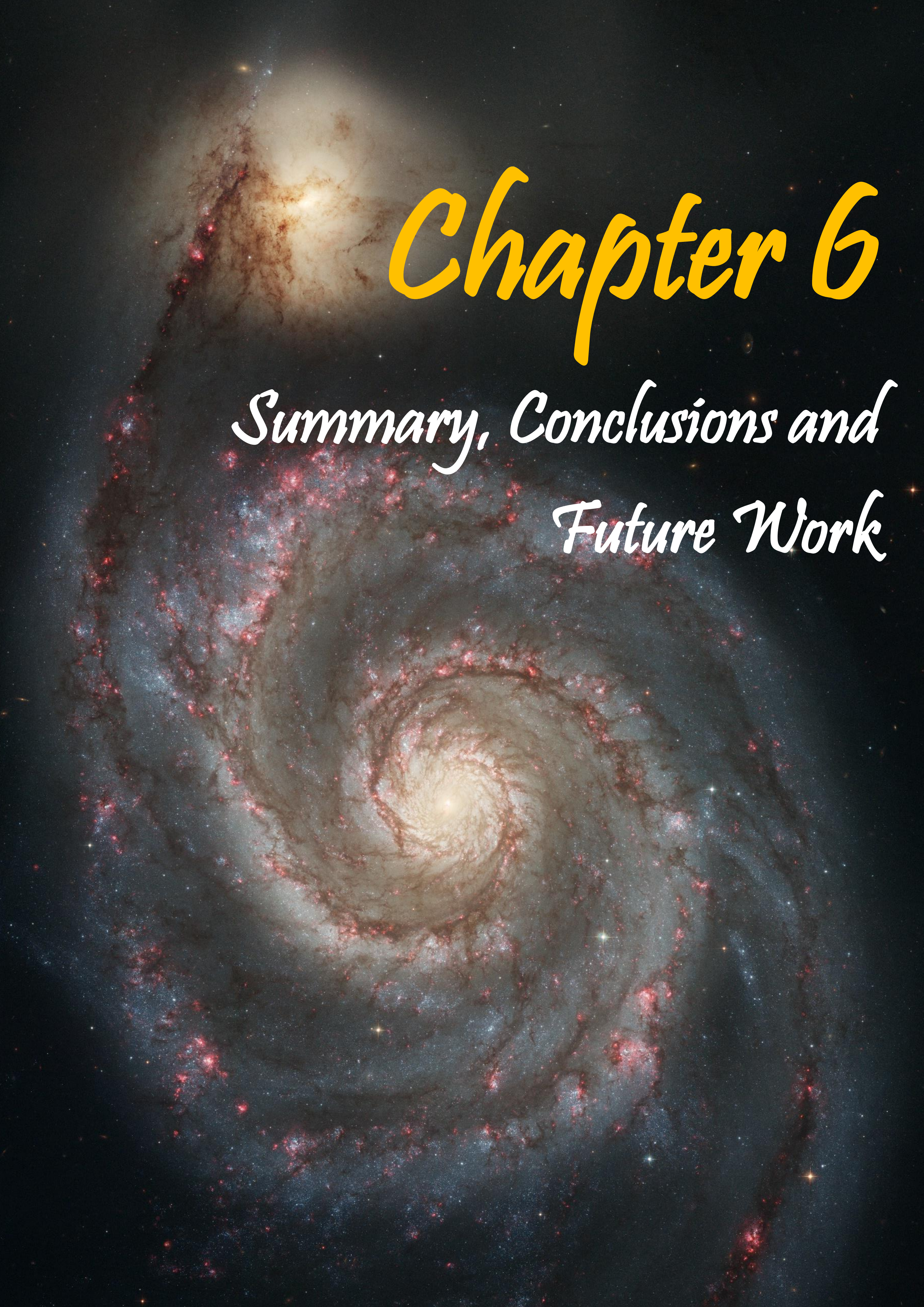

Chapter 6

Summary, Conclusions and Future Work

Chapter 6

Summary, Conclusions and Future Work

6.1. SUMMARY

The main purpose of this work was to study the transformation behaviour, magnetic and magnetocaloric properties of Heusler-type NiMn-based magnetic shape memory alloys (MSMAs) in a ribbon and powder forms, the powders being used for designing printable magnetocaloric inks for implementation in additive manufacturing technology. Different Heusler alloy compositions of NiMnX (X=Sn,In,Ga) doped with Co, Cu, Fe were prepared in a ribbon form and characterized in order to establish a route for the magnetocaloric powder production using selected ribbons. A new metal/polymer inks and their 3D printing technique were elaborated validating the technique using commercial metallic powders followed by its implementation to magnetocaloric powders.

Actually, magnetocaloric inks and the technology for their fabrication were developed for the first time in the present work. The novel technological route comprises two core stages: (a) a room temperature preparation of the MSMA powder from the melt-spun ribbon with already adjusted transformation, magnetic and magnetocaloric characteristics, followed by (b) a room temperature synthesis of the printable ink using this powder and HPC as polymer binder.

An implementation of the melt-spinning of the master bulk alloy into thin ribbon has eliminated big uncertainties always encountered when someone intends to translate functionality of the bulk MSMA into its directly prepared powder, e.g., by a ball-milling. This method allowed avoiding or minimizing the content of residual strains, defects or segregations in the material alongside getting micro-sized grain structure suitable for easy disintegration into powder.

From a long list (nine) of the prepared and studied ribbons in the present work, according to their transformation and magnetic characteristics achieved, three NiMnSn-based ribbons were selected for verification of their magnetocaloric efficiency, preparation of both the MCE powder and printing ink. Finally, the designed inks were used for 2D and 3D printing of the heat exchangers prototypes.

Preparation of MCE powders

The first ribbon, $Ni_{40}Mn_{42.5}Co_7Sn_{9.5}$, showed suitable martensitic transformation (MT) characteristics near room temperature that was possible to optimize after heat treatment. After manually grinding, the MT and magnetic properties of the powder were degraded, but further heat treatment recovered the desired properties. It was verified in the present work that both the ribbon and prepared from it powder exhibit almost identical behaviour in response to the heat treatment, revealing the similar MT, magnetic and MCE parameters. Moreover, the ink prepared from this powder was successfully used for room-temperature 2D screen-printing of mini chips on polymer substrate suitable for MCE cooling of MEMS. It was experimentally verified that these chips exhibit similar magnetocaloric performance as the ribbon: near the room temperature magnetic field induced adiabatic temperature change was measured to be $\Delta T_{ad} = 1.0$ K under $\Delta H = 1.8$ T.

Similarly to the previous alloy, the second Heusler-type magnetocaloric $Ni_{43}Co_7Mn_{39}Sn_{11}$ (at.%) powder was prepared from its ribbon state by the aforementioned technologically simple method of preparation and heat treatment. The transformation behaviour, magnetic and magnetocaloric properties of the powder samples as a function of the heat treatment regime were systematically studied by DSC and magnetic measurements. It was shown that the heat-treated powder exhibited large values of magnetic field induced isothermal entropy change at 2T of $\Delta S_{mag,max}$ =20 J·kg^{-1}·K^{-1} in heating ramp as well as a high refrigeration capacity of RC = 88 J· kg^{-1} at the same magnetic field.

The third powder was a ternary $Ni_{49.8}Mn_{36.6}Sn_{13.6}$ MSMA obtained by gas-atomization. Although it exhibits MT about 50 K below room temperature, due to its abundant availability and promising magnetocaloric properties, it was very useful to elaborate different shapes of 3D printed structures as prototypes of heat exchangers.

After validating of the developed ink technology for a 2D screen-printing using the $Ni_{40}Mn_{42.5}Co_{7}Sn_{9.5}$ powder, a transfer to 3D printing was done using, first, the model objects like pure metals in the powder form and then the second MCE powders.

3D printing of inks made of commercial powder

A lot of efforts had been made for the elaboration of sustainable metal/polymer inks for 3D printing, which appeared to be a new technological approach in additive manufacturing. Several inks were prepared using commercial Iron, Aluminium and Silicon powders to develop a strategy of getting 3D compact structures using the novel cold-extrusion printing technology. After overcoming the most challenging step, consisted in developing optimal ink with proper viscosity and polymer-to-powder volume fraction, several geometries were successfully printed using Hydroxypropyl cellulose as polymeric binder. Printing limitations were found out, whereby the optimal printable structures resulted in honeycomb-like structures and close circuits perimeter-like structures. Post-heat treatment route was studied for polymer removal by calcination and for structure compactification by sintering.

Iron structures were successfully sintered, keeping very good structural integrity. However, aluminium and silicon inks were not sintered properly, due to a reaction of the aluminium with the polymer and due to the lack of power of the laboratory furnaces necessary for silicon sintering, respectively.
Once the 3D printing route was successfully established with the commercial powders, the process was implemented to the magnetocaloric inks produced from three aforementioned powders.

3D printing of inks made of NiMnSn-based MSMAs

The MCE $Ni_{40}Mn_{42.5}Co_7Sn_{9.5}$ ink was used to print labyrinth-like structure having quite thin walls. This structure has shown $\Delta T_{ad,max}$ = 1.0 K under ΔH = 1.8 T and $\Delta S_{m,max}$ =15 J/kg K after calcination at 698 K for 60 min. After sintering the structure lost its magnetocaloric properties. This is because a quantity of this powder was restricted, which was only enough to print mentioned thin-wall structure with a very high surface-to-volume ratio that favoured the manganese evaporation and high level of oxidation in the sintering process.

The MCE $Ni_{49.8}Mn_{36.6}Sn_{13.6}$ ink prepared from gas atomized powder was available in a big quantity, allowing printing large structures that kept the magnetocaloric properties after the sintering, with a little degradation of MT. With this powder, it was also possible a systematic study of sintering route. Particularly, the sintering temperature effect on transformation characteristics and on mechanical integrity was studied in detail. It was found that the higher is the sintering temperature the better structural integrity can be achieved, although the magnetocaloric properties were somewhat deteriorated. The optimal sintering temperature was found to be 1273 K since this resulted in the minimum temperature necessary for full sintering the structure while maintaining adequate magnetocaloric properties ($\Delta S_{m,max}$= 3.7 J/kg K at 2 T).

This result strongly supports the fulfilment of the main goal of the present work. The general conclusions of the work are summarized as follows.

6.2. CONCLUSIONS

From this thesis we summarize the following conclusions:

1. A series of Heusler-type NiMnX (X=Sn,In,Ga) magnetic shape memory alloys doped with Co, Cu, Fe were prepared in the ribbon form by melt-spinning technique. The optimal heat treatment that improved both the transformation characteristics and magnetocaloric properties was found to be 1173K for 60’ plus 723K for 30’, both heat treatments followed by quenching in iced water.

2. Selected ribbons were used to prepare powders by manual grinding. It was found that the transformation and magnetocaloric properties of powders, which were degraded in the grinding process, were recovered after the same heat treatment performed to the ribbons.

3. Hydroxypropyl cellulose (HPC) was validated as a suitable environmentally-friendly polymer for 2D and 3D printing of metallic structures. Its high processability capacity combined with ease of use allowed to print flexible 2D chips by screen-printing and rigid 3D structures with more than 200 layers. The room temperature metal/polymer printing inks were developed for the first time as a novel additive manufacturing technique, which was validated using commercial Iron, Aluminium and Silicon powders.

4. Post heat treatment route was systematically elaborated for polymer removal by calcination followed by a sintering process for obtaining 100% metallic structures. Iron inks were successfully calcinated and sintered. The sintering stage was not effective for Aluminium and Silicon structures: in the case of the Aluminium due to a reaction with the remaining carbon and in the case of Silicon due to the instrumental restriction.

5. Selected magnetocaloric powders were implemented in the 2D screen-printing being able to print 10 layered flexible chips that kept the magnetocaloric properties of the precursor material.

6. $Ni_{40}Mn_{42.5}Co_7Sn_{9.5}$ magnetocaloric powders were printed by 3D cold-extrusion printing technique. It was found that as-printed structures inherited magnetocaloric properties from the ribbons, which were deteriorated after sintering process due to a partial evaporation and oxidation of Mn resulting from high surface-to-volume ratio of the printed structures.

7. Magnetocaloric $Ni_{49.8}Mn_{36.6}Sn_{13.6}$ powders were successfully 3D printed and sintered. A systematic study of sintering route showed the optimal sintering temperature to be 1273K while maintaining a proper structural integrity and slight magnetocaloric performance detriment.

6.3. FUTURE WORK

The Heusler-type MCE materials investigated in the present work exhibit enhanced hysteresis of MT which is making difficult to explore them in a cycling regime. Although there exist in the literature some recipes handling with enhanced hysteresis, e.g., incorporating the elastocaloric part in the cooling cycle, it would be more rational to elaborate MSMAs exhibiting MT hysteresis below 5 K. According to the literature, alongside six-component NiMn(In,Sn,Sb)+three dopants, the good candidates are also Heusler NiMnGa(Cu,Fe,Co) MSMAs showing merged MT and Curie temperature. In any case, before or after resolving hysteresis issue, the next step can be focused on the implementation of a larger printed structures, using already known MCE Heusler alloys, as the heat exchangers in a magnetic refrigerator prototypes. This would enable the full characterization of the efficiency of both the MSMA material and the 3D printing technique. In turn, the developed magnetocaloric chips can be evaluated by integration with MEMS and flexible electronics as prototypes of cooling microdevices.

Annex: Scientific Contributions

Publications part of the thesis

1. B. Rodríguez-Crespo, D. Salazar, S. Lanceros-Méndez, V. Chernenko; "*Development and magnetocaloric properties of Ni (Co)-Mn-Sn printing ink*" *Journal of Alloys and Compounds*, vol. 917 (2022) 165521.

2. Bosco Rodriguez-Crespo, Natalia Rio-Lopez, Patricia Lazpita, Mariana Rios, Daniel Domenech, José Alberto Rodríguez-Velamazán, Volodymyr Chernenko, Jose Maria Porro, Daniel Salazar; "*Unraveling the Impact of Atomic Ordering on the Magnetocaloric Performance of Powdered Nicomnsn Metamagnetic Shape Memory Ribbons*", Submitted to *Journal of Alloys and Compounds*, 2023

Other publications

1. Bosco Rodriguez-Crespo, Andrés García-Franco, James Janderson Rosero-Romo, Christina Echevarria-Bonet, Jose Maria Poroo, Paula G. Saiz, Daniel Salazar; "*Magnetic properties of tetragonal SmFe12-xMox alloys in bulk and melt-spun Ribbons*", *Physica Status Solidi*, vol. 219 (2022), nº15 2100725.

2. Marisela Benitez, Lorena Marín, Bosco Rodríguez-Crespo, Daniel Salazar, Jesús A Tabares, Juan Sebastián Trujillo, Germán A Pérez, Luis A Rodríguez, Ligia E Zamora; "*Synthesis and characterization of LaFe11. 57Si1. 43 and LaFe11. 57Si1. 43H alloys for magnetic refrigeration applications*", *Journal of Alloys and Compounds*, vol. 969 (2023) 172393.

3. E. Villa, F. Villa, B. Rodriguez Crespo, P. Lazpita, D. Salazar, H. Hosoda, V. Chernenko; "*Shape memory and elastocaloric properties of melt-spun NiMn-based Heusler alloys*", *Journal of Alloys and Compounds*, vol. 965 (2023) 171437.

4. M Norouzi-Inallu, P Kameli, A Ghotbi Varzaneh, I Abdolhosseini Sarsari, M Abbasi Eskandari, I Orue, B Rodríguez-Crespo, V Chernenko; "*Influence of W doping on the structure, magnetism and exchange bias in Ni47Mn40Sn13− x W x Heusler alloys*", *Journal of Physics: Condensed Matter*, vol. 34, n. 22 (2022) 225803.

Invited talks

1. JEMS 2020. Lisbon, Portugal (December 7th – 11th, 2020) – Invited Talk. "*Development of Heusler-type magnetocaloric screen-printing inks*". Bosco Rodriguez-Crespo, Daniel Salazar, Volodymyr Chernenko.

Oral presentations

1. EMR-S Spring meeting 2021. Strasbourg, France (May 31st – June 3rd , 2021) – Oral Presentation. "*Manufacturing and processing of metamagnetic shape memory alloys with magnetocaloric effect for screen-printing inks*". Bosco Rodriguez-Crespo, Daniel Salazar, Volodymyr Chernenko.

2. Eurotherm 2021. Netherlands (July 13th– 15th, 2021) – Oral Presentation. "*Development of Heusler-type magnetocaloric materials inks for additive manufacturing*". Bosco Rodriguez-Crespo, Daniel Salazar, Volodymyr Chernenko.

3. TMS 2022. Anaheim (LA), USA (February 27th – March 3rd, 2022) – Oral Presentation. "*Additive manufacturing of 3D metallic structures: An environmentally-friendly way of printing Cellulose-based metallic inks*". Bosco Rodriguez-Crespo, David Payno, Daniel Salazar, Volodymyr Chernenko.

4. JEMS 2022. Warsaw, Poland (July 24th – 29th, 2022) – Oral Presentation. "*Additive manufacturing of 3D metallic structures: An environmentally-friendly way of printing Cellulose-based metallic inks*". Bosco Rodriguez-Crespo, Daniel Salazar, Volodymyr Chernenko.

5. JEMS 2023. Madrid, Spain (August 27th – September 1st). Oral Presentation. *"Additive manufacturing of magnetocaloric 3D structures: a cost-effective way for printing cellulose-based metallic structures"*. Bosco Rodriguez-Crespo, Daniel Salazar, Volodymyr Chernenko.

Poster presentations

1. EMR-S Spring meeting 2021. Strasbourg, France (May 31st – June 3rd, 2021) – Poster Presentation. "*Magnetic properties of tetragonal SmFe12-xMox in bulk and melt-spun ribbons*". Bosco Rodriguez Crespo, Daniel Salazar, Cristina Echevarria, Jose J.S. Garitaonandia, Manuel Barandiaran.